INFORMATION TO USERS

This manuscript has been reproduced from the microfilm master. UMI films the text directly from the original or copy submitted. Thus, some thesis and dissertation copies are in typewriter face, while others may be from any type of computer printer.

The quality of this reproduction is dependent upon the quality of the copy submitted. Broken or indistinct print, colored or poor quality illustrations and photographs, print bleedthrough, substandard margins, and improper alignment can adversely affect reproduction.

In the unlikely event that the author did not send UMI a complete manuscript and there are missing pages, these will be noted. Also, if unauthorized copyright material had to be removed, a note will indicate the deletion.

Oversize materials (e.g., maps, drawings, charts) are reproduced by sectioning the original, beginning at the upper left-hand corner and continuing from left to right in equal sections with small overlaps. Each original is also photographed in one exposure and is included in reduced form at the back of the book.

Photographs included in the original manuscript have been reproduced xerographically in this copy. Higher quality 6" x 9" black and white photographic prints are available for any photographs or illustrations appearing in this copy for an additional charge. Contact UMI directly to order.

Multiplicity distributions from p̄-p collisions at 1.8 TeV center of
mass energy

Wang, Chi-Ho, Ph.D.

Iowa State University, 1991

NOTE TO USERS

THE ORIGINAL DOCUMENT RECEIVED BY U.M.I. CONTAINED PAGES WITH SLANTED AND POOR PRINT. PAGES WERE FILMED AS RECEIVED.

THIS REPRODUCTION IS THE BEST AVAILABLE COPY.

Multiplicity distributions from p̄-p collisions

at 1.8 TeV center of mass energy

by

Chi-Ho Wang

A Dissertation Submitted to the

Graduate Faculty in Partial Fulfillment of the

Requirements for the Degree of

DOCTOR OF PHILOSOPHY

Department: Physics and Astronomy
Major: High Energy Physics

Approved:

In Charge of Major Work

For the Major Department

For the Graduate College

Members of the Committee:

Iowa State University
Ames, Iowa
1991

TABLE OF CONTENTS

LIST OF TABLES

LIST OF FIGURES

ACKNOWLEDGEMENTS

CHAPTER 1. INTRODUCTION

The study of the basic constituents of matter and the forces of nature has progressed remarkably in the past two decades. In 1970, there was basically no real theory about weak or strong interactions. The list of 'elementary particles' then consisted of leptons and hadrons, including an embarrassingly large number of resonances. Today, we believe quarks and leptons are the fundamental building blocks of matter which interact via exchange of gauge bosons, and from these quarks hadrons are built. The weak force and the electromagnetic force, described by the theory of quantum electrodynamics (QED), have been unified into the electroweak force, whose gauge bosons are the photon and the $W^{\pm}$ and Z°. The strong force is described by quantum chromodynamics (QCD), whose gauge bosons are the eight gluons. QCD and the electroweak theory now form the framework of what is referred to as the 'standard model'.

When two elementary particles collide at high energy, a significant amount of energy can contribute to creation of other elementary particles, which may result in a complicated multiparticle final state. If there is large momentum transfer between the two colliding particles or their constituents, the process can be described very well by perturbative QCD, since the coupling strength decreases with impact parameter, and perturbation techniques may be used. On the other hand, if the momentum transfer is

small, perturbation theory fails and the phenomena are not directly calculable. These soft collisions, involving small momentum transfer, are, nevertheless, responsible for most of the collision cross section. Thus, an understanding of these processes is of great importance.

In multiparticle final states, the multiplicity distributions are directly measured, and reflect the underlying physics. The form of these distributions can contribute to the development of a phenomenological picture of nonperturbative QCD.

The ultimate in "soft" physics would be the formation of a quark-gluon plasma where individual hadrons dissolve into a "soup" of quarks and gluons at very high energies. Such a state, if deconfined, would result in events with high multiplicity final states. Experiment 735 in Fermilab was designed to search for a possible phase transition to a quark-gluon plasma using $\bar{p}$-p collisions in the Fermilab Tevatron collider at 1.8 TeV c.m. energy. One of the proposed signatures[1, 2] would be evidenced in the average transverse momentum ($\langle P_t \rangle$) as a function of charged particle multiplicity in the central rapidity region ($dN_c/dy |_{y=0}$). According to statistical thermodynamics, $\langle P_t \rangle$ is proportional to the temperature, and dN/dy is proportional to the entropy density. The entropy and energy densities, if normalized to a Stefan-Boltzman model, for example, would have the same functional dependence on $\langle P_t \rangle$. Thus, if there is a first order phase transition from hadronic matter to quark-gluon plasma, the curve will look similar to the phase transition for liquid into vapor (Figure 1.1). For this analysis the multiplicity of each individual event is required.

In this thesis we will study the multiplicity distributions obtained from the multiplicity hodoscope in E-735 during the data acquisition period of 1988-1989.
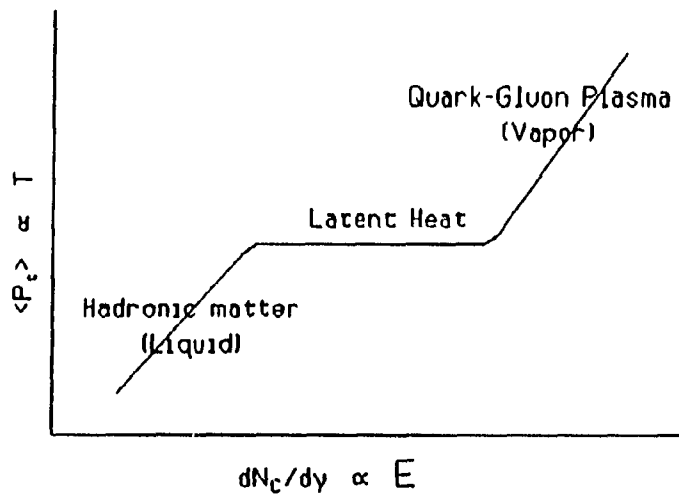
Figure 1.1:   A first order phase transition

CHAPTER 2. MULTIPLICITY DISTRIBUTIONS

In high energy collisions of particles, if secondaries were produced randomly and independently, one would expect their multiplicity distributions to be Poisson distributed. In reality, the multiplicity distributions deviate significantly from a Poisson distribution, and the differences may be regarded as a source of information on the underlying production mechanism. In recent years, KNO-G and the negative binomial distributions (NBD) have been shown to fit the data quite well for center of mass energies up to 546 GeV[3, 4, 6, 7]. Here, we will discuss the characteristics of these distribution functions and the nature of the data collected from elementary particle collisions.

In our notation, the "genuine" multiplicity, which counts the number of "charged pairs" produced in the interaction, is denoted by n, and the total charged multiplicity is denoted by n_{ch}. For a given type of elementary particle collision, they can be trivially converted into each other, e.g. for a p-$\bar{\text{p}}$ collision :

$$n \; = \; n_- - 1 \; = \; n_+ - 1 \; = \; (n_{ch} - 2)/2, \tag{2.1}$$

and for a p-p collision :

$$n \; = \; n_- \; = \; n_+ - 2 \; = \; (n_{ch} - 2)/2. \tag{2.2}$$

The momentum components of a particle are conveniently expressed by its lon-

gitudinal rapidity and its transverse momentum relative to the incident beam(s). Let the incident beam(s) be along the z axis. The transverse momentum is :

$$p_t = \sqrt{p_x^2 + p_y^2}, \tag{2.3}$$

and the longitudinal rapidity is :

$$y = \frac{1}{2} \ln \frac{E + p_z}{E - p_z}, \tag{2.4}$$

where E is the total energy of the particle. The rapidity is, by definition, the rotation angle between the time and the space coordinates when one treats the Lorentz transformation as a rotation in four dimensional space-time. Thus, it has the convenient property of being an additive quantity under Lorentz transformation. A related quantity frequently used is the pseudo-rapidity (η) which is the rapidity of a particle with its mass assumed to be 0 :

$$\eta = \frac{1}{2} \ln \frac{|\vec{p}| + p_z}{|\vec{p}| - p_z} = \ln(\cot(\frac{\theta}{2})), \tag{2.5}$$

where θ is the polar angle against z axis, and the quantity η becomes purely geometrical.

The choice of these variables is for the convenience of describing the characteristics of particle production as we understand them today. The inclusive invariant cross section for the production of a particle is :

$$f = E \frac{d^3\sigma}{d^3\vec{p}} = \frac{1}{\pi} \frac{d^2\sigma}{dy dp_t^2}. \tag{2.6}$$

It was found experimentally that at a fixed energy, the cross section can be "approximately" factorized into two terms, with each term a function of one of the
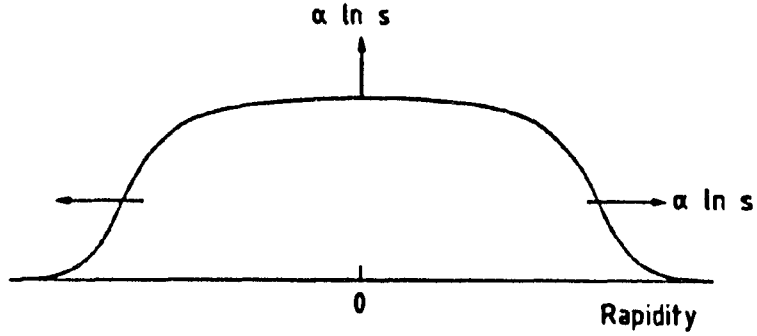
Figure 2.1: A typical rapidity distribution in soft hadron collisions.

independent variables.

$$f = \frac{1}{\pi}\frac{d^2\sigma}{dydp_t^2} \simeq Ae^{-Bp_t} \cdot F(y). \tag{2.7}$$

Experimentally $\langle p_t \rangle \sim 350$ MeV/c and is slowly increasing with total center of mass (c.m.) energy. The rapidity distribution function, $F(y)$, exhibits a plateau around $y = 0$ in the c.m. frame (Figure 2.1). The plateau defines the central region, delimited on both sides by the fragmentation regions loosely defined by $|y| > y_{max} - 2$ [9]. At high energies :

$$y_{max} = \ln\frac{E_0 + p}{m} \tag{2.8}$$

$$\approx \ln(2E_0/m) \tag{2.9}$$

$$\approx \ln(\sqrt{s}/m) \tag{2.10}$$

The height of the $y = 0$ cross section increases with increasing energy.

The First Two Moments

The first two moments of a distribution determine much of the shape and the characteristics of the distribution. Let P_n be the probability of having an event with genuine multiplicity n. The first moment is the mean or the average multiplicity :

$$\langle n \rangle = \sum_{n=0}^{\infty} n P_n \qquad (2.11)$$

which serves as a scale in the multiplicity study. The second moment is the dispersion of the distribution :

$$D_2 = [\sum_{n=0}^{\infty} (n - \langle n \rangle)^2 P_n]^{1/2} \qquad (2.12)$$

which gives information about the width of the distribution.

The mean

The average multiplicity is a slowly rising function of energy. A few functions motivated by various dynamical concepts have been suggested to describe the energy dependence. Feynman scaling[12] leads to :

$$\langle n \rangle = a + b \ln s. \qquad (2.13)$$

In Fermi statistical[13] and Landau hydrodynamic[14] models :

$$\langle n \rangle = A s^{1/4}. \qquad (2.14)$$

In a later QCD approach[15] :

$$\langle n \rangle = A \exp(\sqrt{B \ln s}). \qquad (2.15)$$
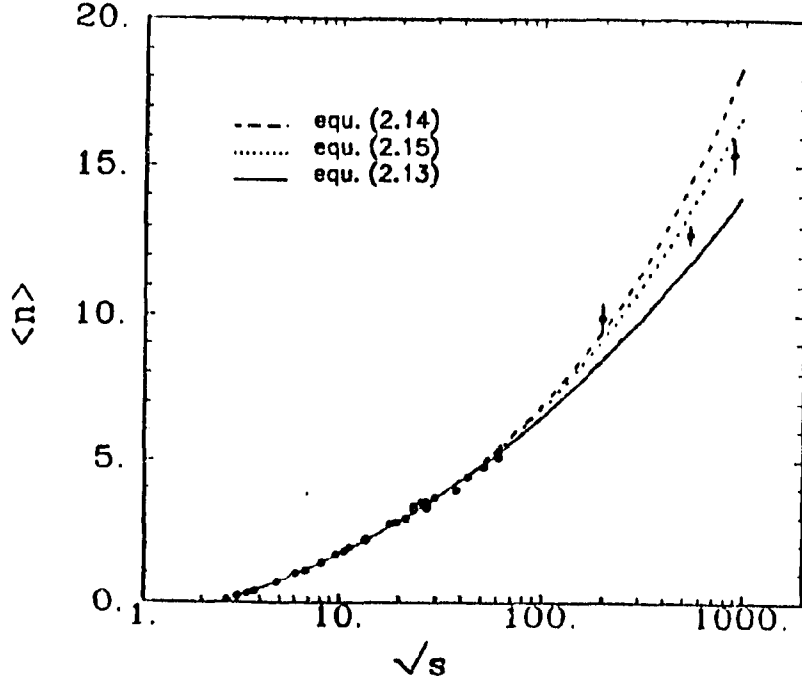
Figure 2.2: Energy dependence of average multiplicity from inelastic p-p̄ (highest 3 points) and p-p data.

These simple formulae above, however, do not fit very well to the data, and usually modifications are made :

$$\langle n \rangle \quad = \quad a + b\ln s + c(\ln s)^2 \tag{2.16}$$

$$\langle n \rangle \quad = \quad n_0 + Bs^\alpha \tag{2.17}$$

$$\langle n \rangle \quad = \quad A\exp(\sqrt{B\ln s}) + \gamma \tag{2.18}$$

With a little sacrifice of their theoretical clarity, these formulae all fit well to the data. Figure 2.2 shows the earlier data and fits to these functions[7].

The dispersion

The second moment, dispersion, is related to the width of the multiplicity distribution. The linear dependence of the dispersion on the average multiplicity, first
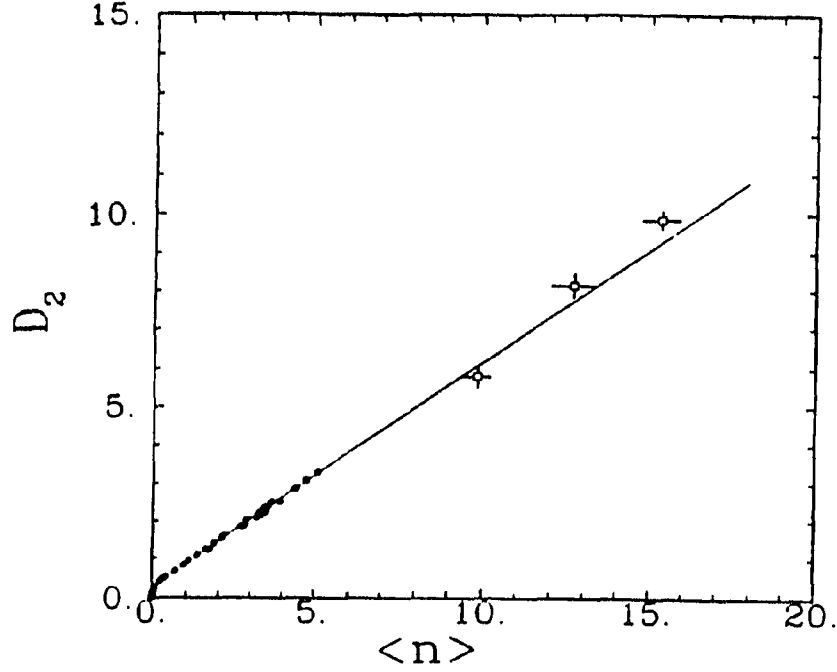
Figure 2.3: Dispersion as a function of mean from inelastic p-p (full circle) and p-p̄ (open circle) data.

observed by Wroblewski[16] in p-p inelastic data, is one of the best established empirical laws in the multiplicity study. It can be written as :

$$D_2 = A(\langle n \rangle + 1/2) \tag{2.19}$$

or

$$D_2^{ch} = A(\langle n_{ch} \rangle - 1) \tag{2.20}$$

in either p-p or p-p̄ interactions. Figure 2.3 shows the p-p and p-p̄ data up to 900 GeV. The linear dependence is obeyed starting from as low as $\langle n \rangle \approx 0.4$. The dependence at even lower energies is not expected to be linear since it approaches the energy threshold where $D_2 = 0$ and $\langle n \rangle = 0$.

KNO Scaling and KNO-G

The KNO scaling[17] was originally derived from Feynman scaling[12] for asymptotic energies. Despite of the fact that Feynman scaling is not observed, as is shown for example by the continuous rise of particle density in the central region as energy increases[28], the KNO scaling is still a useful phenomenological framework for the comparison of distributions at different energies. The original formulation was :

$$\langle n \rangle P_n = \psi(z)(1 + O(\frac{1}{\langle n \rangle})) \tag{2.21}$$

$$P_n \cong \frac{1}{\langle n \rangle}\psi(z) \tag{2.22}$$

where $z \equiv n/\langle n \rangle$, and $\psi(z)$ is an energy independent function normalized to unity :

$$
\begin{aligned}
1 &= \sum_{n=0}^{\infty} P_n = \sum_{n=0}^{\infty} \frac{1}{\langle n \rangle}\psi(\frac{n}{\langle n \rangle}) \\
&\approx \int_0^{\infty} \frac{dn}{\langle n \rangle}\psi(\frac{n}{\langle n \rangle}) = \int_0^{\infty} \psi(z)dz = 1
\end{aligned}
\tag{2.23}
$$

$$
\begin{aligned}
1 &= \langle z \rangle = \sum_{n=0}^{\infty} \frac{n}{\langle n \rangle}P_n = \sum_{n=0}^{\infty} \frac{n}{\langle n \rangle}\frac{1}{\langle n \rangle}\psi(\frac{n}{\langle n \rangle}) \\
&\approx \int_0^{\infty} \frac{n}{\langle n \rangle}\frac{dn}{\langle n \rangle}\psi(\frac{n}{\langle n \rangle}) = \int_0^{\infty} z\psi(z)dz = 1.
\end{aligned}
\tag{2.24}
$$

When the theory was applied to p-p inelastic data in the region $\sqrt{s} = 4.93 - 23.88$ GeV, it was found that the scaling function $\psi(z)$, which is supposed to be the same for all energies, changed with energy[16] ! KNO scaling was then considered violated in this energy range. However, when the finite energy correction terms were taken into account, it violated the scaling itself more than the observed violation in the data[18]. Thus, an explanation other than Feynman scaling was sought.

The argument was made on the approximate equality "$\approx$" in the normalization relations (2.23) and (2.24) for large $\langle n \rangle$. The average genuine multiplicity $\langle n \rangle$

instead of the energy itself is serving as a scale here, and, even for earlier lower energies for which $\langle n \rangle \sim 10$, the equations are so badly approximated that it is impossible to normalize P_n and $\psi(z)$ at the same time. A reformulation was made by Golokhvastov[19, 20] to make them self-consistent at all energies and is now called the KNO-G scaling.

KNO-G formulation

In KNO-G, the scaling relation (2.22) was reformulated as :

$$P(\tilde{n}) = \frac{1}{\langle \tilde{n} \rangle} \psi(\frac{\tilde{n}}{\langle \tilde{n} \rangle}), \tag{2.25}$$

where $\tilde{n}$ is a continuous variable. And P_n is redefined as :

$$P_n = \int_n^{n+1} P(\tilde{n})d\tilde{n} = \int_{n/\langle \tilde{n} \rangle}^{(n+1)/\langle \tilde{n} \rangle} \psi(z)dz, \tag{2.26}$$

where n assumes only integral values, and $z \equiv \tilde{n}/\langle \tilde{n} \rangle$. The normalization relations become :

$$1 = \sum_{n=0}^{\infty} P_n = \sum_{n=0}^{\infty} \int_{n/\langle \tilde{n} \rangle}^{(n+1)/\langle \tilde{n} \rangle} \psi(z)dz = \int_0^{\infty} \psi(z)dz = 1 \tag{2.27}$$

$$1 = \sum_{n=0}^{\infty} \frac{n}{\langle n \rangle} P_n = \int_0^{\infty} \frac{\tilde{n}}{\langle \tilde{n} \rangle} P(\tilde{n})d\tilde{n} = \int_0^{\infty} z\psi(z)dz = 1. \tag{2.28}$$

There is no change in terms of physics concept here; however, one should note that, after the reformulation, it is the continuous probability distribution $P(\tilde{n})$ instead of P_n that takes part in the scaling equation (2.25). Consequently, the quantities that should be tested for the scaling are different. For instance, the continuous moment of the kth order :

$$\tilde{C}^k = \frac{\langle \tilde{n}^k \rangle}{\langle \tilde{n} \rangle^k} = \int_0^{\infty} z^k \psi(z)dz \tag{2.29}$$

should be a constant in energy. While the discrete moment :

$$C^k = \frac{\langle n^k \rangle}{\langle n \rangle^k} = \sum_{n=0}^{\infty} \frac{n^k}{\langle n \rangle^k} P_n \qquad (2.30)$$

is allowed to change with energy. Although the two formulations are identical at asymptotic energies, where $s \to \infty$ and $\langle n \rangle \to \infty$, their differences are significant when applied to finite energy data.

Conventionally, KNO scaling was tested by plotting data in the form of $\langle n \rangle P_n$ versus $n/\langle n \rangle$ to display the scaling function $\psi(z)$ in eq. (2.22). A similar test in KNO-G is, however, not so straight forward due to the normalization. To simplify the fitting, an integral form was used :

$$\phi(z) = \int_0^z \psi(z) dz - 1. \qquad (2.31)$$

The normalization conditions for $\phi(z)$ are derived from eq. (2.27) and (2.28) :

$$\phi(0) = -1 \qquad (2.32)$$

$$\int_0^{\infty} \phi(z) dz = -1. \qquad (2.33)$$

And the probability distribution P_n is obtained by :

$$P_n = \phi(\frac{n+1}{\langle \tilde{n} \rangle}) - \phi(\frac{n}{\langle \tilde{n} \rangle}). \qquad (2.34)$$

A graphical test of KNO-G follows the cumulative relation :

$$S_n = \sum_{i=n}^{\infty} P_i = \int_{n/\langle \tilde{n} \rangle}^{\infty} \psi(z) dz = -\phi(z), \qquad z = \frac{\tilde{n}}{\langle \tilde{n} \rangle} \qquad (2.35)$$

where $\langle \tilde{n} \rangle$ can be well approximated by the relation :

$$\langle \tilde{n} \rangle = \langle n \rangle + 0.5, \qquad (2.36)$$

which is already true at $\langle n \rangle \geq 0.4$ [22]. A comparison of KNO and KNO-G with p-p inelastic data[22] at $\sqrt{s} = 2.7 - 62.2\text{GeV}$ is shown in Figure 2.4. The KNO-G is in much better agreement with data. The scaling function was chosen[21] with the form :

$$\phi(z) = -\exp(-az - bz^2),\qquad (2.37)$$

where a and b are related through eq.(2.33), and there is actually only one free parameter. The fitted values are[7] :

$$a = 0.1550 \pm 0.0034, \quad b = 0.6349, \quad \chi^2/NDF = 1.1. \qquad (2.38)$$

Generalized Wroblewski relation

A further attractive feature of KNO-G scaling is the relationship among the moments. Over the years, rules about moments have been derived from the data empirically. The origin of these rules remained a riddle until KNO-G came to the stage. The well established Wroblewski relation, as mentioned before, comes naturally from the KNO-G formulation :

$$
\begin{aligned}
D_2 \approx \tilde{D}_2 &= (\int_0^\infty (\tilde{n} - \langle \tilde{n} \rangle)^2 P(\tilde{n}) d\tilde{n})^{1/2} \\
&= (\int_0^\infty (\frac{\tilde{n}}{\langle \tilde{n} \rangle} - 1)^2 \frac{1}{\langle \tilde{n} \rangle} \psi(\frac{\tilde{n}}{\langle \tilde{n} \rangle}) d\tilde{n})^{1/2} \langle \tilde{n} \rangle \\
&= (\int_0^\infty (z - 1)^2 \psi(z) dz)^{1/2} \langle \tilde{n} \rangle \\
&= const \langle \tilde{n} \rangle \\
&= A(\langle n \rangle + 0.5). \qquad (2.39)
\end{aligned}
$$
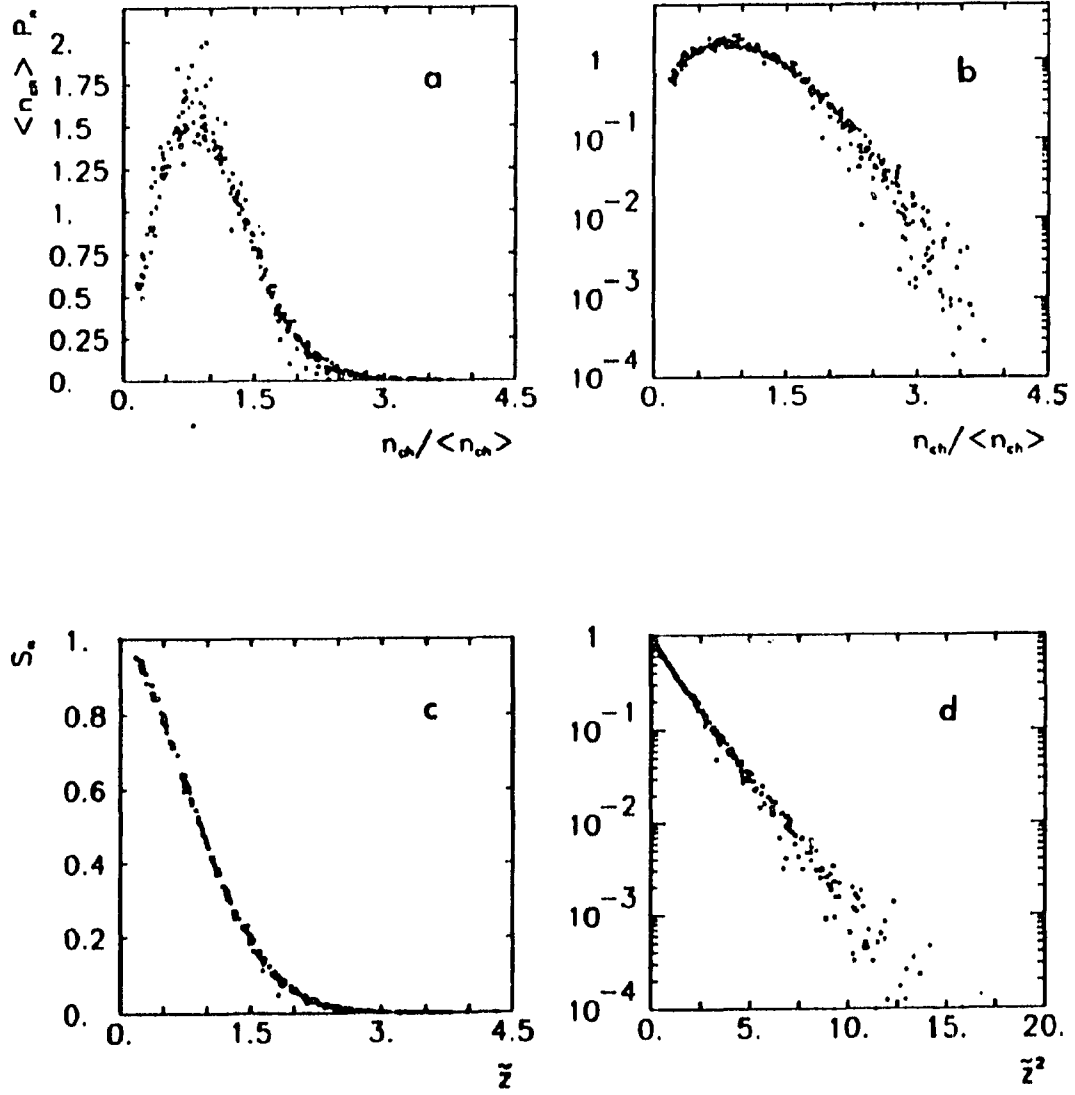
Figure 2.4: KNO(a,b) and KNO-G(c,d) for inelastic p-p data at $\sqrt{s} = 2.7 - 62.2$ GeV.

where we have made use of eq. (2.25) and (2.36). Similar arguments apply to any k^{th} order moment and leads to the "generalized Wroblewski relation"[23] :

$$D_k = A_k(\langle n \rangle + 1/2),\tag{2.40}$$

where n is the genuine multiplicity. For n_{ch} :

$$D_k^{ch} = A_k(\langle n_{ch} \rangle - 1).\tag{2.41}$$

Figure 2.5 shows D_3 and D_4 as a function of $\langle n \rangle$ from p-p inelastic data. The agreement is excellent[7].

Negative Binomial Distribution

The Negative Binomial Distribution (NBD) belongs to the family of the Poisson transforms of some probability functions frequently used in statistical physics[24]. The distribution can be written as :

$$P_n = P(n; \bar{n}, k) = \frac{k(k+1)...(k+n-1)}{n!}(\frac{\bar{n}}{\bar{n}+k})^n(\frac{k}{\bar{n}+k})^k,\tag{2.42}$$

where $\bar{n}$ is the average multiplicity and k is related to the dispersion by :

$$\frac{D_2^2}{\bar{n}^2} = \frac{1}{\bar{n}} + \frac{1}{k}.\tag{2.43}$$

The distribution can be characterized by a recurrence relation between P_n and P_{n+1} :

$$g_n = \frac{(n+1)P_{n+1}}{P_n} = a + bn\tag{2.44}$$

with $a = \bar{n}k/(\bar{n}+k)$ and $b = \bar{n}/(\bar{n}+k)$.

For $k = \infty$, $a = \bar{n}$ and $b = 0$, the distribution becomes a Poisson distribution :

$$P_n = \frac{\bar{n}^n e^{-\bar{n}}}{n!},\tag{2.45}$$
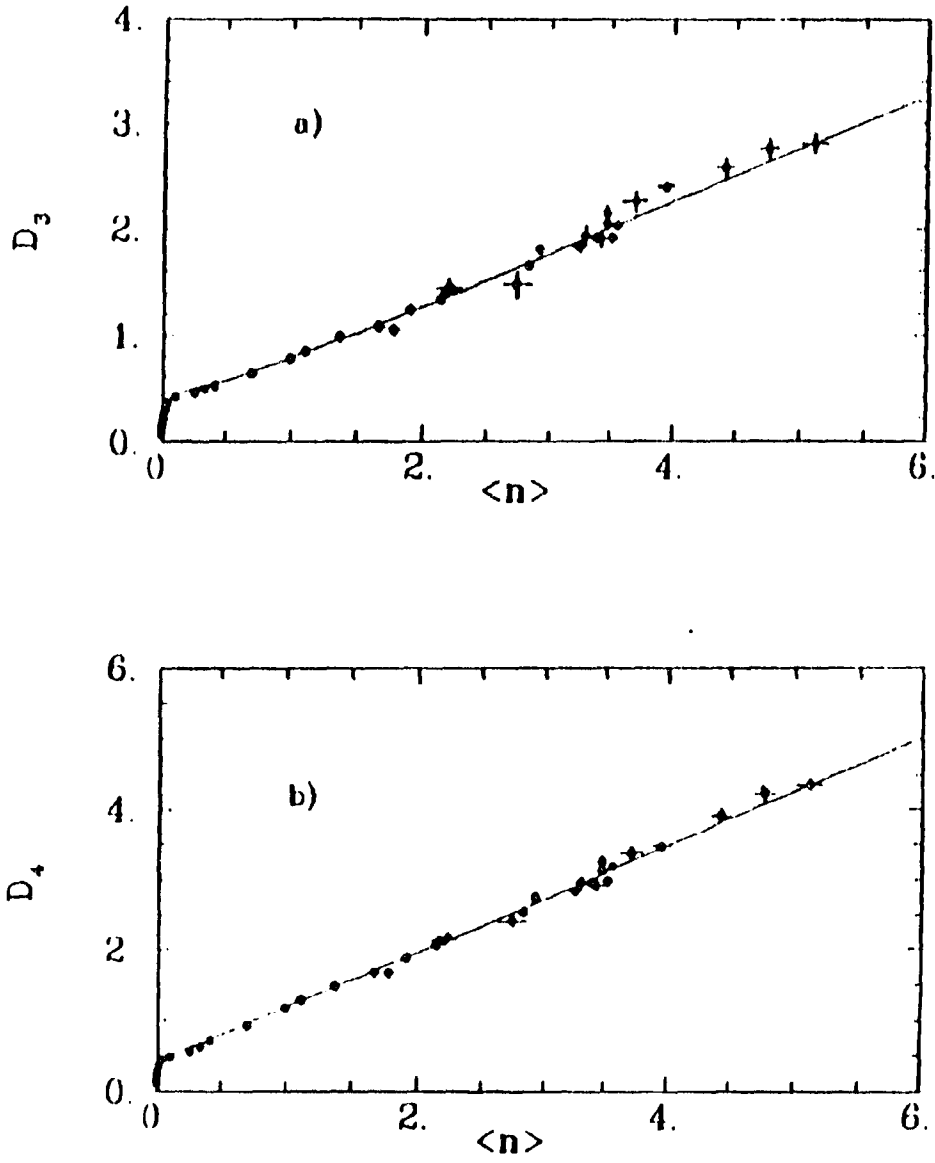
Figure 2.5: $\langle n \rangle$ dependence of D_3 and D_4 moments from inelastic p-p collisions at $\sqrt{s} = 2.7 - 62.2$ GeV.

which corresponds to independent emission of particles.

For $k = 1$, $a = b = \bar{n}/(\bar{n} + 1)$, the distribution is exponential :

$$P_n = (\frac{\bar{n}}{\bar{n} + 1})^n \frac{1}{\bar{n} + 1}, \tag{2.46}$$

which is the Bose-Einstein distribution for a single state and corresponds to full stimulated emission[25].

For $k > 0$, the distribution is a negative binomial and $D^2 > \bar{n}$. When k is a negative integer, the distribution becomes a normal binomial and $D^2 < \bar{n}$.

Cascade processes[26], for example, can be represented by negative binomial distributions. Assuming N particles ("clans") are originally emitted from the collision and each gives rise to n_c^i particles. If the production of N is Poissonian and n_c^i is logarithmic, the final distribution is NBD and the parameter $1/k$ measures the degree of aggregation :

$$\frac{1}{k} = \frac{P_1(2)}{P_2(2)}, \tag{2.47}$$

where $P_1(2)$ is the probability of finding two particles in one clan and $P_2(2)$ is the probability of finding two particles in two different clans. Models of this kind, however, suffer from the fact that when fitted to data at some lower energies, k becomes negative – a value which does not easily admit to a physical meaning.

Application of NBD to data

NBD has been shown to describe the charged multiplicity distributions well, not only for the full phase space but also for particles produced in a limited rapidity window. Figure 2.6 shows the charged multiplicity distributions in different rapidity windows[10]. The distribution becomes narrower as the rapidity bin increases and is reflected in the increase of k as shown in Figure 2.7 [10].
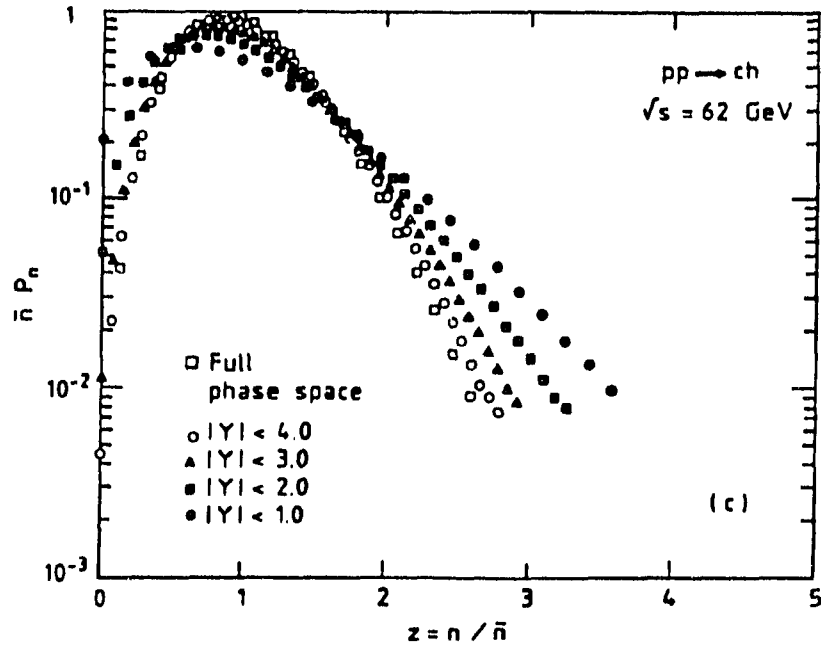
Figure 2.6: Charged multiplicity in KNO format in different rapidity windows for
p-p interactions at 62 GeV ($y_{max} = 4.2$).
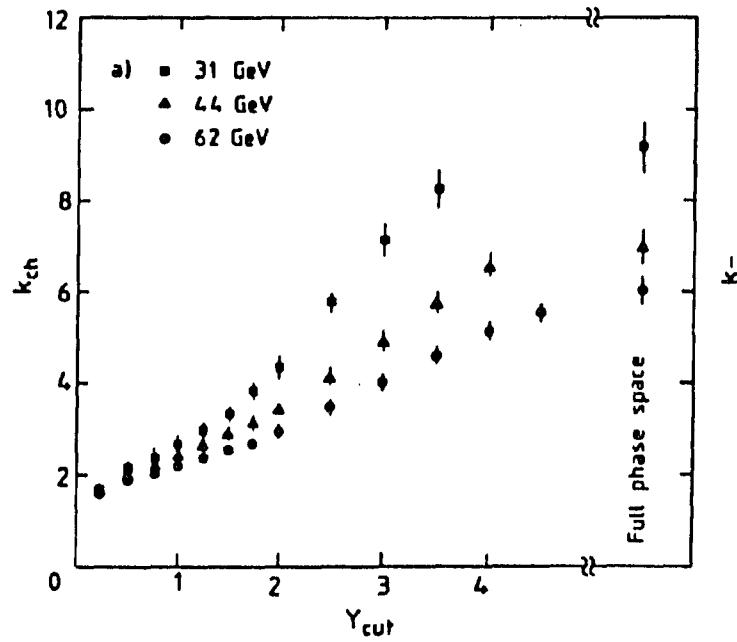
Figure 2.7: k_{ch} of the NBD in different rapidity windows Y_{cut}.

In applying NBD to full phase space data, two different methods of fitting have been used and their results are different. One method is to fit NBD to the total charged multiplicity n_{ch}. Due to charge conservation, n_{ch} is always even. Fitting NBD to n_{ch} means taking only even integer bins from NBD and renormalize the whole distribution. This renormalized function is not exactly NBD and is sometimes called the "Fake Negative Binomial Distribution" (FNBD). The other method is to fit NBD to the negative multiplicity n_-, or the genuine multiplicity n. In this method n_- or n can take any positive integer and was usually considered as more appropriate. In a limited rapidity window this kind of problem does not occur.

The energy dependence of k and $\bar{n}$ resulting from NBD fits to full phase space non-single-diffractive data are usually parametrized by :

$$k^{-1} = \alpha + \beta \ln \sqrt{s} \tag{2.48}$$

$$\bar{n} = A + B \ln s + C \ln^2 s \tag{2.49}$$

where eq. (2.49) is just repeating eq. (2.16). Figure 2.8 shows the energy dependence of k_{ch}^{-1} for $\sqrt{s} > 10$ GeV. The fitted parameters with charged multiplicities (FNBD) and negative multiplicities (NBD) are shown in table 2.1 and 2.2[9].

Table 2.1: Fits of the average charged and negative multiplicities to the formula $\bar{n} = A + B \ln s + C(\ln s)^2$.

Multiplicity Distribution	A ± Δ A	B ± Δ B	C ± Δ C	χ^2/DoF
Charged	3.06 ± 0.64	−0.54 ± 0.16	0.196 ± 0.008	3.3
Negative	1.16 ± 0.27	−0.38 ± 0.07	0.114 ± 0.004	3.5

A point worth noting made by R.Szwed, et al.[24], is that the parameterization of k in eq. (2.48) is not consistent with the Wroblewski relation (2.19). For genuine
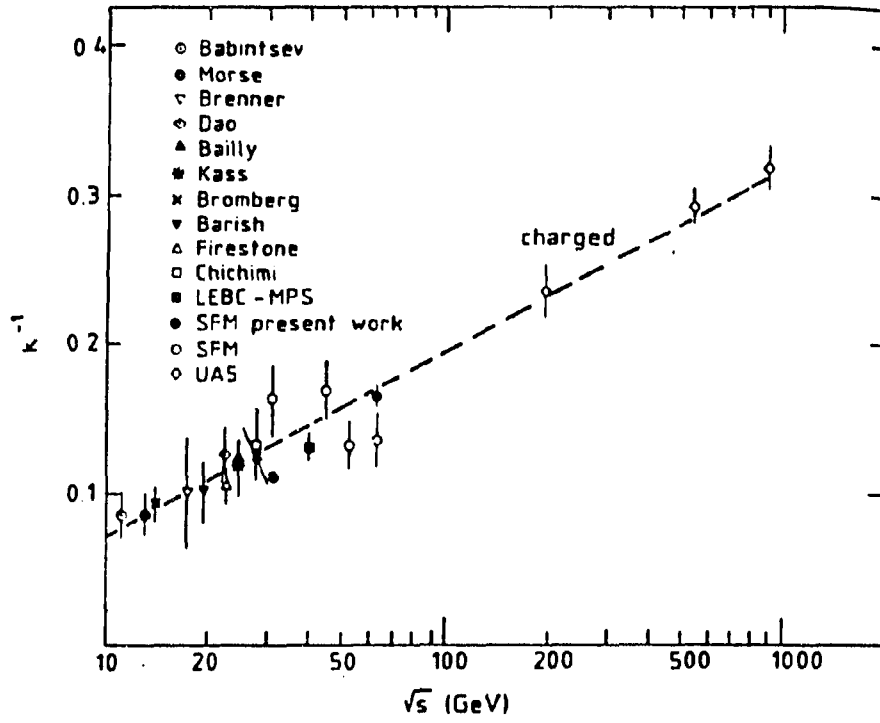
Figure 2.8: Energy dependence of k^{-1} in FNBD fits to charged multiplicities in the full phase space non-single-diffractive data.

Table 2.2: Fits of the k^{-1} to the formula $k^{-1} = \alpha + \beta \ln s$.

Multiplicity Distribution	$\alpha \pm \Delta\alpha$	$\beta \pm \Delta\beta$	χ^2/DoF
Charged	-0.059 ± 0.010	0.054 ± 0.003	1.0
Negative	-0.121 ± 0.012	-0.062 ± 0.003	0.7

multiplicity n, adding Wroblewski relation into the Dispersion relation (2.43) would lead to :

$$k^{-1} = A^2 + \frac{A^2 - 1}{\bar{n}} + \frac{A^2}{4\bar{n}^2} \tag{2.50}$$

which depends on energy through $\bar{n}$. The behavior of the two k dependences are very different. As $s \to \infty, \bar{n} \to \infty$:

$$(2.48) \implies k^{-1} \to \infty$$

$$(2.50) \implies k^{-1} \to A^2.$$

With the Wroblewski relation, the asymptotic value of $k_{NBD} = 1/A^2 = 3$. As shown in Figure 2.9, for the total inelastic data sample the linear dependence of k^{-1} in (ln s) is clearly ruled out[24] !

KNO-G vs NBD

In the formalism of KNO-G scaling there is no restriction on what the scaling function $\psi(z)$ should be. However, once the function is determined at one energy, data from all other energies must fall in the same curve. This scaling test is very severe. For the moment KNO-G seems to work for inelastic pp & p̄p samples and naturally gives the Wroblewski relation of the moments. It is not clear, though, how the scaling rule should be applied to data in a finite rapidity window. The rapidity
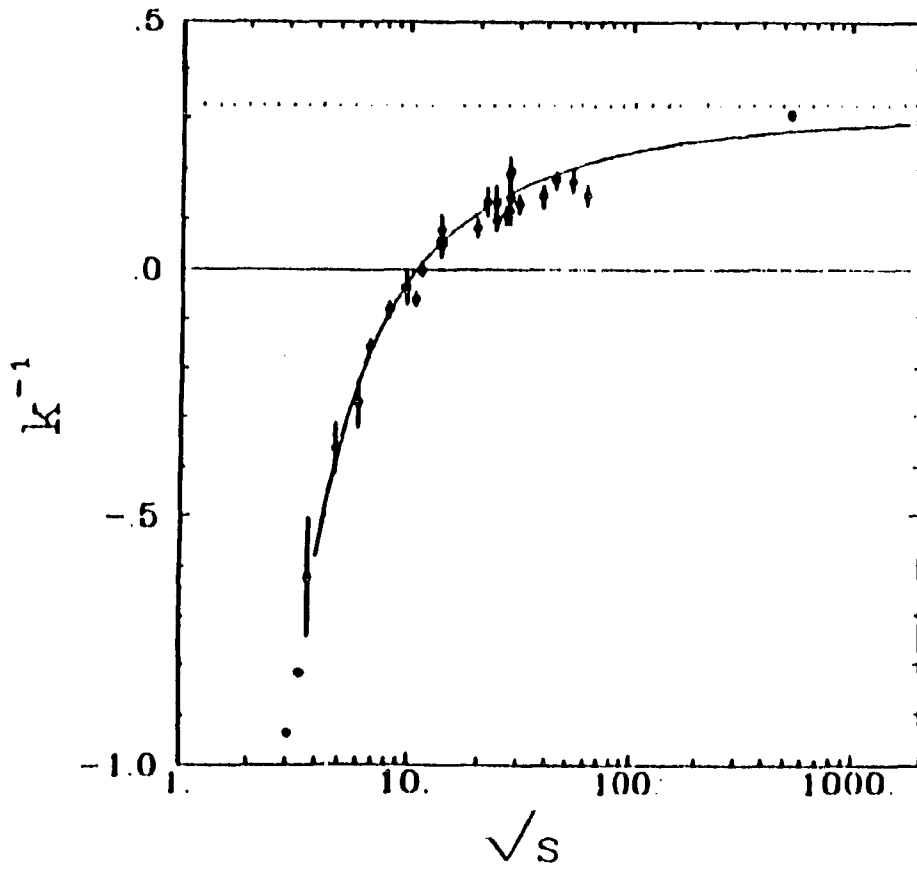
Figure 2.9: Energy dependence of k^{-1} for total inelastic data sample, curve is given by eq. (2.46).

distributions widen with increasing energy and in order to pick up the same data over different energies the rapidity cuts have to change with energy in an unknown manner.

The negative binomial distribution has two free parameters in fitting the data. However, there has been some inconsistency in the literature in applying NBD and FNBD to the full phase space data. Nonetheless, the function is well suited for fitting various types of data and well motivated on theoretical grounds[25].

Recent results from UA5 at 900 GeV[5, 8] indicates a violation of both KNO-G scaling and NBD. As shown in Figure 2.10, a shoulder has emerged and the distribution can no longer be fitted to a single concave function. This suggests the onset of a new production mechanism, which is either negligible or not available at lower energies. QCD mini-jet has been suggested[27] to account for this new phenomenon.
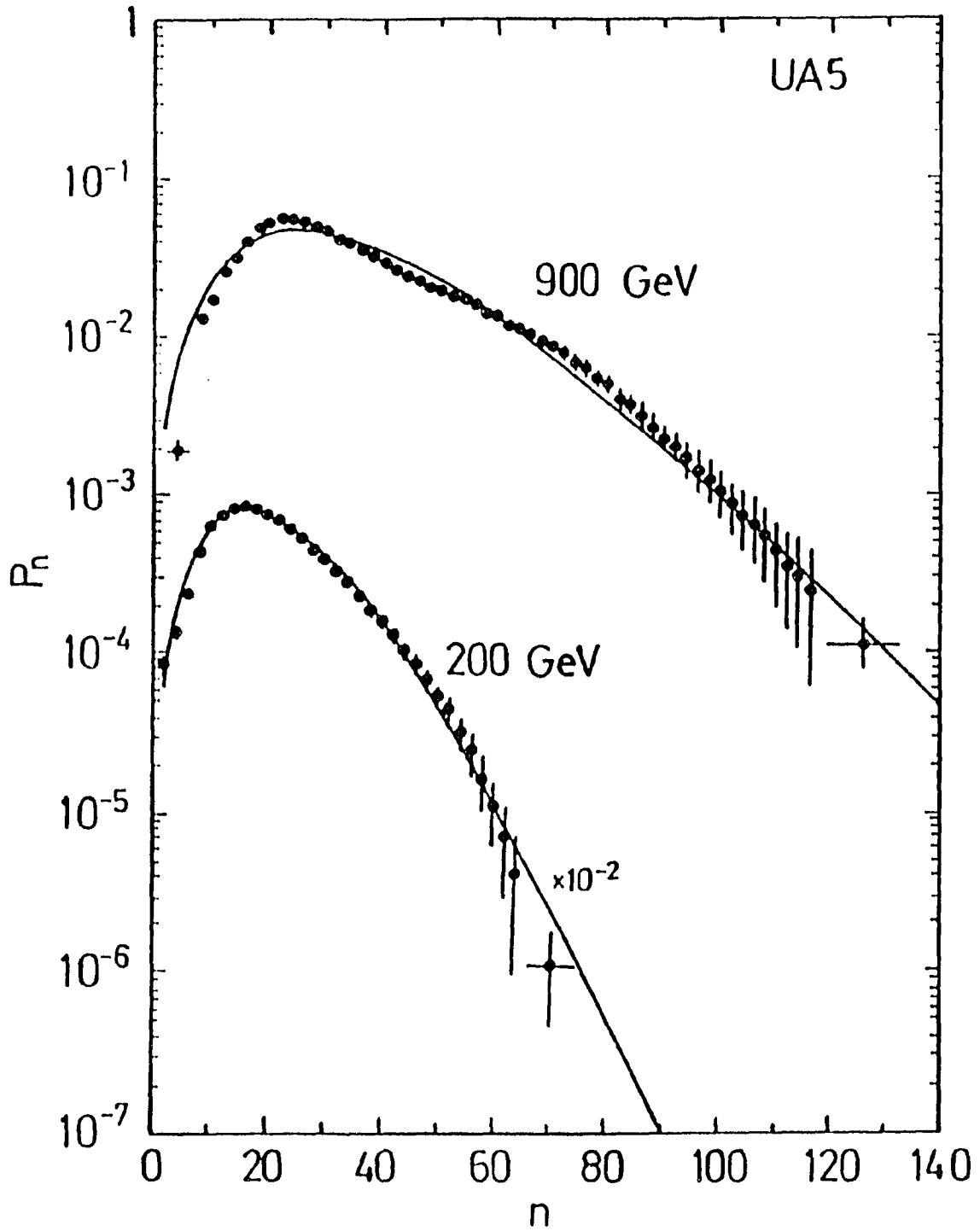
Figure 2.10: Charged multiplicity distributions at 200 and 900 GeV. Curves are fitted NBD.

CHAPTER 3.   EXPERIMENTAL SETUP

The basic technique of experimental particle physics is the analysis of the consequences of a stream of particles impacting at very high energy on a target or with another stream of particles. The advantage of using colliding beams is the higher total center of mass energy achieved. On the other hand, with a fixed target experiment, it is easier to achieve a higher luminosity, or, equivalently, a higher total event rate. Experiment 735 at Fermilab is a collider experiment using the Fermilab Tevatron $\bar{p}$-p colliding beams. The major elements of the E-735 detector are: a central tracking chamber system, a hodoscope for triggering and counting charged particle multiplicity; a single arm magnetic spectrometer, and a time-of-flight (TOF) system for particle identification. The various parts of the instrument will be discussed in the following sections.

Tevatron Collider

The Fermilab Tevatron Collider[36] is the culmination of a series of accelerators required to produce collisions of protons and antiprotons at several experimental points with a center of mass energy of 1.8 TeV. In this section we will outline this sequence and emphasize the major components. A layout of the facility is shown schematically in Figure 3.1.

LINAC

p̄ SOURCE

BOOSTER

SWITCHYARD

p EXTRACT
p̄ INJECT

p INJECT

A0

RF

B0
OVERPASS

F0

B0 DETECTOR
& LOW BETA
(CDF E-741)

ENERGY DOUBLER
(TEVATRON)

MR

E0

(E-735)
C0

p̄ ABORT

p̄/p TRANSFER

p

p̄

(E-740)

p ABORT

D0
OVERPASS
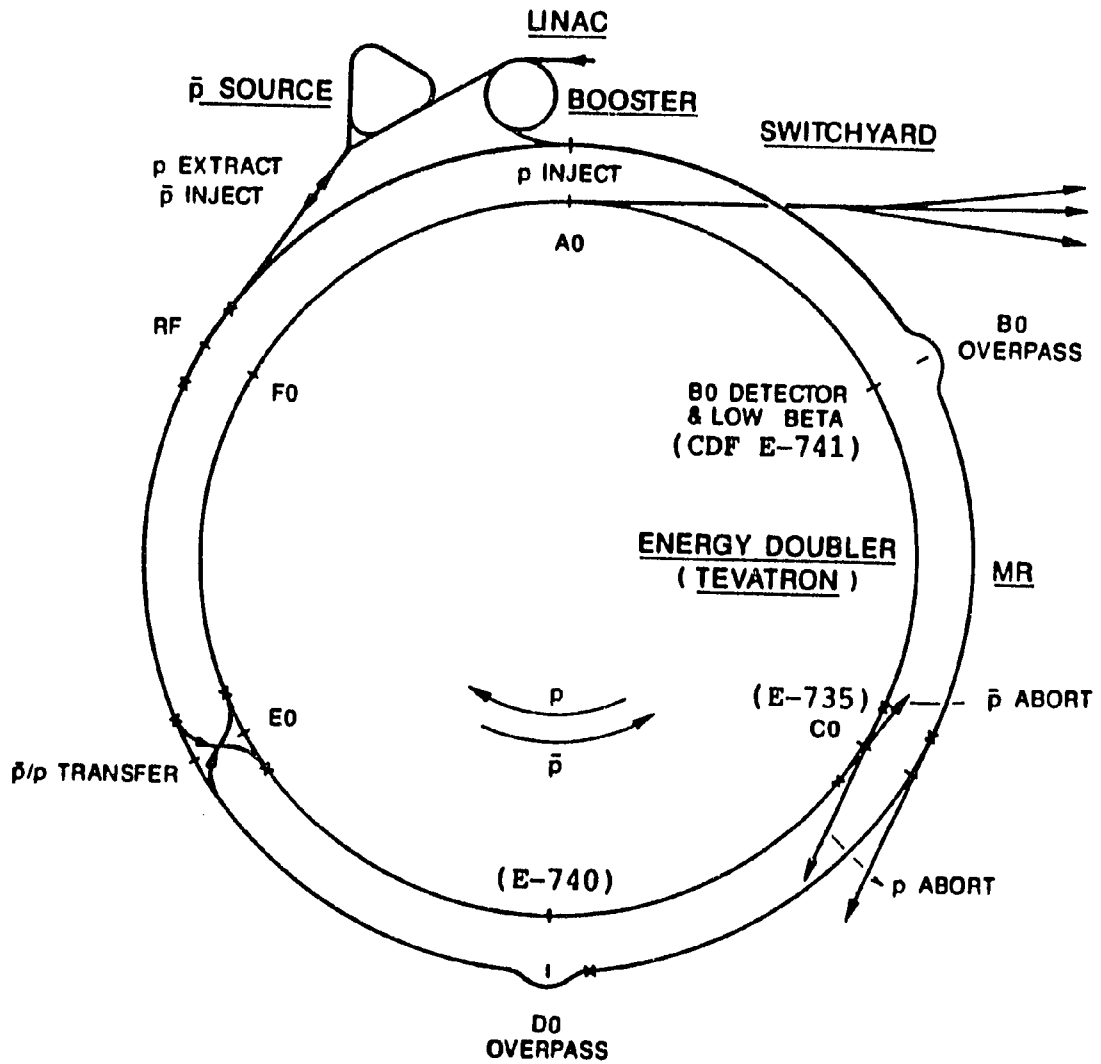
Figure 3.1: Tevatron accelerator system.

The beam starts at the ion source inside a Cockcroft-Walton generator where electrons are added to hydrogen atoms to make H^- ions[30]. The resulting H^- ions emerge from the high voltage accelerator with an energy of 750 keV.

The 750 keV H^- ions enter the linear accelerator (Linac)[31]. The Linac is approximately 500 feet long with 290 copper electrodes. Oscillating electric fields are induced between electrodes and tuned to generate an electrical surf wave. The incoming H^- ions are bunched to ride the crest of the surf wave and accelerated to 200 MeV by the end of the line.

The 200 MeV H^- ions are injected into the circular Booster. The Booster is approximately 500 feet in diameter, located in a tunnel 20 feet below the ground. It's a rapid-cycling synchrotron which goes through its accelerating cycle 15 times per second. During the injection, the H^- ions are stripped of their electrons with a carbon foil[32, 33, 34, 35]. The resulting protons are then accelerated to 8 GeV (kinetic energy) for injection into the Main Ring.

The Main Ring (MR) is a synchrotron about four miles in circumference, and contains 1000 conventional, copper-coiled, water-cooled magnets. It is responsible for both producing antiprotons and injecting protons/antiprotons into the Tevatron.

In order to produce antiprotons ($\bar{p}$), the protons in the MR are accelerated to 120 GeV, coalesced, and directed onto a tungsten target in the $\bar{p}$ target station (see Figure 3.2) . Behind the target, negatively charged particles with a momentum of 8.89 GeV/c are collected by a lithium lens and transported to the Debuncher. After circulating in the Debuncher for a millisecond, only antiprotons survive. The Debuncher reduces the momentum spread of the antiprotons from 3.5% to 0.25% and reduces the transverse emittance[37] by a factor of three by stochastic cooling
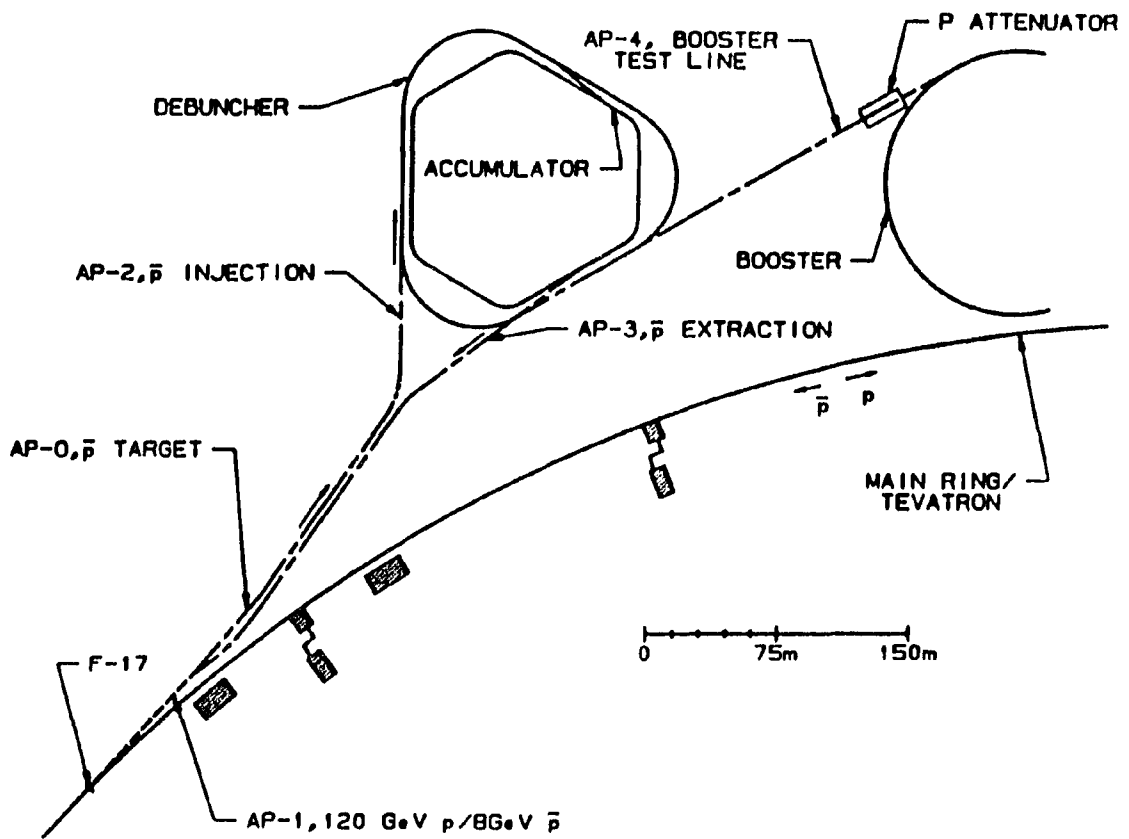
Figure 3.2: The antiproton source.

[38]. Two seconds later, the antiprotons are transferred to the Accumulator, and the Debuncher is ready for another batch of antiprotons. The Accumulator is a smaller ring inside the Debuncher in the same tunnel, which continues to cool the antiprotons by stochastic cooling and gradually builds up a dense stack of antiprotons.

The Accumulator extraction orbit is very similar to that of the Booster's. They have the same orbit length, same energy (8 GeV), same rf harmonic number (84) and frequency (52.8 MHz). The Main Ring rf is also 52.8 MHz at 8 GeV. This allows the three machines to be phase locked with one another for bunch-to-bucket beam transfer.

The final acceleration component is the Tevatron which is a synchrotron about 4 miles in circumference, located 65 cm below the Main Ring in the same tunnel. It's the world's first large scale application of superconducting materials. The helium cooled superconducting magnets of the Tevatron include 772 bending magnets, 224 quadrupoles, and 720 small correction and adjustment elements. To date, the machine produces the highest energy proton-antiproton collisions in the world.

To put colliding proton-antiproton beams in the Tevatron, the antiprotons in the Accumulator are first accelerated to the extraction orbit, which is only 132 MeV more energetic than the core orbit, and extracted to the Main Ring. In the Main Ring they are accelerated to 150 GeV, coalesced, and injected into the Tevatron. This process is repeated six times to bring six bunches of antiprotons into the Tevatron. Then, six bunches of protons are also prepared directly from the Linac-Booster-MR cycles and injected into the Tevatron. Because protons and antiprotons have the same mass but opposite charge, they can be kept in the same orbit in opposite directions. The Tevatron then ramps the 12 bunches to 900 GeV and adjusts them to cross at the

right places for the experiments. In the '87 run, the setup was three bunches of protons colliding with three bunches of antiprotons. In the '88-'89 run there were six bunches of protons colliding with 6 bunches of antiprotons as just described. In principle, the counter-rotating beams of protons-antiprotons would simply be lost in their circular orbits after 30 hours, as collisions deplete their number. In practice, the residual gas in the vacuum beam pipe reduced the beam lifetime to typically 10 hours. Table 3.1 lists some of the performance parameters of the Collider[39]. The first column is a typical good store in May 1987. The second column is the Tevatron I project design goal. The last column is one of the highest luminosity stores in the 1988-1989 runs.

Detector

The E-735 detector was located at the C0 interaction region where the Main Ring and the Tevatron also have their abort beam lines (see Figure 3.1). The Main Ring beam and its abort tube are about 65 cm above the Tevatron. The Tevatron beam is located in a 0.08" thick Aluminum beam pipe with an inner radius 3" and a length of 185". The beam pipe is offset from the circulating beam at C0 by $1.3cm$ vertically and $3.8cm$ horizontally. The C0 coordinate system is defined with z the proton beam direction, y vertically upward and x horizontally into the side spectrometer arm. The nominal beam-beam collision point is at (0,0,0). We will be using this coordinate system unless otherwise stated.

Figure 3.3 and Figure 3.4 are the plan view and the side view of the detector. The detectors surrounding the beam line are the central tracking chamber (CTC)[40], endcap chamber, multiplicity hodoscope[43], p-p̄ time-of-flight counters and the Halo

Table 3.1:   Collider performance parameters.

Parameter	May 1987 Achieved	Tev I Design	1988-1989 Achieved
Number of bunches	3	3	6
Protons/bunch($\times 10^{10}$) at low-β	5	6	7.2
$\bar{P}$/bunch($\times 10^{10}$) at low-β	0.8	6	2.9
$\bar{P}$ extracted from core/bunch($\times 10^{10}$)	2.3	6	4.5
MR transmission efficiency (%)	77	100	88
MR coalescing efficiency (%)	70	100	80
Tev transmission efficiency (%)	65	100	95
Transverse emittance (95% π mm-mrad)			
Proton	24	24	23
Antiproton	36	24	18
$\bar{P}$ stacking rate (10^{10}/hour)			
Peak	1.1	10.	2.0
Average	0.77	10.	1.4
Luminosity lifetime (hours)	8.	20.	10.-25.
Operational efficiency (%) (Store hrs/total hrs)	40	–	65
Average stack before transfer ($\times 10^{10}$)	25.	40.	60.-70.
Average stacking time (hours)	10.	–	20.
Initial luminosity ($\times 10^{29}/cm^2/sec$)	1.3	10.	20.7

Veto Counters. The side arm spectrometer consists of the Z chamber[44], pre-magnet chamber, magnet, post-magnet chamber, straw chamber and the TOF1, TOF2 time-of-flight system. Following, we will describe these systems with emphasis on how they function.

Central and endcap tracking chambers

In general, a multiwire drift chamber consists of an array of anode wires surrounded by cathode planes made of metal foil, wire mesh or wires. A charged particle passing through the chamber ionizes the gas and leaves behind a string of electrons
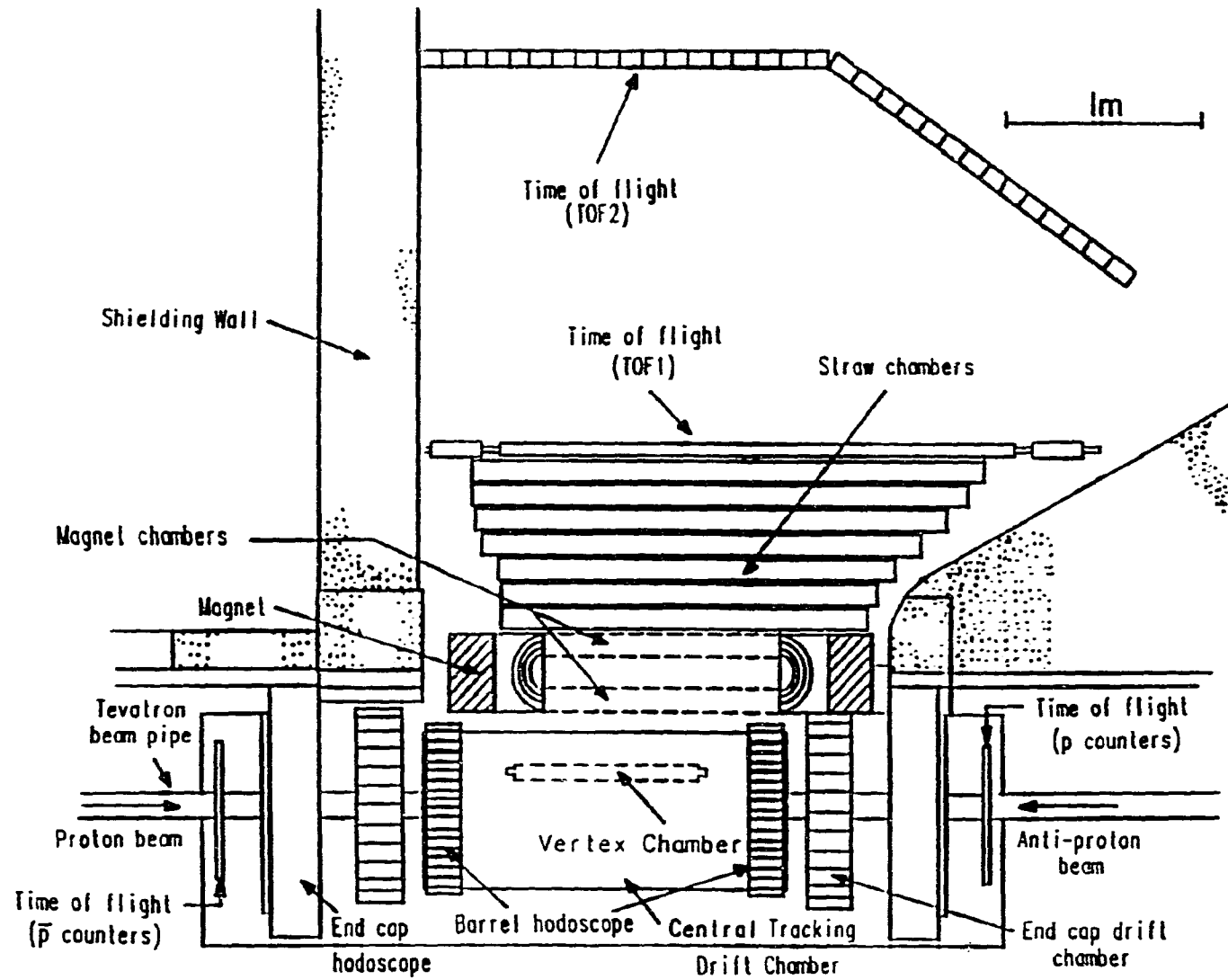
Figure 3.3: Plan view of E-735 detector.

Time of flight
(TOF2)

1m

Shielding Wall

Time of flight
(TOF1)

Straw chambers

Magnet chambers

Magnet

Tevatron
beam pipe

Time of flight
(p counters)

Proton beam

Vertex Chamber

Anti-proton
beam

Time of flight
($\bar{p}$ counters)

End cap
hodoscope

Barrel hodoscope

Central Tracking
Drift Chamber

End cap drift
chamber

32

Figure 3.4: Side view of E-735 detector.

33
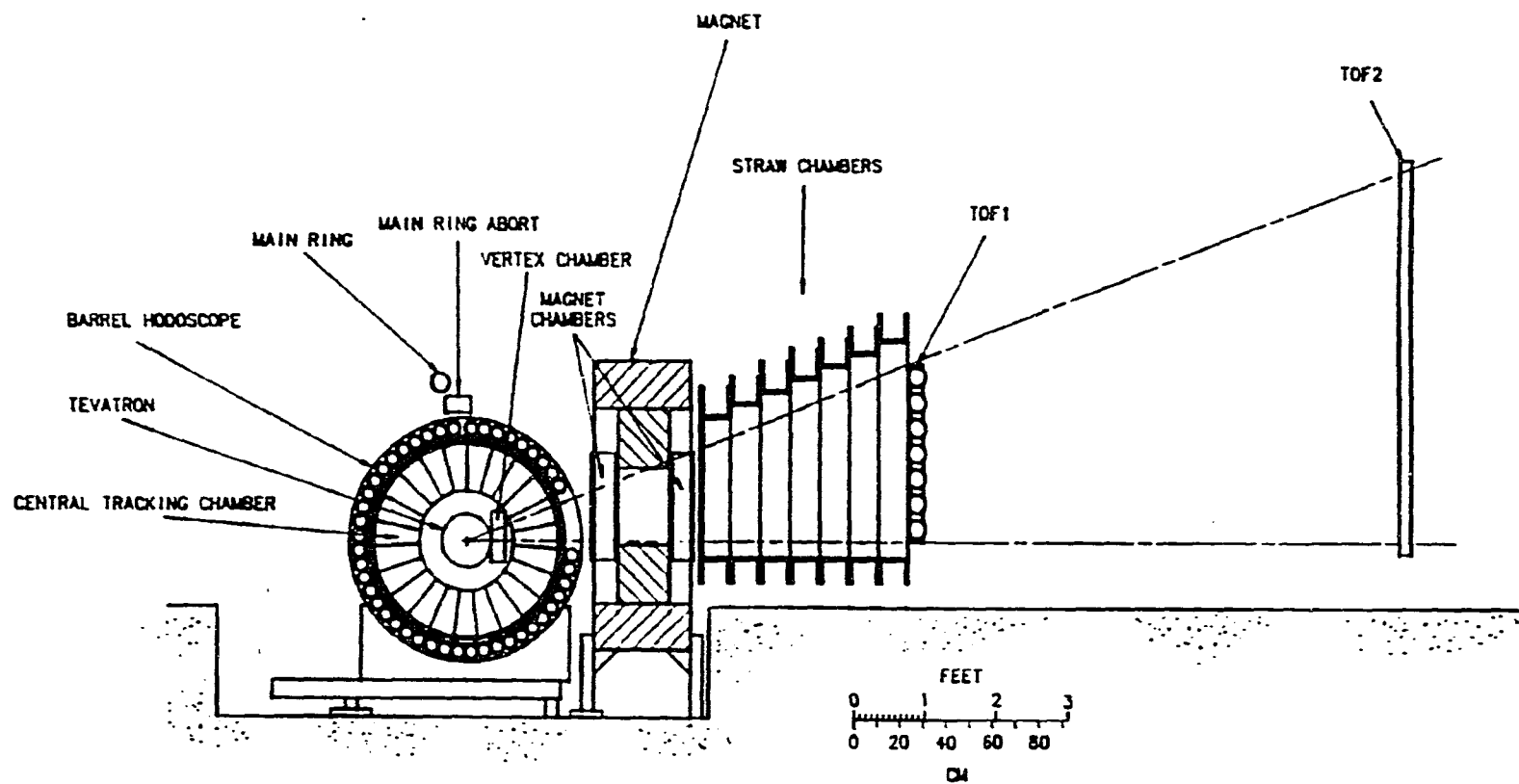
and ions. Electrons drift along the electric field to one of the anode (sense) wires. When they come close enough to the wire, the energy gained by the electron between two collisions exceeds the ionization threshold of the gas molecules, secondary ionization then begins to avalanche and induces a pulse on the sense wire. Determination of the track position usually uses the electron drift time and other information unique to the specific type of chamber.
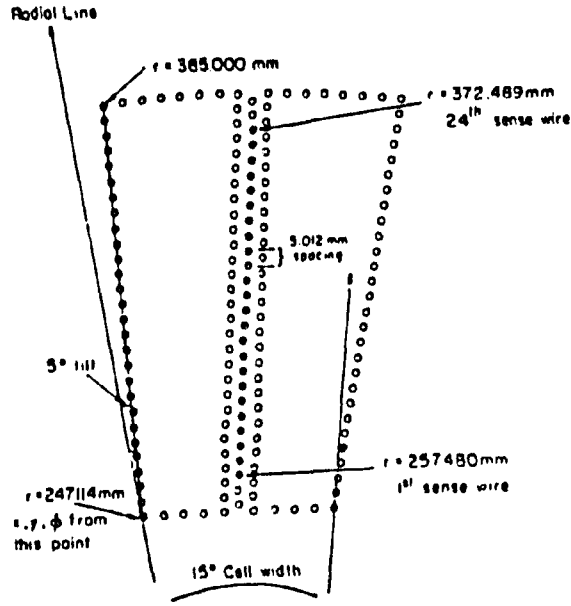
Figure 3.5: Cross section of a CTC supercell.

The central tracking chamber (CTC) and the two endcap chambers are multiwire drift chambers designed to detect charged secondary particles from a p p̄ collision. The CTC covers the pseudo-rapidity region $|\eta| \leq 1.62$ and the two endcaps extend it to $|\eta| \leq 2.88$.

The CTC has an inner radius of 22 cm, an outer radius of 42 cm and is two

meters long. The chamber is azimuthally divided into 24 cells. Sense wires in each cell are parallel to the beam line. Figure 3.5 shows the cross section of one cell. Each cell has 24 sense wires aligned in a plane tilted 5° away from the beam line in order to resolve left-right ambiguities. The sense wires have a resistance of 190 Ω/m, and hit position along the z axis is obtained by charge division. A 100 MHz flash ADC (Analog to Digital Converter) readout allows multiple hits in the same sense wire. The gas used for the CTC was a mixture of 95% argon, 4% methane and 1% of CO_2.
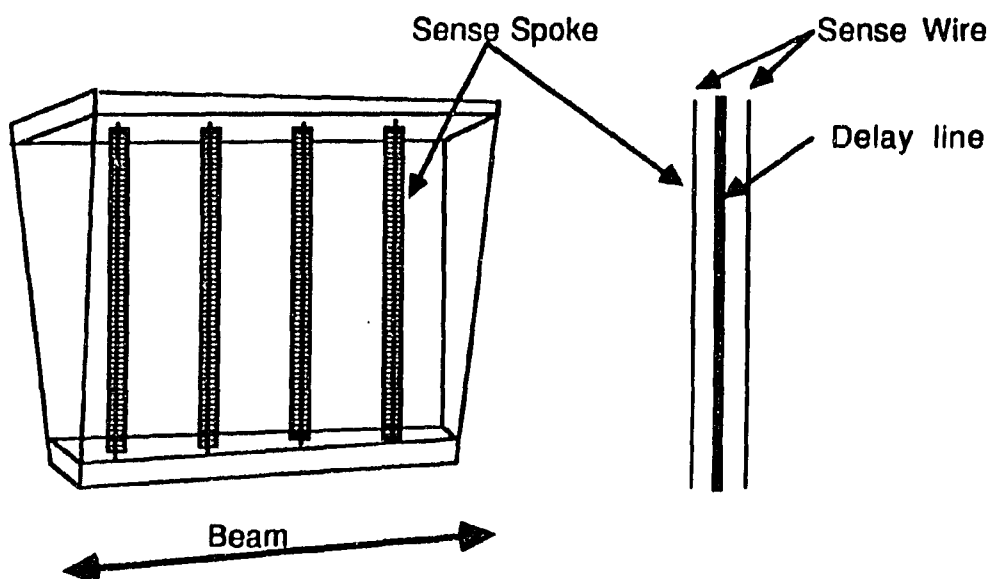
Figure 3.6: An endcap chamber segment and sense spokes.

The two endcap chambers are 12 cm in inner radius, 49 cm in outer radius, 25.4 cm in length and are positioned at $z = \pm 128.4$ cm. An endcap chamber has 32 pie-shaped segments, each consisting of a plane of four radially going sense spokes. The sense spoke is a delay line at ground potential with two positive potential sense

wires spaced 2mm on each side of the delay line. Figure 3.6 shows a segment of the chamber and the sense spokes. When electrons avalanche on the sense wire, a pulse is also induced on the delay line. The sense wires and both ends of the delay line are read out by TDCs (Time to Digital Converter). The sum of the top and bottom times of the delay line gives the drift distance, while the difference of the times gives the radial distance along the delay line. The sense wires further tell on which side of the delay line the hit originated. Thus, a unique r-φ coordinate is determined with each hit[41]. The TDCs allow multiple hits if the pulses are more than 10 ns apart. The gas used for the endcap chambers was a mixture of 85% argon and 15% CO_2.

Multiplicity hodoscope

The hodoscope consists of an array of 240 scintillation counters, outside the CTC and the endcap chambers. The hodoscope is designed to provide a fast estimate of the event multiplicity and the event topology for on-line trigger decision making. Its ADC and TDC information is also used in off-line analysis as a tool for background discrimination and as a complement to tracking chambers in finding the charged track multiplicity.

The hodoscope is separated into a barrel and two endcaps (Figure 3.3,3.4). The barrel consists of two halves of 48 counters azimuthally surrounding the CTC. The pseudo-rapidity coverage of the barrel is $|\eta| \leq 1.57$. The counters are 97cm-long slats running parallel to the beam line. A window at $|z| \leq 60.1cm$ and $-0.59^\circ \leq \varphi \leq 20.59^\circ$ is cut for the spectrometer arm.

The two endcap hodoscopes, which stand behind the two endcap drift chambers, consist of three rings of 24 counters in each ring, and span the pseudo-rapidity region

$1.65 \leq |\eta| \leq 3.25$. The three rings divide the pseudo-rapidity region into roughly equal intervals. Because the Main Ring and the abort beam pipes are so close, the uppermost counters in each endcap have to be cut to fit in. The dimensions and locations of the counters are shown in Figure 3.7

All counters are made of the same materials. The scintillator is polyvinyltoulene (PVT) based Bicron BC-408, which was found to be more durable than acrylic or polystyrene based scintillators after being exposed to tunnel radiation for up to about 60 krad[42]. The light guide is made of the same PVT with no scintillation fluor additive. In addition, 1% of benzyl-phenone was added by Bicron as a quencher to suppress the natural scintillation of PVT. Scintillators and light guides are wrapped in aluminum foil and covered with opaque paper.

The photomultiplier tube (PMT) is a 10-stage Hamamatsu 1398 tube with an UV glass window. The tube is 28.5 mm in diameter, protected with a thin μ−metal tube inside an iron tube. It has a 2ns rise time with a gain of 6×10^6 at 1.5KV. The maximum HV is 1.9KV and the recommended maximum averaged anode current is $200\mu A$. The PMT was run in a grounded anode mode with a low current resistor base. In the beginning of the experiment, the counters were efficient for minimum ionizing particles at a HV several hundred volts below the maximum. Therefore, it was possible to increase the gain up to a factor of two or three to compensate the degradation of scintillators during the run.

The anode output of the PMT is connected to a RG8 50Ω cable which brings the signal to our counting room ~ 30 meter distant. In the counting room the RG8 cable is terminated on a transformer type signal splitter (Mini-Circuits, Model PSC-2-1). One splitter output was connected to a LeCroy 2285 ADC for charge integration, and
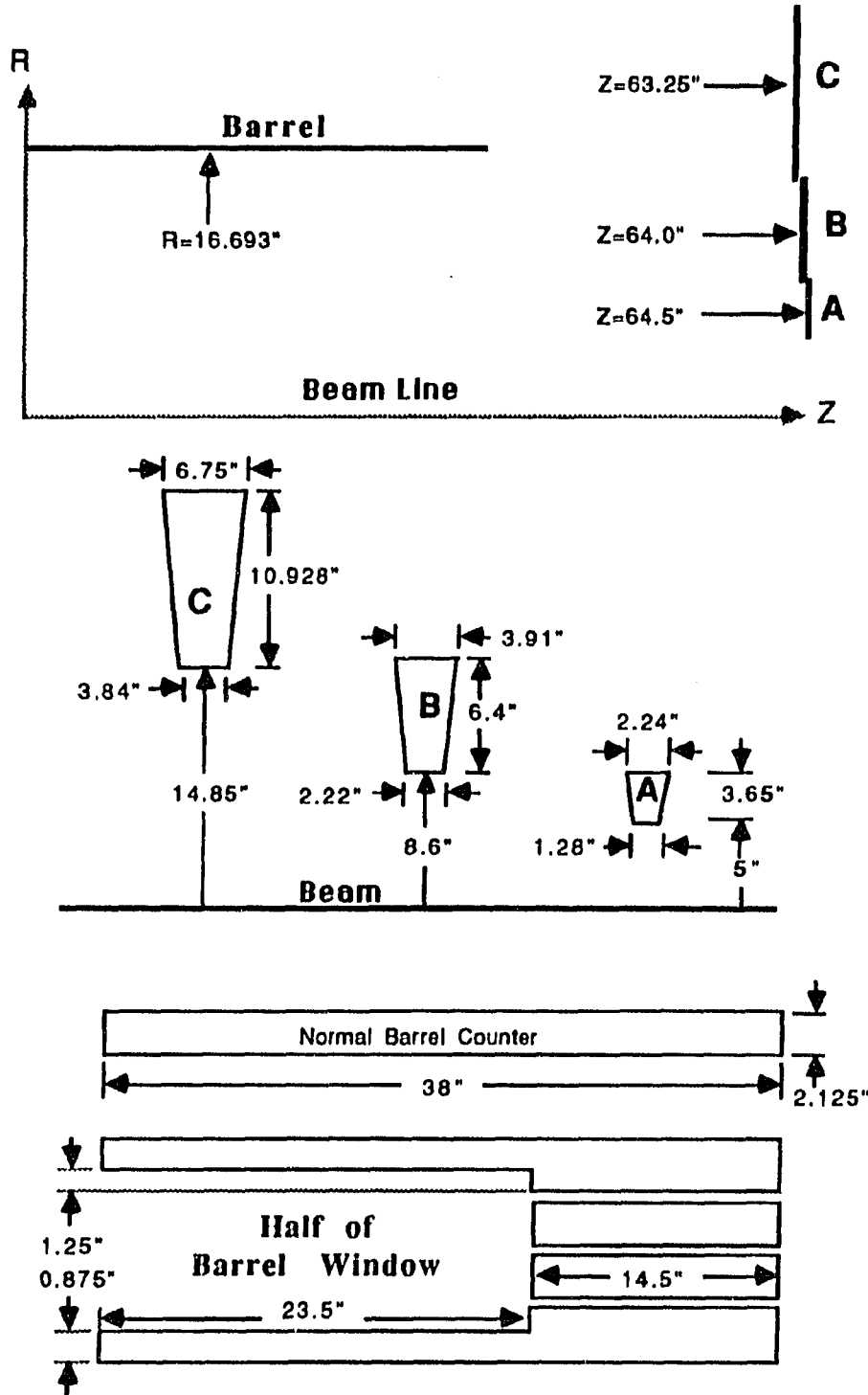
Figure 3.7: Dimensions and locations of hodoscope counters.

the other was sent to a 30mV discriminator to generate a 100ns NIM pulse. One of the discriminator outputs was connected to a LeCroy 2228A TDC for hit time and a second one was converted into a differential ECL signal and fed into the trigger processor for trigger decision making. A schematic of the setup is shown in Figure 3.8
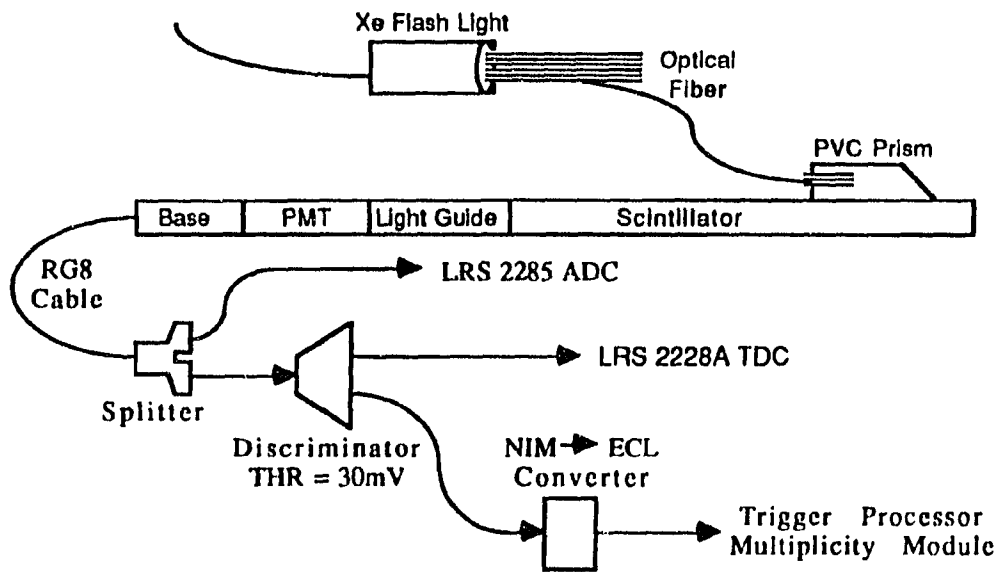
Figure 3.8: Arrangement of a hodoscope counter.

During data taking the pulse height distribution of each counter was continuously monitored. A light pulser system was also implemented for testing the counters when there was no beam. Each scintillator has a small prism glued at the end opposite to the light guide. A 30m long plastic clad silica light fiber is plugged into the prism and led to a xenon flash light in the control room. The control and data read out can be performed with the online data acquisition system or by an IBM PC. Counting the single's rate of each of the 240 counters can also be done simultaneously with the

PC controlled trigger processors.

Magnet spectrometer

The magnet spectrometer is a series of wire drift chambers placed before and after a dipole magnet to determine the path and momentum of a charged track. Together with the time-of-flight system, the particle ID of the track can also be determined. Figure 3.9 shows the positioning of wires and TOF counters in the $x - z$ plane. The geometrical acceptance of the spectrometer is $-0.3 \leq \eta \leq 1.0$ and $0 \leq \varphi \leq 20^{\circ}$, which is about 1% of the coverage of the hodoscope in $\eta - \varphi$ space. The tracking system consists of a Z chamber and a pre-magnet chamber before the magnet and a post-magnet chamber followed by seven straw chambers behind the magnet.

The Z chamber is made of three separated wire planes with 96 sense wires per plane. The first plane is 13.126 cm from the beam line, centered at $y = 2.7cm$, $z = 6.714cm$. Sense wires in the same plane are spaced $1.1cm$ apart, which is the same as the distances between wire planes. All wires are $10cm$ long running in the vertical direction. Wires in different planes are staggered one-half cell to help resolve left-right ambiguities. Because the chamber is placed very close to the beam, a slanted track can hit more than one cell in the same plane. Technically, when there is a cluster of adjacent hits, only the ones that give the minimum drift times with respect to their two adjacent neighbours are used.

The pre- and post- magnet chambers are basically the same design except for the number of wires. Each chamber has four planes of wires. Wires in the same plane are spaced $5cm$ apart and the plane separation is $1.9cm$. Wires in different planes are staggered by $0.5mm$ ($\Delta z = 1mm$) to resolve left-right ambiguities. The

Figure 3.9: Location of wires and counters of spectrometer arm.
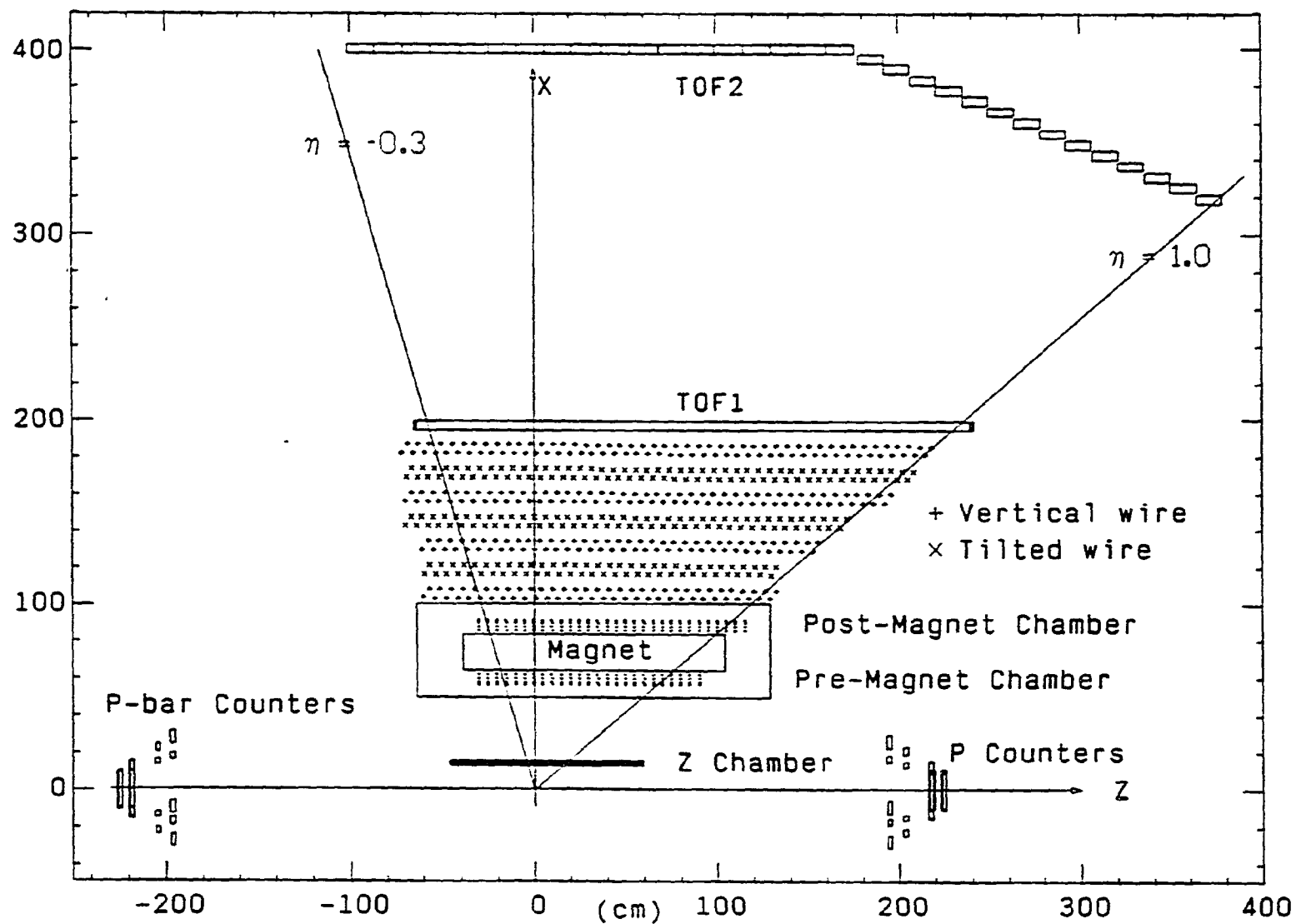
pre-magnet chamber contains 25 sense wires per plane and the post-magnet chamber 30. Figure 3.9 and 3.10 show their positions relative to the magnet. The two magnet chambers and the Z chamber make no y measurement. All of them use the same kind of gas as the endcap chambers (85% Ar + 15% CO_2). They are also read out with the same TDC system as the endcap chambers. In addition to tracking, the pre- and post- magnet chambers were also incorporated into the trigger system to enhance spectrometer acceptance in '89 runs.

The straw chambers are seven chambers, each contains two rows of staggered straw tubes. Four of the chambers have their straw tubes in the vertical direction. The other three have their tubes tilted $4°$ away from y in the $y - z$ plane. Vertical chambers and tilted chambers are arranged to alternate with each other as shown in Figure 3.9. This gives the straw chambers the ability to find the y position of a track. The straw tubes are $5cm$ in diameter with a sense wire at the center. The transverse distance between wires in the same row is $6.096cm$. The distance between the two wire planes is $4.684cm$ The gas used was 90% Ar, 10% methane.

The magnet is made of 4.3 tons of iron and 0.7 tons of copper coil. The position and dimensions are shown in Figure 3.9 and 3.10. Normally the magnet ran a current of 1000 Amps with a central field strength of 3.8 kGauss and provided a momentum kick of $\int Bdl \approx 50MeV$, which allowed the spectrometer to adequately measure a track momentum up to 3 GeV/c.

Time-of-flight system

The time-of-flight system has four arrays of scintillation counters, with "p" and "$\bar{p}$" arrays in the tunnel and "TOF1", "TOF2" in the spectrometer arm.
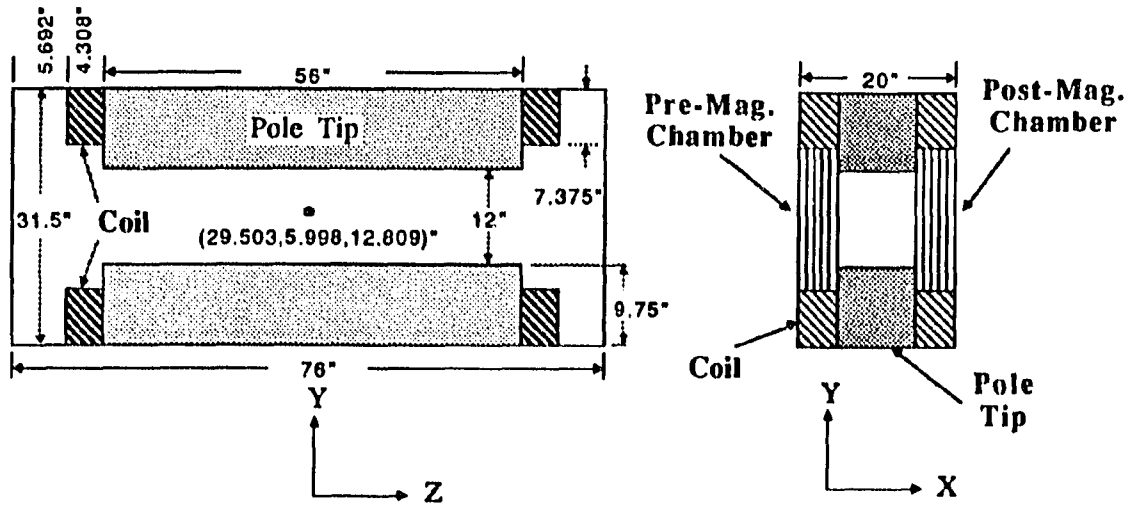
Figure 3.10: Magnet and magnet chambers.

The p and p̄ arrays each contain 15 scintillators surrounding the beam pipe. Figure 3.9 and 3.11 show the projection of the counters in different planes. The two arrays are mirror images of each other. These counters are designed to determine the interaction time (T0) as well as the vertex position along z axis. They are also used to form the fundamental beam-beam trigger in this experiment.

TOF1 is an array of seven counters positioned two meters from the beam. Each counter is $3.05m$ long, $10.16cm$ high and $5.08cm$ thick. Counters are placed horizontally along the beam axis, stacked one on top of the other.

TOF2 is located about four meters from the beam, and consists of 32 counters. Each counter is $15.39cm$ wide, $152.4cm$ high and $5.08cm$ thick, standing vertically and lined up as shown in Figure 3.9.

The scintillators and light guides used for TOF counters are the same as those for the multiplicity hodoscope. Each TOF counter is read out with TDCs and ADCs
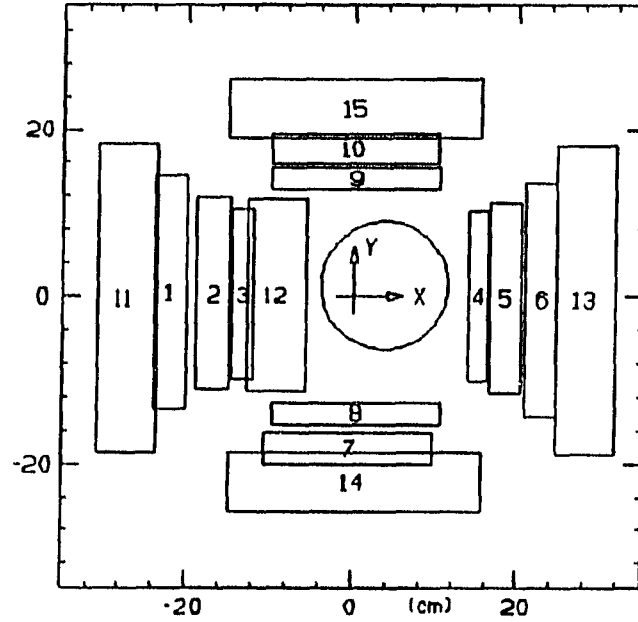
Figure 3.11:   Projection of p p̄ counters on x-y plane.

from both ends. The ADCs are used to identify minimum ionizing hits and correct TDC slewing due to different pulse heights (time-walk correction). TDCs read out from different counters are aligned and calibrated before they are used [46]. The particle ID of a track is determined in the following manner:

1. The sum of TDCs from both ends of a counter gives the hit time, and their difference gives the hit position along the counter.

2. The sum of hit times between P and P̄ counters gives the interaction time (T0), and the difference gives vertex position in Z.

3. The difference between the hit time of a TOF1 or TOF2 counter and the interaction time gives the flight time of a particle.

4. With the path length and momentum given by tracking chambers, the velocity of the particle is determined, and the mass estimated from $m = p/\beta\gamma$.

The functions of TOF1 and TOF2 are complementary to each other. TOF2 has a longer flight path to allow identification of higher momentum particles. Specifically, $K - \pi$ separation is possible up to 1.7 GeV/c. On the other hand, TOF1 has a shorter flight path, which allows it to detect more low momentum short lived particles.

Other than the velocity analysis as described above, dE/dX is also implemented on the TOF1 counters by adding an additional ADC readout from dynode nine of each 12-stage phototube, which provides a better linearity and a wider ADC range due to the smaller gain. The dE/dX method is expected to improve the identifications of slow heavy particles.

CHAPTER 4. DATA ACQUISITION

During a typical "store" of counter-rotating beams in the Tevatron, a proton bunch and an antiproton bunch crossed each other at the interaction region every $3\mu sec$. To register the results of the crossing, the readout electronics were synchronized with the beam and initiated for digitizing signals coming from the detectors. To be efficient, a mechanism was set up to determine, on each crossing, whether a desired event had occurred or not. If a desired event did occur, the electronics were allowed to finish the digitization and the front end computers were triggered to read out the data. This sequence could take longer than tens of milliseconds to complete, and caused a "dead time" during which no other events could be taken. If an event was determined to be rejected, the electronics were stopped and cleared for the next beam crossing.

Readout System

The computer readout system consisted of three branches, each reading a part of the detector with a different type of data transfer protocol. Figure 4.1 is a schematic of the configuration. The protocol used in each branch was :

- A VME system for reading FADCs from CTC
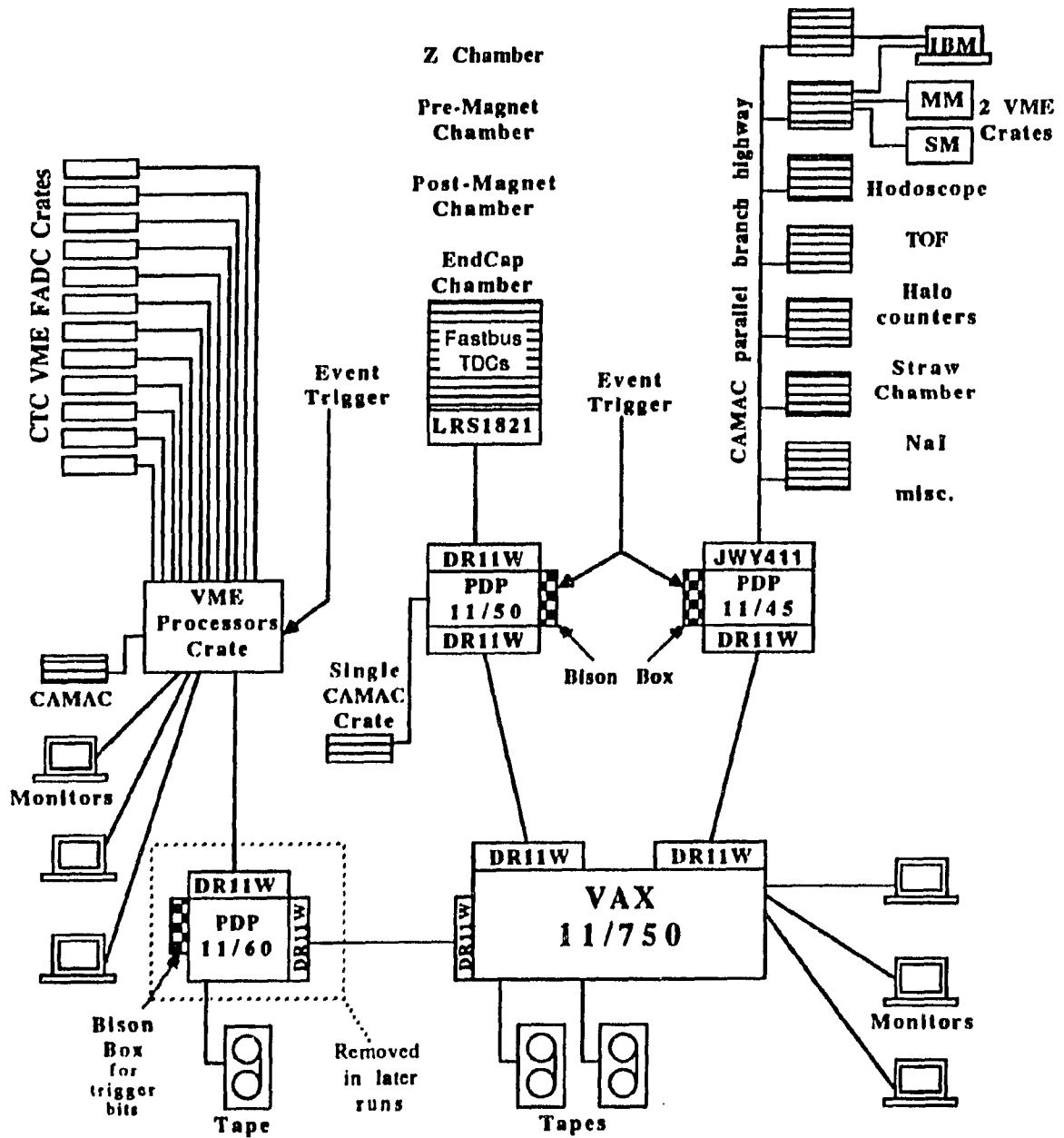
Figure 4.1: Computer read out system.

- A Fastbus system for reading TDCs from endcap chambers, Z chamber, pre- and post- magnet chambers.

- A CAMAC system for reading ADCs, TDCs and other data from the rest of the detectors including TOF, hodoscope, straw chamber and halo counters.

The CAMAC and Fastbus branches were controlled by a PDP 11/45 and a PDP 11/50 respectively. Data from these two branches were sent to a VAX 11/750 via DR11W links[48], and concatenated before being written to the tape. The CTC VME system was an independent branch and wrote its own tapes with a PDP 11/60. For identifying different pieces of an event, an unique Event Time Clock was read by all three branches. For communicating with the trigger system, each front end computer was implemented with a Bison Box[49].

Both PDP 11/45 and 11/50 ran RSX DA, and worked closely with the VAX ON-LINE system in the VAX 11/750. The start of a run was from the RUN_CONTROL program in the VAX, which initiated and synchronized the start run sequence in 11/45 and 11/50. The sequence allowed users to initialize their electronics and activated DA in each front end. The 11/45 controlled a Jorway 411 CAMAC driver, driving a parallel branch highway with 7 CAMAC crates. The DA running in the 11/45 executed a "CAMAC list" which controlled CAMAC operations with a set of macros. The other branch, 11/50, was connected to a LeCroy 1821 Fastbus Segment Manager with a DR11W, and its DA executed a "Fastbus list".

The two pieces of data from the PDP's were sent to the VAX asynchronously due to different lengths of read time. A process called EVENT_BUILDER resided in the VAX waited for both pieces to arrive, and combined them into one "event" record. This concatenated event was declared in the EVENT_POOL to be accessible

by other processes. The EVENT_POOL was a sharable event buffer installed as part of the DAQ system[50] that allowed other processes access through a set of routines. EVENT_BUILDER was a VIP client of the DAQ that put events into the pool. The opposite of this procedure was another VIP client called OUTPUT which read events from the pool and wrote them onto the tape. During data taking, several other processes also used DAQ system to access events for online monitoring.

The Fastbus and CAMAC branches were integrated under the same trigger system, usually called the spectrometer trigger. The dead time of this system was about $24ms$, set by the slower CAMAC branch. The running criterion was to take data with about 20% dead time so that rare events have a fair chance of occurrence. This gave an event rate of about 10Hz.

The data stream and trigger logic of the CTC were both separated from the spectrometer branch. During early runs the PDP11/60 was linked with the VAX for monitoring purposes. Under this scheme, a process in the VAX could request a CTC event from the 11/60 and combine it with its counter part in the EVENT_POOL. This link was, however, disabled when a VME tape controller became available and the 11/60 was removed from the data stream. The typical dead time of the CTC branch was initially $700ms$, which was later improved to $200ms$. The running criterion was also $\sim$20% dead time, which gave an event rate of $\sim$1Hz, about 1/10 of the spectrometer branch.

Trigger Logic

The Primary Trigger (PT) of the experiment was to identify events from the beam-beam interactions. This was done by first requiring a triple coincidence of at

least one hit in the TOF p counters and at least one hit in TOF $\bar{p}$ counters to occur at the time when the secondaries from a beam-beam interaction are expected to hit the counters. The coincidence (BB) was vetoed if any hits occurred too early in the p or $\bar{p}$ counters. These early hits (ET) could come from beam halo or leading satellite bunches. In addition, the result was required to pass the veto of the late proton satellite beam-gas coincidence (SBG). The satellite bunches were separated $19ns$ from the main bunch and the p & $\bar{p}$ counters were $\sim 13ns$ apart. The halo carried by a late proton satellite would hit the $\bar{p}$ counters $6ns$ later than a normal beam-beam event and $19ns$ later in the p counters. The use of the SBG veto, instead of a "late-hit" veto to cut events with satellite beam-gas contamination, preserved events with slow particles. The actual setup of trigger logic is summarized in Appendix A. In symbols, the PT trigger was defined as :

$$PT = BB * \overline{ET} * \overline{SBG},$$

where $\overline{ET} = \overline{PET} + \overline{\bar{P}ET}$.

The PT trigger was the building block of most of the other triggers. New triggers were generated by putting more restrictions on PT. For instance, the ST trigger was $PT * (\bar{P} > 1)$, which helped screen out background events when luminosities were low, and, the S1 trigger was PT * (at least 3 out of 4 wire planes of pre-magnet and post-magnet chambers were hit), which enhanced spectrometer acceptance.

During the '88-'89 runs the luminosity of a good store could be as high as $20 \times 10^{29}/cm^2/sec$ at CDF. This number was reduced by two orders of magnitude at C0. However, the interaction rate $R = \sigma L \approx 1kHz$, still far exceeded the capability of the data acquisition system. Since only about 1% of the events could be taken, a mechanism had to be setup to choose the events. This was done with the Trigger

Processors.

Trigger Processors

In the search for the quark-gluon plasma, special interest was placed on high multiplicity events where the phase transition is expected to take place. From previous knowledge of multiplicity distributions at lower energy experiments, however, events with high multiplicities are expected to be rare. The purpose of the trigger processor was to scale down the event rates in different multiplicity regions, so that high multiplicity events were enhanced and events with different multiplicities were triggered with roughly the same frequency.

The trigger processor was a VME based system consisting of 13 multiplicity modules (MM) and nine summing modules (SM). The multiplicity modules registered hit patterns of the hodoscope and TOF counters and provided multiplicities in different parts of the counter array to the summing modules. The summing modules summed up multiplicities from different multiplicity modules and scaled events according to hodoscope multiplicities and other requirements. Figure 4.2 shows how the system was organized. The hodoscope branch was summed step by step to get the total multiplicity in the last two summing modules. The TOF branch had p, $\bar{p}$, TOF1 and TOF2 counters all going into the same summing module. In practice, only one set of the counters was programmed to pass through and was used to impose restrictions on the triggers rather than for scaling. The most frequently used one was the $\bar{p}$ counter array, which was in the ST trigger as mentioned before, and in most of the high multiplicity triggers, as will be discussed later.

TRIGGER PROCESSOR
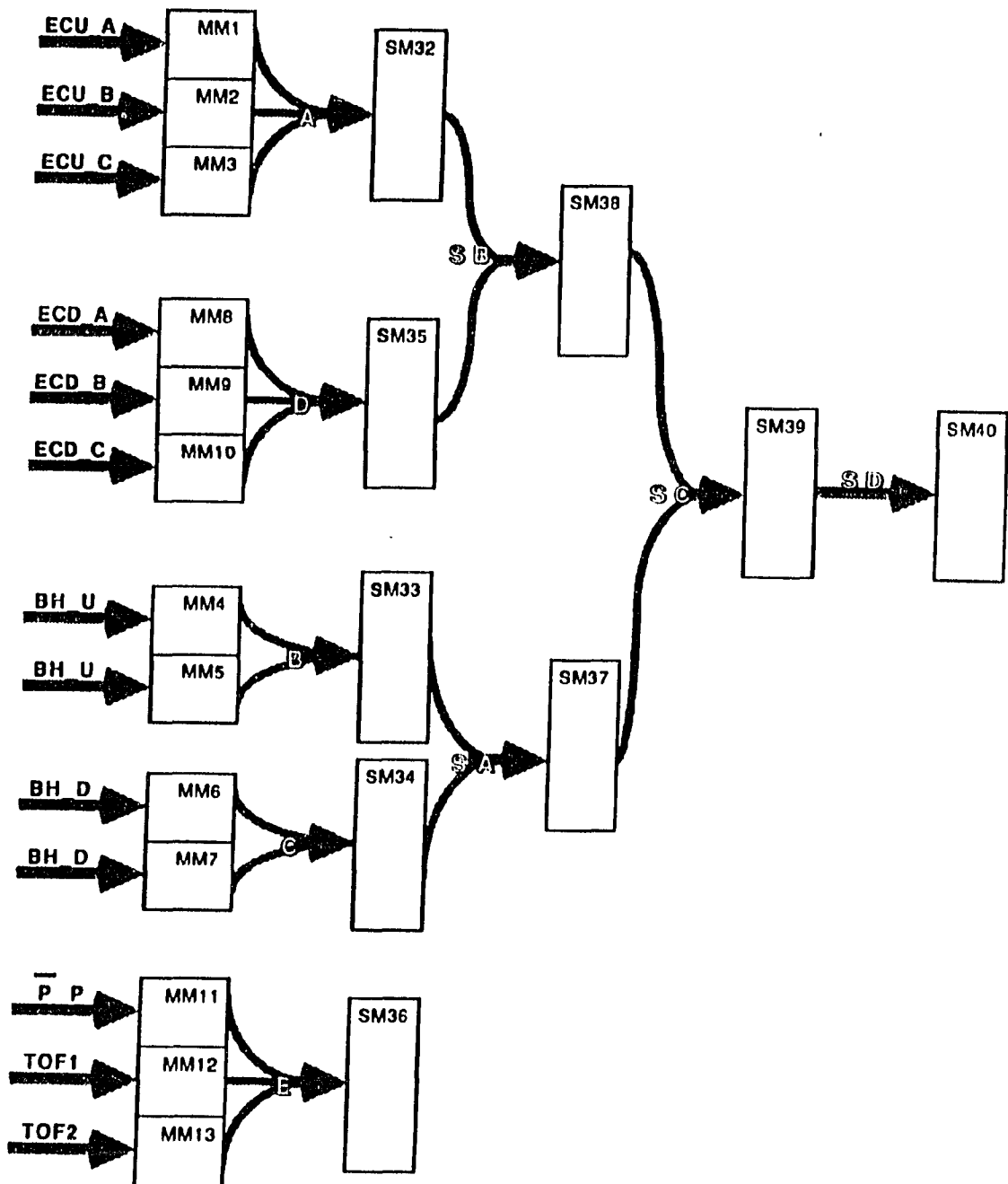
Figure 4.2: Organization of trigger processors.

Multiplicity module

Figure 4.3 is a simplified block diagram of a multiplicity module. The major components of the module are the four Random Access Memory (RAM) chips. Each RAM has an 11-bit address and an eight-bit data output. The highest bit of the address was used as a mode switch, toggling the module between the 'multiplicity mode' and the 'pattern mode'. Apart from the 'mode bit', the RAM was treated as having a 10-bit address. The lower two bits of the address were reserved for address concatenation across RAMs and were not used. The upper eight bits each accepted an input from a hodoscope or TOF counter, effectively using the hit pattern of the counters as the RAM address. The signal from a counter came as a 100ns ECL pulse and was latched by a NIM level strobe before going into the RAMs. Each multiplicity module could accept 32 ECL inputs transported in two ribbon cables. The NIM strobes were derived from the beam crossing signals to match the proper hit times of different sets of counters.

The RAMs were read-writable with VME bus commands. Before using the modules the RAMs had to be pre-loaded. In multiplicity mode, (highest address bit = 0), the eight-bit RAM data were loaded as counting the number of "1"s in the higher eight-bit address, and hence gave the multiplicity of the counters coming to this RAM. In pattern mode, (highest address bit = 1), the eight-bit data were loaded the same as its higher eight-bit address, thus preserving the hit pattern of the counters.

In normal operation, the modules were set in the multiplicity mode. When the signals arrived at the RAMs, each RAM output gave the number of hits it saw. Because there were at most eight counters connected to a RAM, the lower four bits
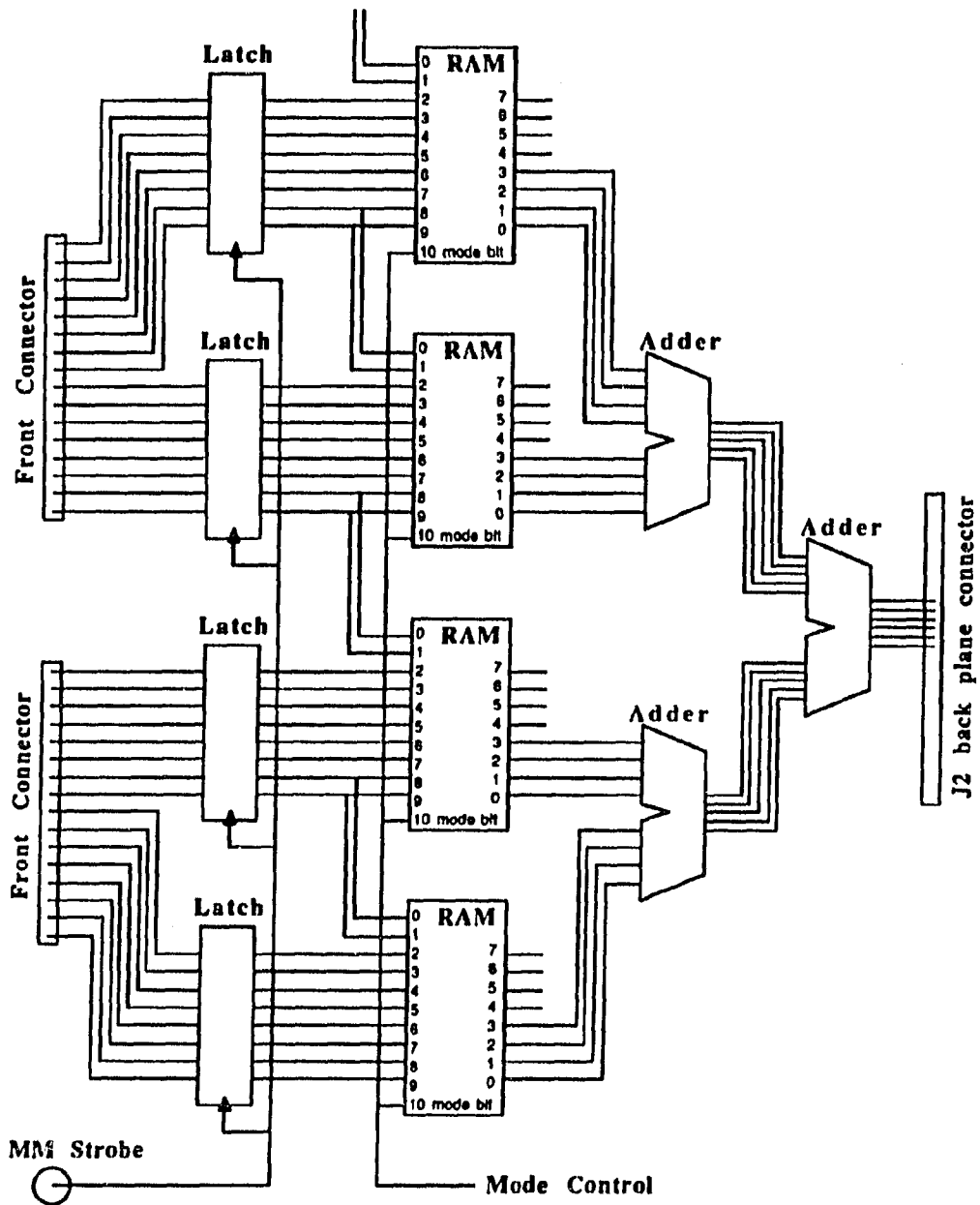
Figure 4.3: Simplified multiplicity module block diagram.

of the output were sufficient for carrying the multiplicity. The lower four bits of the four RAMS were added by adders and the resultant 6-bit total multiplicity was provided to the VME backplane connector for transportation to summing modules.

The pattern mode was not involved in triggering, but was read out in each event to identify how that event was treated. The operation of pattern mode disrupts the functioning of a module as a multiplicity provider, since the lower four bits of the RAM outputs that get summed and sent to a summing module becomes the hit pattern instead of the multiplicity. Therefore, this mode can only be accessed when the system is not in the process of determining a trigger.

Summing module

Figure 4.4 shows a simplified block diagram of a summing module. An internal switch sets a summing module to either accept three six-bit data from three multiplicity modules or two eight-bit data from two other summing modules. Either type of data came from the VME backplane connector at different pin locations. Whichever mode it was, the data were summed with adders into an eight-bit data. These data were driven to a front panel connector for transportation to other modules and also brought to a RAM chip as its address input.

The RAM used was the same as those for the multiplicity modules, although only the lower eight-bit addresses were used. Each of the eight output bits of the RAM was programmed to give a "1" or "0" according to the multiplicities coming as the RAM address, and was used to enable or disable the clock input of a prescaler.

The prescaler was a counter with an input register. The clock input was an external NIM signal, usually the preliminary event trigger. The prescaler could be
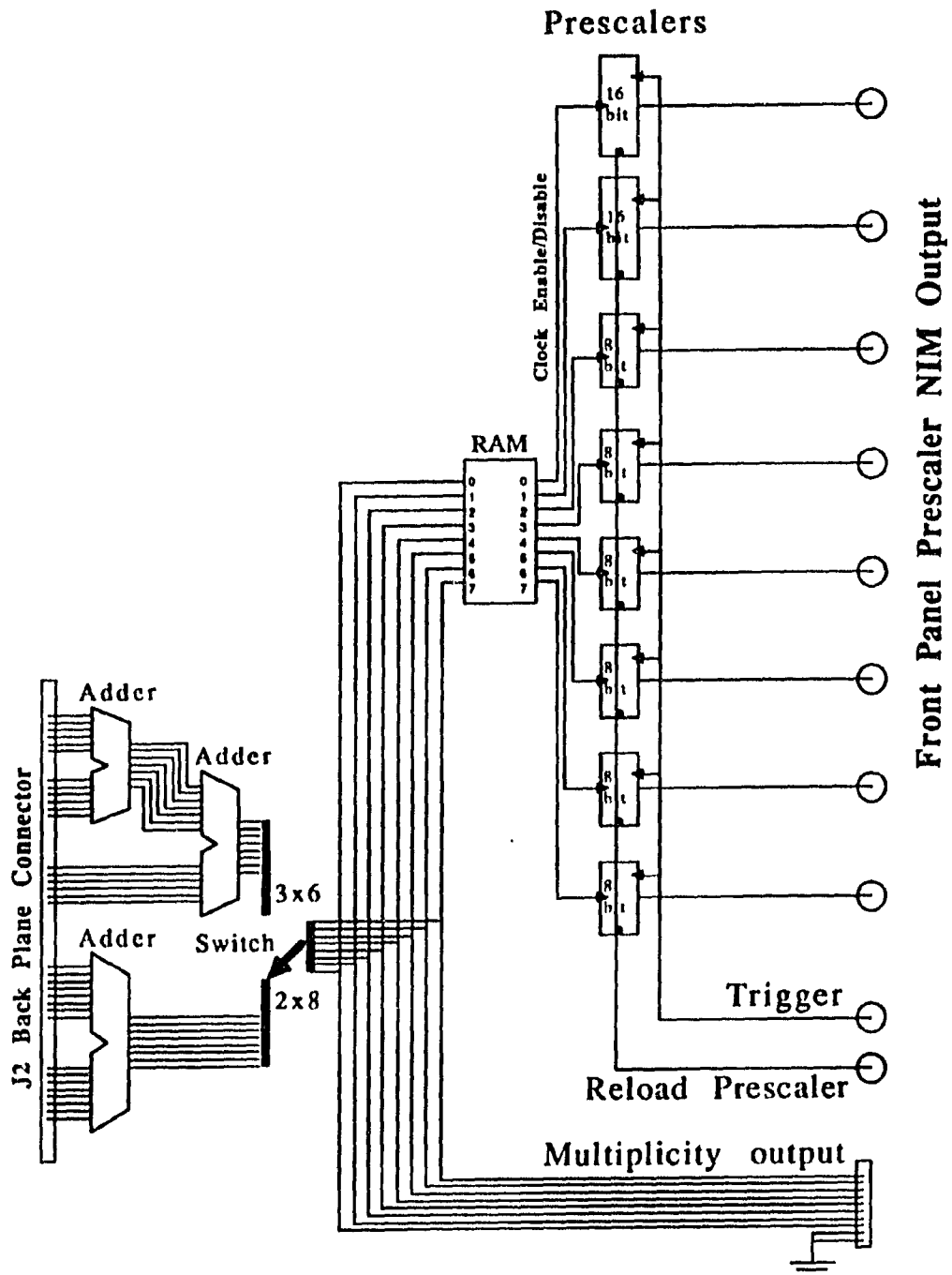
Figure 4.4: Simplified summing module block diagram.

pre-loaded with an initial number. When a trigger signal came , if the clock input was enabled, the number counted down by one. When the number counted down to 0, the prescaler sent out a NIM pulse and reloaded itself to the initial number. The NIM outputs of the eight prescalers were available in the front panel for event trigger or for further manipulation. The two prescalers controlled by the lower two bits of the RAM output were 16-bit's, and the upper six were eight-bit's. The prescalers could also be reset to their pre-loaded values by an external NIM pulse at any time.

System control

The multiplicity modules and summing modules were housed in two separate VME crates, each controlled by a QVI module (Q-bus VME Interface) which accepted instructions from a CVI module (CAMAC VME Interface) in a CAMAC crate. The CAMAC crate was in the branch highway and also accessed by an IBM PC via an auxiliary crate controller. Programming of the trigger processors was done with the PC which operated at a data rate of $\sim 100\mu s$ per non-DMA transfer. A program MMSET was used to load RAMs in the multiplicity modules, which allowed users to determine whether the multiplicity of a group of counters was to be passed to a summing module or to be inhibited. A program SMSET was used to load RAMs and prescalers in the summing modules, which determined the multiplicity range of each prescaler and its scaling factor.

The loading of trigger processors could only be done between runs. During the run a program MONIT was run in the PC, making the system a slave of the online DA system. The communication between the PC and the PDP 11/45 was done with a CAMAC memory module and the IBM DAC system. In the beginning and at the
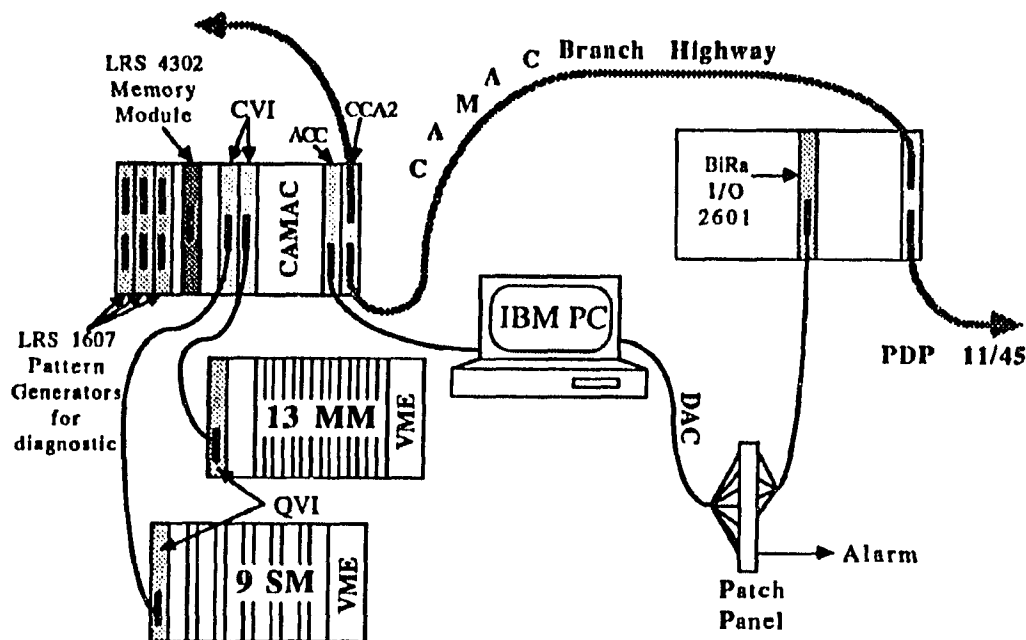
Figure 4.5: Trigger processor control system.

end of a run, IBM reported the trigger processor setup and its checking summary to 11/45, which became part of the run records written to the tape. During data taking, when DA was executing "CAMAC list", IBM was instructed to check and correct the setups loaded in the trigger processors. If an error was found, an alarm was triggered and the status was displayed on the monitor. Figure 4.5 is an illustration of the system.

Multiplicity Scaling

In the '88-'89 runs, scaling was applied to the total hodoscope multiplicities, which was different from the '87 runs, when only the barrel multiplicities were used.

The trigger processor setup of the '88-'89 runs evolved with time and resulted in three different configurations. Here, we will call them Pre-HNC, HNC and HS configurations.

In the Pre-HNC configuration, the spectrometer and the CTC each used a summing module and scaled events independently. Either branch divided hodoscope multiplicities into four regions. The multiplicity divisions for the two branches could either be the same or different . Due to independent scaling, it could happen that one of the branches triggered an event while the other did not. To make events as complete as possible, either branch could be allowed to force a trigger on the other. The result was every CTC event had an accompanying spectrometer part, but not the other way around because of the long CTC dead time. In this configuration non-scaling triggers (e.g. PT) did not need the trigger processors. Figure 4.6 and 4.7 show the setup and the typical accepted multiplicity distributions.

In HNC configuration, the spectrometer and the CTC shared the same summing module (SM39). Each branch still owned four trigger channels. However, the usages were different. One of the channels was assigned to accept events of any multiplicity and scaled them by a large factor. The other three were high multiplicity windows which did not scale the events but could be just opened or closed. These windows were complemented with endcap asymmetry cuts to reduce background events. The number of windows to open was determined by the luminosity and dead time requirements. Starting from this configuration an independent $0.5Hz$ T0 trigger was mixed in for background study. Also, the non-scaling triggers were blocked and required to use trigger processors. The trigger setup and accepted multiplicity distributions are shown in Figure 4.8 and 4.9.

The HS configuration was derived from combining the spectrometer and the CTC branches in the HNC configuration. At SM39 hodoscope multiplicities were divided into eight channels each with an endcap and $\bar{p}$ counter requirement. Events passing SM39 were scaled at SM40 and used for the spectrometer trigger. The CTC trigger was basically the spectrometer trigger scaled by a factor, plus the highest multiplicity bin without its being scaled. Figure 4.10 and 4.11 show the setup and its effect.

The settings of trigger processors in each configuration are summarized in appendix B.

61
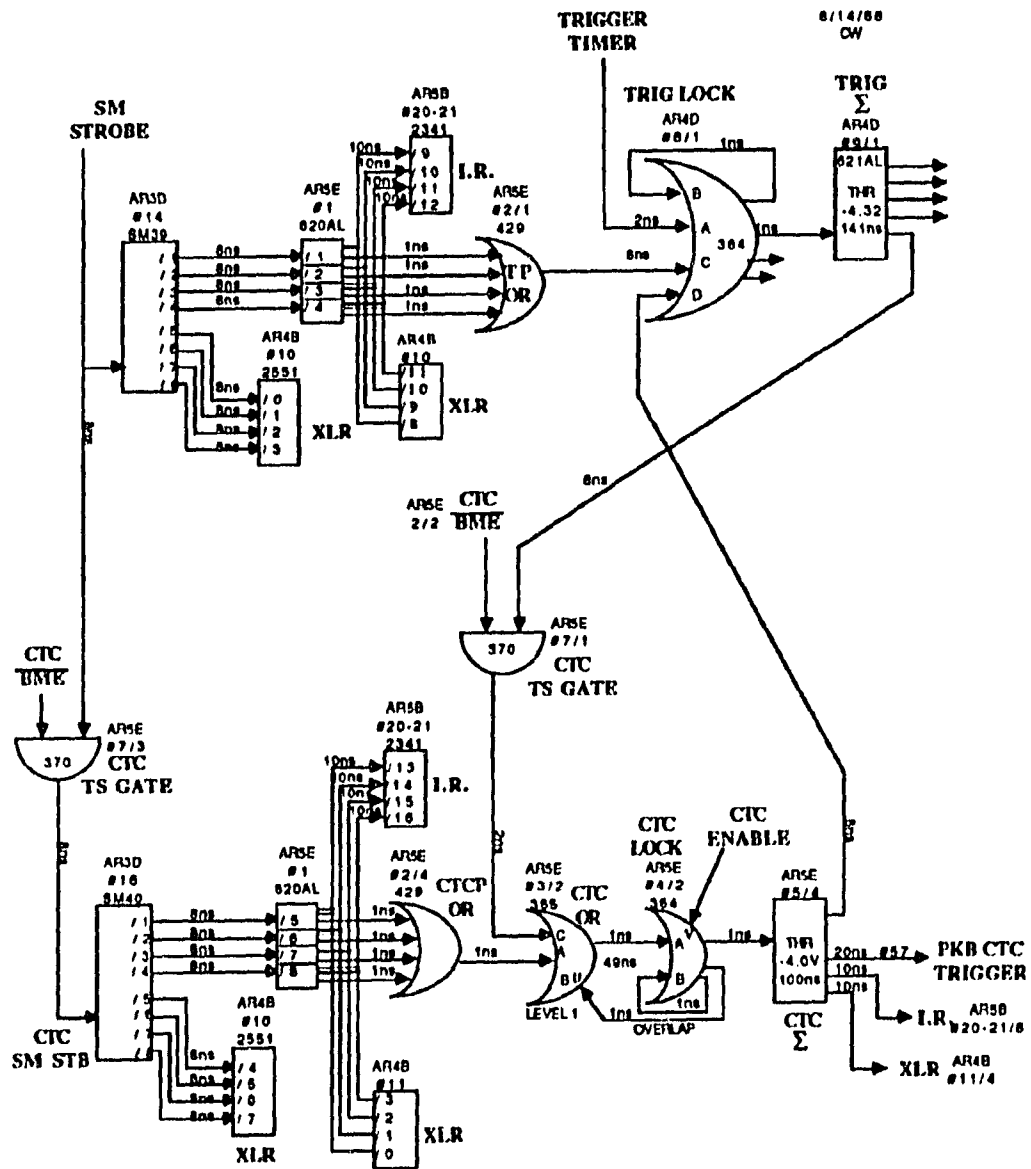

Figure 4.6: Pre-HNC configuration.
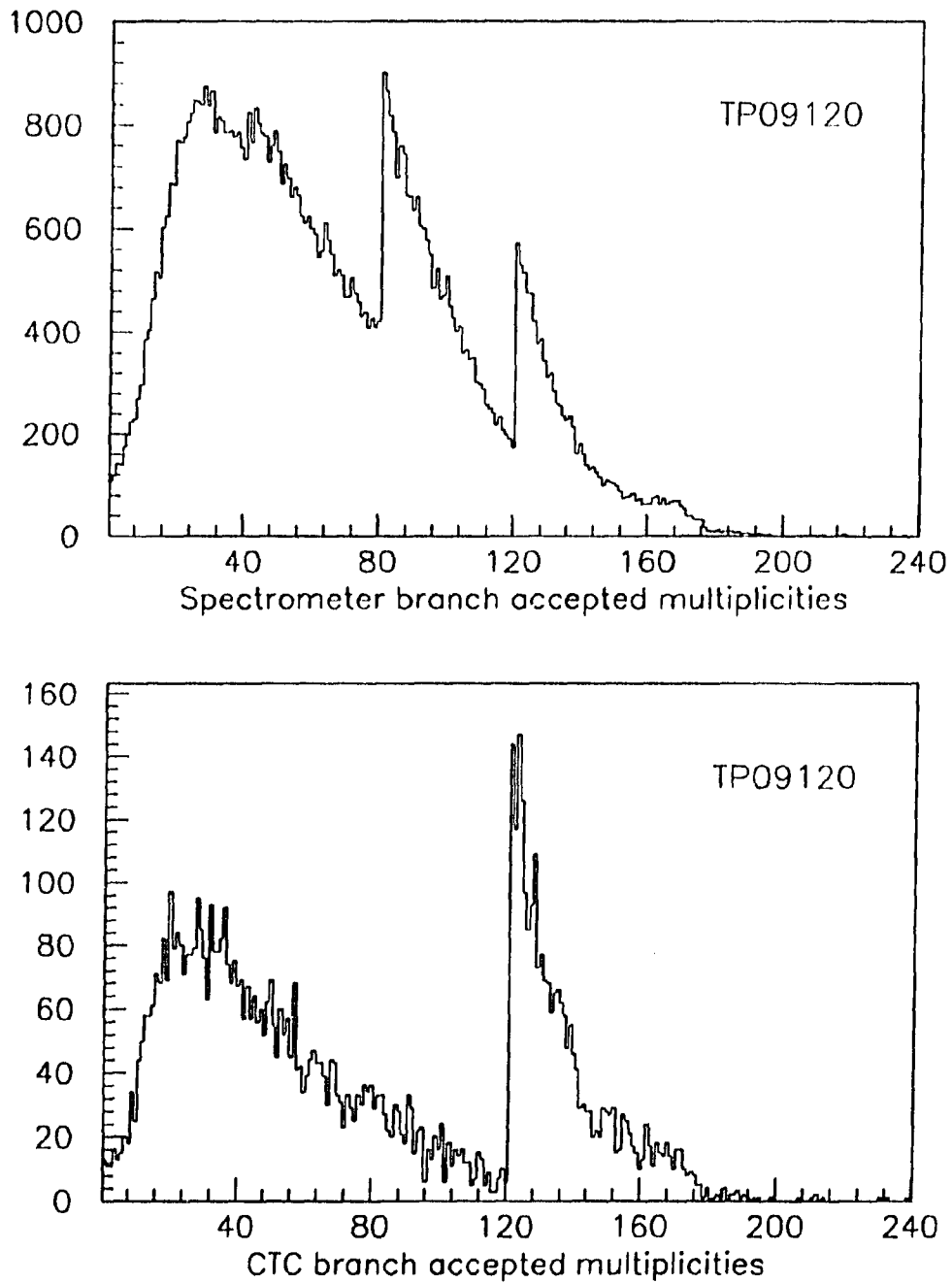
Figure 4.7:   Scaling effects of pre-HNC configuration.

63
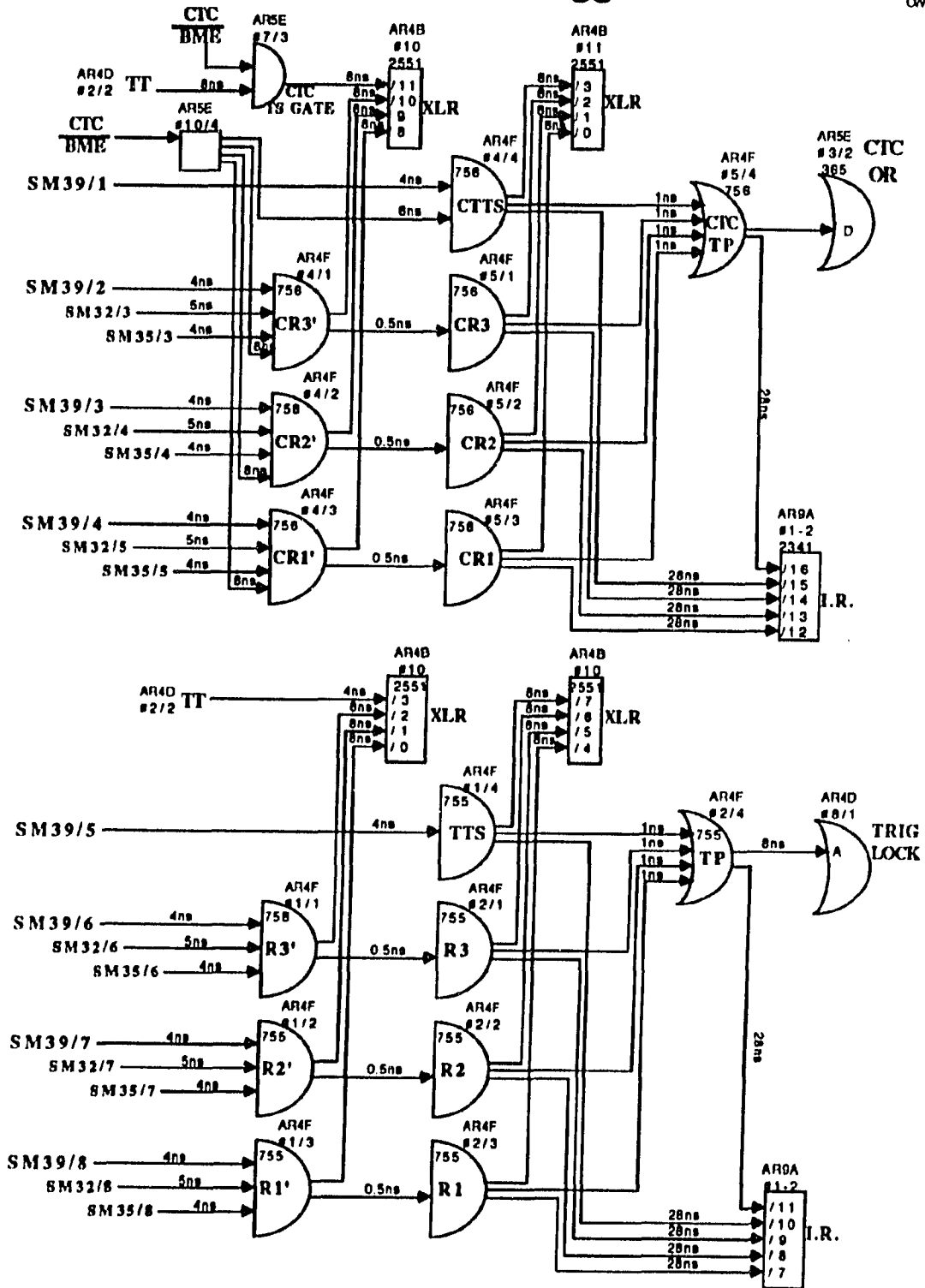

Figure 4.8: HNC configuration.
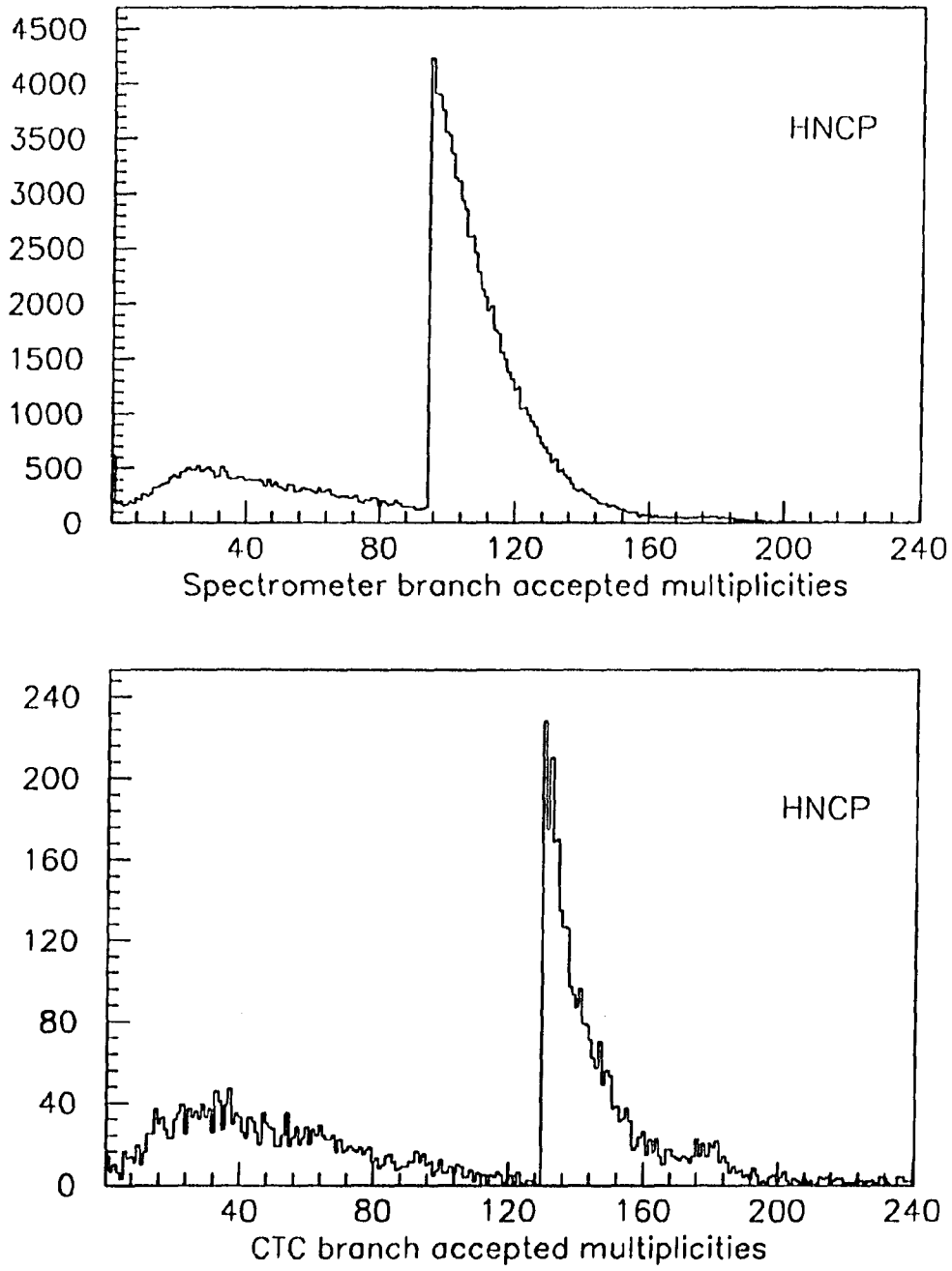
Figure 4.9: Scaling effects of HNC configuration.

HS Trigger

SM32 = ECU
SM35 = ECD
SM39 = TOTAL
SM40 = TOTAL
SM36 = P_bar or P
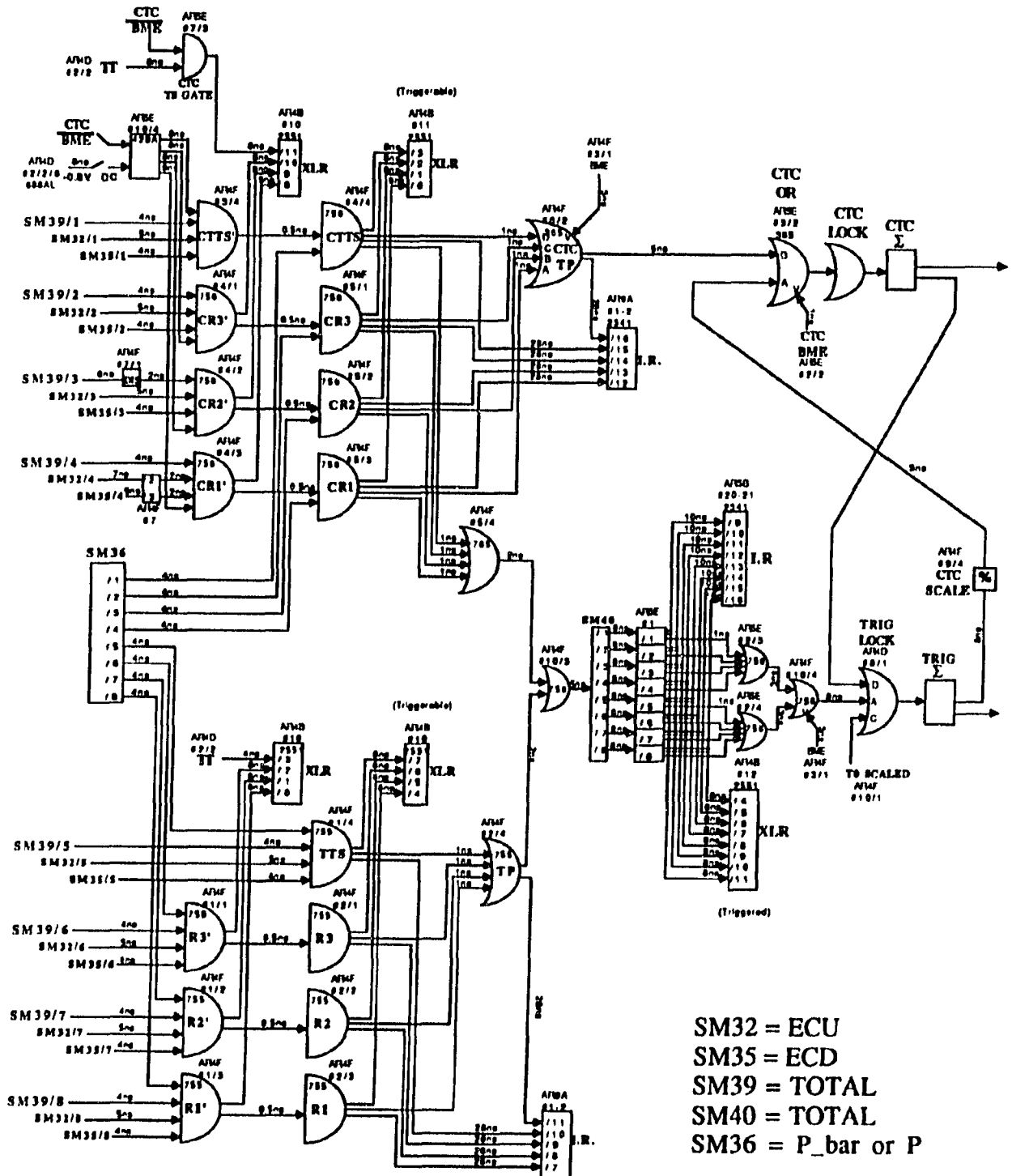
Figure 4.10: HS configuration.
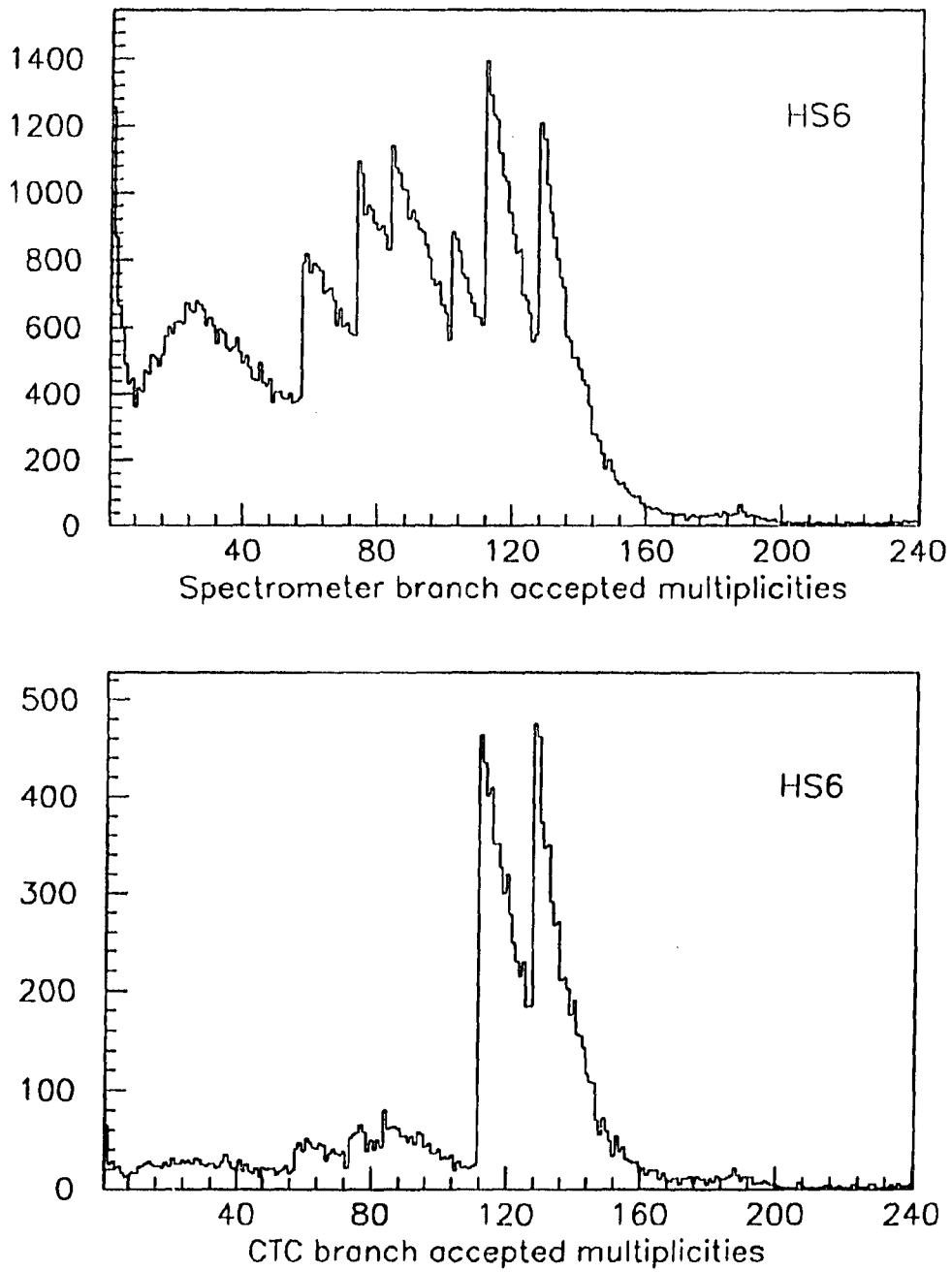
Figure 4.11: Scaling effects of HS configuration.

CHAPTER 5.   DATA ANALYSIS

In this analysis we mainly used the data from the p & p̄ TOF counters and the multiplicity hodoscope. These detectors are scintillator counters implemented with ADC and TDC readouts as described in chapter three. With this information, the vertex of the interaction was determined and backgrounds were discriminated against. For the study of the multiplicity distributions, we selected PT trigger events which we considered as the minimum biased trigger of this experiment. In '88-'89 runs we have 2,792,785 PT events at 1800 GeV, and 265,703 at 546 GeV. We also used missing bunch runs for background study.

Data Manipulation

Hodoscope

The thickness of a hodoscope counter is 0.635 cm . A minimum ionizing particle passing vertically through a counter is expected to loose $\sim$ 1.3MeV of its energy. The ADC readout is a charge integrator with 12-bit resolution and a scale of 10 counts/pC. Figure 5.1 shows typical ADC distributions of counters in different hodoscope rings. Particles hitting a counter can come from different directions and pass through different lengths in the counter. The variation of energy loss due to different path length is large, and in our case the identification of multiple hits in a
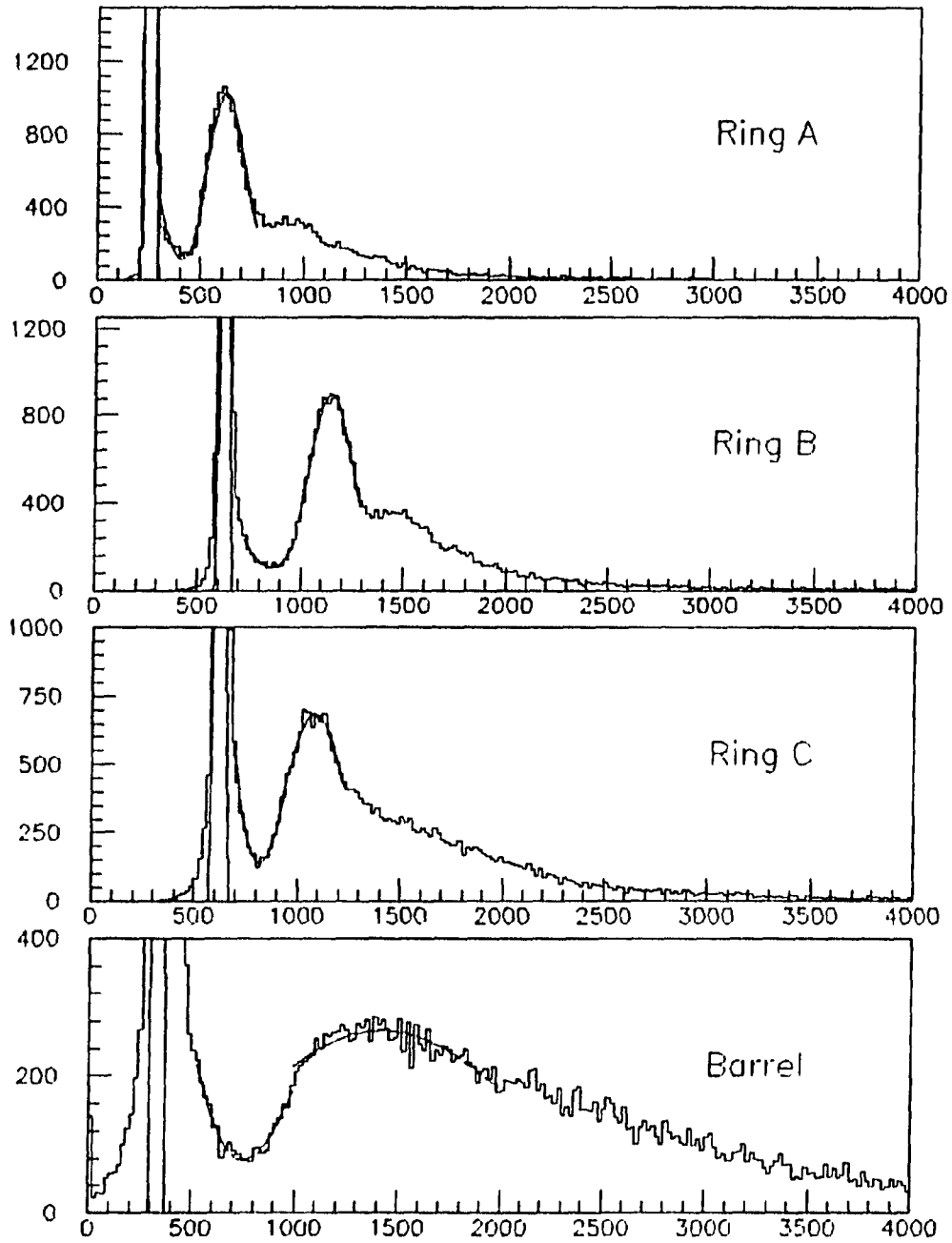
Figure 5.1: Typical ADC distributions from hodoscope counters in ring A, B, C and the barrel.

single counter is not possible. For identifying a valid hodoscope hit, an ADC cut was made at the bottom of the valley between the pedestal and the Minimum Ionizing Peak (MIP).

The TDC readout has an 11-bit resolution with 20 counts/ns. Figure 5.2 shows typical TDC distributions from different hodoscope counters. The spectrum reflects the time structure of the colliding beams. The calibration of each TDC was done to align the main peak of all hodoscope counters, and hence, define a nominal hit time. This nominal hit time is set to 1000 TDC count and defined as time 0 (ns) for the hodoscope.

p p̄ counters

The p & p̄ TOF counters have the same kind of ADC & TDC as the hodoscope, except that they are implemented on both ends of each counter. The thickness of a counter is 2.54 cm, which corresponds to an energy deposition of ~ 5.2 MeV from a minimum ionizing particle. As shown in Figure 5.3 the ADC resolution depends on their size, location and high voltage. Multiple hits can be identified in a few counters, but this is not generally possible.

To determine whether a counter is hit or not, first, ADCs from both ends are required to pass the 'minimum cut', that is, the mid-point between the pedestal and the first MIP, and TDCs from both ends are required to be set. Then, after TDCs are calibrated, if a "valid" hit time of the counter is found, the counter is accepted as being hit.
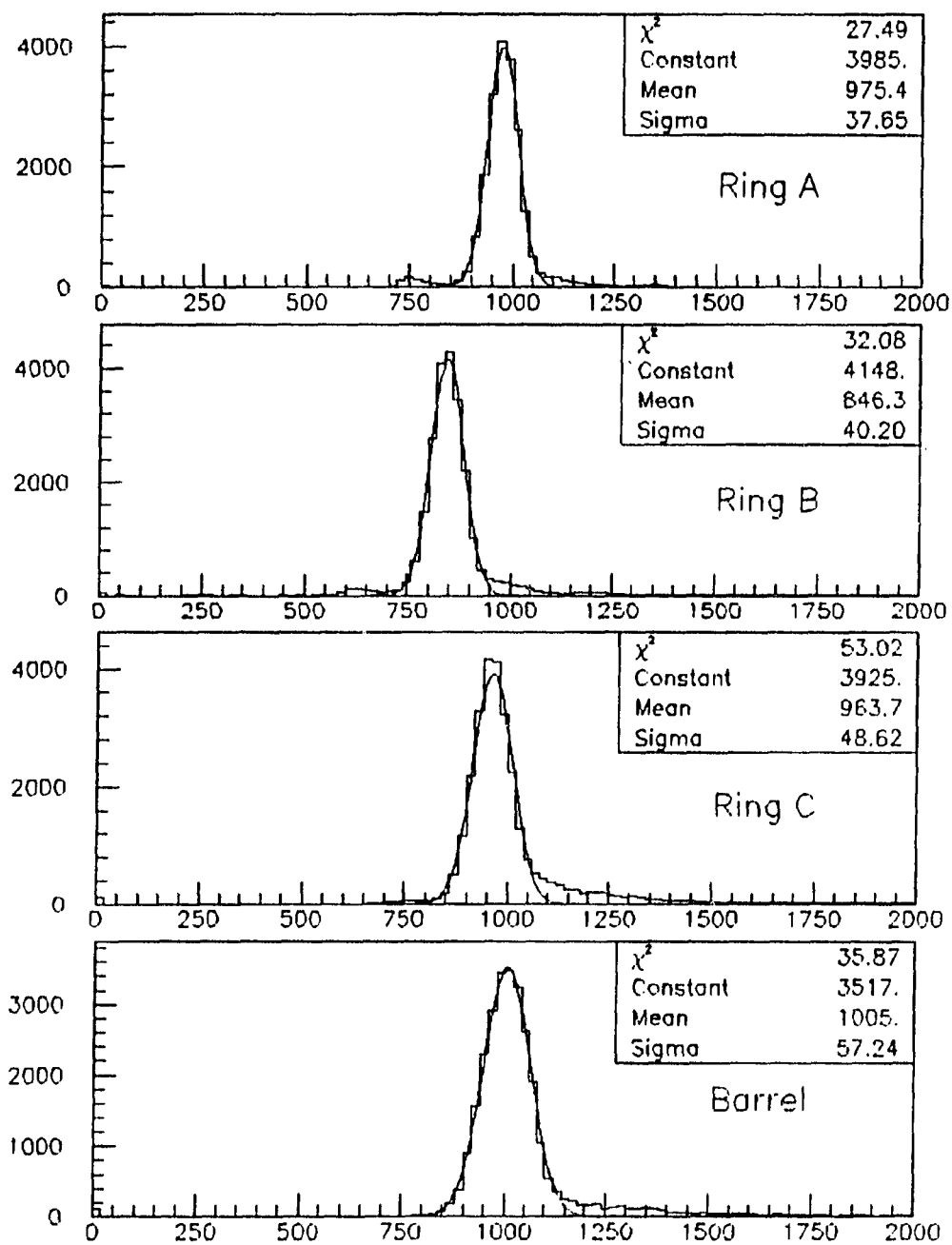
Figure 5.2: Typical hodoscope TDC distributions of ring A,B,C and barrel.
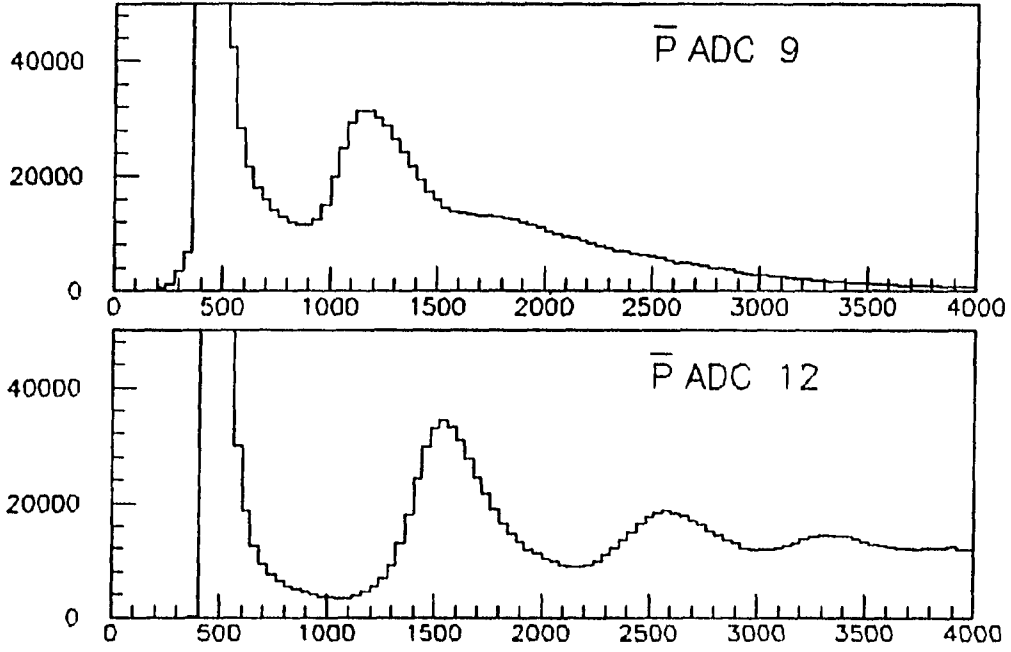
Figure 5.3: ADC distribution of a typical p p̄ TOF counter.

TDC calibration As the p & p̄ counters are also used to obtain an event-vertex position, their calibration is much more elaborate than the hodoscope. A raw TDC readout is first corrected for the non-linearity of the TDC module by an empirical relation :

$$TDC = a \cdot (TDC_{raw}) + b \cdot (TDC_{raw})^2 \qquad (5.1)$$

If $TDC < 180$, the hit is ignored because of the poor resolution at that region. For the next step time-walk correction, the ADC value $A > 150$ is further required[1] , where A is the pedestal subtracted ADC. The time-walk correction corrects time slewing due to different pulse heights. Figure 5.4 shows the dependence of time slewing (T)

---

[1]The full scale of a TDC is 2000 counter = 100 ns. The full scale of an ADC is 4000 counts = 400 pC.
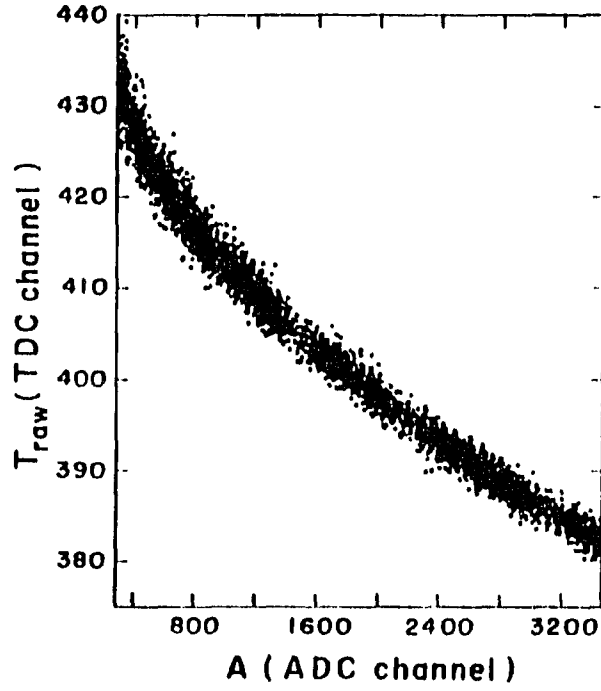
Figure 5.4:   Data from Laser runs showing TDC value as a function of ADC value.

on ADC (A).   It has the relation :

$$\ln T(A) = a + b\ln A + c\ln^2 A. \tag{5.2}$$

An arbitrary reference pulse height was chosen at $A_0 = 1000$, and a correction term $\Delta T(A) = T(A) - T(A_0)$ is subtracted from TDC. After corrections, a TDC is assumed valid if $100 < TDC < 2000$. The average of TDCs from both ends of a counter is then corrected for relative time-alignment within the same set of counters and provides a "valid" hit time of the counter.

Vertex determination

To find a vertex from p & p̄ TOF counters we use the Piekarz-Cole version of "Averaged Time" algorithm. First, hits that come too late are thrown away, in

this case, 30 ns for $\bar{p}$ and 36 ns for p counters. The difference is due to different time-alignment in p and $\bar{p}$ counters. Then, hit times of the counters in each set are averaged. If there are more than three hits in the set, hits outside of one standard deviation are thrown away and the average recalculated. If there are hits deviating from the mean by more than 0.5 ns, those hits are also thrown away and the average recalculated. After these screenings, if the average hit time of p and $\bar{p}$ counters both exist, they are used for calculating the interaction time and the event vertex. The sum gives the interaction time and the difference gives the vertex. The results are offset for time-alignments and fine adjusted according to different run number and hodoscope multiplicity. Figure 5.5 shows the corrected vertex distribution. It is Gaussian in shape with a $\sigma = 37cm$. The average vertex location varied from store to store, but usually within a few cm from C0. Compared with vertices from good Z chamber tracks, the difference of the two vertices has a σ of 5 cm as shown in Figure 5.6, and reflects the accuracy of TOF vertices so determined. About 95.9% of the events passing a standard event cut, described below, have a valid TOF vertex.

Event Characteristics and Cuts

In an ideal experiment one would only like to take events which have occurred from beam-beam interactions. In reality, this has never been possible. Other events, such as beam-gas interactions, beam-beam-pipe interactions, background radiation, satellite bunches and, in our particular setup, beam-gas interactions in the Main Ring, are all possible and can trigger an event. We collectively call these contaminations BG events. Figure 5.7 shows the characteristics of various types of events. Based on time structure and hit pattern in the counters, most of the BG events can be discriminated
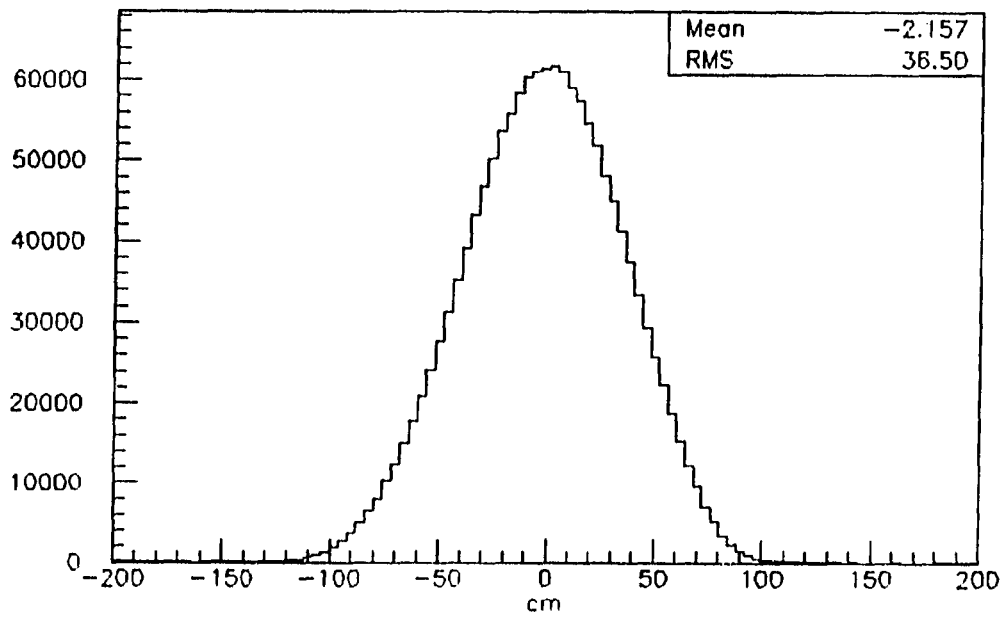
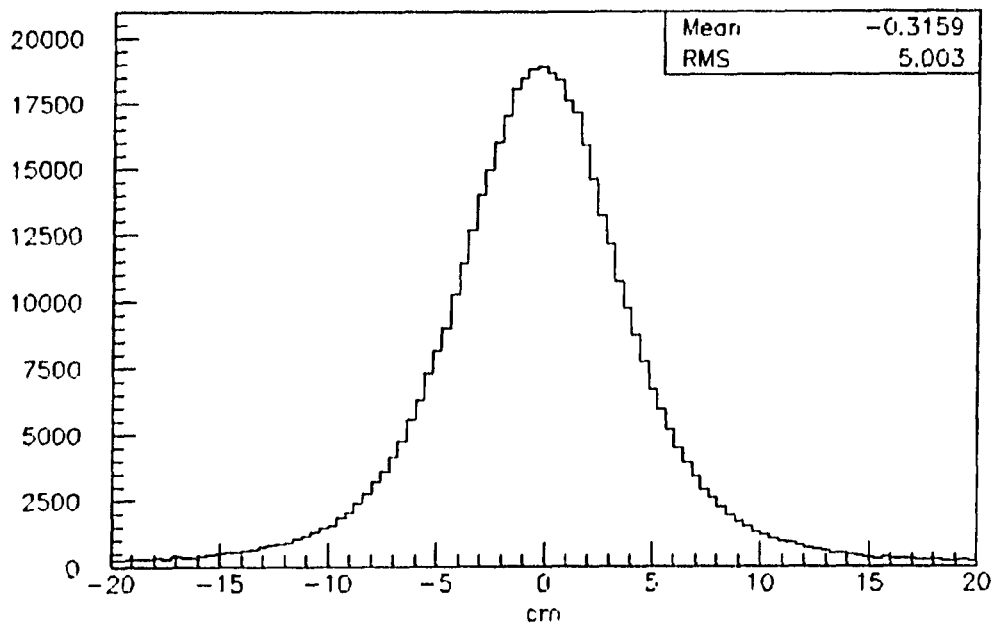Figure 5.5: TOF vertex distribution from events passing BG cut.

Figure 5.6: (TOF vertex)−(good tracking vertex).

A Typical Beam-Beam Event

A Typical Single Diffractive Event

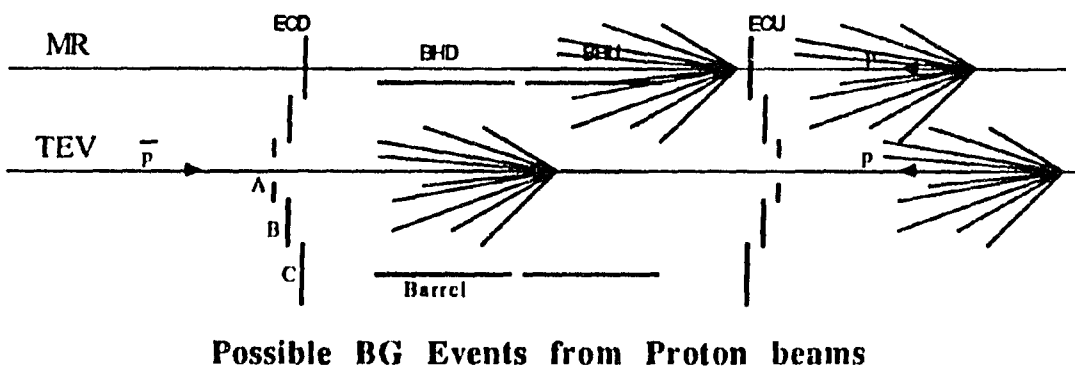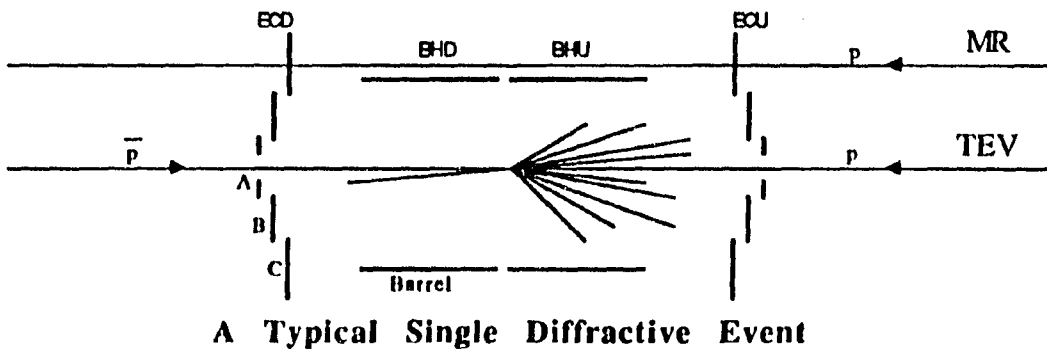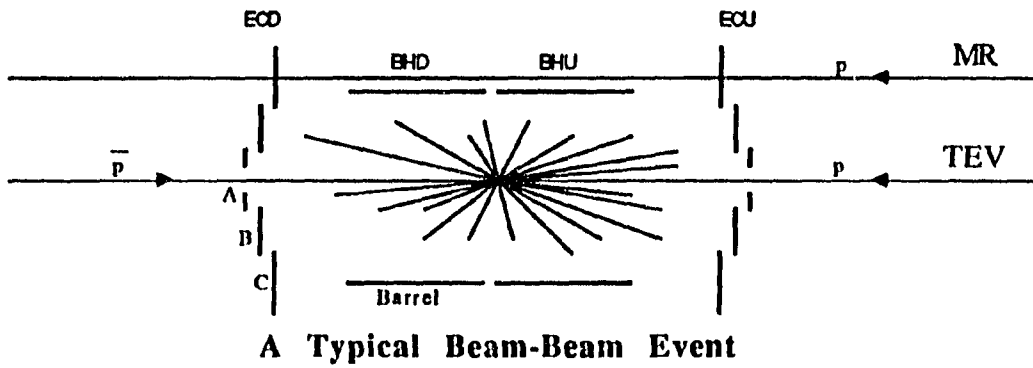Possible BG Events from Proton beams

Figure 5.7: Sources of events.

from a real beam-beam event; however, some fraction remains indistinguishable. In particular, single-diffractive events are similar to BG events. The object of the event selection mechanisms will be to extract non-single-diffractive events.

Time information

Figure 5.8 shows the hit time distributions from three different beam conditions in the Tevatron: p-$\bar{p}$, p-only, and $\bar{p}$-only. The Main Ring was simultaneously accelerating protons for $\bar{p}$ production. The entries in the scatter plots are pairs of hits from ECUA (End Cap Upstream ring A) and ECDA (... Down-stream ...), which are the closest end-cap counters to the beam. The scale is 20 counts/ns. Nominal hit time of a beam-beam event is at 1000. As can be seen, there are several clusters apparent in the plots. In the proton only plot, cluster 1 can be identified as due to the proton beam halo which sweeps across the counters from up-stream to down-stream hitting ECDA at a correct nominal time, but 10 ns too early at ECUA. Along the 45° line, about 13 ns later, cluster 2 is generated from the same mechanism but by the trailing proton satellite bunch. Cluster 3 indicates the occasions that ECDA's were hit by proton main bunch halo while ECUA's were hit by satellite bunch halo. This cluster is difficult to distinguish from the beam-beam cluster in the p-$\bar{p}$ plot, since the only difference is ECUA being hit 3 ns too early, while the proton bunch itself is $\sim 5ns$ wide. The same arguments hold for the $\bar{p}$ only stores except that the relative hit time is reversed.

Based on time information, a time cut was developed to remove out-of-time hodoscope hits and events.

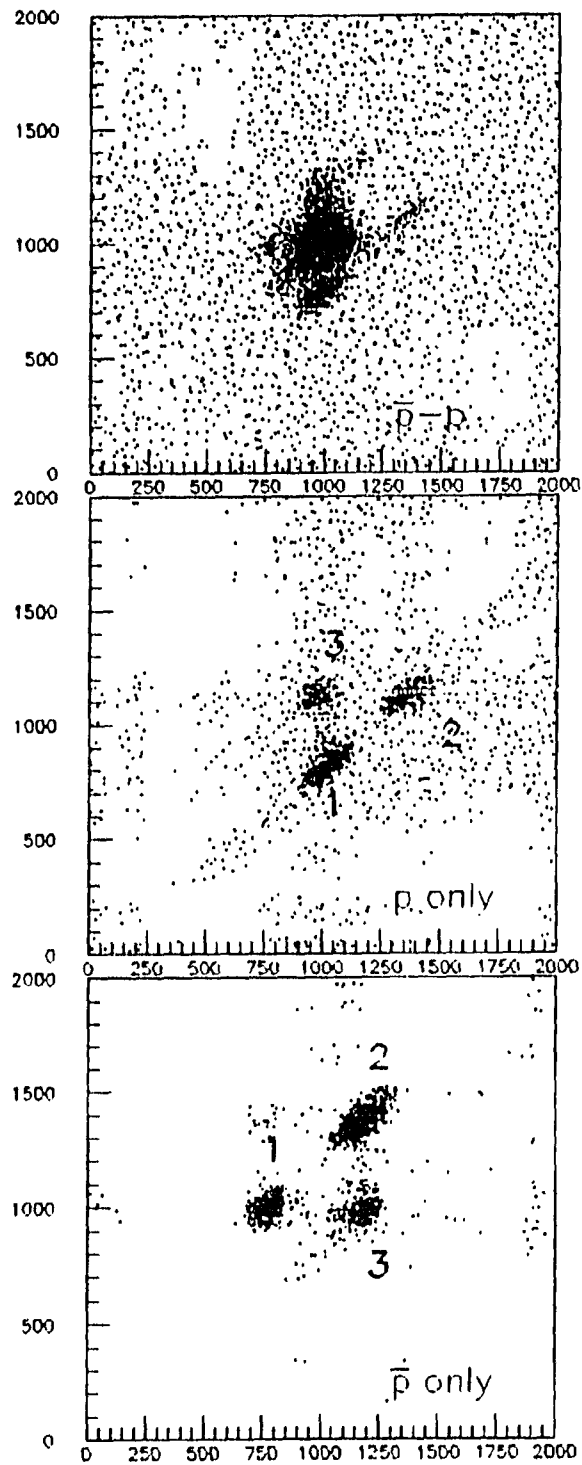For a hodoscope hit, in addition to passing the ADC threshold cut, the TDC is

Figure 5.8: Hit time combination, ECUA vs ECDA.

also required to fire within a time window between -10 ns and 50 ns with respect to the hodoscope nominal hit time.

For an event, the averaged hit time of ECU, ECD and the whole hodoscope were calculated; first with all the counters passing the ADC threshold cut and TDCs $<$ 50 ns, then recalculated with only hits near the averages. For the whole hodoscope, hits within 2.5 ns of the first average were used. For ECU and ECD, hits within 5.0 ns of the first average were used. If any of the three recalculated averages deviates from the nominal hit time by more than 6 ns, the event is excluded. Figure 5.9 shows the events passing and failing the cut.

Forward backward asymmetry

Other than timing difference, BG events are also characterized by their forward-backward asymmetry since their interactions are from a target at rest in the laboratory system. Figure 5.10 shows the difference between end-cap multiplicities as a function of total hodoscope multiplicity. As an event selection tool, a maximally allowed difference of end cap multiplicities is assigned as a function of hodoscope multiplicity. Events lying outside of the boundary are taken as BG events. The boundary is determined by joining a set of points in Figure 5.10. Table 5.1 shows the points used as in our standard cut.

Table 5.1: Standard setting of end cap asymmetry cut.

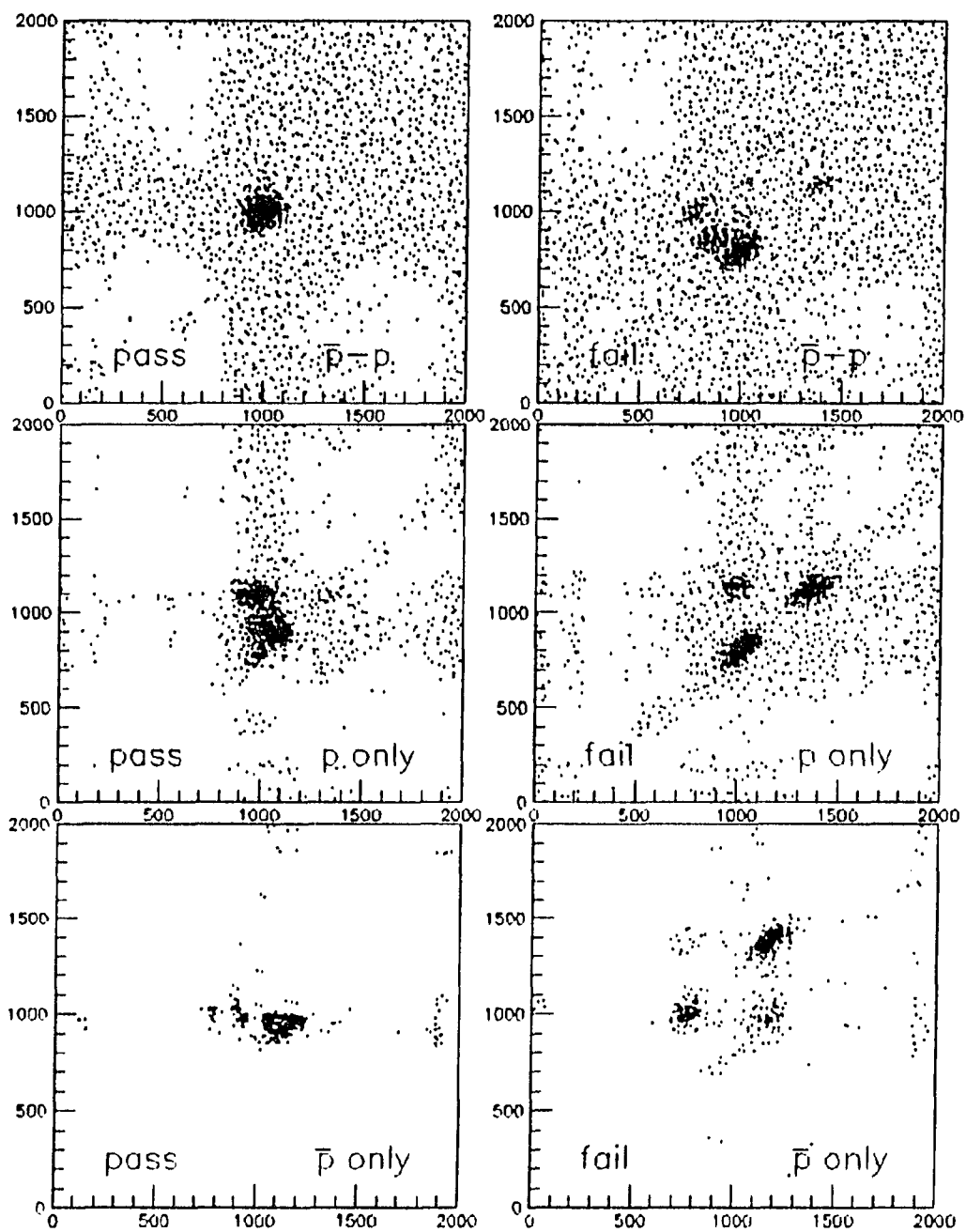| $|N_{ecu} - N_{ecd}|$	7	7	13	17	20	23	24 - 24
N_{hodo}	0	10	20	30	40	50	60 - 240

Figure 5.9:   Hit time combination, ECUA vs ECDA of events passing time cut (left) and failing time cut (right).
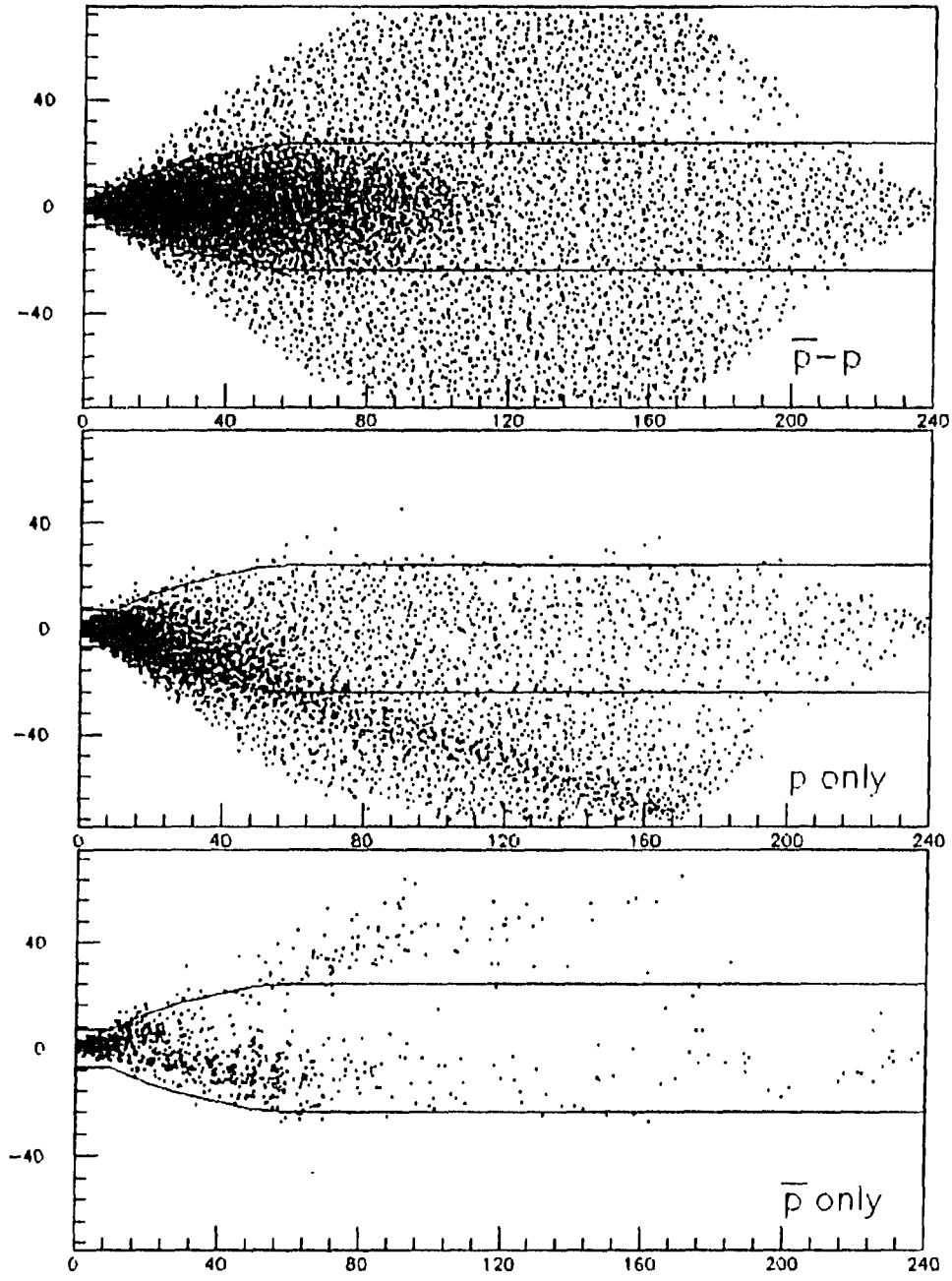
Figure 5.10: $N_{ecu} - N_{ecd}$ vs N_{hodo}.

P P̄ counter multiplicity

The PT trigger event requires at least one hit in p and at least one hit in p̄ counters. This requirement, however, is derived from only one end of the counters wired into the trigger logic. The p and p̄ counters have phototubes on both ends. A hit determined offline as described earlier will be much more restrictive and definite. Figure 5.11 shows p & p̄ counter multiplicities so determined from various beam situations.

A great majority of BG events have a low multiplicity going near the beam line. For singly diffractive events from beam-beam interactions this is also the case. The p p̄ counters are the closest to the beam line. A requirement on p p̄ multiplicities can effectively eliminate these two kinds of events. In our standard cut the requirement is at least two hits in p counters and at least two hits in p̄ counters.

Main ring contamination

BG events from the Main Ring have the same characteristics as those from the Tevatron. In addition, due to their peculiar geometrical origin, events from the Main Ring usually demonstrate an asymmetry in φ. Figure 5.12 shows the frequency of hits for each individual hodoscope counter. Labeling of counters in each ring starts from $\varphi = 0$ to $\varphi = 360$ in C0 coordinate. Thus, right underneath the Main Ring are counter # 6 in each end caps rings, and # 12 in each barrels rings. The dips in ring C are due to a cut away for Main Ring pass-through and the dips in the barrel are due to the spectrometer window. 78% of our PT data were taken while Main Ring beams were circulating in the beam pipe. For events failing the BG cut, the modulation can be clearly seen in each ring and is more significant in outer rings closer to the Main
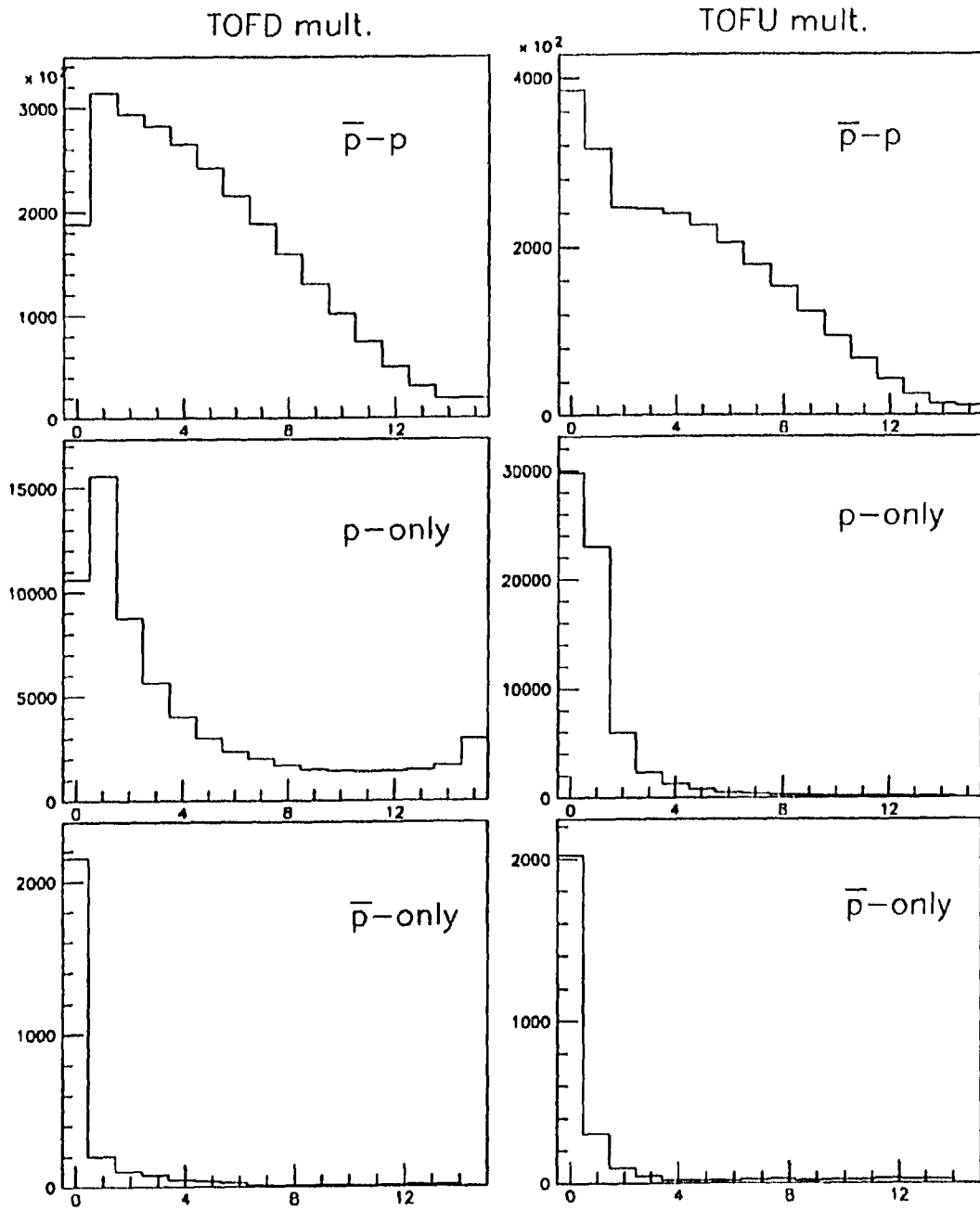
Figure 5.11:   p & p̄ counter multiplicity distributions from p-p̄, p and p̄ beams.

Ring. This is certainly due to the contamination from the Main Ring.

However, events passing BG cut also demonstrate a modulation in the same azimuthal region except that the modulation is more significant in inner rings than in the outer rings, which requires an explanation other than the Main Ring effect. A fast Monte Carlo[51] assuming a flat $dn/d\eta$ with a simple material interaction model shows that the modulation can be accounted for if the Tevatron beam was shifted by ~ 0.8 cm in the y direction, which is consistent with the x-y vertices determined from the central tracking chamber[52].

Effects of the BG cut

The application of cuts can be separated into two levels: hit identification and event selection. Details of their implementation are described above. To summarize, the standard BG cut for event selection includes the following :

- $(N_p \geq 2)$ and $(N_{\bar{p}} \geq 2)$.

- $Z_{vertex} \leq 60$ cm.

- End cap upstream-downstream asymmetry cut.

- Averaged time cut on the whole hodoscope, upstream end cap and downstream end cap respectively.

Table 5.2 shows percentage of events failing each cut under various beam conditions. For p-$\bar{p}$ and p-only beams PT events are used. For $\bar{p}$-only beam we have no pure PT events, and mixture of T0 and S1BC (actually : PT × online asymmetry cut) events are used. The "exclusive" entries show how much data will be removed by a
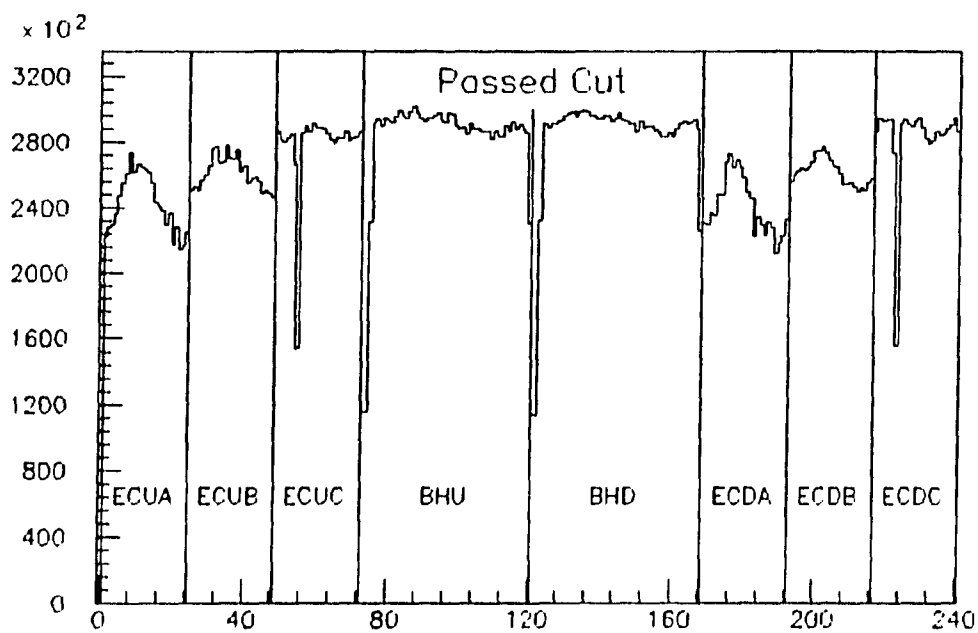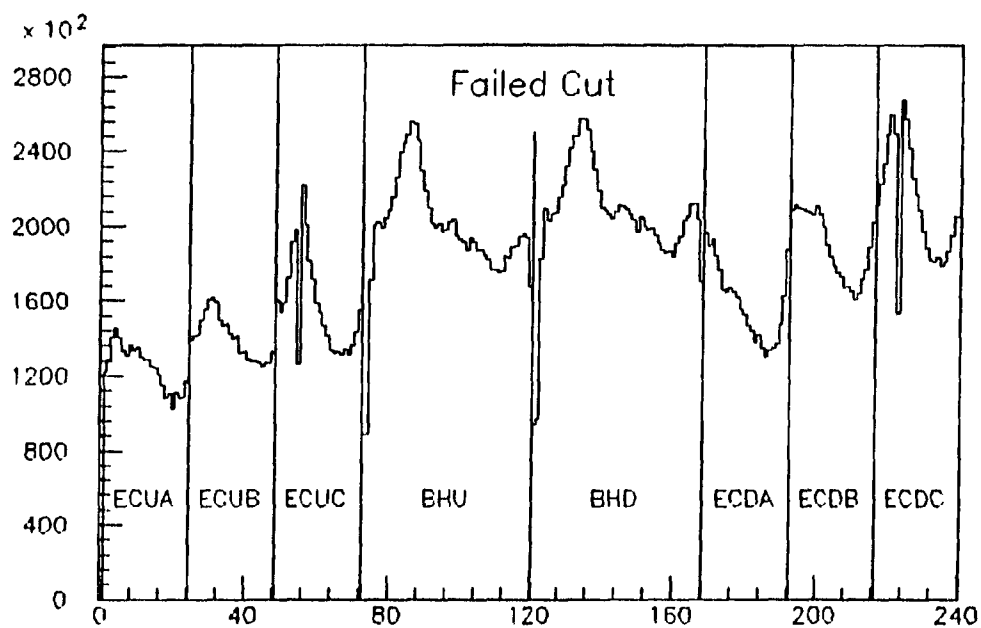
Figure 5.12: Hodoscope counter map for events failed BG cut (upper) and events passed BG cut (lower).

particular cut while passing all other cuts. The large difference between "inclusive" and "exclusive" in the table indicates that most of the events failing BG cut are failing on more then one cut.

Table 5.2: Percentage of events fail each cut inclusively and exclusively.

Beams	types	$N_p, N_{\bar{p}} \geq 2$	$Z \leq 60$	EC Asym	Tav	Any	Events
p̄-p	Inc.	37.2	33.3	6.6	17.5	49.7	2,575,826
	Exc.	10.7	8.0	1.0	1.9		
p-only	Inc.	88.3	67.4	18.4	58.0	99.0	65,563
	Exc.	9.5	0.9	0.6	3.9		
p̄-only	Inc.	95.7	93.4	4.9	28.8	99.9	2,708
	Exc.	1.4	0.4	0.0	1.5		

In the p-p̄ beam data, 49.7% of the events failed BG cut. These events are actually a mixture of good events and BG events with a proportion depending on beam conditions. If we assume they are all BG events; from p-only and p̄-only data we see that less than 1% of BG events can pass the BG cut, we can then estimate an upper limit of the residual BG contamination in the after-cut data :

$$\frac{0.497 \times \frac{0.01}{0.99}}{1 - 0.497} = 1.0\%. \tag{5.3}$$

Figure 5.13 and 5.14 show the multiplicity distributions from p-p̄ and p-only data. The two curves that failed BG cut, (curve 3 from Figure 5.13 and curve 6 from Figure 5.14) are compared in Figure 5.15. The two curves are able to match each other at both high and low multiplicity regions by a simple adjustment of their vertical scales. Specifically, curve 6 is magnified by a factor of 9 in Figure 5.15. The matching of the two curves is consistent with our model of BG events shown in Figure 5.7.
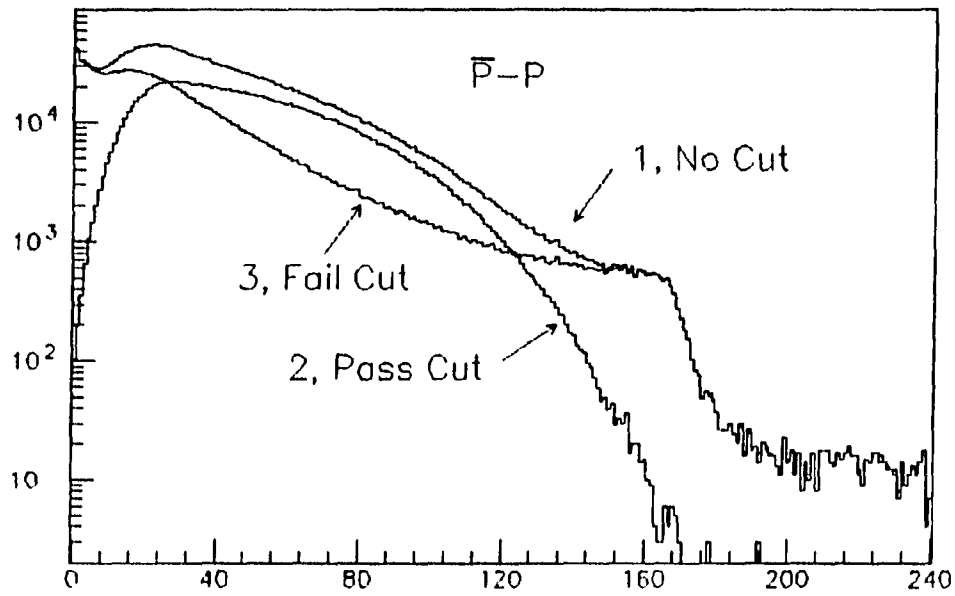
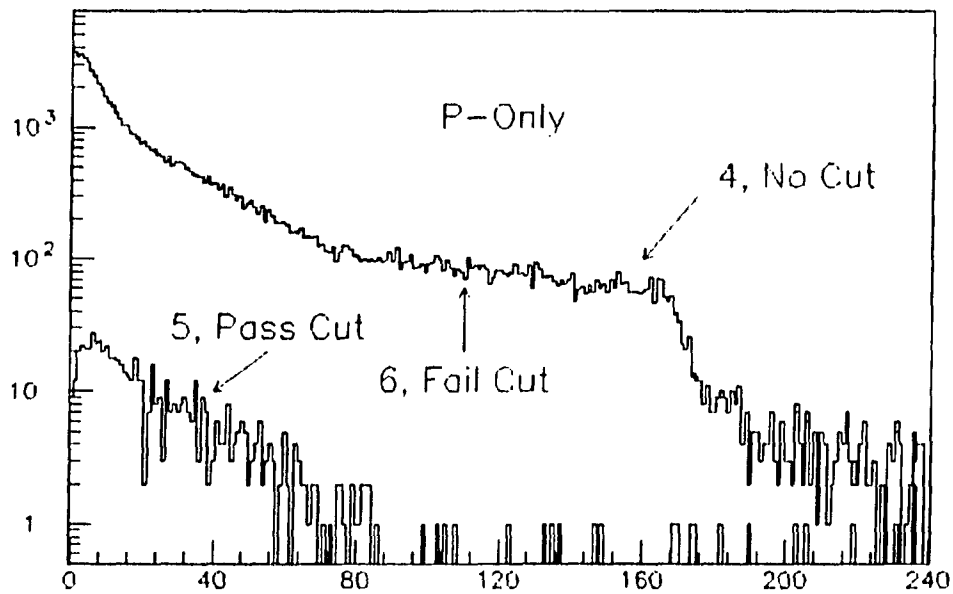Figure 5.13:   Hodoscope multiplicities from p-p̄ store.

Figure 5.14:   Hodoscope multiplicities from proton only store.

The sudden drop at $N_{hodo} \sim 168$ is an indication of the asymmetric nature of BG events. An end cap contains 72 counters, and $240 - 72 = 168$. If a proton hits a gas molecule near the upstream end cap, the secondary particles produced can hit the barrel and the down-stream end cap in the forward direction, while very few will hit backwardly to the upstream end cap.

The extra hump at $N_{hodo} \sim 15$ in curve 3 is evidently due to beam-beam events failing the BG cut. The difference of the two curves, representing the "cut bias", is shown in Figure 5.16. This bias, however, does not include the "trigger bias" which occurred when events were actually triggered and taken.

The consistency between curve 3 and curve 6 in Figure 5.15 suggests that the distribution of BG events that failed BG cut have the same shape in both p-$\bar{p}$ and p-only stores. Hence the distribution of BG events that passed BG cut should also be the same. Namely, curve 5 in Figure 5.14 is the BG contamination of curve 2 in Figure 5.13 except for a multiplicative factor which we determined to be 9 as we tried to match curves in Figure 5.15. The fractional contamination of BG cut is then :

$$\frac{(\text{Curve 5}) \times 9}{(\text{Curve 2})}, \tag{5.4}$$

as shown in Figure 5.17. In doing this, we have implicitly assumed that there were no additional background sources not adequately accounted for by the p-only data.

If one feels that subtracting Beam-Beam events from curve 3 is risky, one can also assume that curve 3 is totally BG events and estimate a "maximal" fractional contamination by :

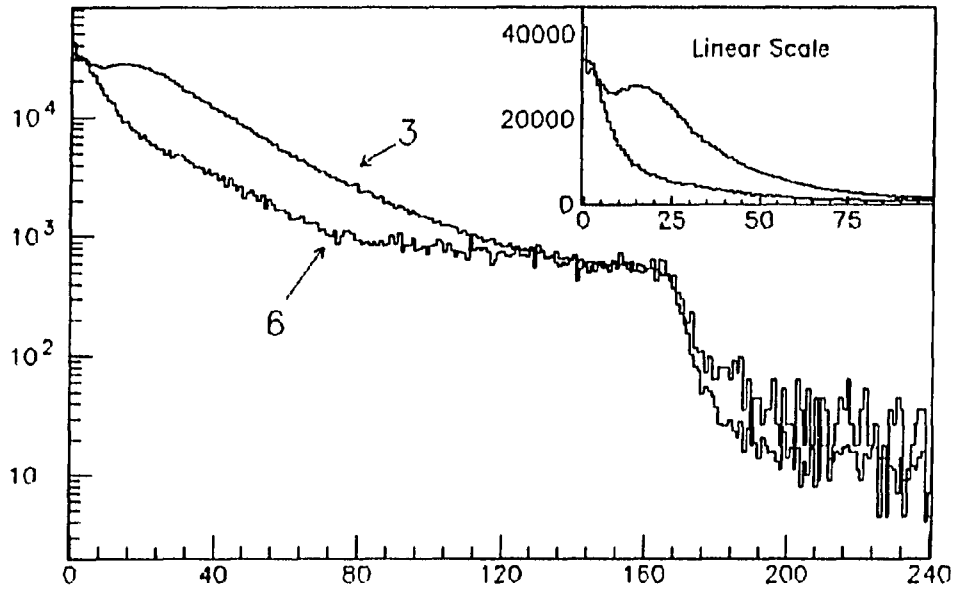$$\frac{(\text{Curve 3}) \times \dfrac{(\text{Curve 5})}{(\text{Curve 6})}}{(\text{Curve 2})}. \tag{5.5}$$

Figure 5.15: Hodoscope multiplicities from p-p̄ (3) and p-only (6) events that failed BG cut.
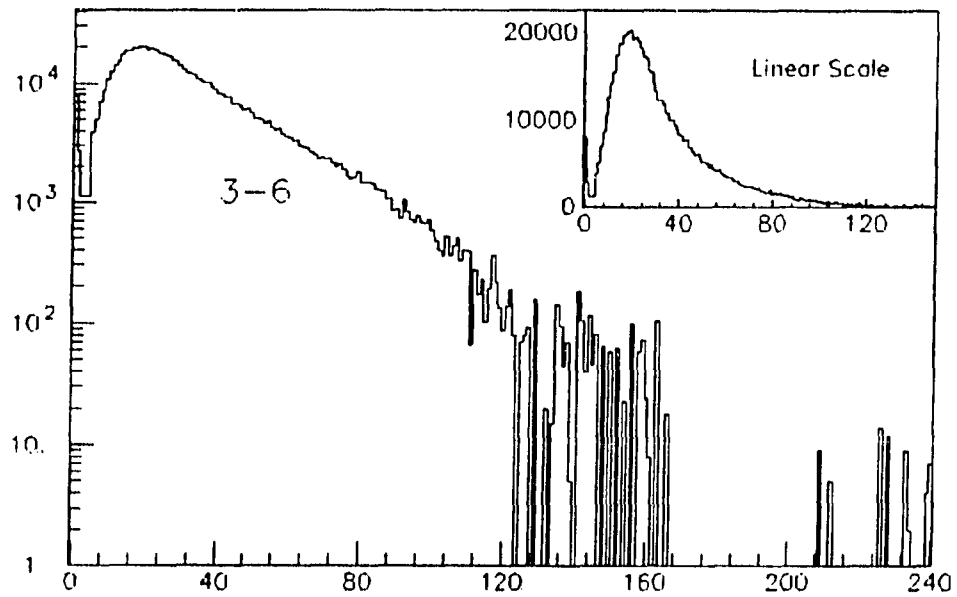

Figure 5.16: "Cut bias" from the difference of figure 5.15.

This result is shown in Figure 5.18. In either method one sees that BG contamination is predominantly at low multiplicities and is significant.

The same procedures are repeated for the barrel region to estimate BG contamination as a function of barrel multiplicity (N_{bh}). Figure 5.19–5.24 are analogous to Figure 5.13–5.18. Note that there are two common conclusions from the two sets of plots.

1. In both cases, p-only data are able to match p-$\bar{\text{p}}$ BG with the same multiplication factor (9) for BG subtraction (Figure 5.15 and 5.21) .

2. The BG shoulder ends where the barrel and one end cap are completely hit.

The scenario is consistent with our understanding of the BG events. The contamination in barrel is also concentrated at low multiplicity region but relatively lower in intensity. This is because the multiplicity distribution for barrel concentrates more to the lower bins.

Monte Carlo Simulation

As no detector can be perfect, there are always differences between what one has observed and what has actually happened. In our multiplicity study, there are questions about how our event selection mechanism would have biased our event samples, and when we have an event, how the number of hodoscope hits (N_{hodo}) corresponds to the number of actually produced charged particles(N_c). There are no a priori answers for these questions, and the Monte Carlo method (MC) is what we have to rely on for an educated guess.

Figure 5.17:   Fractional contamination after BG cut as a function of hodoscope multiplicity.
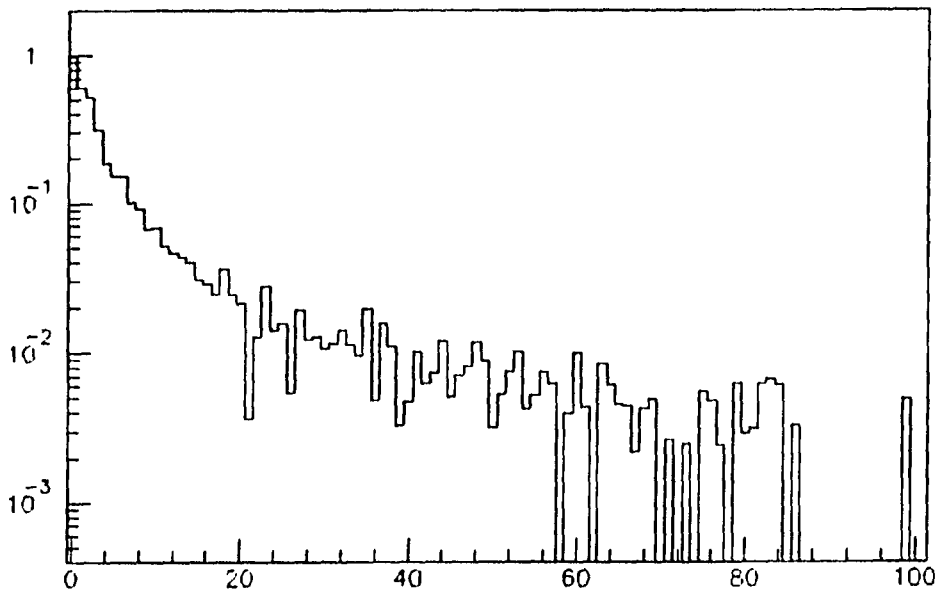
Figure 5.18:   Maximal fractional contamination after BG cut as a function of hodoscope multiplicity.

Figure 5.19: Barrel multiplicities from p-p̄ store.

Figure 5.20: Barrel multiplicities from proton only store.

Figure 5.21: Barrel multiplicities from p-p̄ (3) and p-only (6) events that failed BG cut.

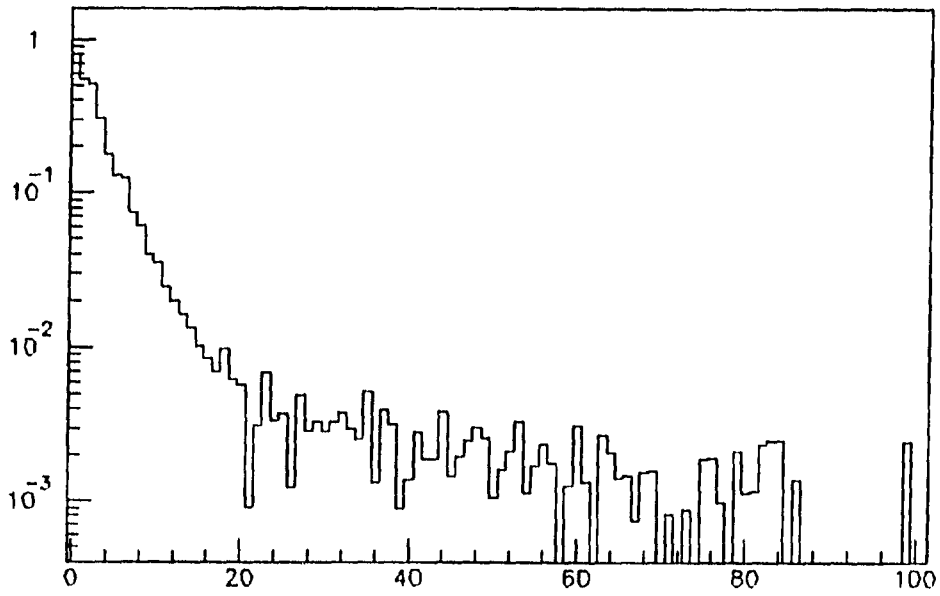Figure 5.22: "Cut bias" from the difference of figure 5.21.

Figure 5.23: Fractional contamination after BG cut as a function of barrel multiplicity.

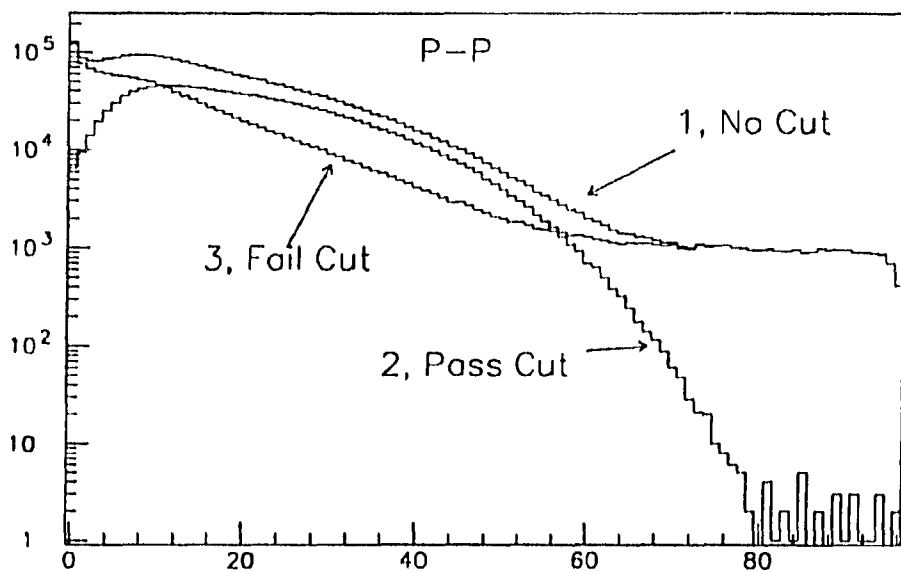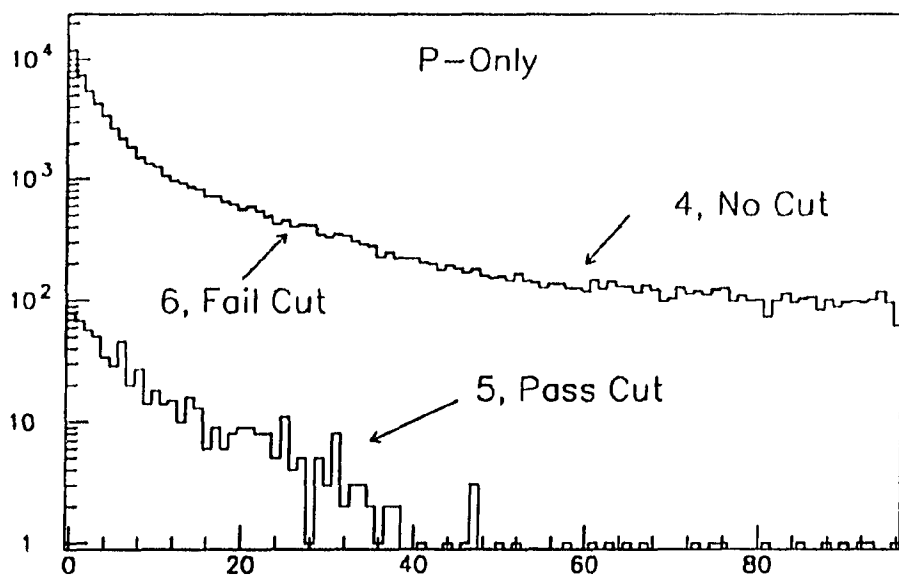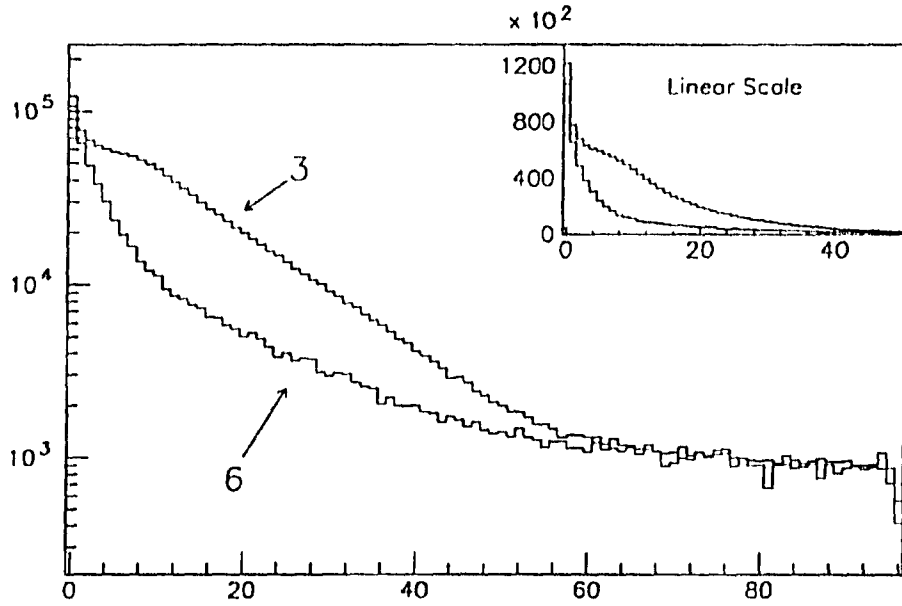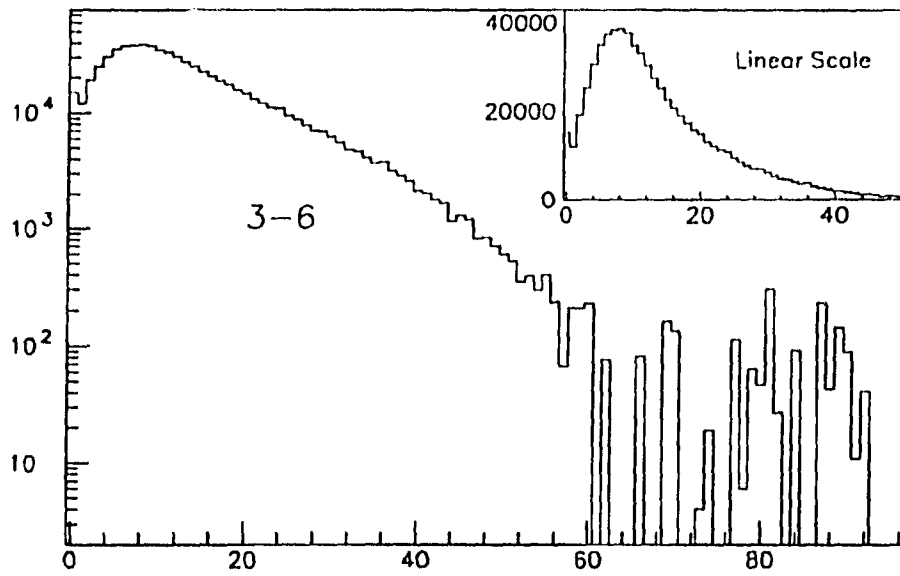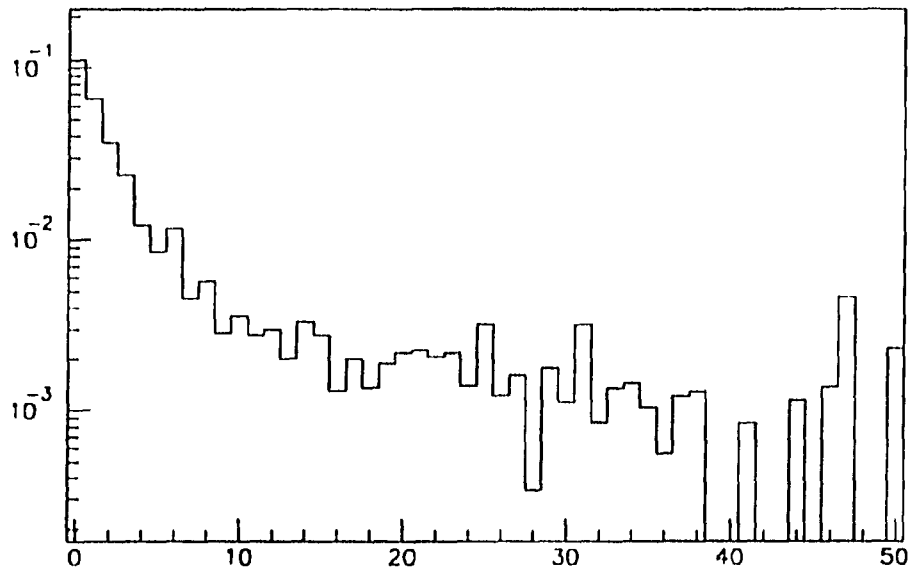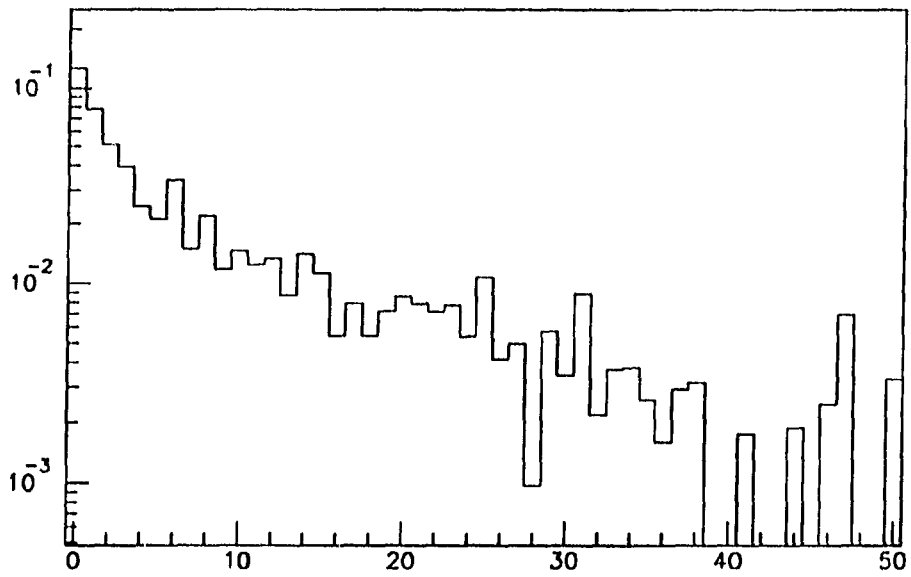Figure 5.24: Maximal fractional contamination after BG cut as a function of barrel multiplicity.

Unlike an analysis, Monte Carlo does not start from the clues and try to figure out what is causing them. Instead, it assumes that it knows what nature is and then develops the consequences. The starting assumption is, of course, usually wrong! However, if one can make a reasonable guess, the result can be compared with the reality and used to improve the guess. In our application we are only interested in getting an estimate of the corrections required to correct systematic bias in our detector response. The recurrence procedure is of the second or higher order nature and is not performed.

Our simulation consists of two parts: first, events are generated with UA5 event generator GENCL[53], then the produced particles are tracked through the detector with the GEANT simulation package[54].

Event generator

The UA5 GENCL is an ad hoc model for generating non-single-diffractive events. Particles are generated in groups of small clusters and decayed into their final states. Particle compositions and phase space variables carry logarithmic energy dependences and are tuned to $S\bar{p}pS$ results from 200 to 900 GeV center-of-mass energies. The generator contains short lived particles but no heavier flavor beyond "strange" is produced. The charged multiplicity can be assigned arbitrarily.

What really concerns us in this generator is the pseudo-rapidity distribution of the particles, which is critical to the trigger efficiencies and the N_{hodo}-N_c conversions. Figure 5.25 reproduces this distribution in comparison with UA5 data at 546 GeV.
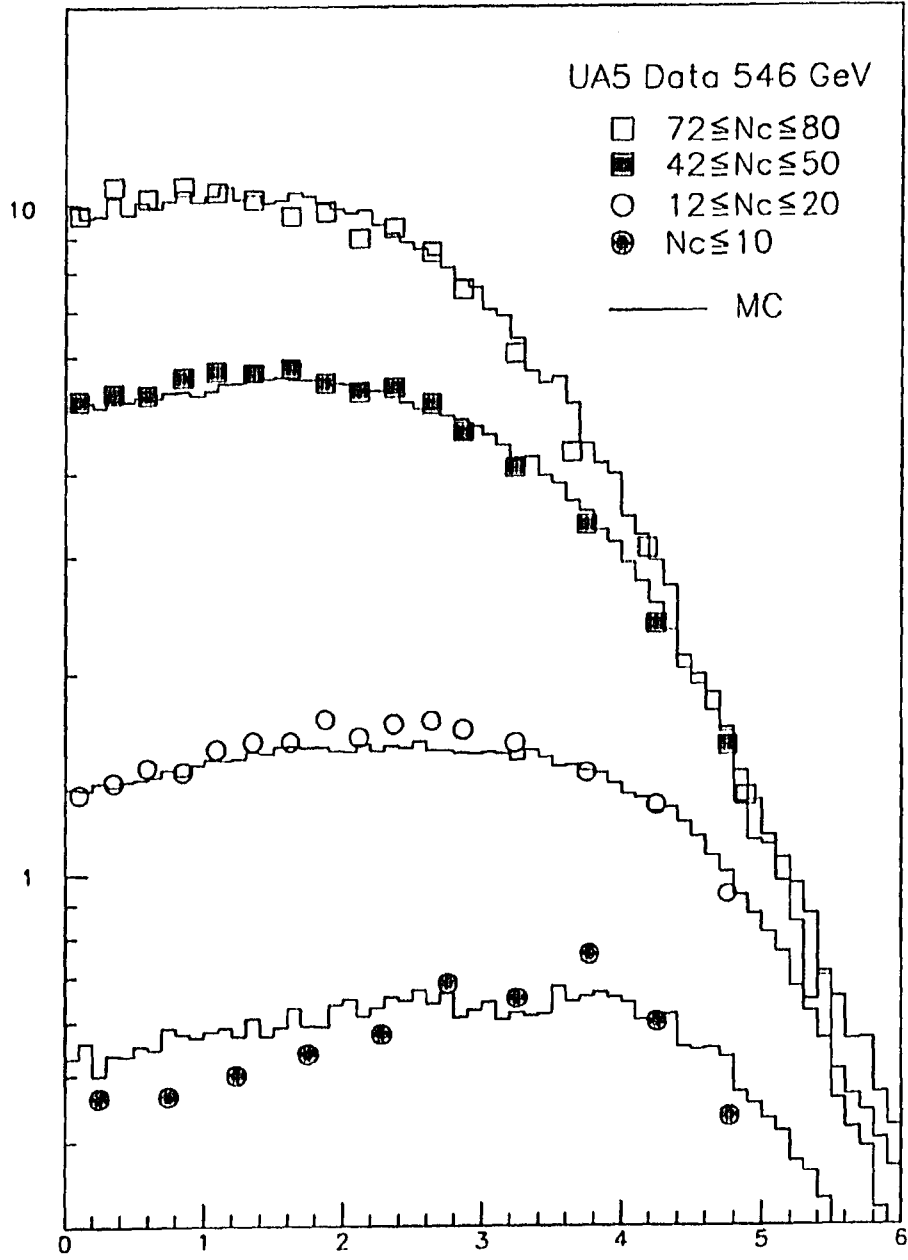
Figure 5.25: $dn/d\eta$ vs η in various multiplicity bins at 546 GeV.

Detector simulation

The GEANT simulation takes care of material interactions when particles are going through the detector. Table 5.3 lists the physics processes taken into account in our simulation. All enabled processes are allowed to effectively generate secondaries, and the secondaries are tracked along with the primaries. All particles are tracked until they either go out of the detector volume or disappear in interactions or drop under their kinetic energy cuts. The kinetic energy cuts are thresholds for particles or processes to be taken in effect. Our settings are listed in table 5.4

Table 5.3: Physics processes enabled in GEANT.

COMP: Compton scattering
PHOT: Photo-electric effect
PAIR : Pair production
ANNI : Positron annihilation
DRAY: Delta ray production
BREM: Bremsstrahlung
HADR: Hadron interaction
MUNU: Muon nuclear interaction
DCAY: Decay processes
LOSS : Average energy loss
MULS : Gaussian multiple scattering

The detector in simulation contains all components in the tunnel and leaves out the spectrometer arm and the magnet. Figure 5.26-5.30 are a series of plots showing the origin of the charged secondaries produced from material interaction. These points roughly outline the detectors and show where materials are located. They are our "eye ball" checks for no major surprises. Checks are also made to trace out space points along various directions to ensure that material contents are as expected.

Figure 5.26: x-y projection of origins of secondaries in $0 \le z \le 114$ cm.

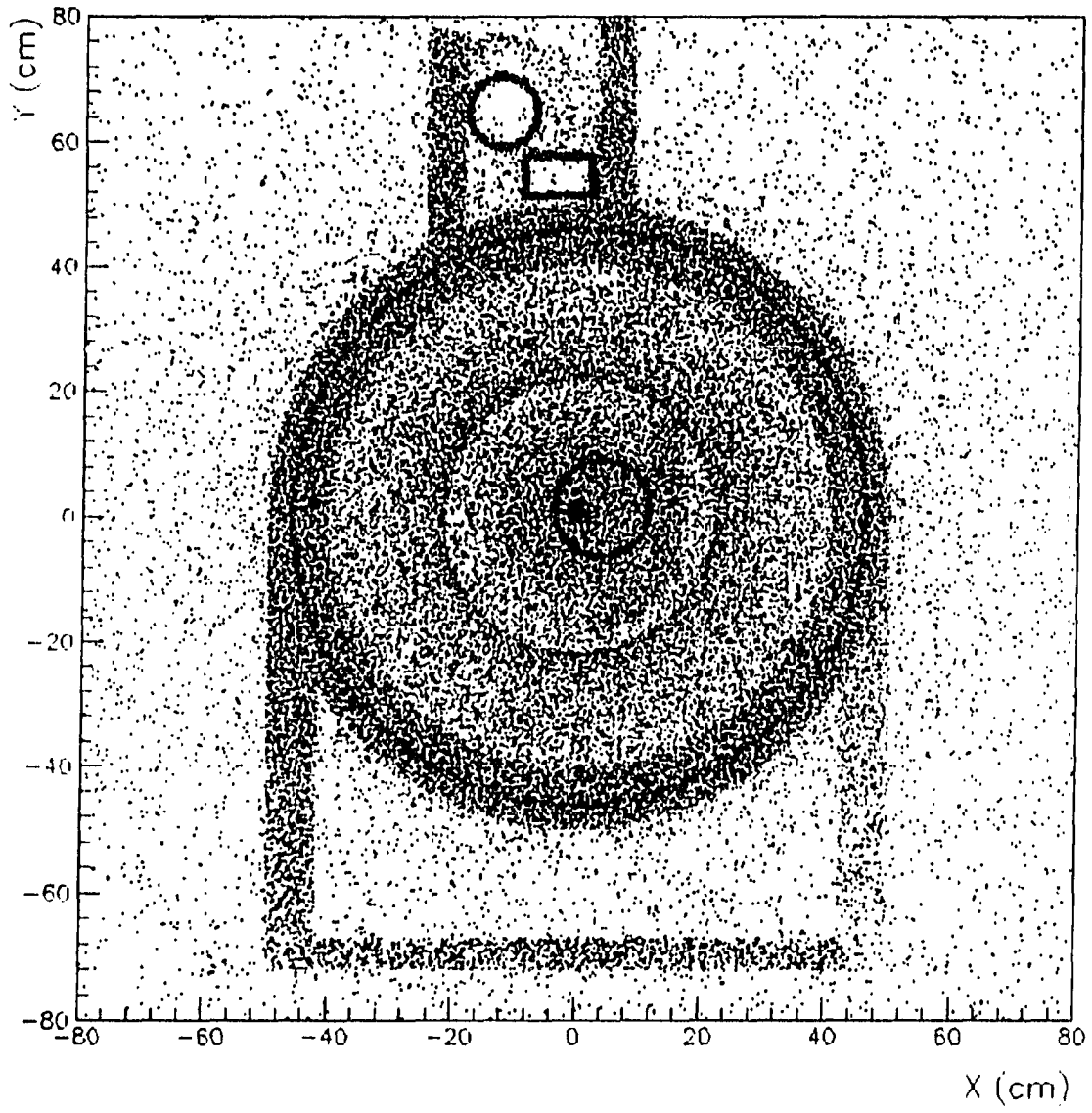Figure 5.27: r-z projection of origins of secondaries in $0 \leq z \leq 114$ cm.

Figure 5.28: x-y projection of origins of secondaries in $112 \leq z \leq 190$ cm.
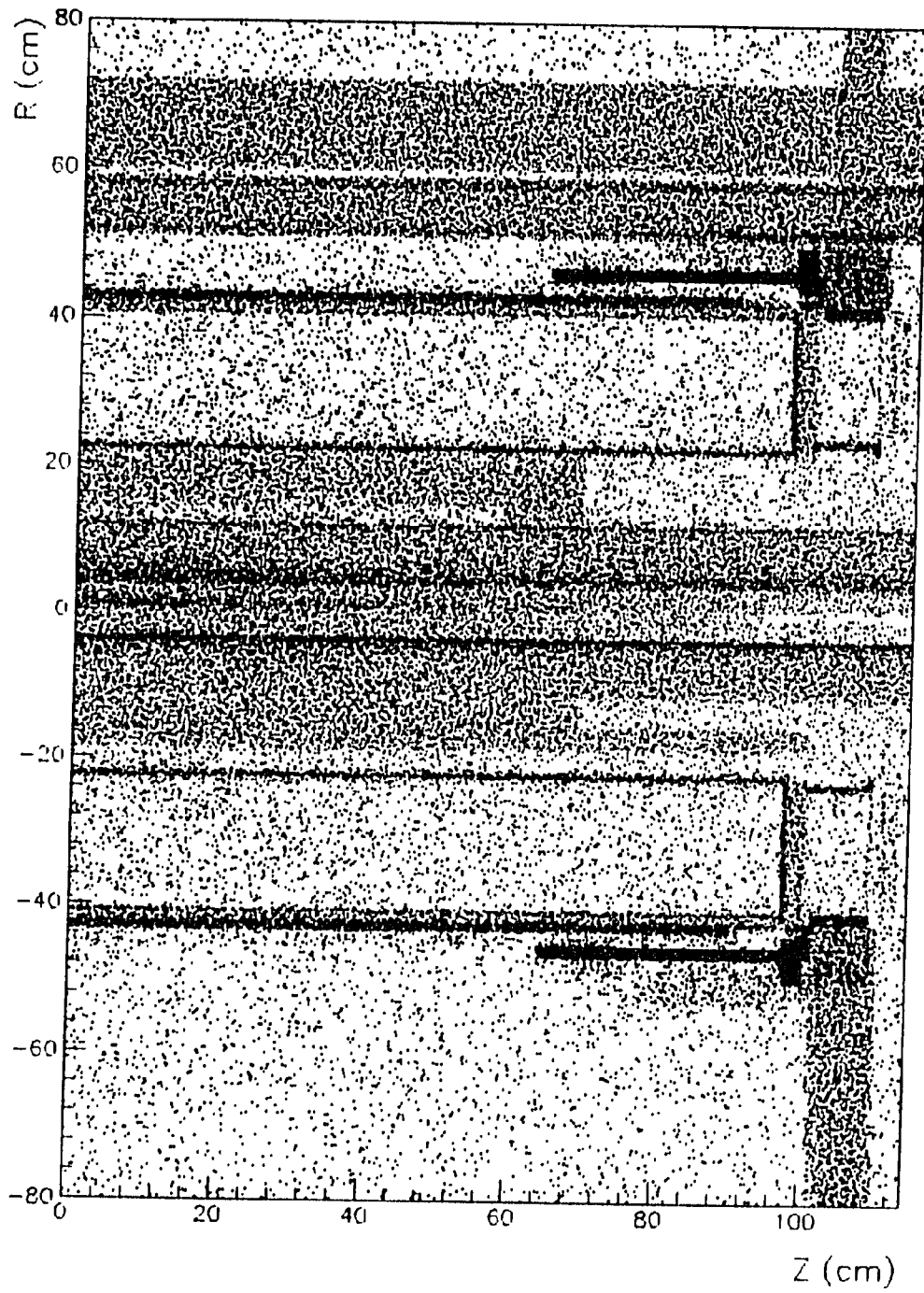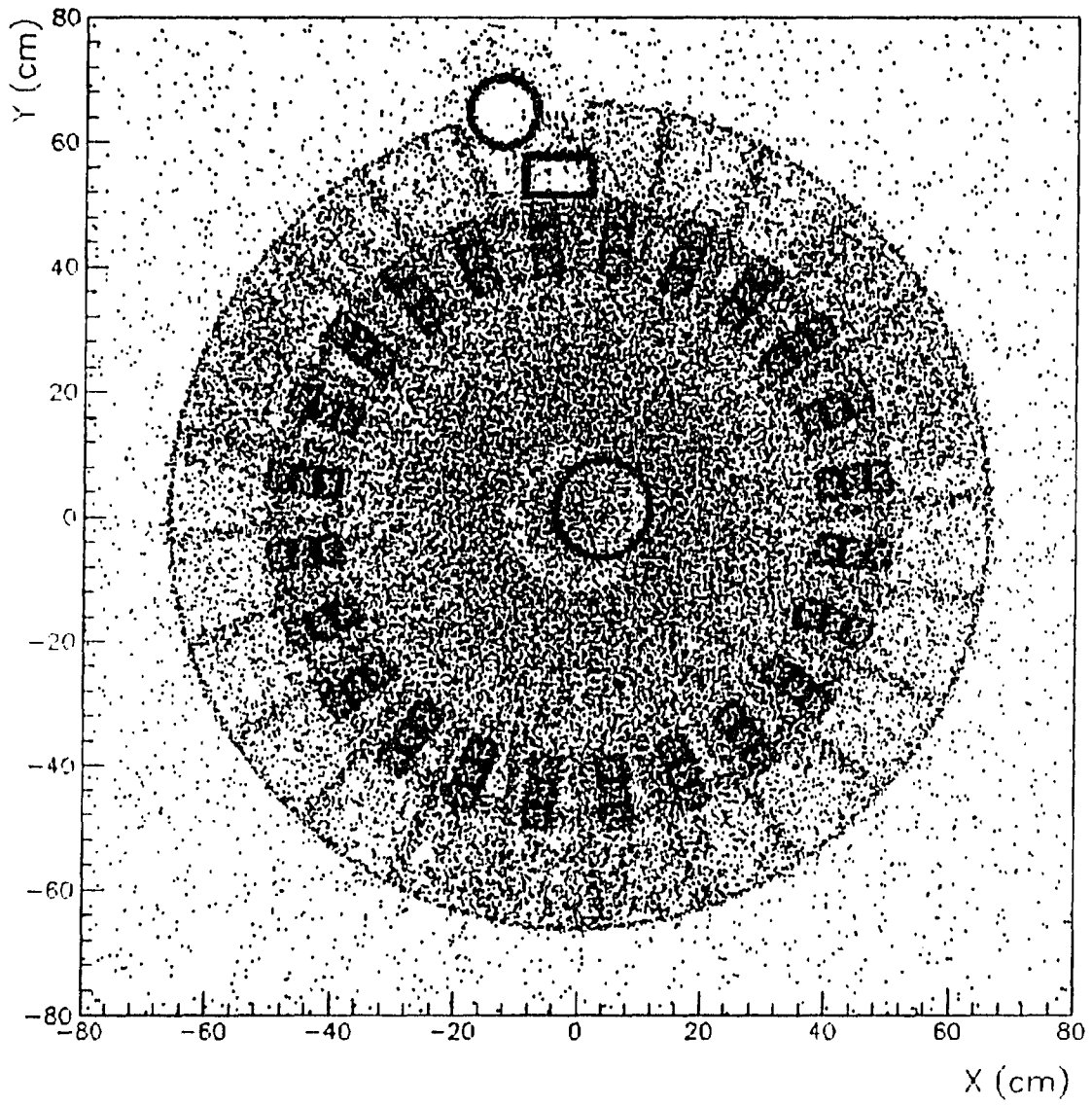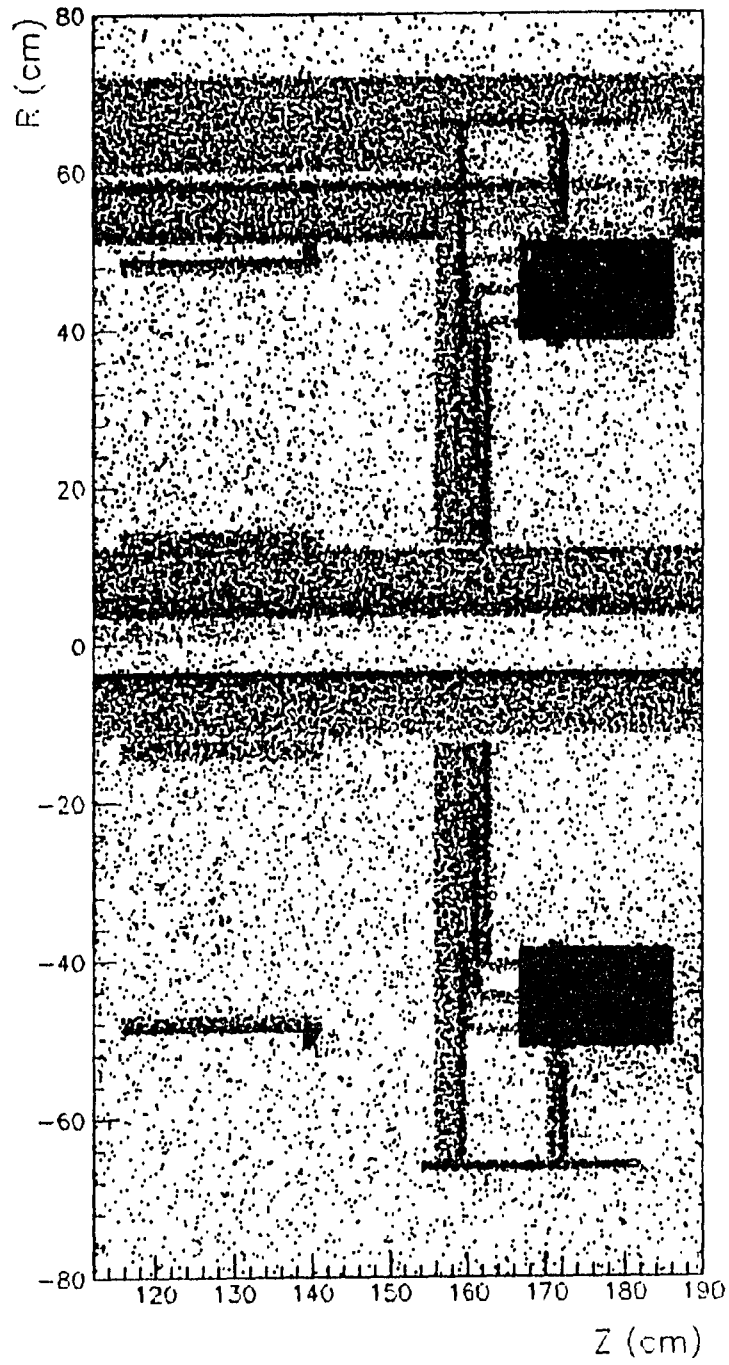
Figure 5.29:   r-z projection of origins of secondaries in $112 \leq z \leq 190$ cm.
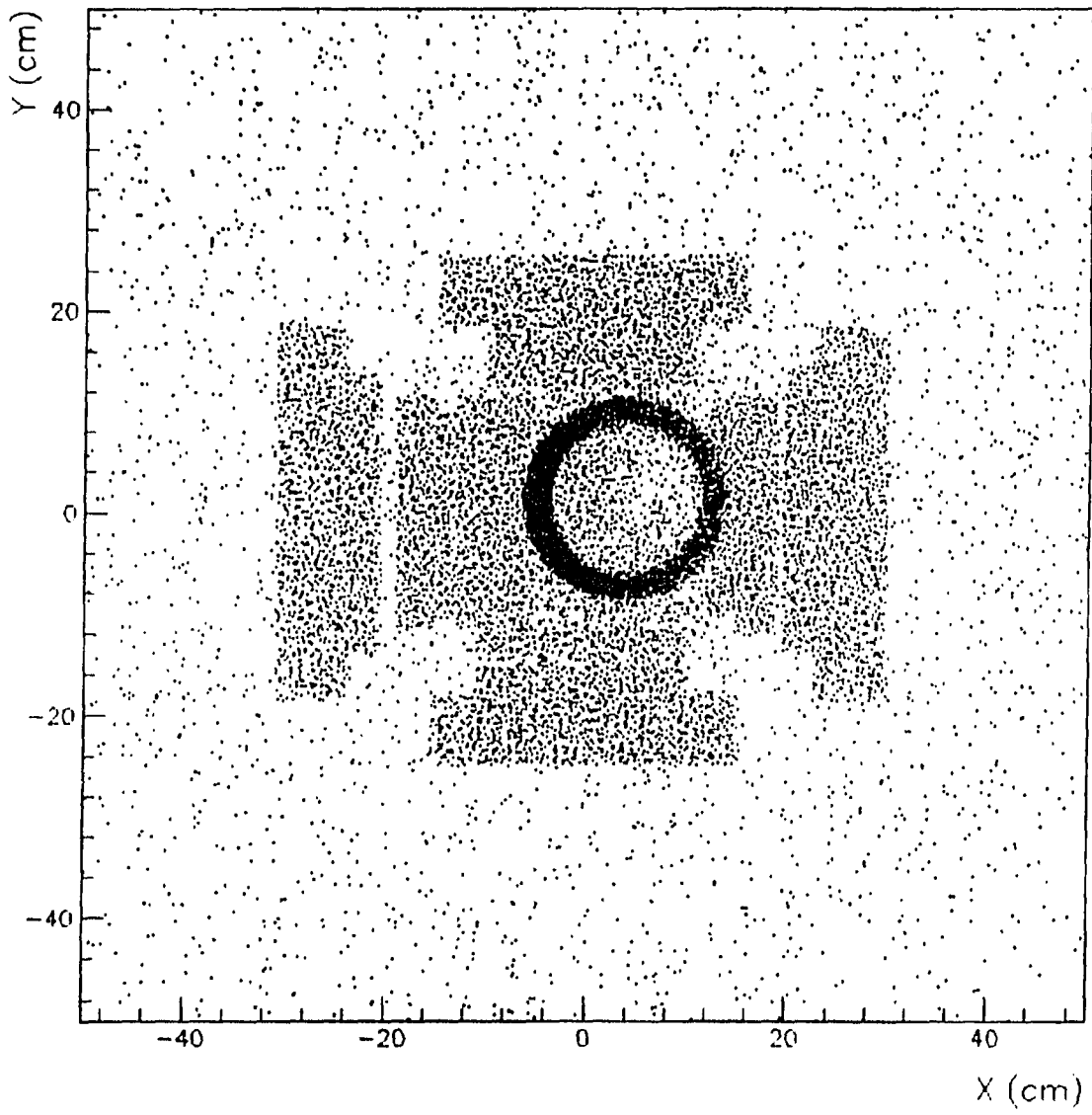
Figure 5.30: x-y projection of origins of secondaries in $190 \leq z \leq 250$ cm.

Table 5.4:   Kinetic energy cuts for GEANT tracking.

Photon	: 1.0 MeV
Electrons	: 1.0 MeV
Hadron	: 10.0 MeV
Muon	: 10.0 MeV
Bremsstrahlung (μ&e)	: 1.0 MeV
Delta Ray ($\mu, e,$ &$Hadron$)	: 1.0 MeV
E_t of e^+e^- pair production by muon : 10.0 MeV	

After collecting events from the event generator and before processing by GEANT, one has to decide where in space to put the event origin. What we have in the program are Gaussian distributions centered at $(0.05, 0.7, 2.0)cm$ with $\sigma = (0.2, 0.2, 37.6)cm$. The vertex location can affect the phase space coverage of our detector. Figure 5.31 and 5.32 show the pseudo-rapidity range of the hodoscope as a function of event vertex.

MC data

In our simulation we used a special version of GEANT program which only recognize p$\bar{\text{p}}$ and hodoscope counters as sensitive detectors. Other detectors in place are only acting as dead material. When a counter was hit by a charged particle, energy deposition and hit time are recorded. At the end of an event, each counter will sum up total energy depositions and find the earliest hit time. This information is equivalent to ADC and TDC in the real data. Figure 5.33 and 5.34 show typical hodoscope energy losses and hit time spectra. The discreteness of energy loss is due to the 0.1 MeV storage resolution. The storage resolution assigned for hit time is 0.01 ns.

Figure 5.31:   Upper and lower limit of hodoscope and barrel in pseudo-rapidity as a function of vertex location.

Figure 5.32:   Pseudo-rapidity coverage of hodoscope and barrel.
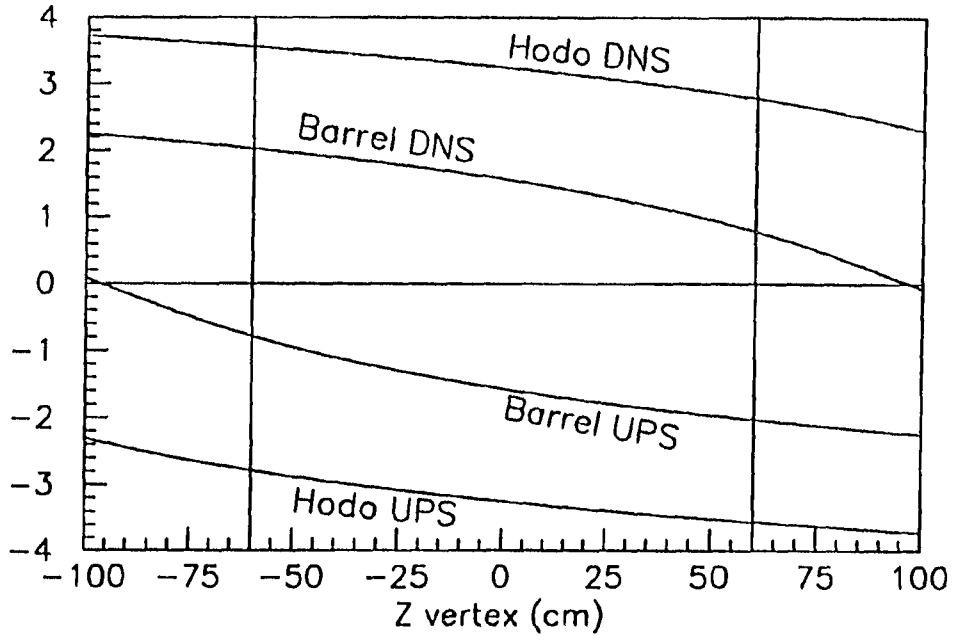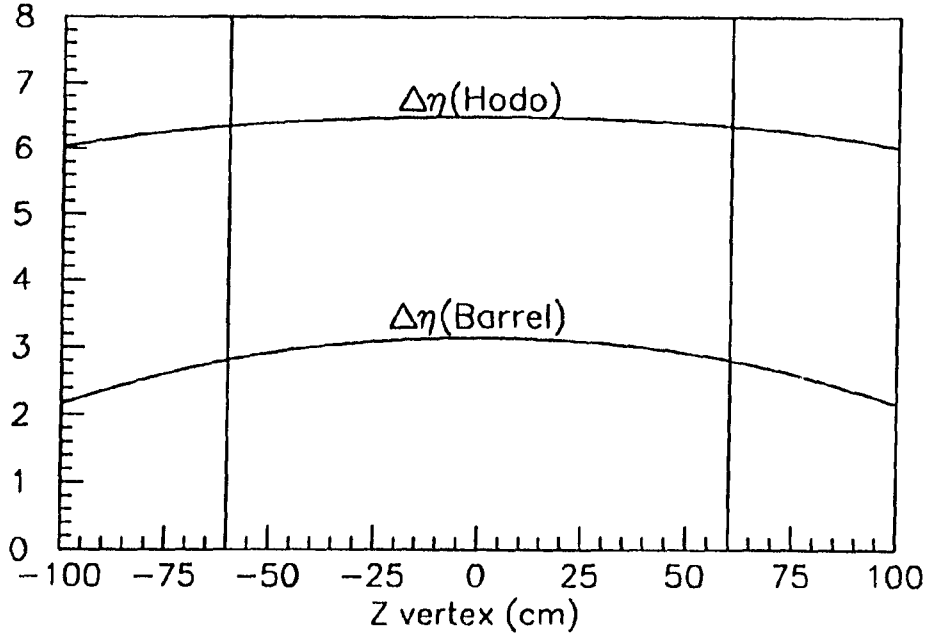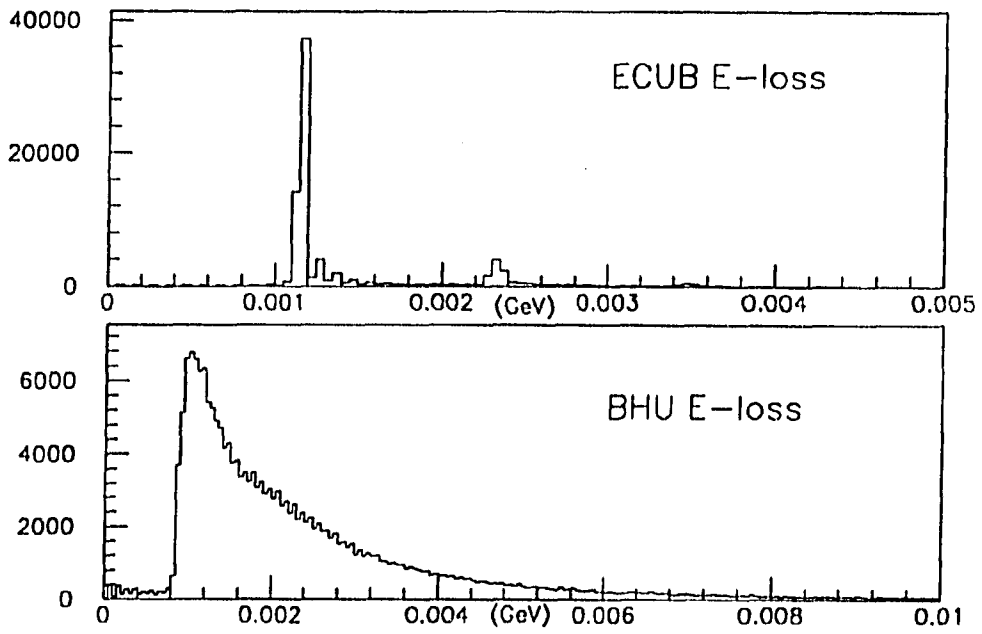
Figure 5.33:   MC hodoscope energy loss spectra.
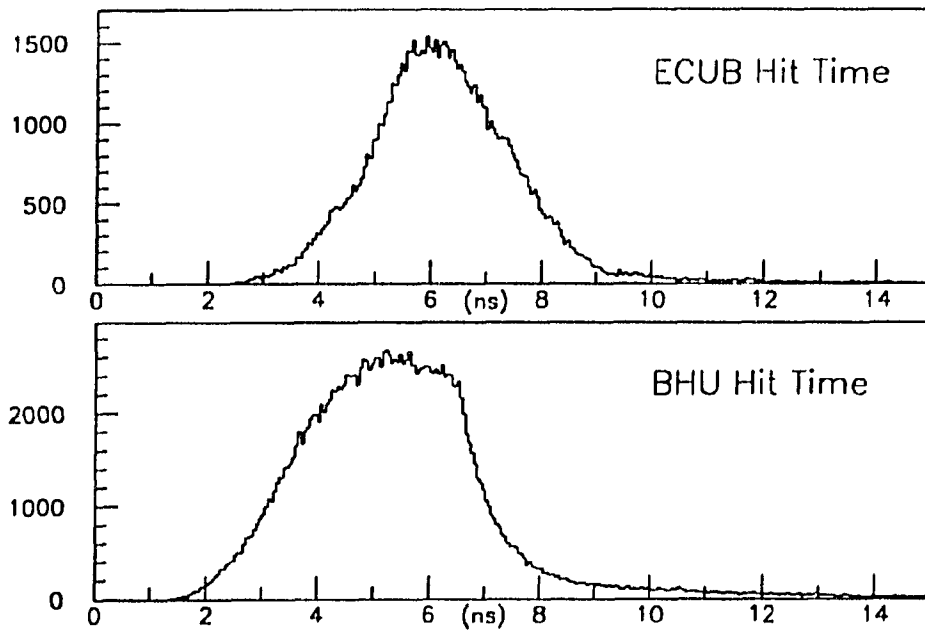
Figure 5.34:   MC hodoscope hit time spectra.

The criteria for identifying an "ADC hit" in MC is an energy threshold cut at 1/3 of the MIP, which is 0.4 MeV for the hodoscope and 1.7 MeV for $p\bar{p}$ counters. Other than the "ADC hit", MC data are treated the same way as the real data by using the same programs.

MC multiplicities

Since we don't know the true multiplicity distributions, MC events are generated flat in multiplicities for up to Nc $\approx$ 280, where Nc is always even because of charge conservation. The number 280 is chosen so that the highest available N_{hodo} in the real data ($\sim$ 160) is reasonably covered. In the first run we generated 500 events per Nc bin. Afterward, we found the need of increasing the statistics at low multiplicity regions and added 500 events per Nc bin up to Nc$\approx$120, and then another 1000 events per Nc bin to Nc$\approx$50. The reason for emphasizing low multiplicity bins is because of their very low acceptance after BG cuts and consequently a very large correction factor to our data. The Nc distribution turns out to be a strange ladder shape as shown in Figure 5.35. In the same figure are also the resultant Nc distributions within the hodoscope, and the barrel region. The distributions shrink to lower Nc because of finite geometrical acceptance. The population of each Nc bin is irrelevant in our problem since we can assign a weighting factor to each event and scale the distribution to whatever we want. Figure 5.36 shows the Nc distributions when full phase space Nc(4π) is scaled to flat.

Saturation due to finite segmentation is one of the major limitations of our hodoscope in counting charged particle multiplicities. Figure 5.37 shows distributions of N_{hodo} when Nc(4π) is a flat distribution. The low N_{hodo} peak is due to finite

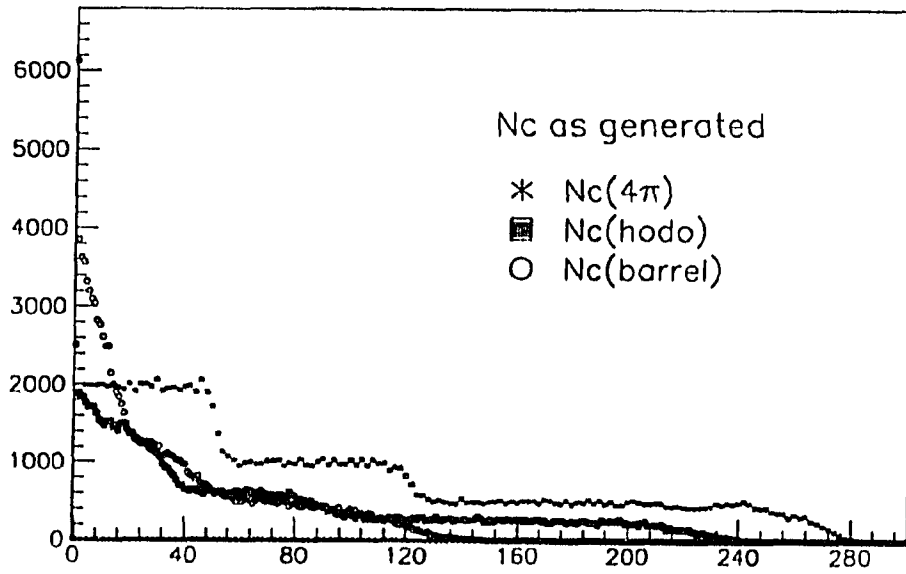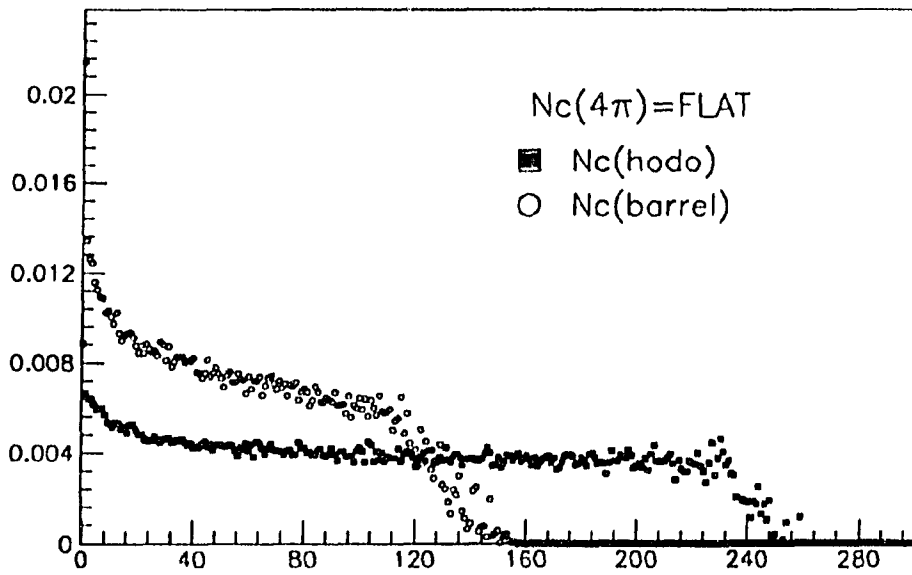Figure 5.35: Nc distributions as produced in MC.

Figure 5.36: Nc distributions when full phase space Nc is scaled to flat.

geometrical acceptance as discussed earlier. Saturation effect takes place at higher Nc and the higher the Nc the worse the saturation. In principle the curve goes to infinity when Nh approaches 240. The sudden drop is due to our running out of MC events. The peak Nh roughly indicates the applicable range of our MC.

Another limitation of the hodoscope is that when a counter is hit we don't know what has caused that hit ! What we would really like to do is to count the number of charged particles directly produced from p-p̄ collisions. However, particles may decay or interact with material on their way out and either generate more particles to hit counters or disappear undetected. Furthermore, neutral particles such as photons are also very effective in creating hits in our scintillator hodoscope. Assuming a FNBD Nc distribution, table 5.5 lists various probabilities when a counter is hit :

Col.1: Average number of strikes by charged tracks per counter hit.

Col.2: Average number of strikes by charged primaries per counter hit.

Col.3: % of counter hits not by a charged primary.

Col.4: % of counter hits struck by non charged-primary.

Table 5.5:   Various probabilities of hodoscope hits.

	Col.1(#)	Col.2(#)	Col.3(%)	Col.4(%)
ECUA	1.24	0.62	40.6	46.4
ECUB	1.22	0.64	39.6	45.6
ECUC	1.27	0.56	47.3	54.1
Barrel	1.23	0.73	33.0	41.0
ECDC	1.28	0.56	47.7	54.6
ECDB	1.21	0.63	40.3	46.3
ECDA	1.24	0.63	40.2	46.2

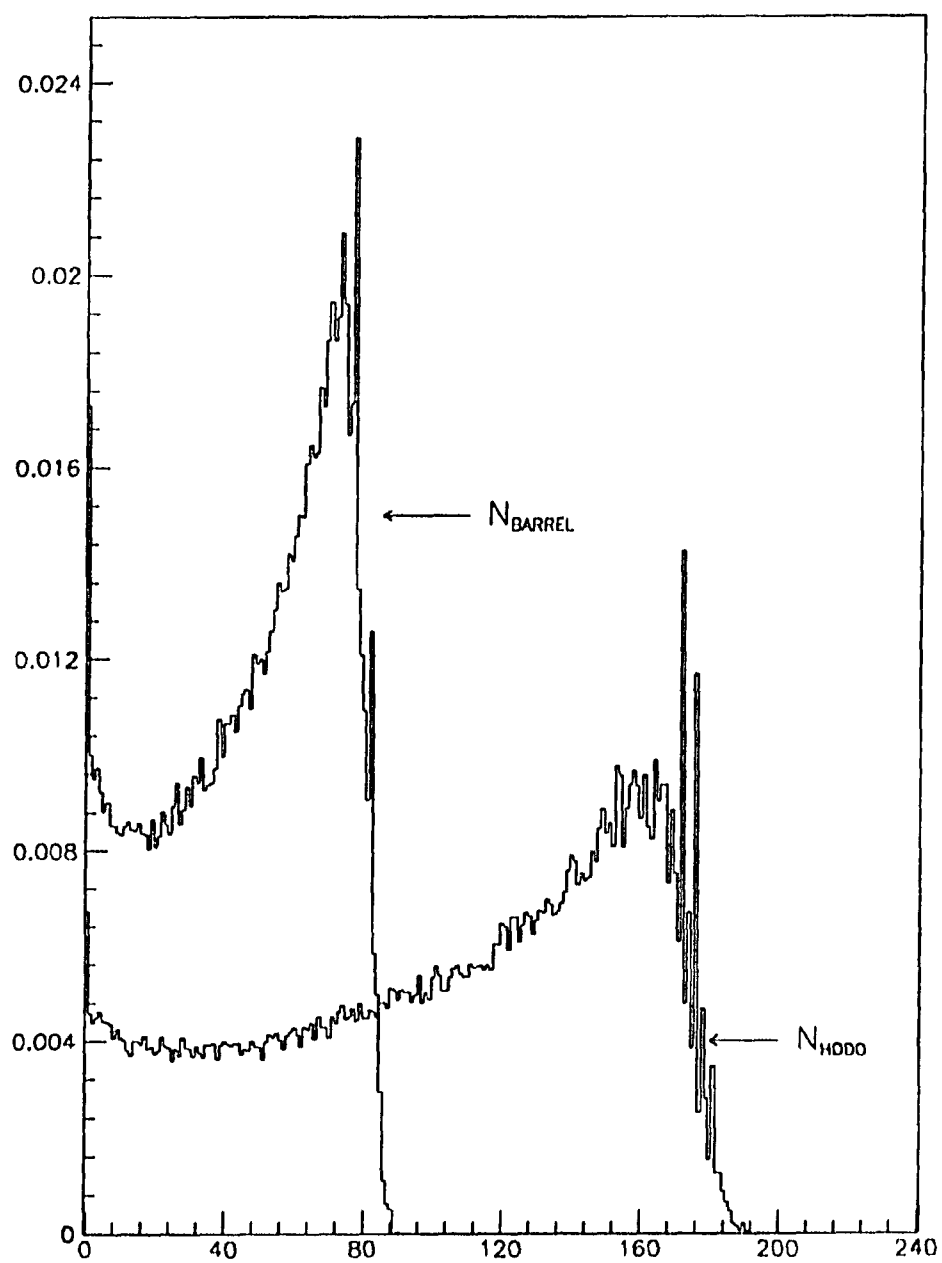Roughly speaking about 40% of the hodoscope hits are not directly from charged

Figure 5.37: N_{hodo} distribution from flat Nc(4π) distribution.

primary tracks. This is one of the major corrections we need to make based on the GEANT simulation.

$\eta - \phi$ distributions

As a consistency check of our simulation, hit frequency of each counter in MC is compared to the real data at 546 and 1800 GeV. This is equivalent to a simultaneous check in η and ϕ space in both event topology and GEANT performance. Figure 5.38 to 5.41 show hit frequencies of each hodoscope and $p\bar{p}$ counter in different N_{hodo} bins at 546 and 1800 GeV. Each curve is normalized to hits per event. The distributions have strong dependence on hodoscope multiplicities. The multiplicity distributions $(Nc(4\pi))$ we used for MC here are FNBD with its $\langle n \rangle$ and k parametrized as[53] :

$$\langle n \rangle = -9.50 + 9.11 \cdot s^{0.115} \tag{5.6}$$

$$k^{-1} = -0.104 + 0.029 \ln(s) \tag{5.7}$$

The agreement between MC and data is very good at 546 GeV. As the UA5 generator was tuned at 546 GeV, this is a confirmation that GEANT is roughly doing things right. At 1800 GeV, disagreements begin to emerge at higher N_{hodo}'s. This could be due to the incorrect extrapolation of pseudo-rapidity distributions at this energy. This discrepancy is around $5 - 10\%$ level.

Reconstruction of Multiplicity Distributions

There are three steps involved in the reconstruction of the original charged multiplicity distributions from the observed hodoscope multiplicity distributions :
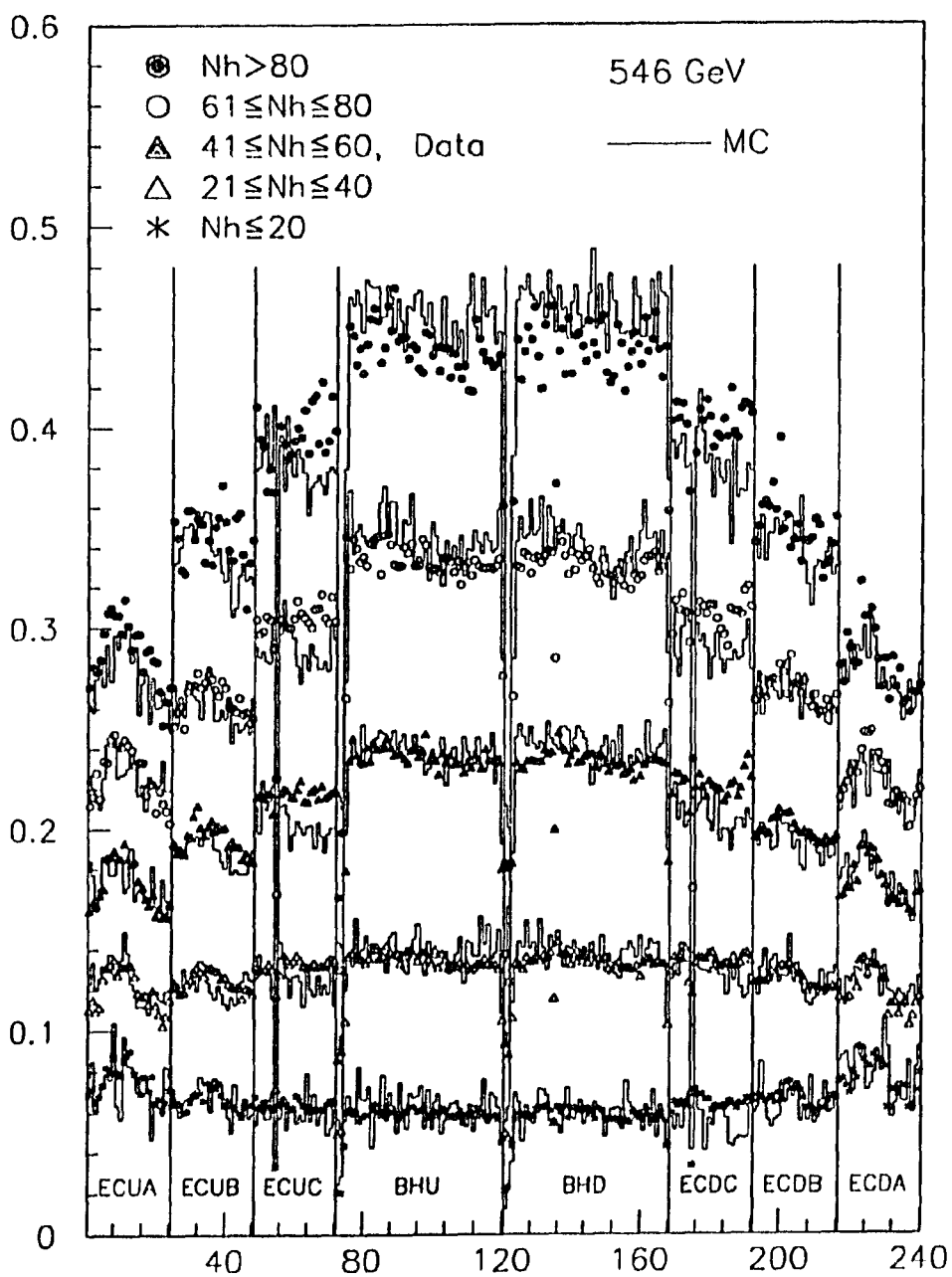
1. Background subtraction.

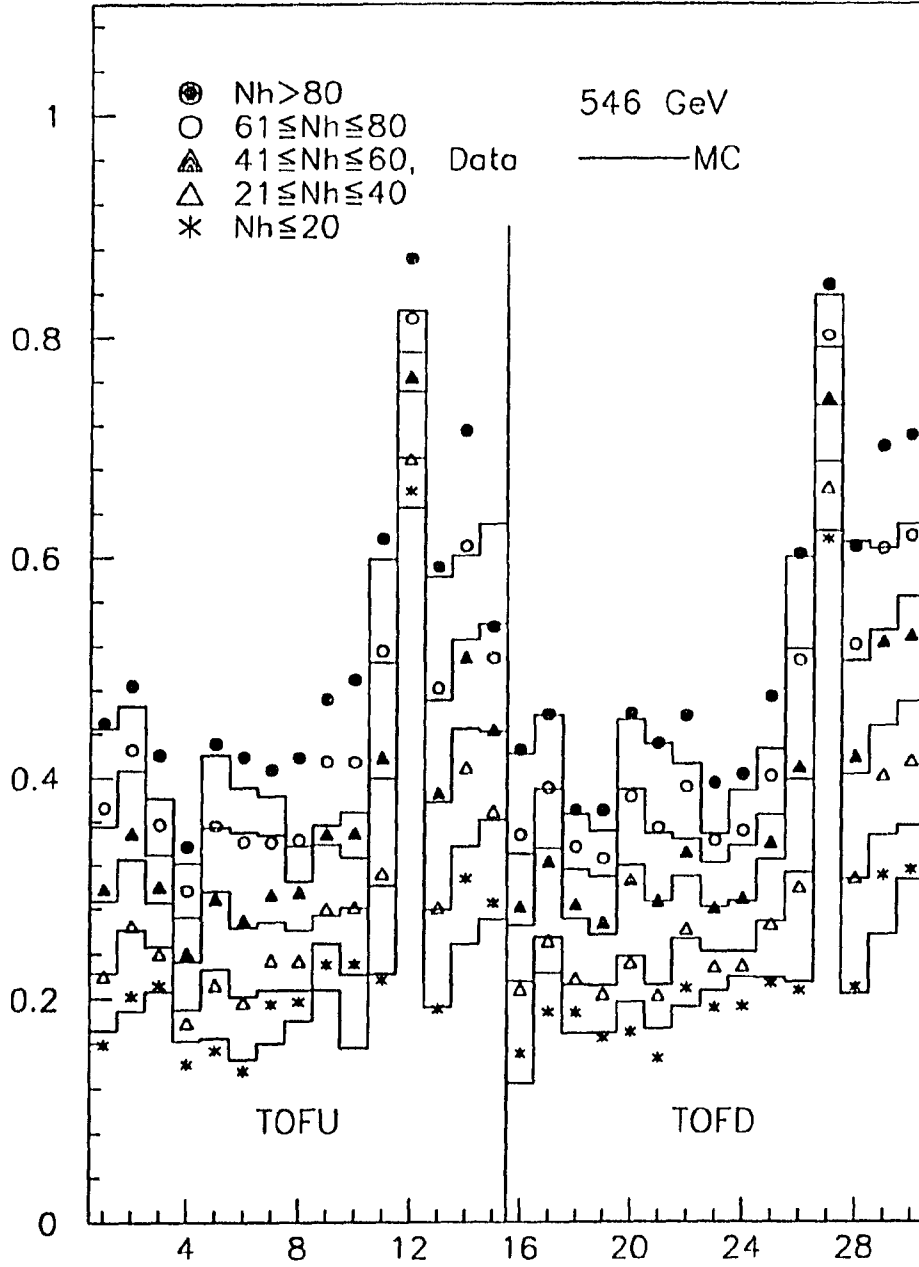Figure 5.38: Hit frequencies of hodoscope counters at 546 GeV.
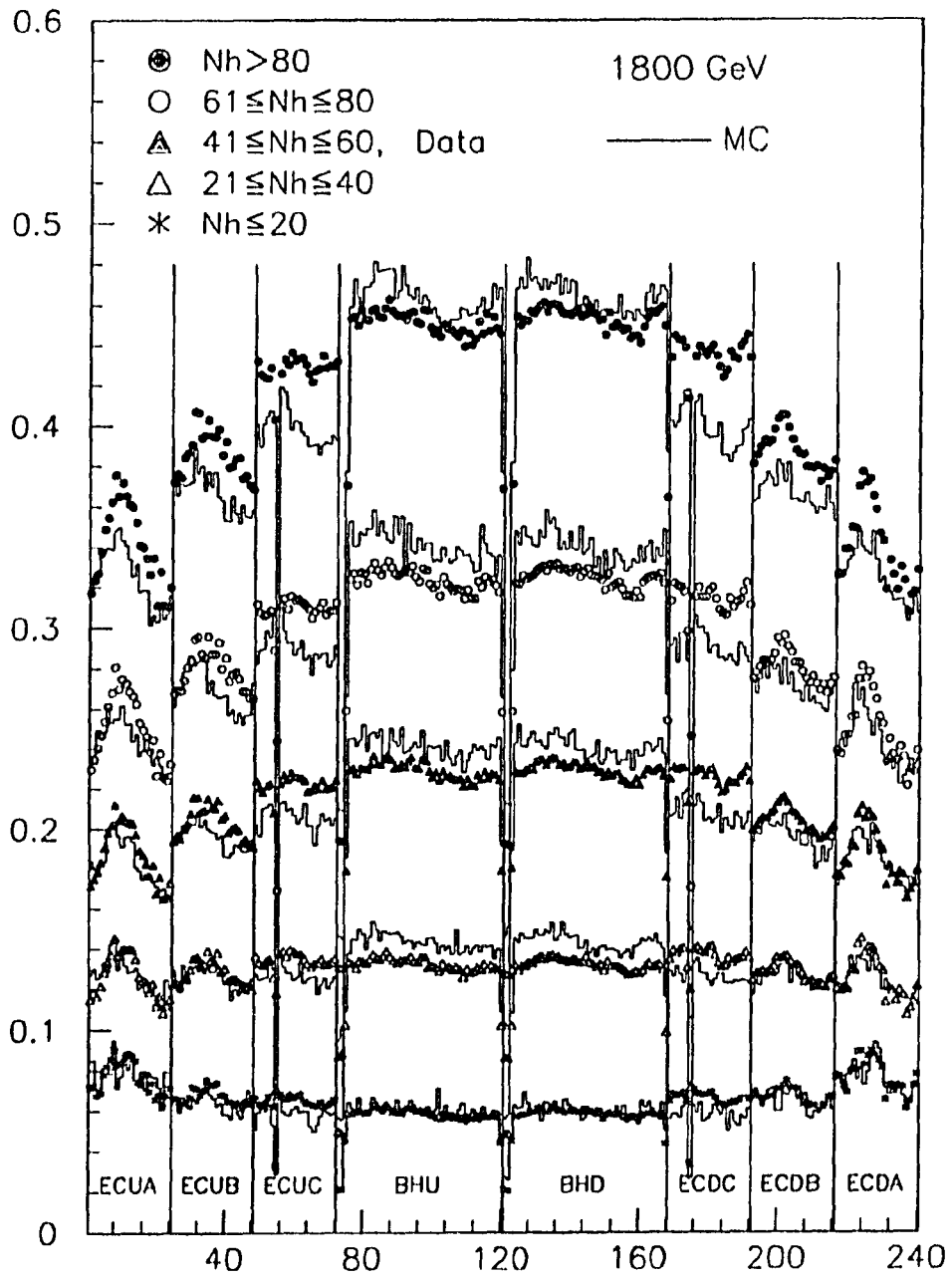
Figure 5.39:   Hit frequencies of p̄p counters at 546 GeV.

Figure 5.40: Hit frequencies of hodoscope counters at 1800 GeV.
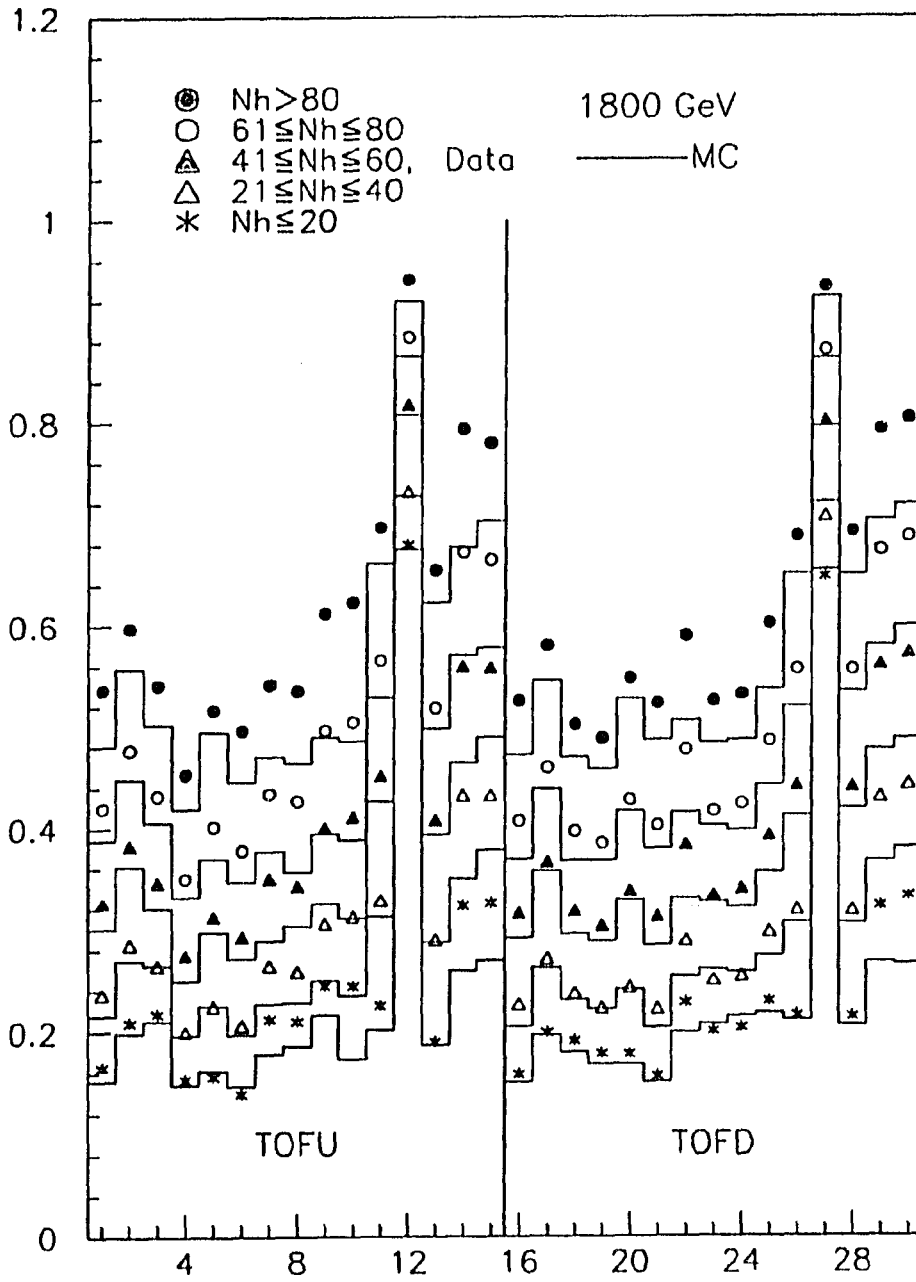
Figure 5.41: Hit frequencies of p$\bar{\text{p}}$ counters at 1800 GeV.

2. $N_{hodo} \rightarrow$ Nc conversion.

3. Acceptance correction (including trigger efficiency and cut bias).

Background subtraction

Our background subtraction is based on the estimations in Figure 5.17 and 5.23. As the statistical error is large, we smoothed the curves and only apply to multiplicity bins with contaminations greater than 1%. This corresponds to $N_{hodo} \leq 15$ and $N_{barrel} \leq 5$. The smoothed percentage contaminations are listed in table 5.6.

Table 5.6: First few bins of smoothed BG contamination (%).

$N_h = \downarrow \oplus \rightarrow$		0	1	2	3	4	5	6	7	8	9
Hodo	00	82.0	59.0	42.3	30.4	21.9	15.9	11.6	8.6	6.4	4.9
	10	3.7	2.9	2.3	1.8	1.4	1.1	0.9	-	-	-
Barrel	00	10.7	6.6	3.7	2.1	1.2	0.9	-	-	-	-

N_{hodo} to Nc conversion

The problem of $N_{hodo} \rightarrow$ Nc conversion can be considered as solving a set of linear equations. Let T_n be the charged multiplicity distribution and O_m the distribution of observed hodoscope hits. Each event with a charged multiplicity n has a probability P_{mn} of becoming an event with m hits in the hodoscope. Thus we have the relation :

$$\sum_n P_{mn} T_n = O_m, \tag{5.8}$$

where $0 \leq m \leq M$ and $0 \leq n \leq N$. O_m is from our observed data and P_{mn} can be obtained from Monte Carlo. If $M = N$, P_{mn} is a square matrix and $T(n)$ can

be solved exactly by matrix inversion. However, our M is limited to the number of hodoscope counters 240, and N, in principle, goes to infinity. Hence, there exist an infinite number of solutions. Moreover, even if we are able to find a solution for these equations, the solution will still be doubtful because of the statistical fluctuations in O_m and P_{mn}. In other words, (5.8) is a set of "fluctuating" equations !

Maximum entropy method To overcome the difficulties mentioned above a method based on maximum entropy principle has been suggested. The maximum entropy method itself is explained in Appendix C. Basically, it's a criterion for choosing a most probable solution if a set of linear equations (such as eq. (5.8)) has an infinite number of possible solutions. A direct application of this method to eq. (5.8), however, still suffers from the "fluctuation" problem. Furthermore, the problem becomes one of solving a set of ~ 200 non-linear equations and is difficult.

These problems were solved by replacing eq (5.8) with another set of equations. Namely, instead of using the observed distribution as constraints, a set of observed moments are used[55].

The problem is transformed into solving the set of linear equations :

$$\sum_n a_{nk} T_n = b_k,$$ (5.9)

where $1 \leq k \leq K$, $K < N$ and

$$a_{nk} = \sum_m m^{q_k} P_{mn},$$ (5.10)

$$b_k = \sum_m m^{q_k} O_m,$$ (5.11)

The right hand side of eq. (5.9) is the q_k^{th} order moment of the observed distribution. The left hand side is the same quantity derived from T_n through the conversion

eq. (5.8). The K moments q_k are to be determined. For any set of chosen q_k's, a unique solution for T_n is obtained by maximizing the entropy :

$$S = -\sum_n T_n \ln T_n,$$ (5.12)

which leads to a set of K non-linear equations for K unknown Lagrangian multipliers :

$$\sum_n a_{nk} \exp[\sum_k \lambda_k a_{nk} - 1] - b_k = 0.$$ (5.13)

And the final solution is :

$$T_n = \exp[\sum_k \lambda_k a_{nk} - 1].$$ (5.14)

The set of q_ks for constructing eq. (5.9) are chosen such that the resultant $T(n)$ can describe the data well in a statistical sense. The decisions are made based on two quantities.

1) The χ^2 between the data and the solution :

$$\chi^2 = \sum_m \frac{(O(m) - \sum_n P_{mn} T(n))^2}{\sigma_m^2},$$ (5.15)

where σ_m^2 is the quadratic sum of the statistical errors in O_m and in P_{mn}. The χ^2 distribution has an expectation value of $E(\chi^2) = M$, hence a true population $T(n)$ is the most likely to give $\chi^2 \approx M$.

2) The number of sign changes ν in the series :

$$O(m) - \sum_n P_{mn} T(n), \quad m = 1, 2, ..., M.$$ (5.16)

should be close to $\nu \approx M/2$ for a good $T(n)$.

The method for finding the set of q values, hence the set of equations, is ad hoc since the emphasis is on χ^2 and ν instead of the qs themselves. The algorithm starts

from $q = 0$ and 1, equivalent to the normalization condition and the mean. More constraints are added one at a time with a q value either one step up or one step down. The direction is to the faster descent of the χ^2. The process stops when the χ^2 no longer decreases. Usually, if $\chi^2 \approx M, \nu \approx M/2$ is not a problem. In our case we stop at the first minimum of the χ^2, defined by the increase of χ^2s in the next three steps. The resultant qs from this process are a set of consecutive integers. Although in this method the constraints eq. (5.9) becomes a set of "running" equations, the method does give sensible results[55]. However, the $T(n)$ so obtained tends to be smoother due to the smearing of P_{mn} matrix, and if too many constraints were imposed the population tends to become wavy[55].

Iteration method In this thesis we attempted a simpler method for multiplicity conversion. Intuitively, one would try to use the P_{mn} matrix for conversions in both directions (Nc $\leftrightarrow N_{hodo}$), and avoid solving eq (5.8) directly. In fact, this is the only way to convert multiplicities on an event by event basis. This, however, has a problem. The P_{mn} matrix is really $(P_m)_n$. Namely, for each n there is a different probability distribution P_m normalized to

$$(\sum_m P_m)_n = 1. \tag{5.17}$$

This normalization ensures that the conversion of $T(n)$ into $O(m)$ through eq. (5.8) will conserve the probabilities. When one tries to use P_{mn} reversely for conversion from O_m to $T(n)$:

$$\sum_m P_{mn} O_m = T_n, \tag{5.18}$$

one has to renormalize it to :

$$\sum_n P_{mn} = 1 \tag{5.19}$$

so that probabilities are again conserved. However, if we just take the P_{mn} from eq. (5.17) and renormalize it in eq. (5.19), we would have assumed that nature generated $T(n)$ flat ! In fact, P_{mn} can be arbitrarily biased to a function $F(n)$ by normalizing it to

$$(\sum_m P_m)_n = F(n), \tag{5.20}$$

before renormalizing it in eq. (5.19). But then, this function $F(n)$ will bear the meaning of how nature generated n, i.e. the $T(n)$ that we are looking for. Figure 5.42 and 5.43 show P_{mn} matrix and $\langle n \rangle$ as a function of m when P_{mn} is biased with flat and FNBD $F(n)$. The difference between the two curves is evident and becomes more significant at high multiplicity region.

To overcome the indeterminate $F(n)$ problem we used a simple iteration method. Starting from an arbitrary $F(n)$, we can reconstruct $T(n)$ from our data $O(m)$. Using this $T(n)$ as $F(n)$, a new $T(n)$ can be recalculated and the process can be iterated as desired. The convergence of this process is checked by χ^2 and ν as defined in eq. (5.15) and (5.16). Usually, the process converges very quickly and only takes a few iterations for the χ^2/dof to drop under 1. The number of sign changes ν is normally not a problem. More iterations usually further lower the χ^2. For $\chi^2 < 1$ this improvement, however, becomes smaller than the statistical error and may not have much meaning unless ν requires improvement. In some cases, an over iterated $T(n)$ would fluctuate very badly because of trying to match the statistical fluctuation in P_{mn} and O_m.

The iteration method still requires the determination of a starting $F(n)$. In
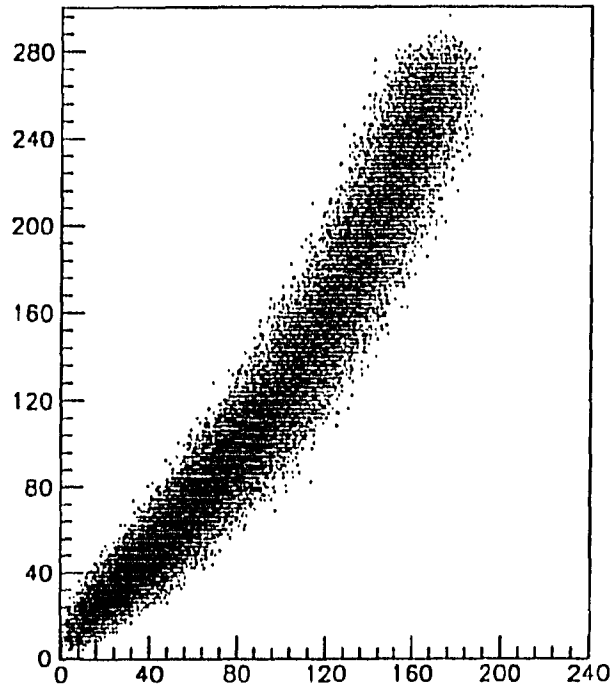
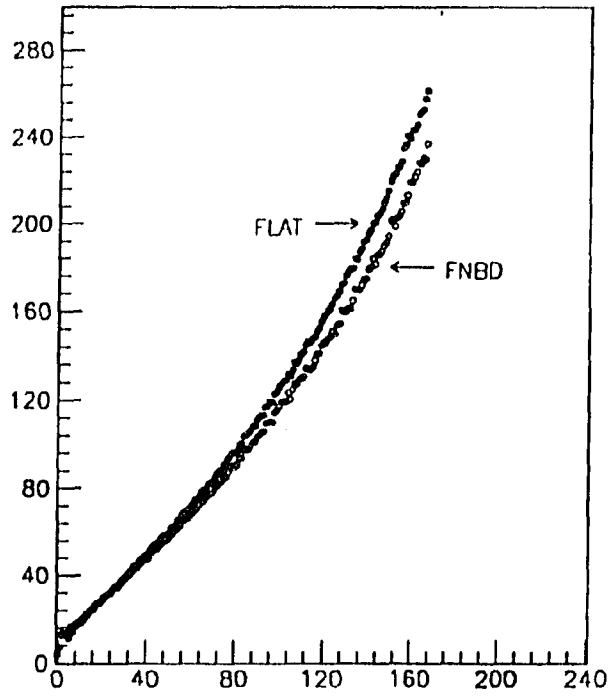Figure 5.42: P_{mn} matrix, $Nc(4\pi)$ vs N_{hodo}.

Figure 5.43: P_{mn} profiles, $\langle Nc(4\pi)\rangle$ vs N_{hodo}.

principle, a different starting $F(n)$ can result in a different $T(n)$. However, we found the difference negligible unless $F(n)$ is dramatically different from the true $T(n)$. Extreme cases are, if the starting $F(n)$ has an opposite curvature the resultant $T(n)$ could cause a kink; and a very narrow starting $F(n)$ can result in a fluctuating $T(n)$. With no prior knowledge of $T(n)$, if one only requires that $T(n)$ be normalized, the maximum entropy method would give a flat $T(n)$. We found that starting from a flat $F(n)$ often gives results close to using the maximum entropy method and reconstructs $T(n)$ well. The arbitrariness of the starting $F(n)$ is not a weakness of this method. In some cases a knowledgeable guess based on prior experiences can enhance the rapidity of convergence.

Figure 5.44-5.46 show the reconstructed Nc distributions in the three different pseudo-rapidity regions by maximum entropy, iteration-flat-$F(n)$ and iteration-NBD-$F(n)$ methods. While the differences are small, the iteration method is more sensitive to small structures since it utilizes the whole distribution for reconstruction rather than just a few of its moments. Subsequent results presented are derived from the iteration-flat method.

Acceptance correction

The $T(n)$ obtained from the last section has not been corrected for trigger bias and cut bias although the P_{mn} matrix is obtained from Monte Carlo after applying cuts. The requirements of the offline BG cut are more stringent than the online PT trigger and includes the PT trigger requirements. Therefore, in our efficiency correction only the BG cut needs be considered. The acceptance as a function of true multiplicity n in different hodoscope regions is shown in Figure 5.47-5.49. The
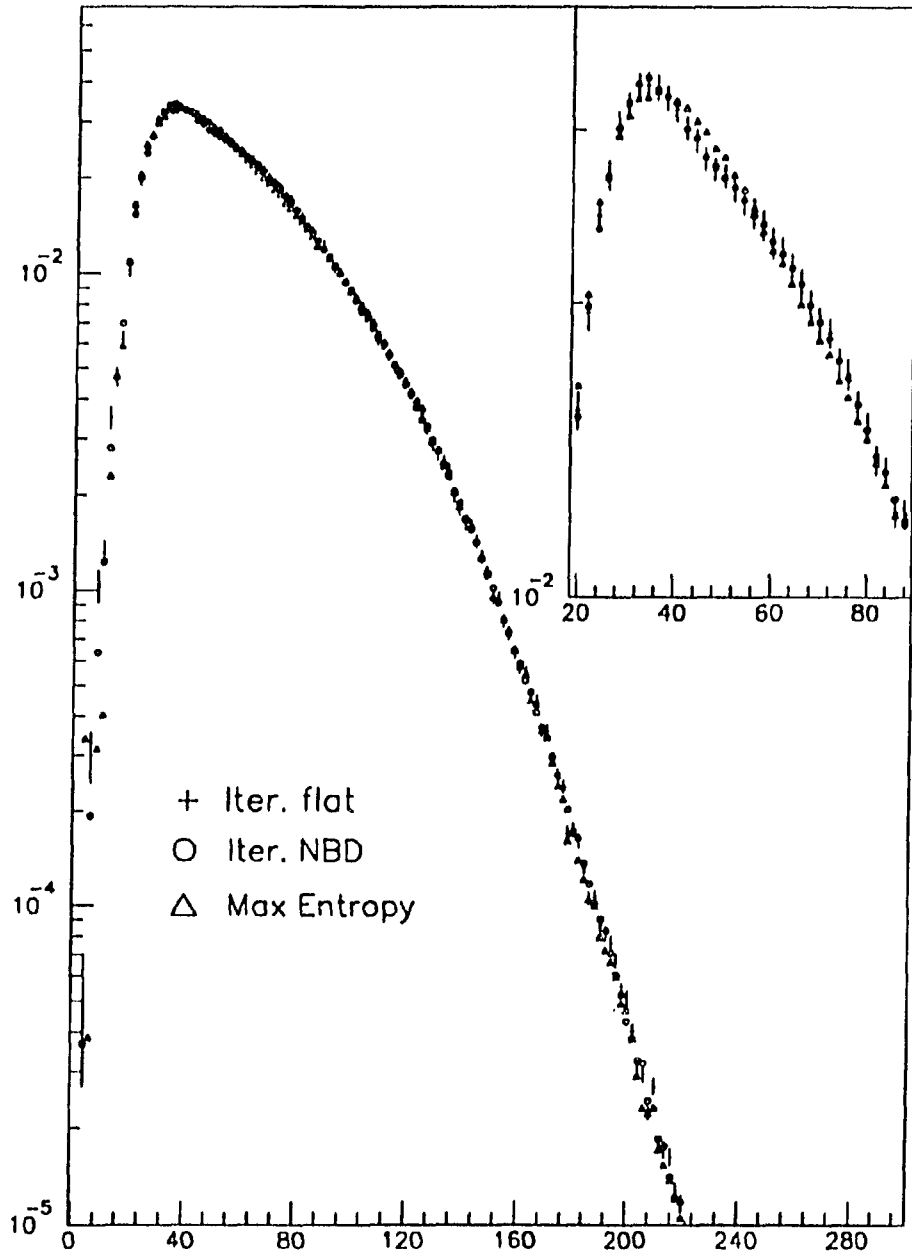
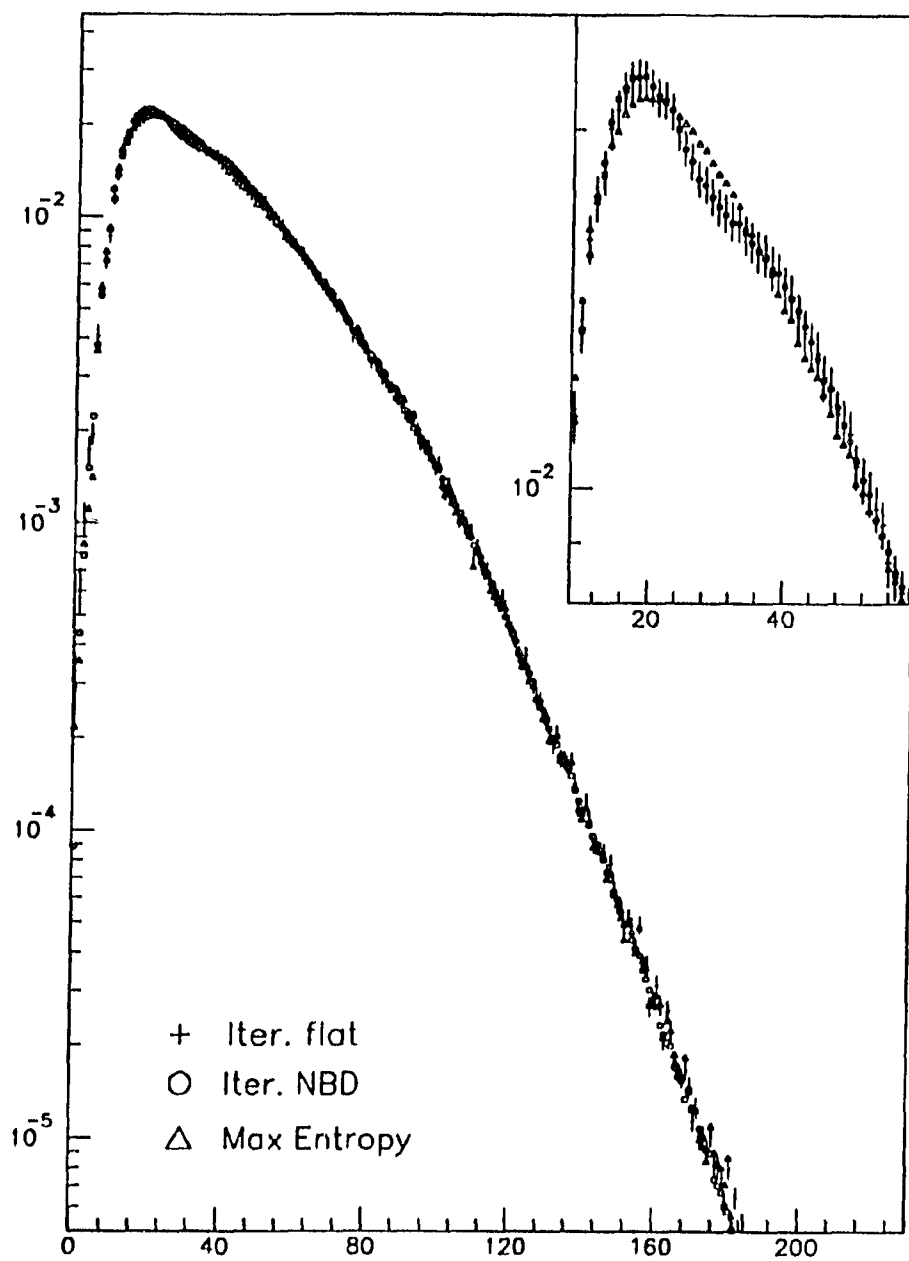Figure 5.44: Reconstructed Nc(4π) using maximum entropy and iteration methods. Before acceptance correction.

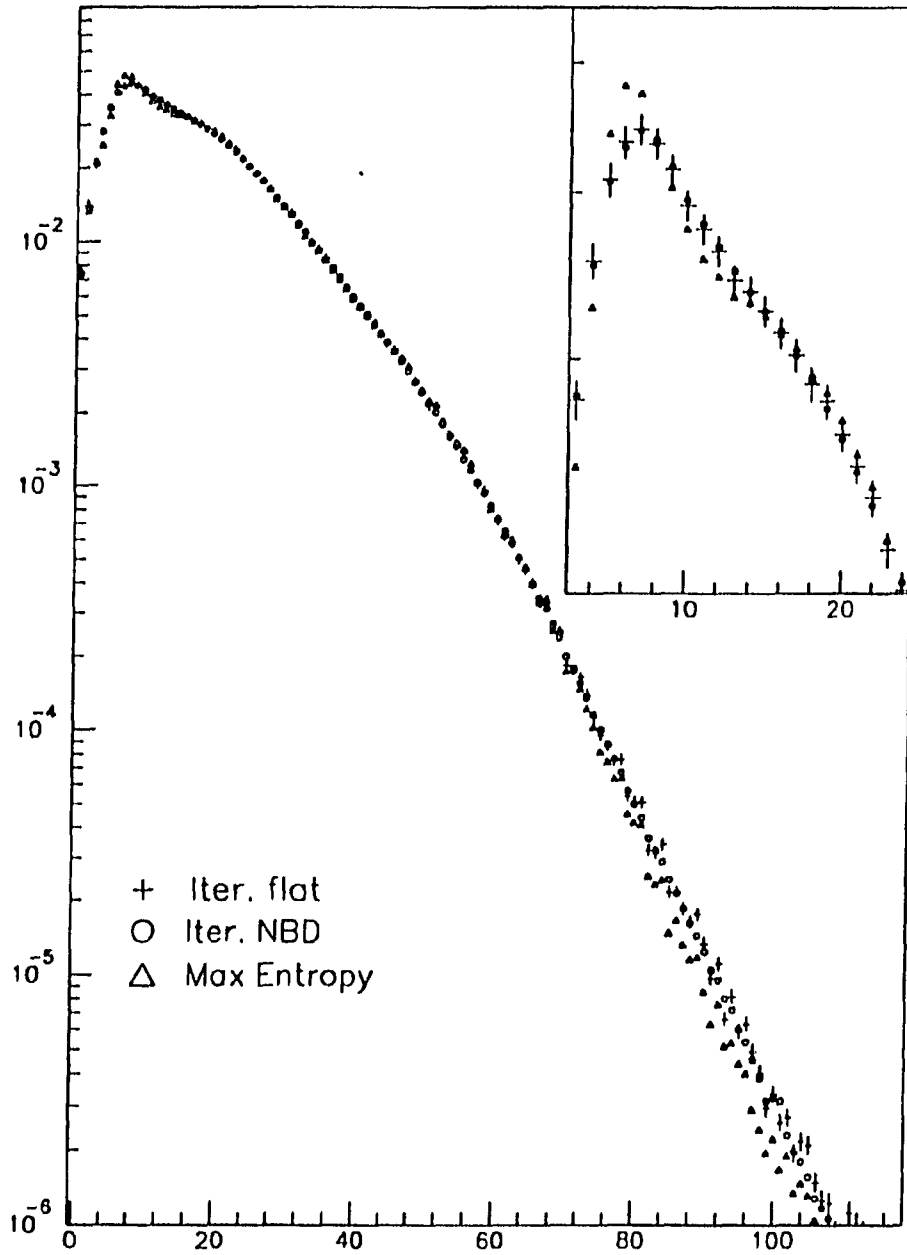Figure 5.45: Reconstructed Nc(hodo) using maximum entropy and iteration methods. Before acceptance correction.

Figure 5.46:   Reconstructed Nc(barrel) using maximum entropy and iteration methods. Before acceptance correction.

acceptance at higher multiplicity region is less than one mainly due to the vertex requirement. The vertex distribution for each $Nc(4\pi)$ bin is the same, therefore Figure 5.49 is flat at high $Nc(4\pi)$. For $Nc(hodo)$ and $Nc(barrel)$ the situation is a little different. When $Nc(4\pi)$ transforms into $Nc(hodo)$ or $Nc(barrel)$, geometrically, an event with a vertex away from the center will have less particles heading into the barrel or the hodoscope and end up with a lower $Nc(barrel)$ or $Nc(hodo)$. Therefore, in $Nc(hodo)$ or $Nc(barrel)$ the vertex distributions are repopulated, and due to the finite upper limit of $Nc(4\pi)$, vertices of higher multiplicity events are more concentrated to the center and less likely to fail the vertex cut. This causes a second rise in Figure 5.47 and 5.48.

Systematic error from different BG cuts

To see how different BG cuts can affect the resultant multiplicity distributions we made 14 variations of the BG cut. Table 5.7 lists the variations. Cut # 14 is our standard BG cut. The number under column "Asym" is the deviation from the standard setting in table 5.1.

Figure 5.50 and 5.51 show the distributions of hodoscope and barrel multiplicities under different cuts. Most of the cut variations do not affect the distributions, except for the p-$\bar{p}$ hit requirements.

The reconstructed Nc distributions from various cuts are shown in Figure 5.52–5.54. Different curves are normalized among one another using a Nc region where statistical errors are small. This prevents faulty mismatches due to huge statistical fluctuations in some bins. For $Nc(4\pi)$ and $Nc(hodo)$ this region is between 40 to 160. For $Nc(barrel)$, 20 to 80 are used. Quite agreeably, the reconstructed 14 curves

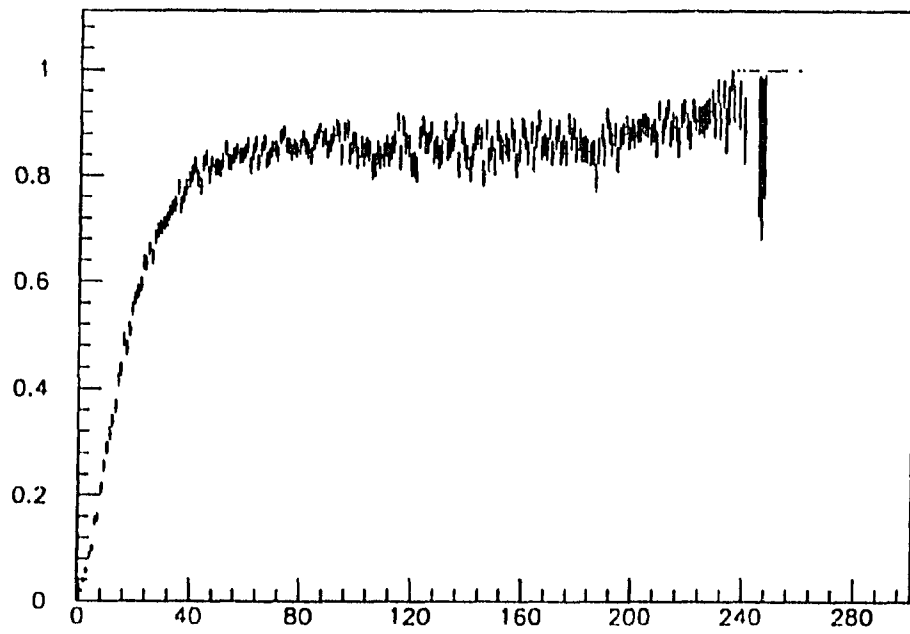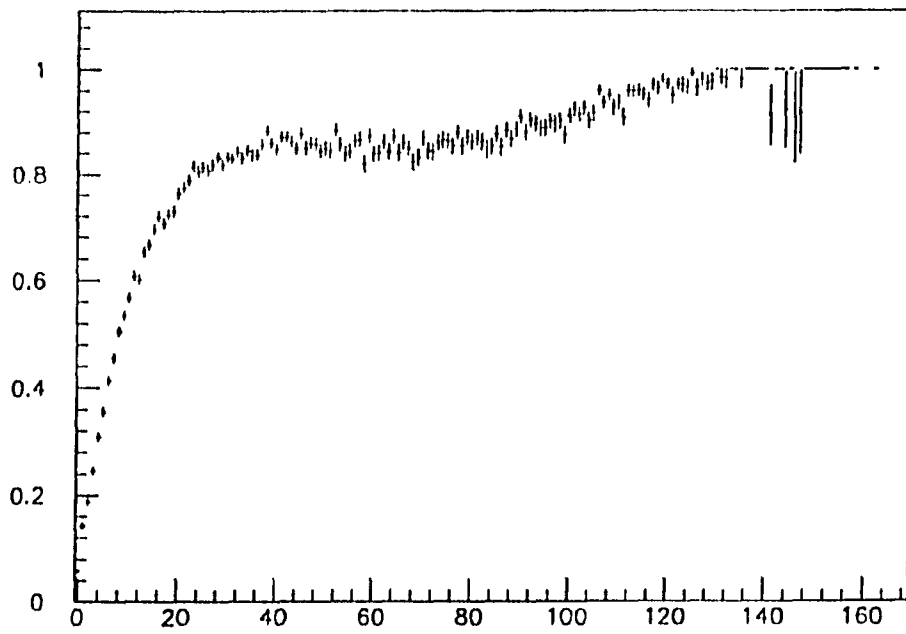Figure 5.47:   Event acceptance as a function of Nc(hodo).

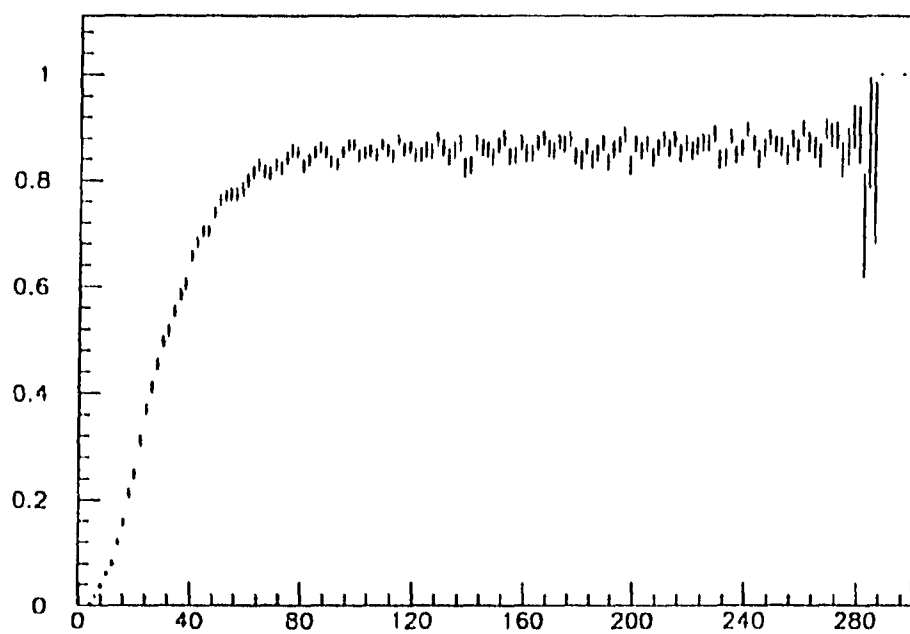Figure 5.48:   Event acceptance as a function of Nc(barrel).

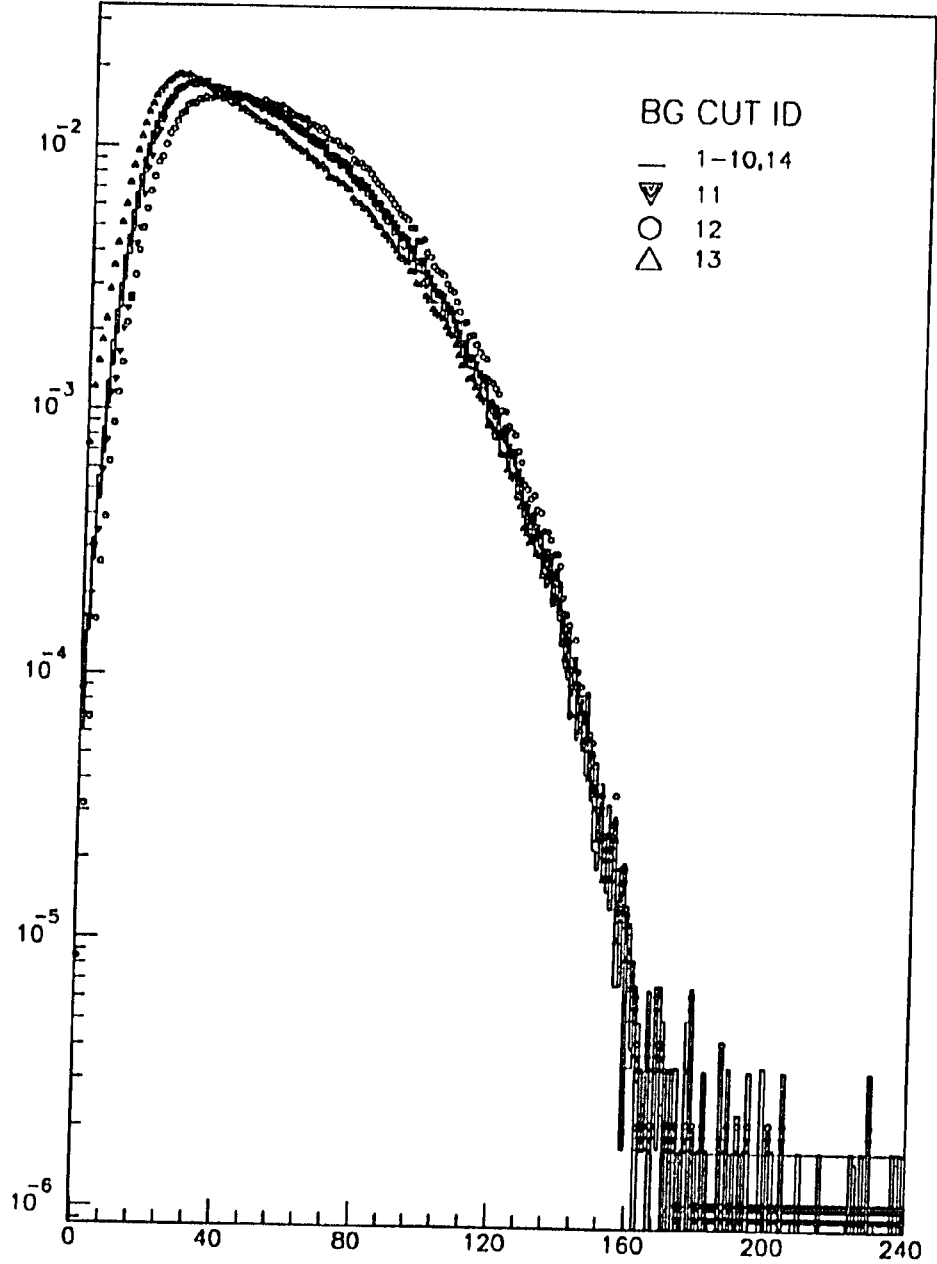Figure 5.49: Event acceptance as a function of Nc(4π).
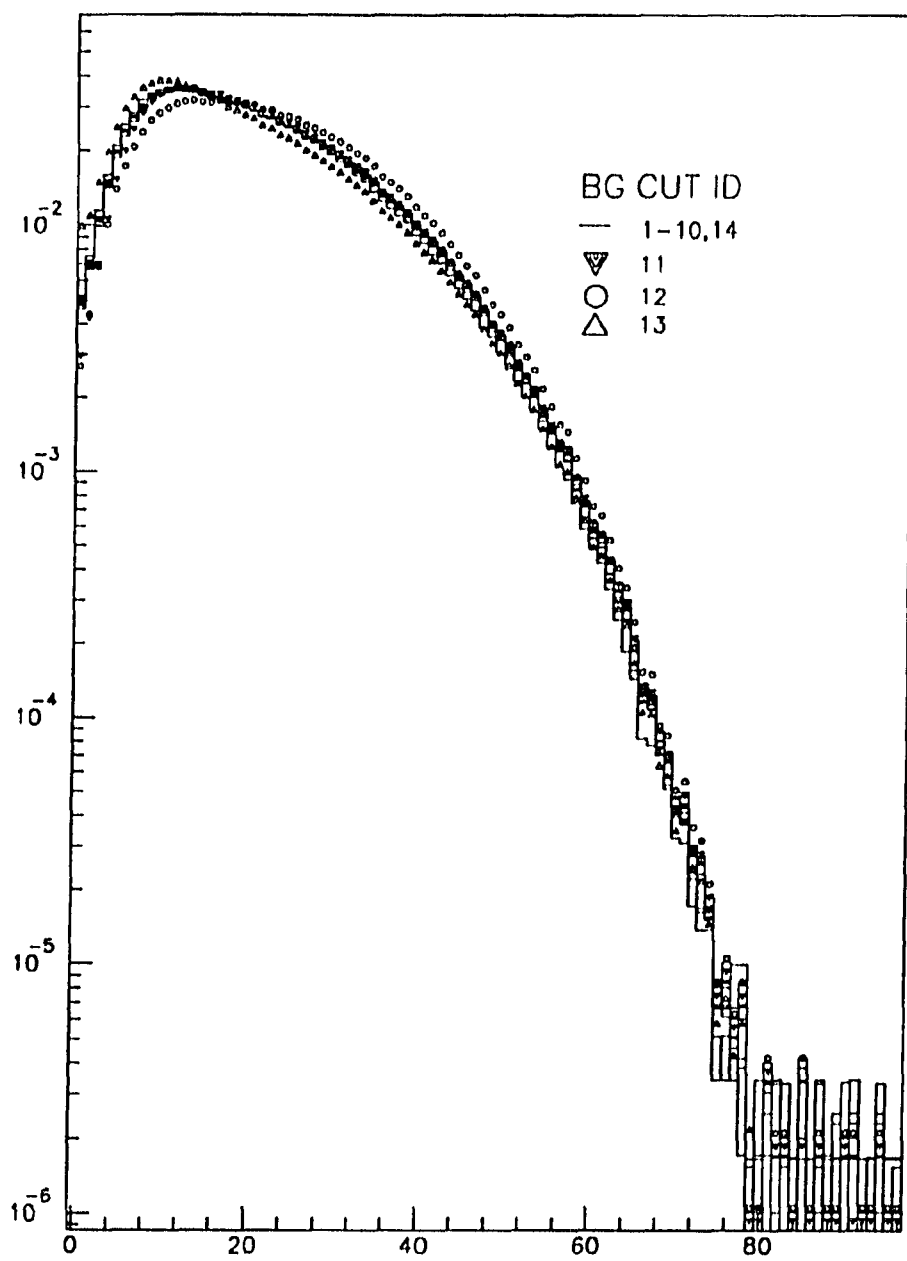
Figure 5.50: N_{hodo} distributions from various BG cuts.

Figure 5.51: N_{barrel} distributions from various BG cuts.

Table 5.7:   Variation of BG cuts.

Cut ID	p̄p≥	Zvrt	Asym	Tav(all)	Tav(ecu)	Tav(ecd)	Thit_up	Thit_lo
1	2.	20.0	0.0	6.0	6.0	6.0	50.0	-10.0
2	2.	50.0	0.0	6.0	6.0	6.0	50.0	-10.0
3	2.	10.0	0.0	6.0	6.0	6.0	50.0	-10.0
4	2.	20.0	0.0	3.0	3.0	3.0	50.0	-10.0
5	2.	20.0	0.0	9.0	9.0	9.0	50.0	-10.0
6	2.	20.0	0.0	6.0	6.0	6.0	20.0	-10.0
7	2.	20.0	0.0	6.0	6.0	6.0	35.0	-10.0
8	2.	20.0	0.0	6.0	6.0	6.0	50.0	-5.0
9	2.	20.0	0.0	6.0	6.0	6.0	50.0	-20.0
10	2.	20.0	5.0	6.0	6.0	6.0	50.0	-10.0
11	2.	20.0	-5.0	6.0	6.0	6.0	50.0	-10.0
12	3.	20.0	0.0	6.0	6.0	6.0	50.0	-10.0
13	1.	20.0	0.0	6.0	6.0	6.0	50.0	-10.0
14	2.	60.0	0.0	6.0	6.0	6.0	50.0	-10.0

overlap one another for a large mid section of the distribution, irrespective of the significant differences in their raw distributions shown in Figure 5.50 and 5.51.

These curves are background subtracted and acceptance corrected. In principle, if our background estimation and Monte Carlo simulation is correct, they should all fall on top of one and other. The differences among them will serve as a measure of the systematic error.

As a final product, our distribution is the weighted mean of the 14 curves. The statistical error is taken as the numerical average of the 14 statistical errors, since averaging different methods on the same data should not change the statistical error. The systematic error is taken as one half of the largest difference in each bin. The fractional statistical and systematic errors are shown in Figure 5.55. Both errors are concentrated in the very high and very low multiplicity regions. The systematic error
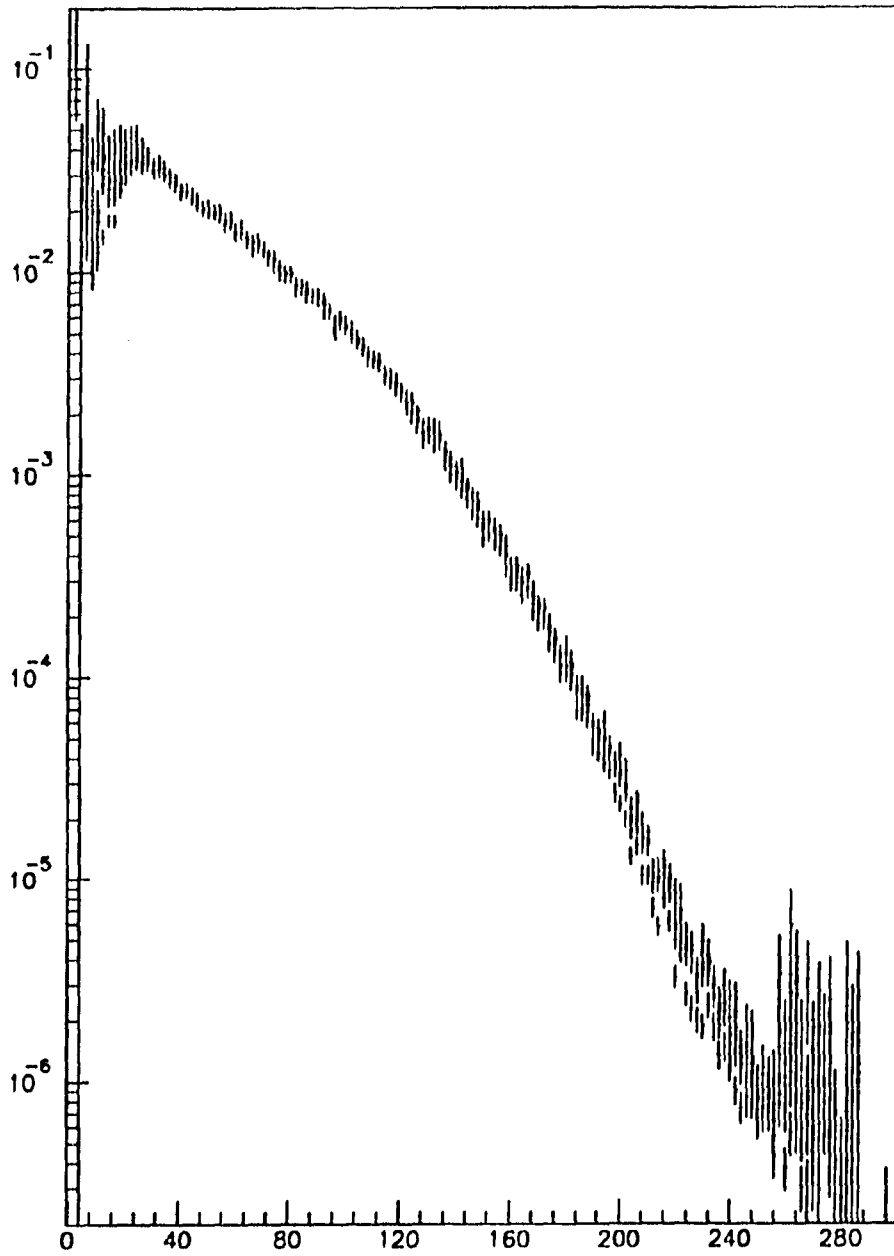
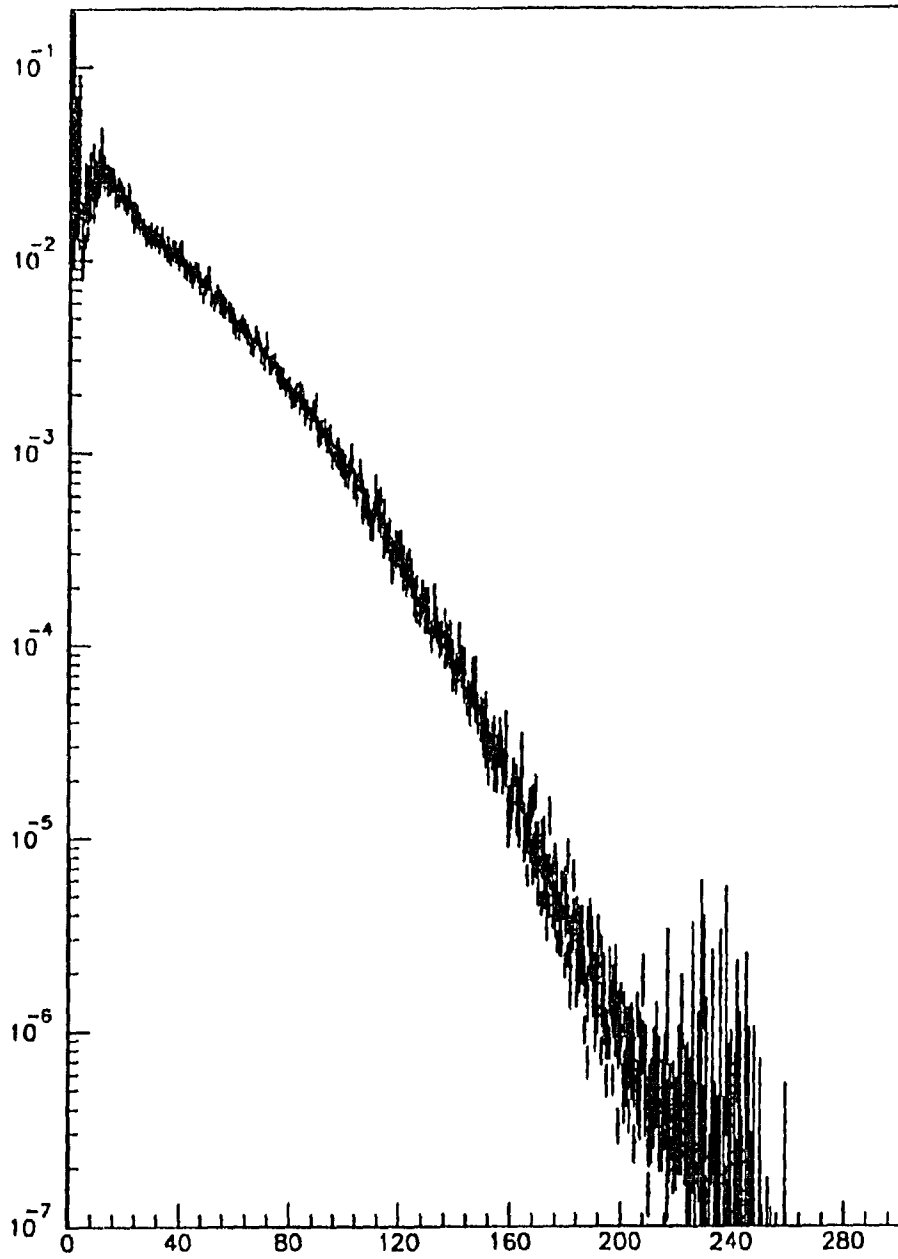Figure 5.52:   Corrected Nc(4π) distributions of 14 different BG cuts.

Figure 5.53: Corrected Nc(hodo) distributions of 14 different BG cuts.
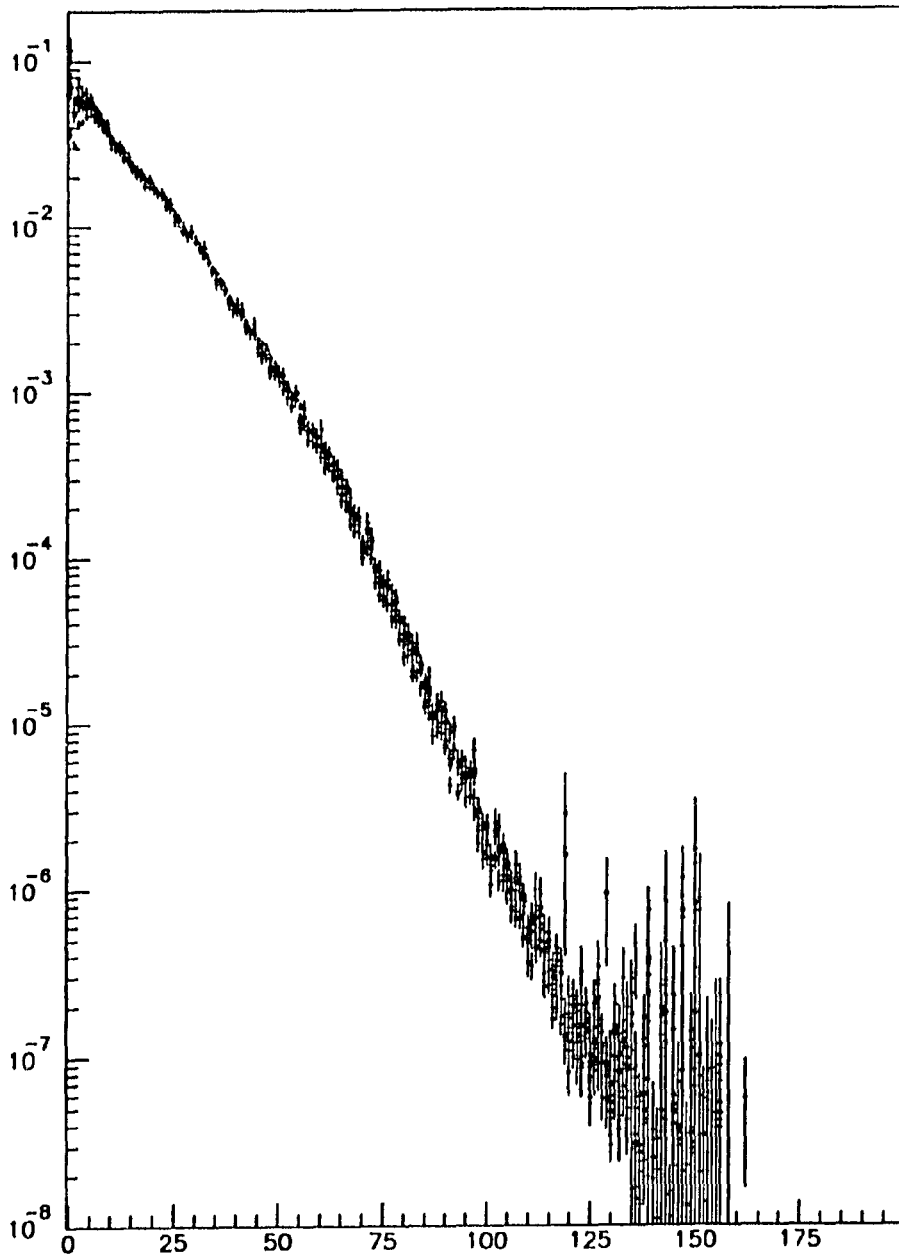
Figure 5.54:   Corrected Nc(barrel) distributions of 14 different BG cuts.

so estimated will contain some fraction of statistical fluctuation. However, these 14 different BG cuts do not exhaust all possible sources of systematic error either. We take root mean square of the two errors as the total error for each bin. The results are shown in Figure 5.56-5.58. The discussion in the next chapter will be based on these distributions.

Figure 5.55: Fractional systematic and statistical errors.

Figure 5.56:   Corrected Nc(4π) distributions.

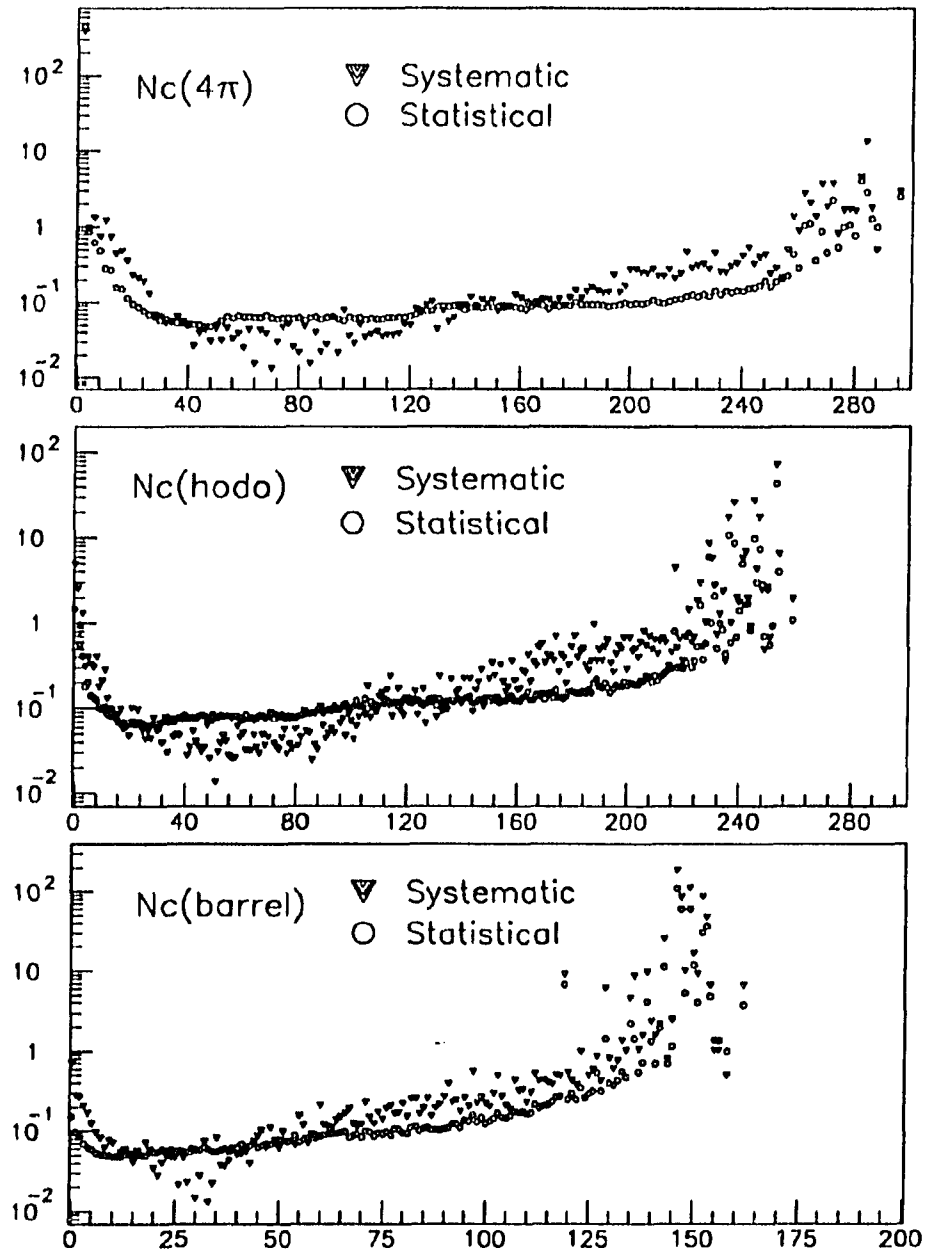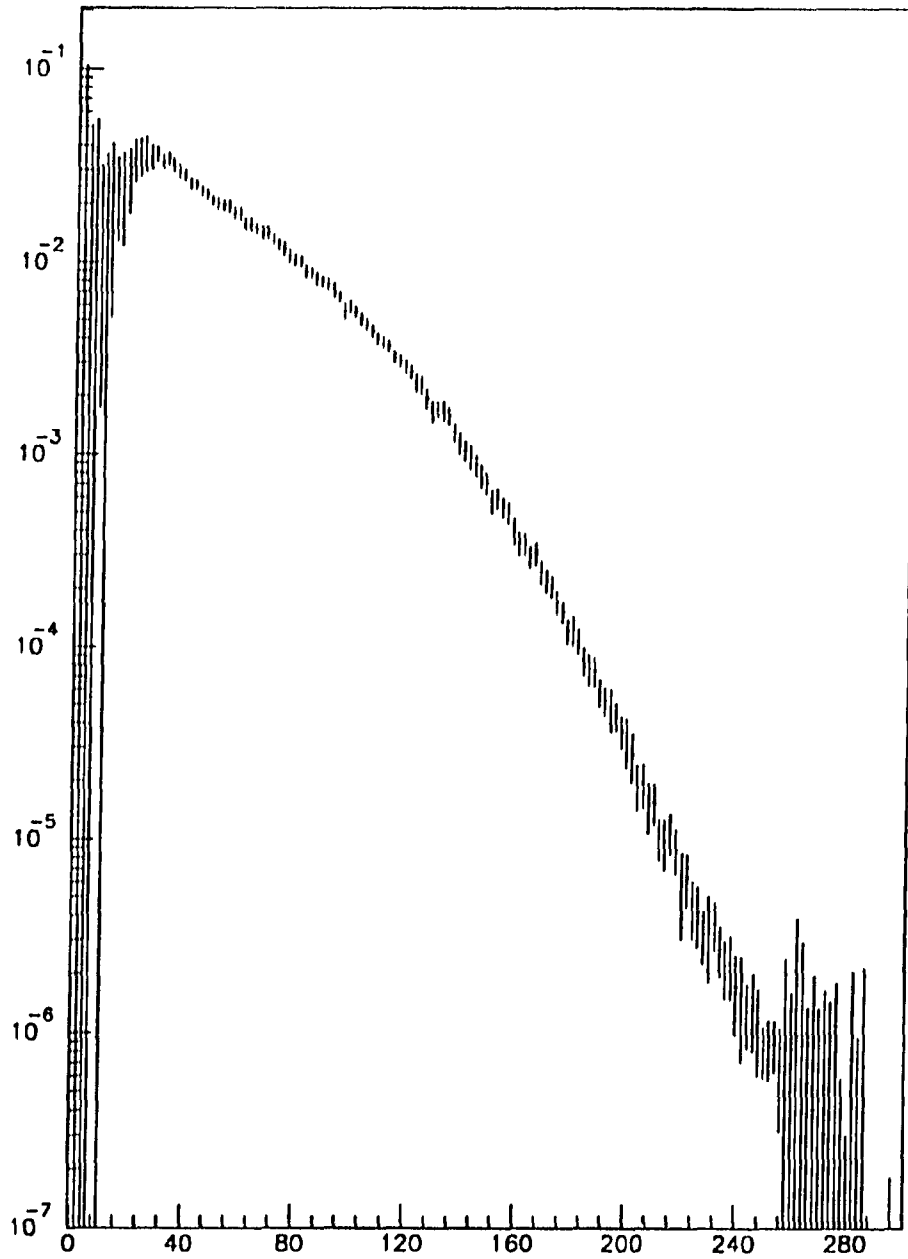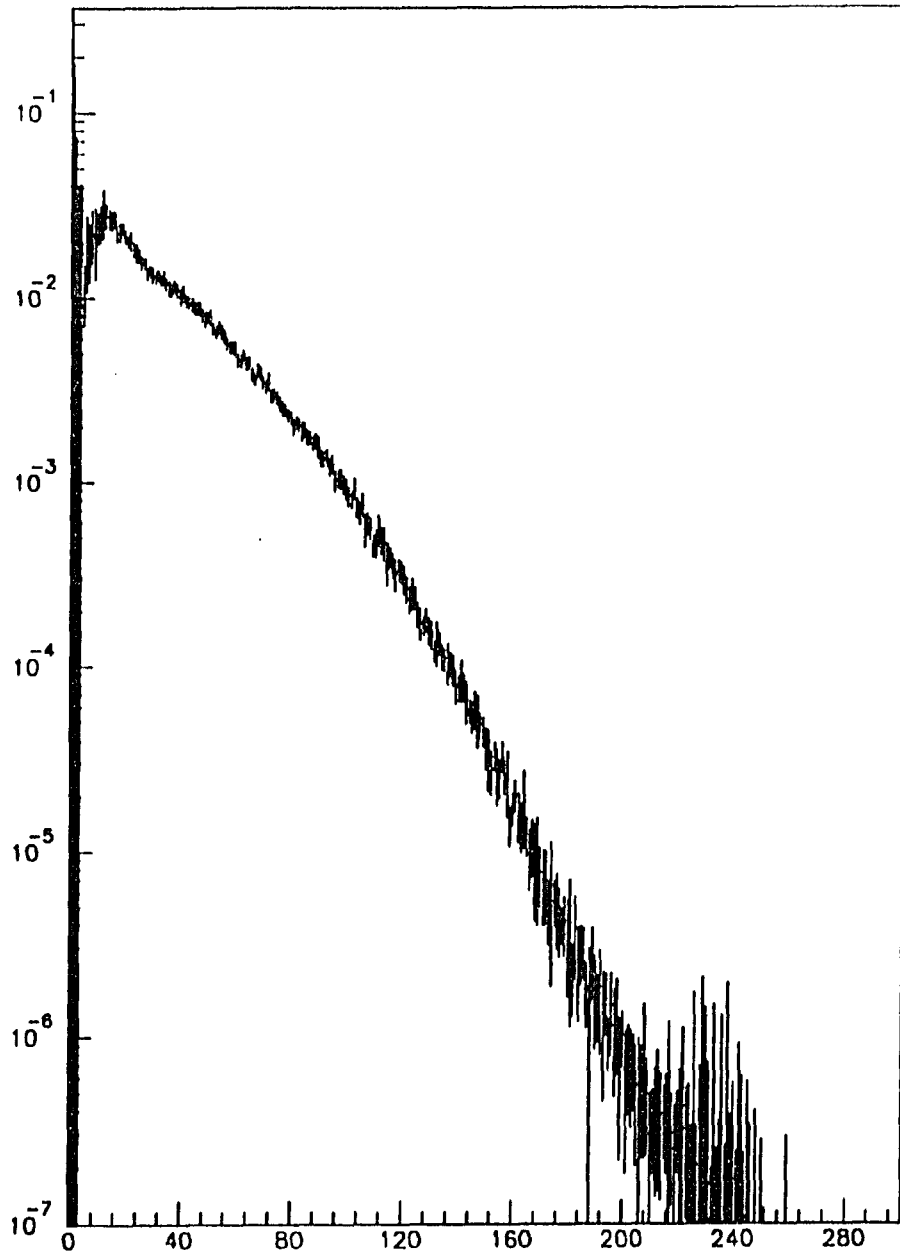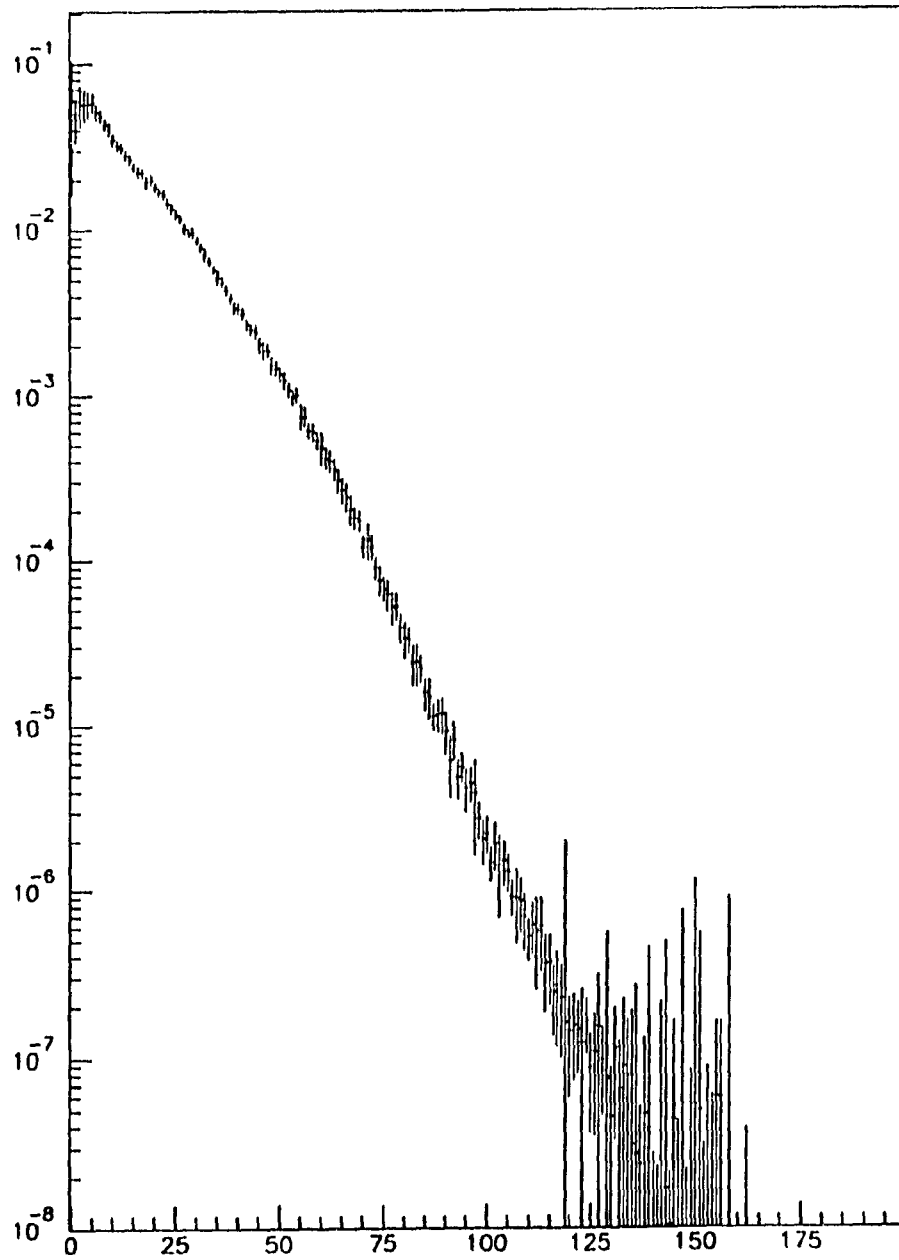Figure 5.57:   Corrected Nc(hodo) distributions.

Figure 5.58: Corrected Nc(barrel) distributions.

CHAPTER 6. RESULTS

In this chapter we will present fitted distributions and moments, and compare them with earlier, lower energy results shown in chapter two.

The Moments

In this section we will discuss the first four moments of Nc(4π). The distribution is first converted into genuine multiplicity with the simple relation eq. (2.1), then the moments are calculated. The first moment is the average multiplicity :

$$\bar{n} = \sum_{n=0}^{\infty} nP_n, \tag{6.1}$$

The error of the mean is estimated analytically :

$$\sigma_{\bar{n}} = [\sum_{n=0}^{\infty} (\frac{\partial \bar{n}}{\partial P_n})^2 \sigma_{P_n}^2]^{1/2} \tag{6.2}$$

$$= [\sum_{n=0}^{\infty} n^2 \sigma_{P_n}^2]^{1/2}, \tag{6.3}$$

where, we have assumed $\sigma_n = 0$. For the higher moments :

$$D_k = [\sum_{n=0}^{\infty} (n - \bar{n})^k P_n]^{1/k}. \tag{6.4}$$

And the error of the moment is estimated :

$$\sigma_{D_k} = [\sum_{n=0}^{\infty} (\frac{\partial D_k}{\partial P_n})^2 \sigma_{P_n}^2]^{1/2} \tag{6.5}$$

$$= [\sum_{n=0}^{\infty}(\frac{\partial}{\partial P_n}(\sum_{n=0}^{\infty}(n - (\sum_{n=0}^{\infty}nP_n))^k P_n)^{1/k})^2 \sigma_{P_n}^2]^{1/2} \qquad (6.6)$$

$$= (\sum_{n=0}^{\infty}(\frac{\sigma_{P_n}}{kD_k^{k-1}}((n-\bar{n})^k - knD_{k-1}^{k-1}))^2)^{1/2}. \qquad (6.7)$$

The calculation of the moments and their errors can also be done with a simple Monte Carlo. The distribution of $Nc(4\pi)$ can be regenerated with each Nc bin assumed a Gaussian distribution according to the content and error of Figure 5.56. For each generated distribution we can calculate its moments. Repeating for many times we will have a distribution for each moment we want to calculate. Then we can take the mean and RMS of the distribution as the value and error of the moment. The moments and errors for the 1800 GeV data using the two methods are listed in Table 6.1. In some $Nc(4\pi)$ bins the error bars are very big and can extend to unphysical negative probability. In the Monte Carlo calculation, when this happens, we reassigned the value to a very small positive number. The differences seen in the two methods listed in the table are mainly due to this effect.

Also listed in Table 6.1 are the calculated moments from our 546 and 300 GeV data. These data are treated the same as the 1800 GeV data, except that we don't have missing bunch data at those energies, and the BG subtraction was done with the estimate from 1800 GeV data.

Table 6.1: The first four moments of genuine multiplicity distribution.

GeV		$\langle n \rangle$	D_2	D_3	D_4
1800	MC	21.94 ± 0.314	16.16 ± 1.033	15.13 ± 1.328	22.44 ± 0.342
	Calc.	21.91 ± 0.324	15.38 ± 1.760	16.01 ± 1.592	22.17 ± 0.580
546	Calc.	14.27 ± 0.461	9.51 ± 1.651	9.64 ± 1.711	13.59 ± 0.568
300	Calc.	11.73 ± 0.303	7.13 ± 0.827	7.06 ± 0.990	10.09 ± 0.369

Figure 6.1–6.4 plots our calculated numbers listed in Table 6.1, together with other Non-Single-Diffractive (NSD) data from ISR[29] and SPS[28] experiments. Also superimposed on the figures are the results of inelastic data sample regenerated from Figure 2.2,2.3 and 2.5.

In Figure 6.1, the curves shown are the ones in Figure 2.2 for the inelastic data. In their descending orders they are eq. (2.17) for the statistical/hydrodynamic model :

$$\langle n \rangle = -2.909 + 2.183 \cdot s^{0.1609}. \tag{6.8}$$

Eq. (2.18) from the QCD approach :

$$\langle n \rangle = 0.2051 \exp(\sqrt{1.430 \ln s}) - 1.004. \tag{6.9}$$

And Eq. (2.16) motivated by Feynman scaling :

$$\langle n \rangle = -0.468 + 0.164(\ln s) + 0.0653(\ln s)^2. \tag{6.10}$$

NSD data are in general higher than the inelastic data sample. Our results at lower energies are in agreement with UA5 points.

Figures 6.2–6.4 are to be compared with the linear Wroblewski relations. The inelastic data and the NSD data are apparently following different lines. Our data is consistent with an extrapolation from lower energies, except perhaps for the D_4 moment at 1800 GeV.

The Distributions

A deviation from the Wroblewski relation in the central moments can be interpreted as an indication of KNO-G scaling violation, since the former is a natural
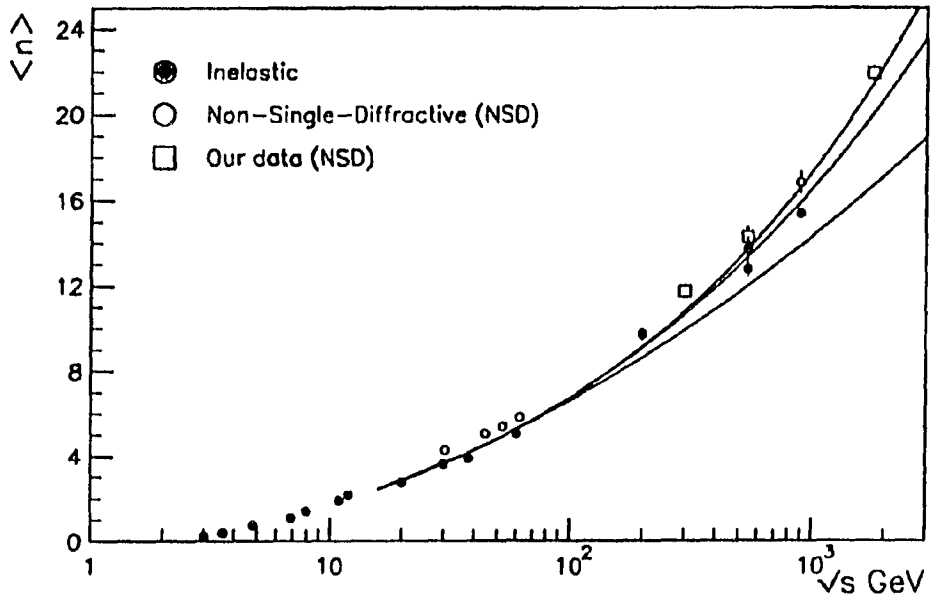
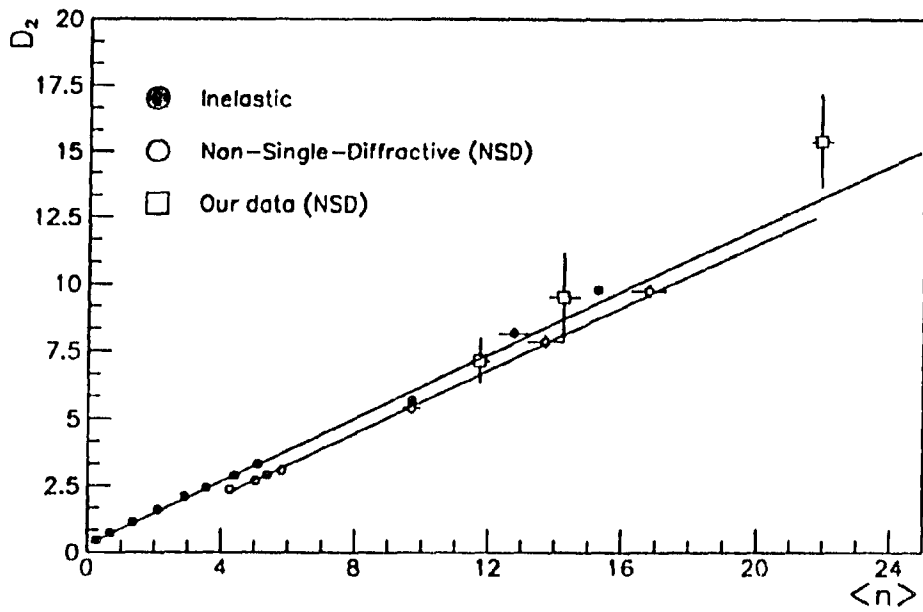Figure 6.1: Energy dependence of averaged genuine multiplicity.

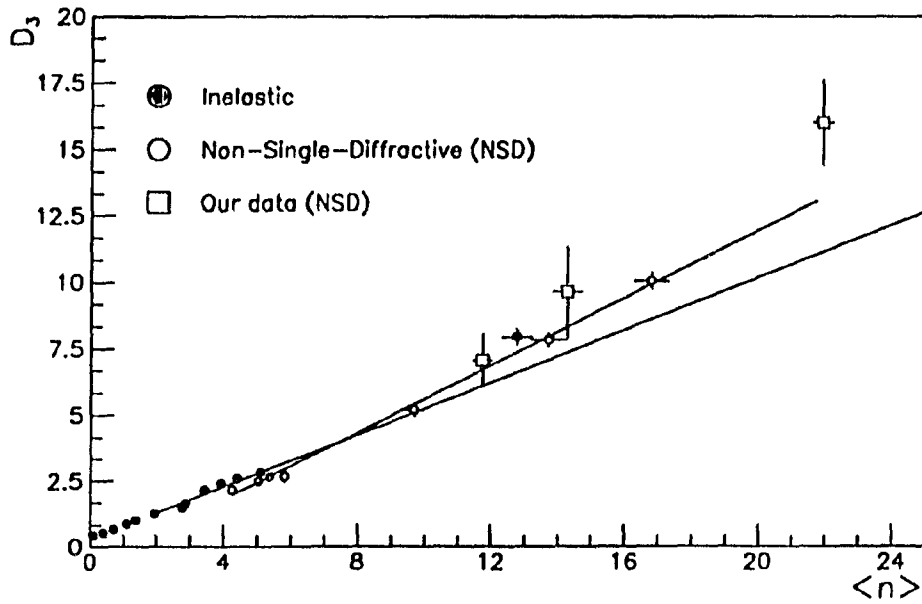Figure 6.2: D_2 moment as a function of $\langle n \rangle$.

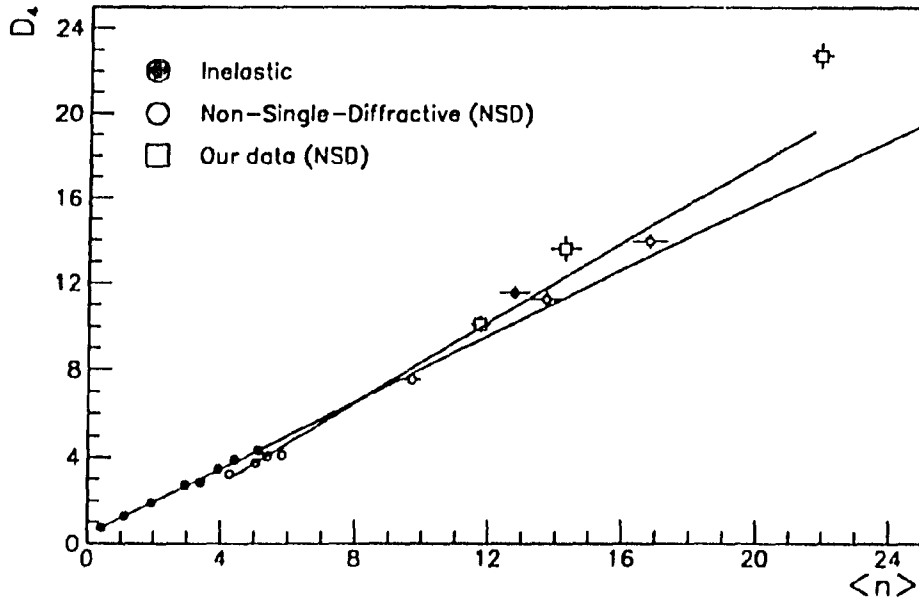Figure 6.3: D_3 moment as a function of $\langle n \rangle$.

Figure 6.4: D_4 moment as a function of $\langle n \rangle$.

derivation of the later. The distributions we have measured at 1800 GeV, indeed do not follow the KNO-G scaling. However, our experimental data does not favor the negative binomial distribution either. Figure 6.5 is a fit to Nc(4π) with KNO-G and FNBD. Clearly, neither function can fit well to the distribution. In the fitting we have limited our fits only to the multiplicity region $10 \leq Nc \leq 240$, to exclude regions of very large systematic errors. The scaling function ϕ used for our KNO-G fit is given in eq. (2.37) and (2.38). The probability distribution P_n is calculated in genuine multiplicity with eq. (2.34) and converted back to charged multiplicity Nc. The fit parameter $\langle \tilde{n} \rangle$ is approximated by eq. (2.36). Converted to Nc, we have :

$$\langle Nc \rangle = 52.265 \pm 0.173, \quad \chi^2/\text{dof} = 13.46.$$

And for the FNBD fit on the same plot :

$$\langle Nc \rangle = 47.471 \pm 0.287, \quad k = 3.105 \pm 0.040, \quad \chi^2/\text{dof} = 5.68.$$

We have also tried a double FNBD and a double KNO-G fit. If the events belong to one of two possible classes, for example, jet versus no jet, or 'soft' versus 'hard'. The distribution would be in the form of :

$$P(Nc) = wF_1 + (1 - w)F_2. \tag{6.11}$$

We assume that F_1 has the same form as F_2; either a FNBD or a KNO-G distribution with different parameters. The result of the fit is given in Table 6.2 and is shown in Figure 6.6 and 6.7. Both double KNO-G and double FNBD can fit the distribution very well.

Finally, the Nc distribution for three different pseudo-rapidity regions is plotted in Figure 6.8 in KNO format. When compared with Figure 2.6 at 63 GeV, the

property of a smaller rapidity interval giving a broader distribution remains the same. The $\langle Nc \rangle$ in each region is :

$$\langle Nc(hodo) \rangle = 28.741 \pm 0.343, \quad |\eta| \leq 1.57$$

$$\langle Nc(barrel) \rangle = 12.607 \pm 0.160, \quad |\eta| \leq 3.25.$$

Table 6.2: Fit to $Nc(4\pi)$ with a double distribution.

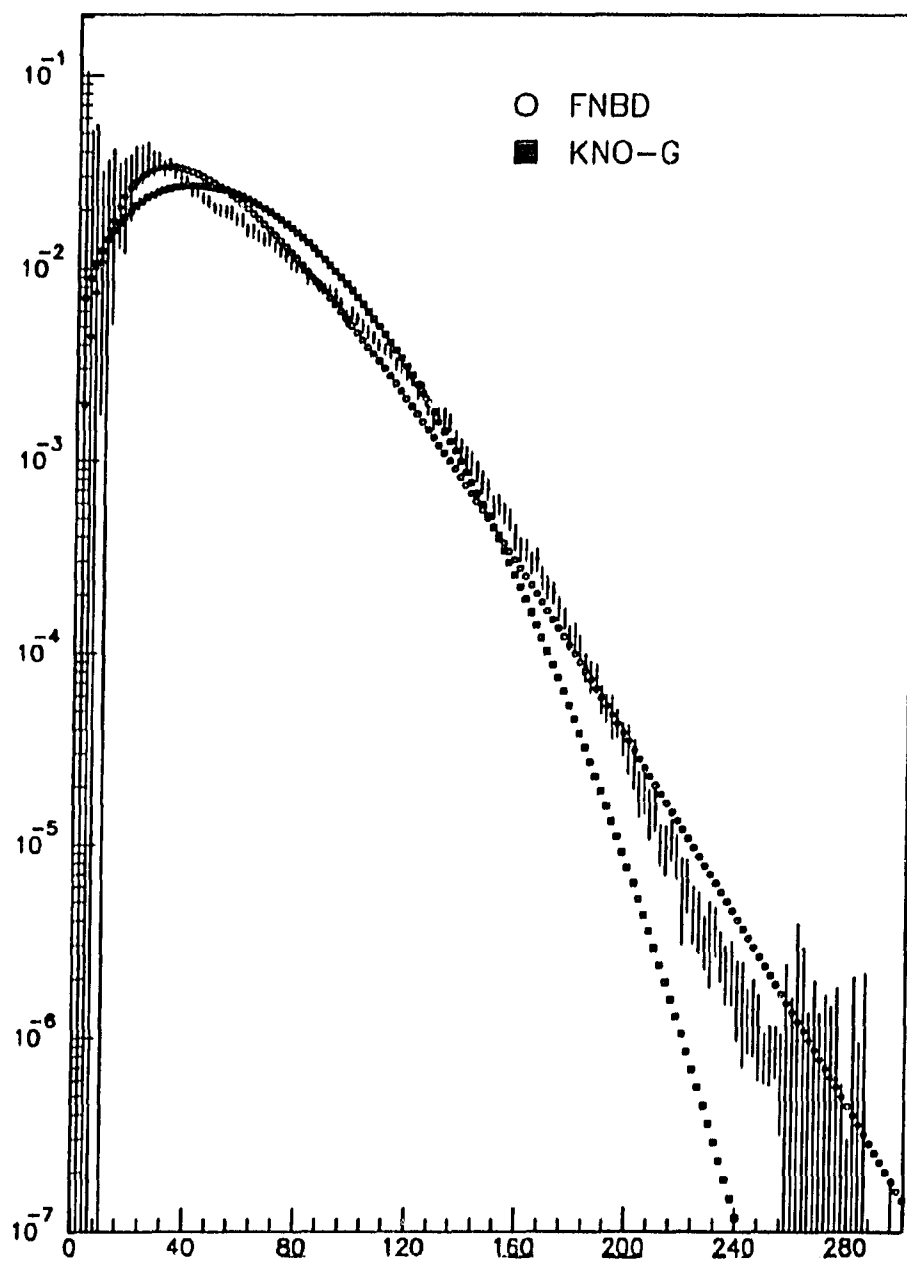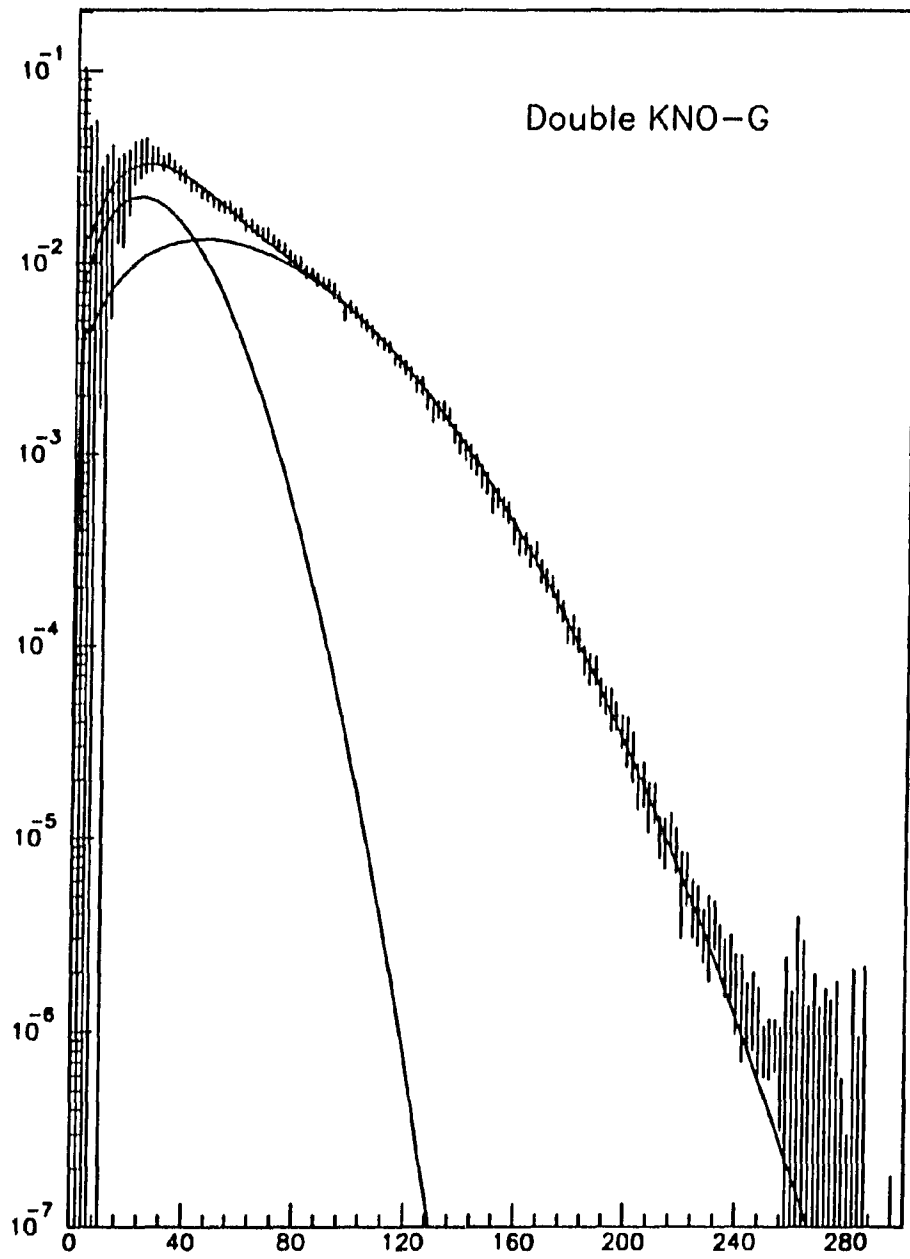| Double FNBD	Double KNO-G
$w = 0.826 \pm 0.0326$	$w = 0.443 \pm 0.011$
$\langle Nc \rangle_1 = 36.955 \pm 1.451$	$\langle Nc \rangle_1 = 28.572 \pm 0.693$
$K_1 = 2.828 \pm 0.190$	
$\langle Nc \rangle_2 = 87.830 \pm 2.688$	$\langle Nc \rangle_2 = 59.049 \pm 0.210$
$K_2 = 10.599 \pm 0.878$	
$\chi^2/dof = 0.266$	$\chi^2/dof = 0.325$

Figure 6.5: $Nc(4\pi)$ fit to KNO-G and FNBD.

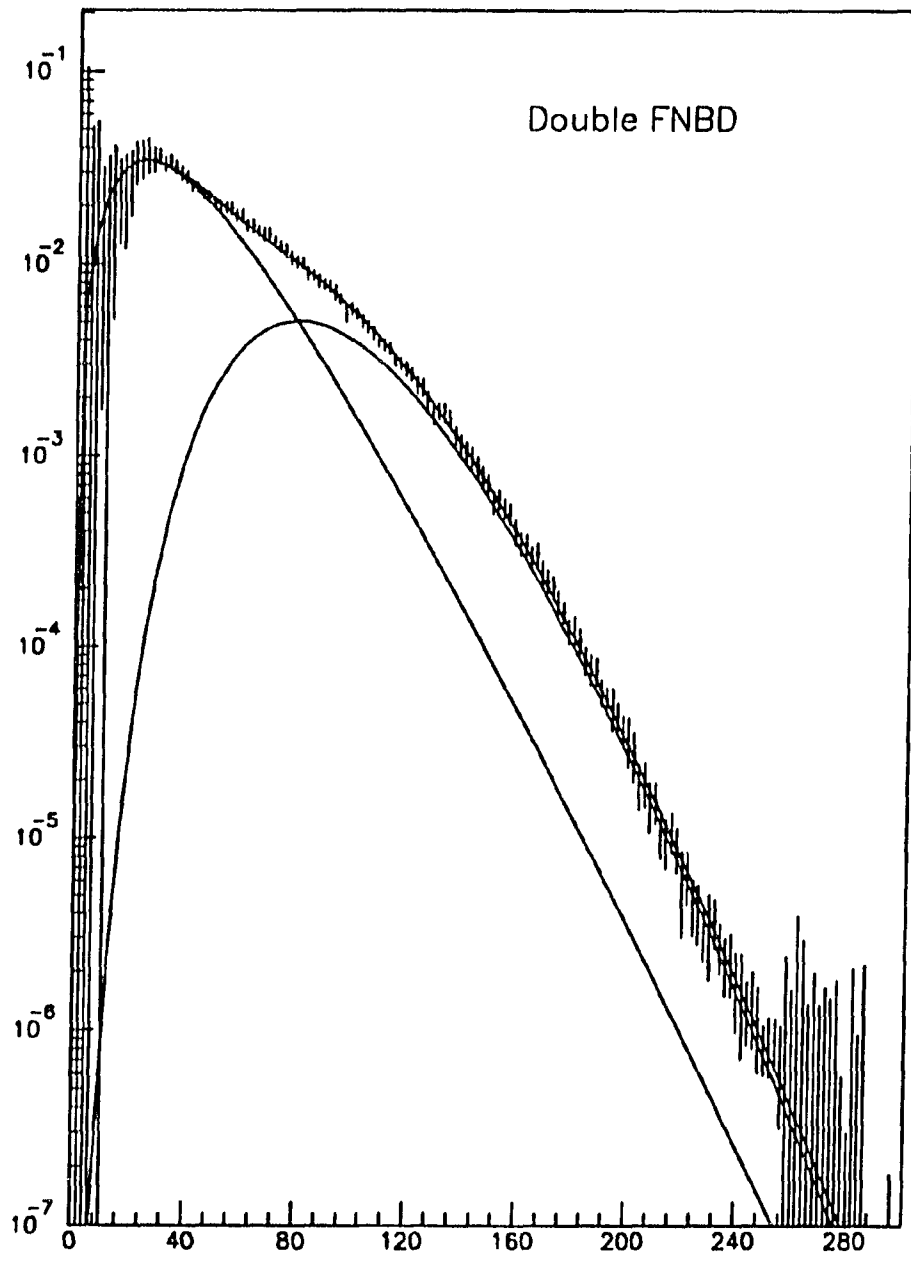Figure 6.6:   A double KNO-G fit to Nc(4π).

Figure 6.7:   A double FNBD fit to Nc(4π).
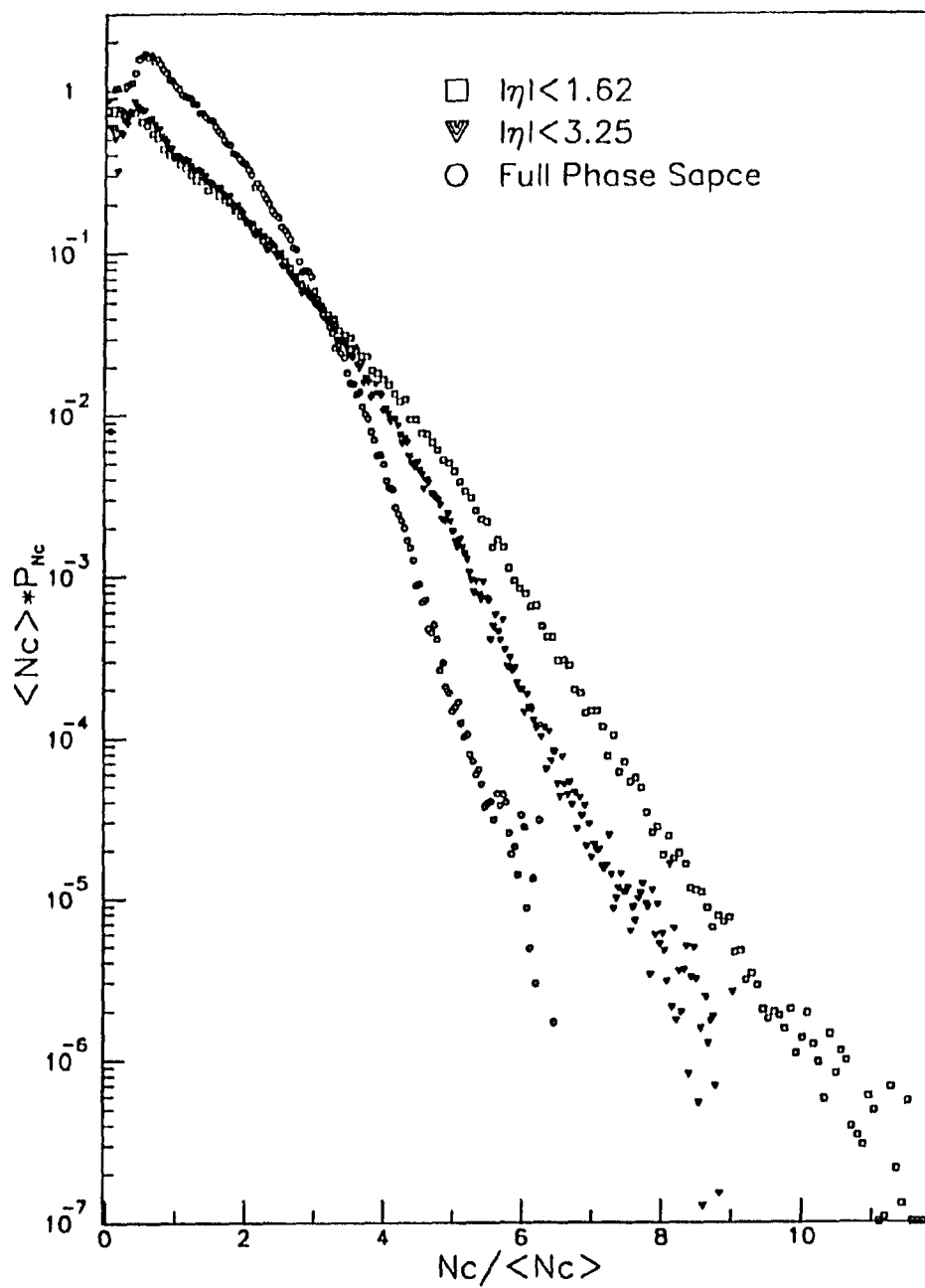
Figure 6.8:   Nc distributions in different pseudo-rapidity regions

CHAPTER 7. SUMMARY

The multiplicity distribution at 1800 GeV is seen to deviate from both single KNO-G and single negative binomial distributions in the same way as was seen in the UA5 900 GeV data. The shoulder structure found by UA5 at 900 GeV is also apparent in our 1800 GeV data. Our distribution, however, fits well to a double KNO-G function or a double negative binomial distribution, which suggests multiple interaction mechanisms.

When the distributions are normalized to KNO format, the tendency of having a broader distribution in a smaller pseudo-rapidity region, seen at lower energies, remains the same in our 1800 GeV data.

APPENDIX A. TRIGGER LOGIC

The Trigger Logic evolved with time. The diagrams collected here is a glimpse of the setups around the end of '88. The main stream of the logic started from the Tevatron beam pickup signal TVBS. The signal was fanned out to start and clear the readout electronics, to synchronize computers with the beams and to generate event triggers. The down stream ends of the trigger generation were the most frequently changed part of the system, while others were seldom touched. Another branch of the logic was from the Main Ring clock signal which generated high voltage gates for protection of the detectors during Main Ring $\bar{p}$ production cycles. The missing figure in this collection is the spectrometer trigger which was implemented in the later '89 runs using the pre- and post- magnet chambers.

151
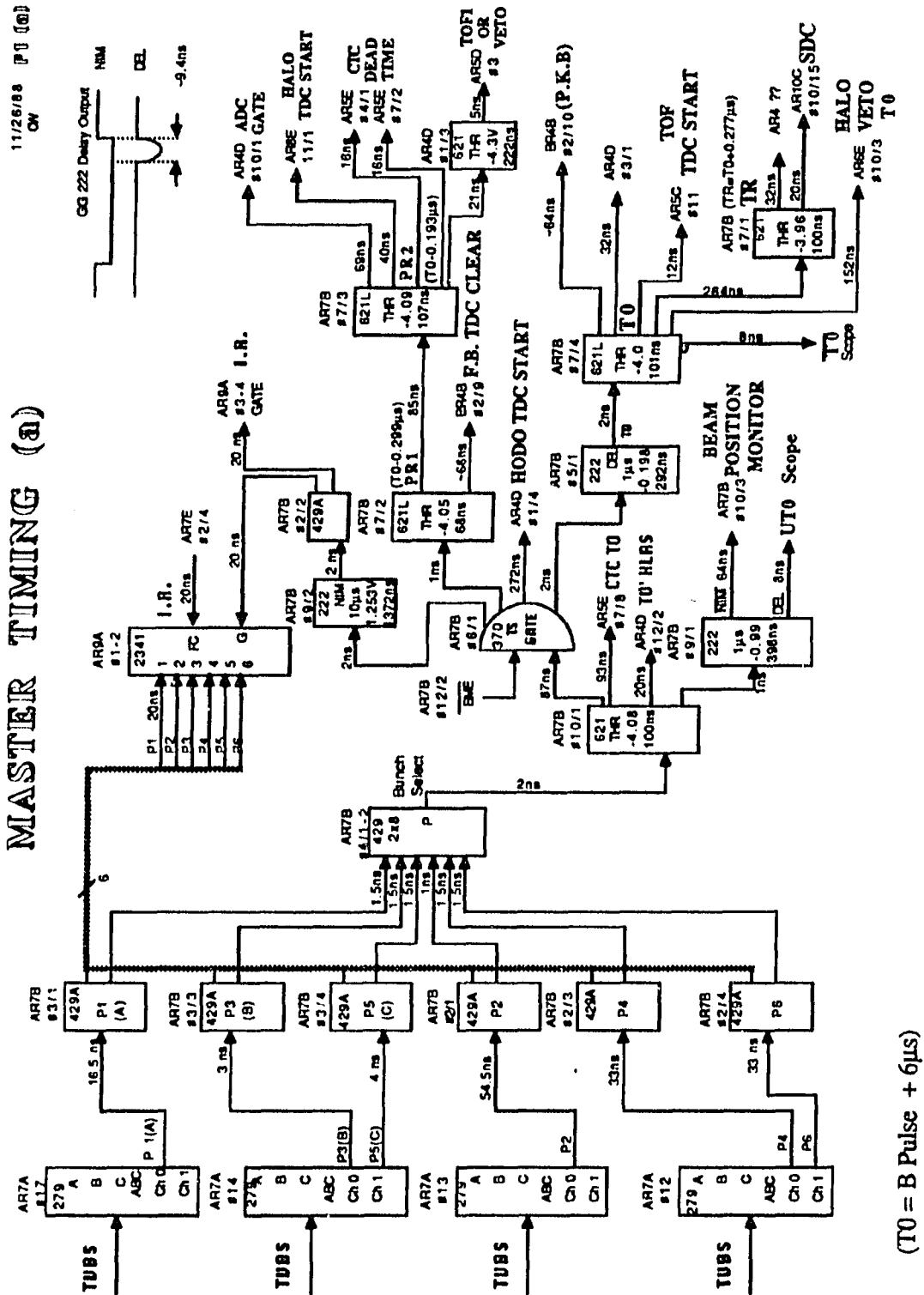
Figure A.1: Trigger timing: A.
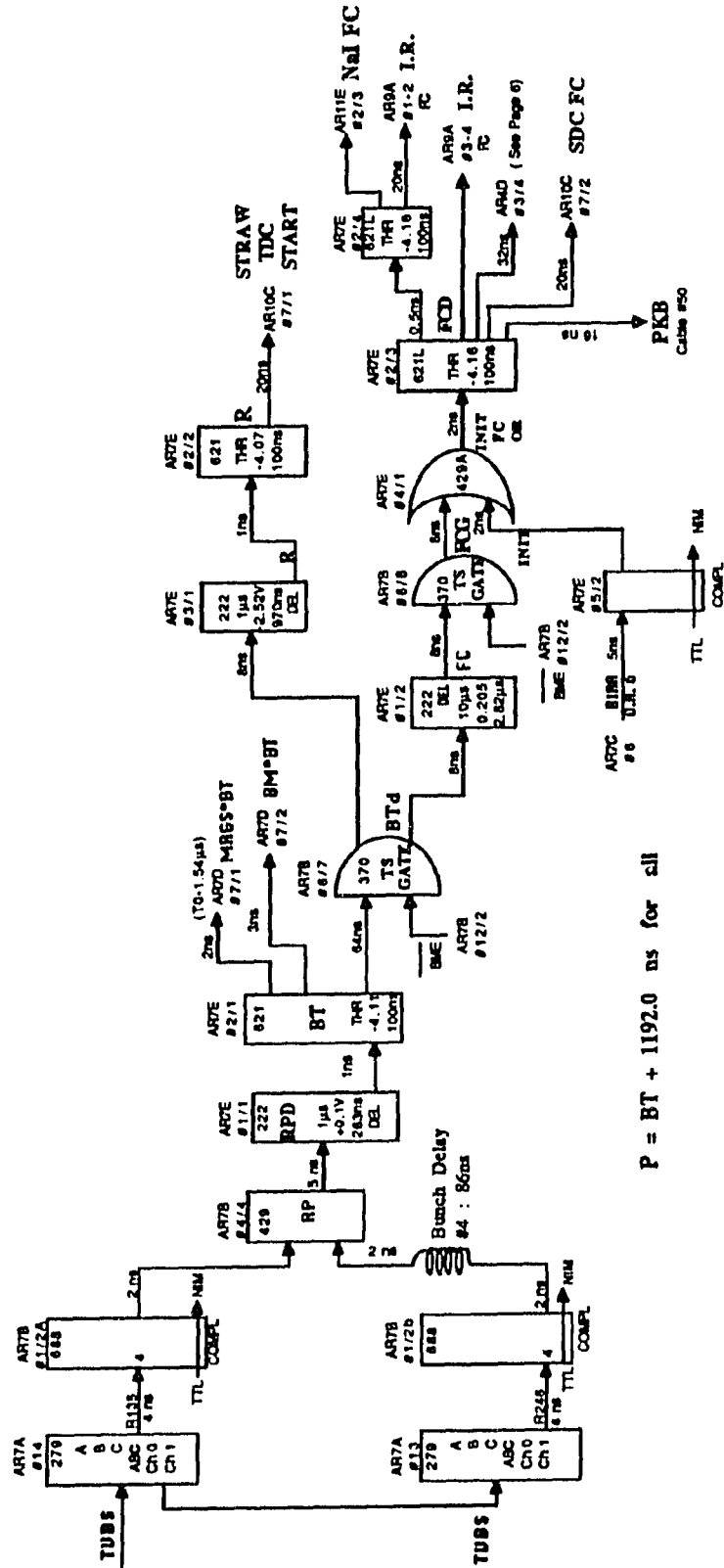
Figure A.2: Trigger timing: B.

Figure A.3: Trigger gating.
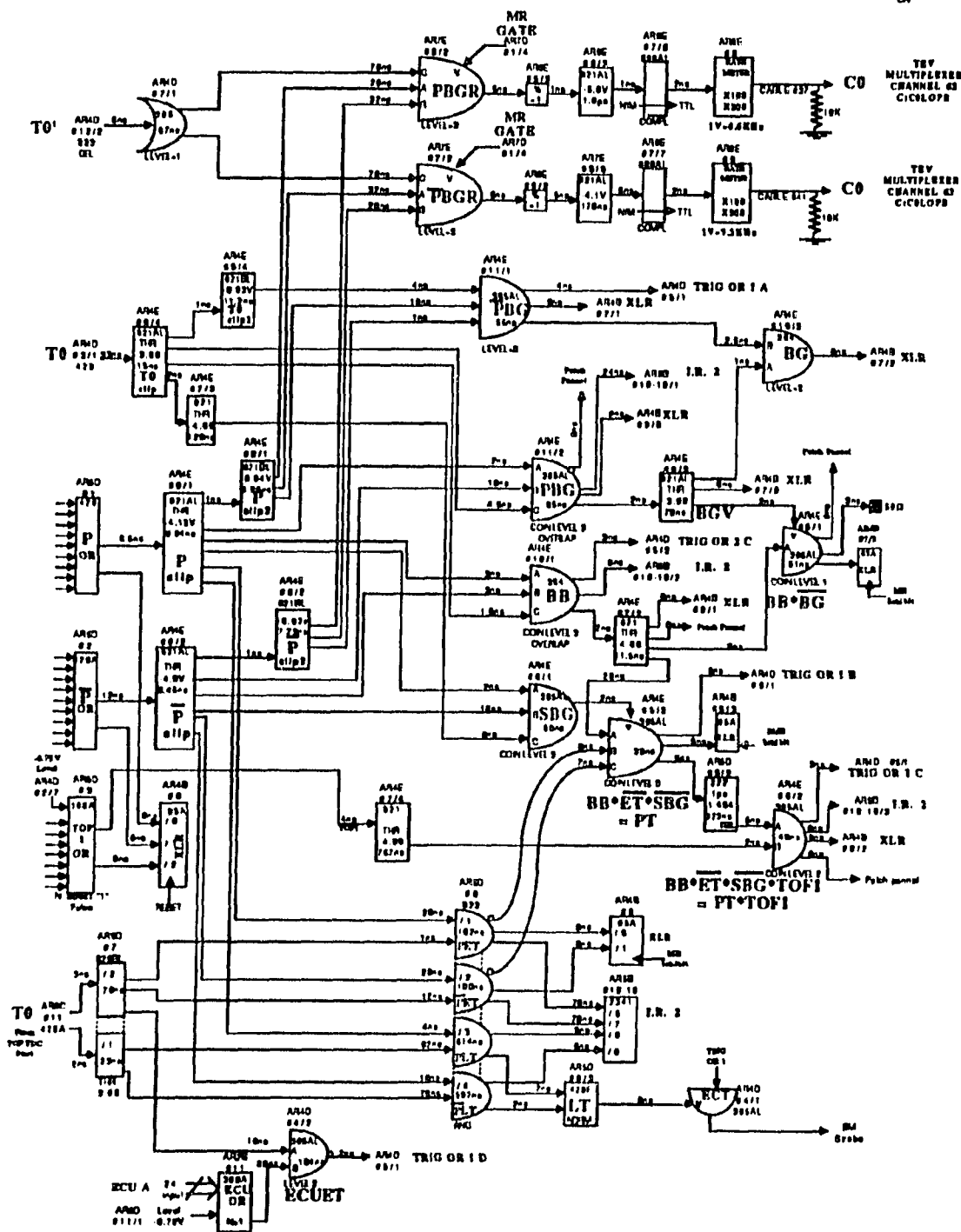
TRIGGER SOURCES

Figure A.4: Trigger sources.

Figure A.5: Trigger summation.

155

CTC TRIGGER

CTC DEAD TIME

Figure A.6:   CTC trigger.

Figure A.7: Hodoscope and TOF.

158

SDC TDC

12/8/88
CW   P 7
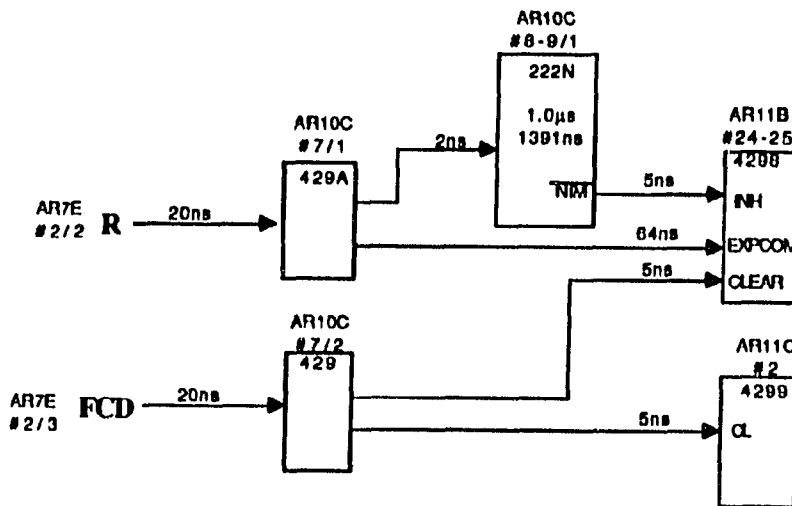
BEAM POSITION MONITOR
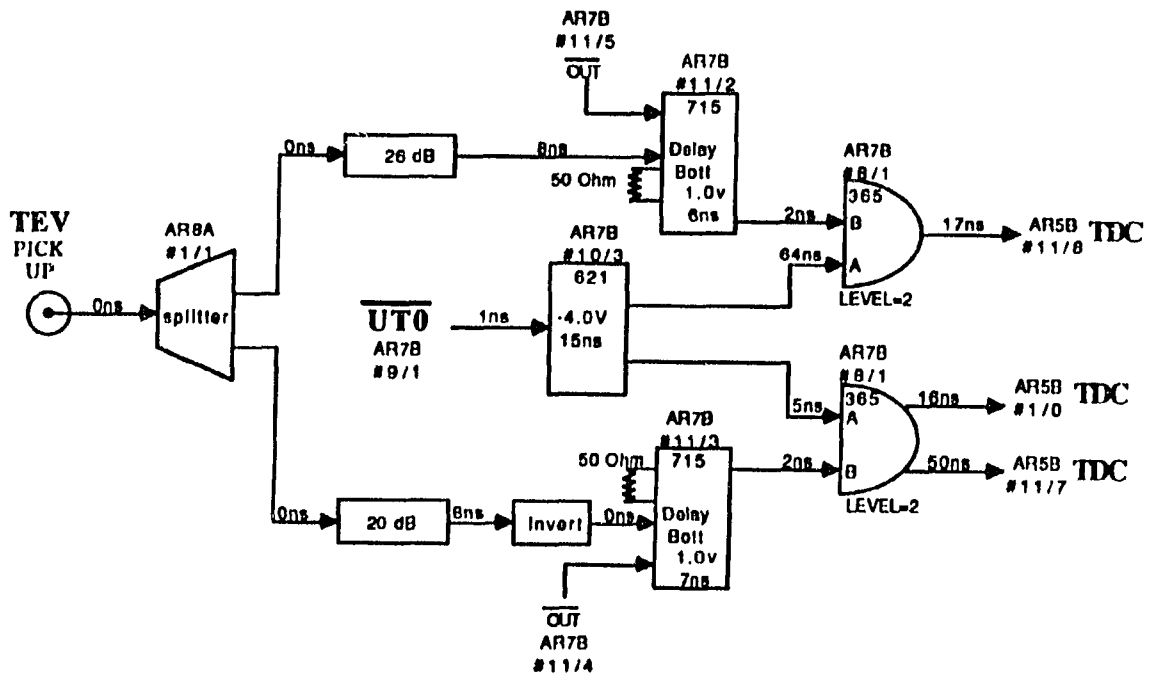
Figure A.8:   Straw chamber TDC and beam position monitor.
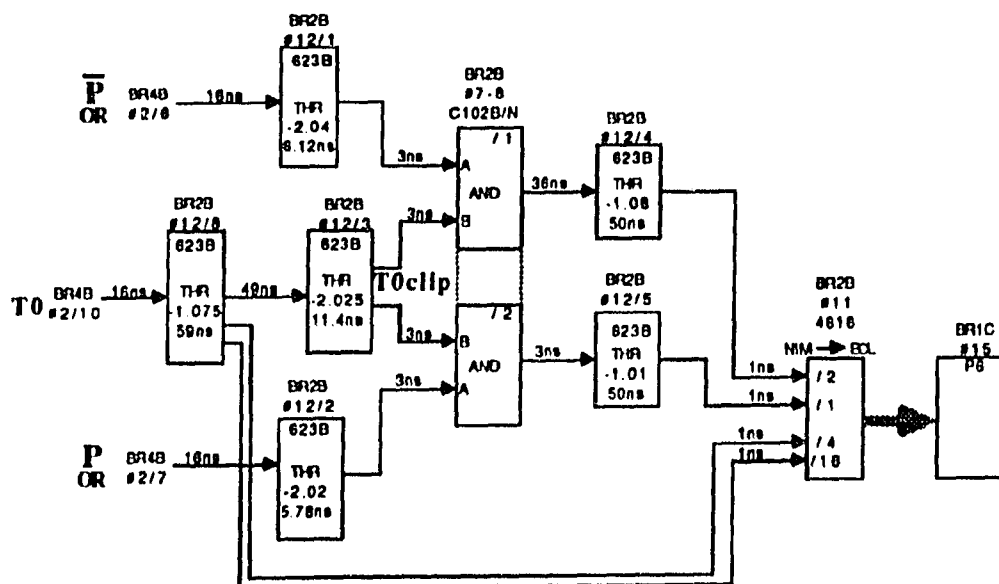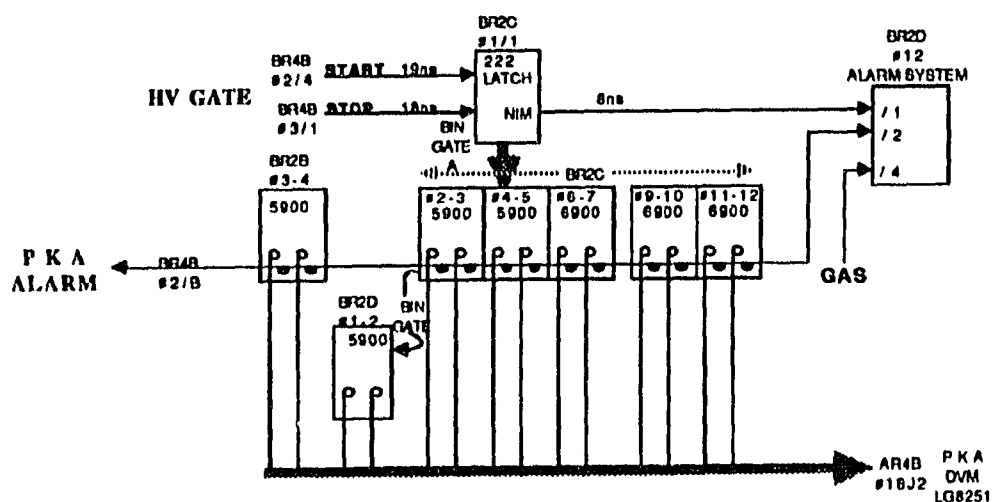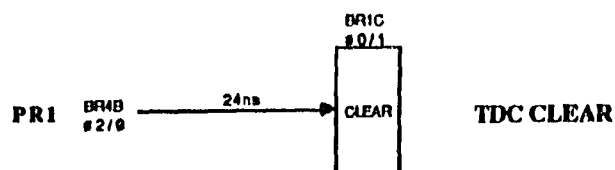
Figure A.9: Wisconsin systems.

160
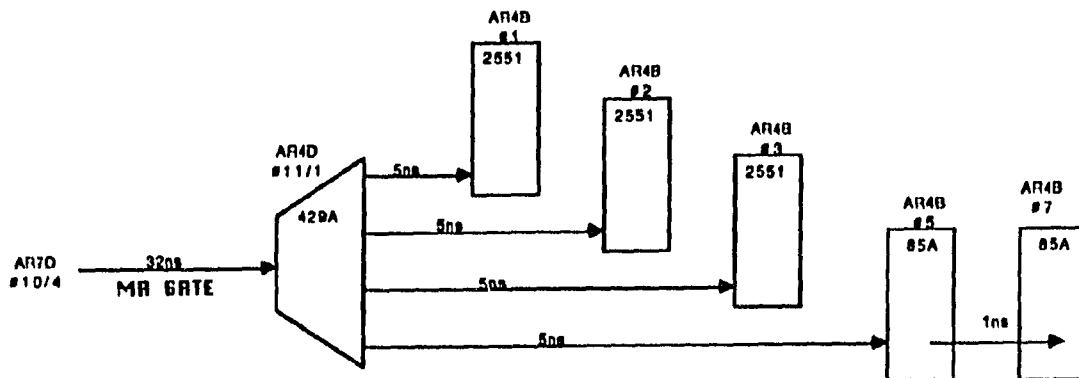
Figure A.10: Scaler inhibit and luminosity counters.
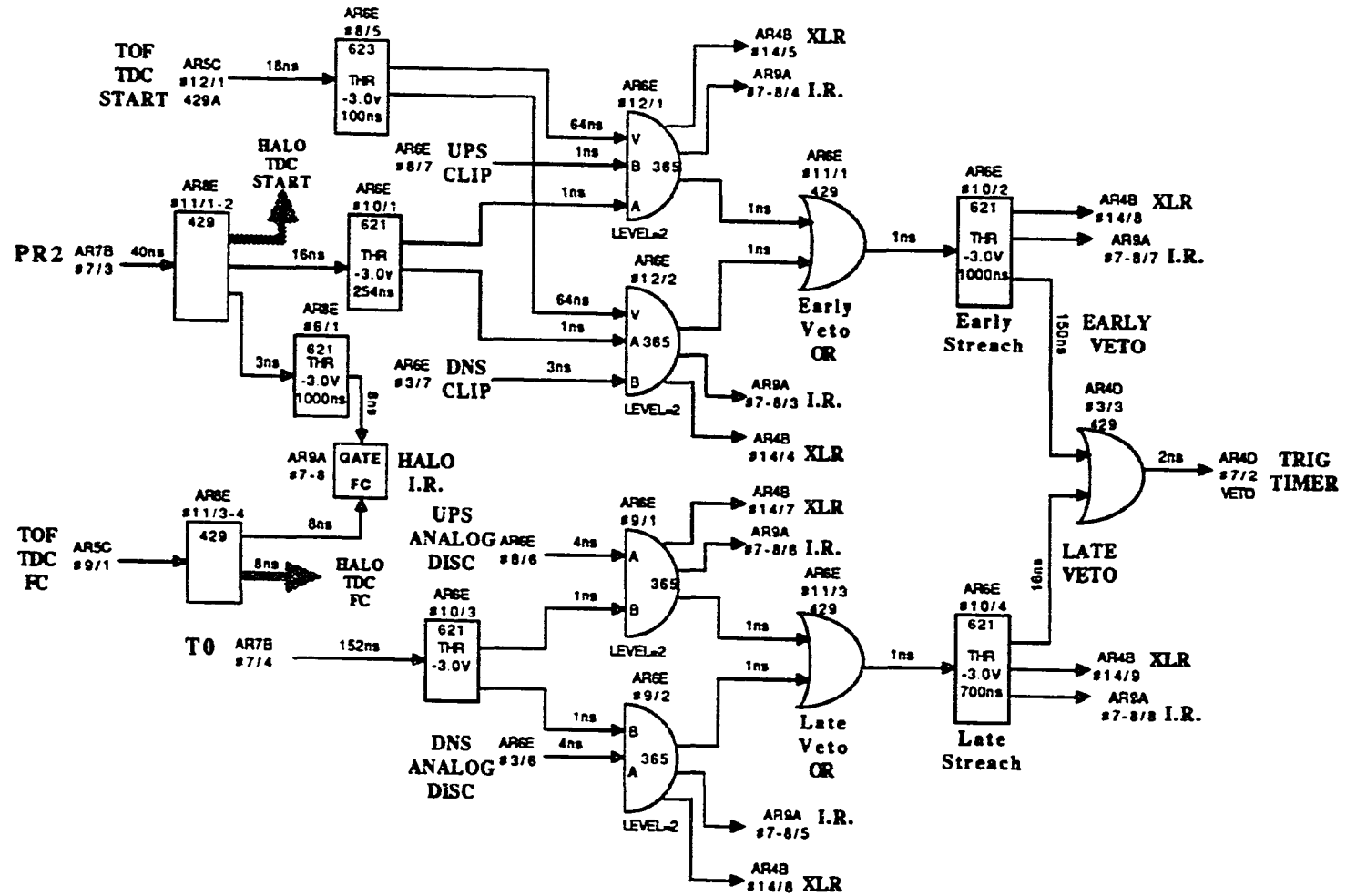
Figure A.11: Halo veto counters.
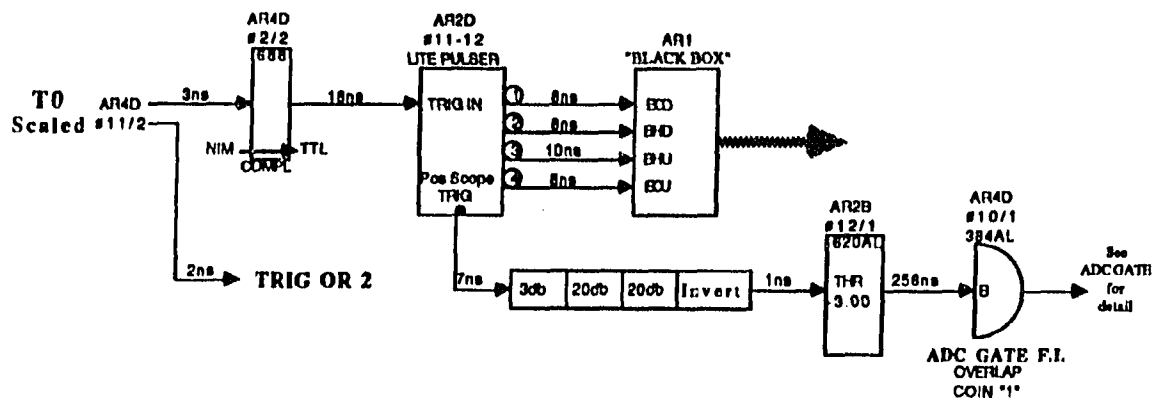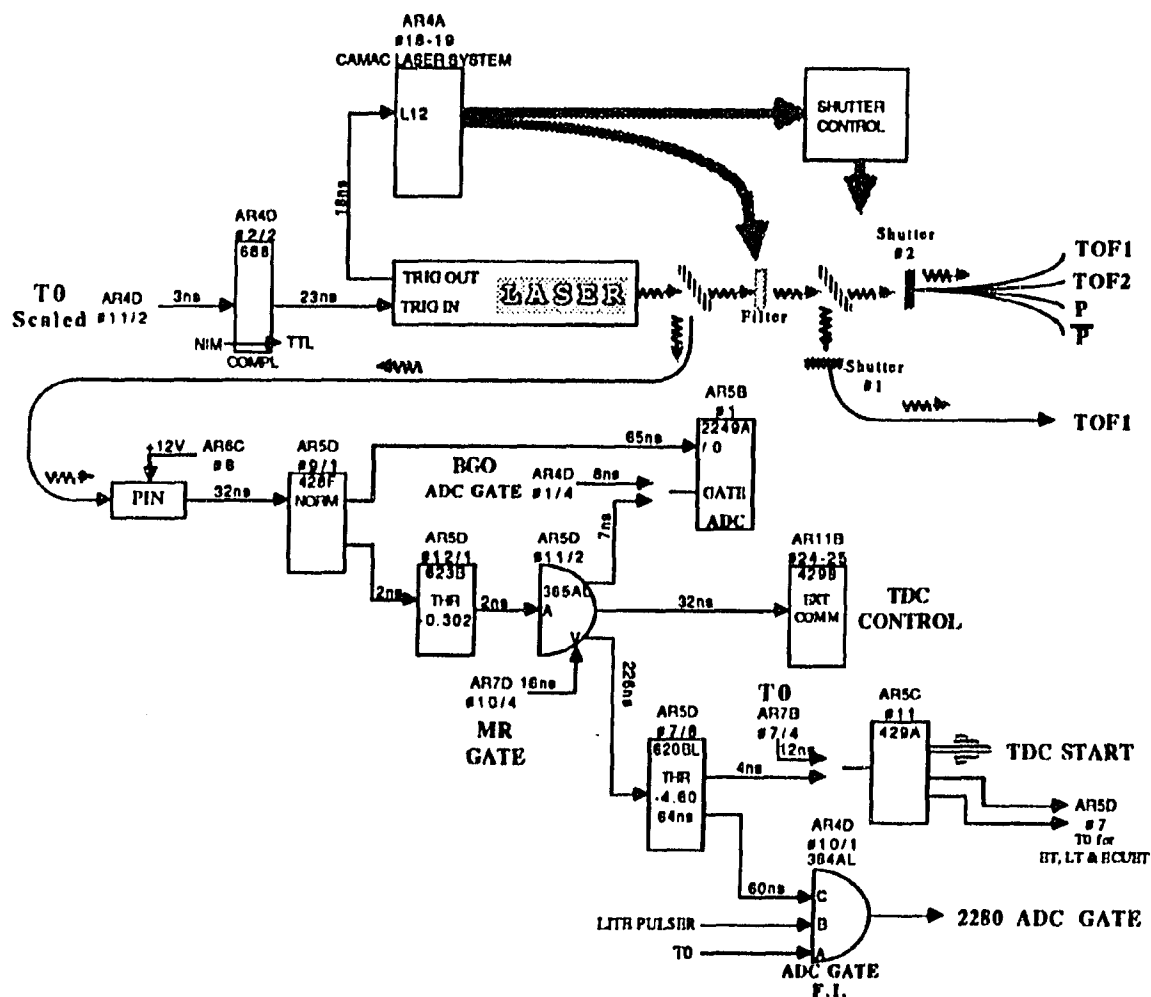
Figure A.12: Light pulser and laser trigger.

APPENDIX B. TRIGGER PROCESSOR SETUP

Trigger processor settings in the '88-'89 runs are summarized here as a reference for un-scaling the multiplicity distributions. Use of trigger bits is essential in identifying the source of a trigger and how an event was to be treated. The correspondence of trigger bits and trigger channels can be found in figure 4.6, 4.8 and 4.10. In Wisconsin DST notations they are:

- AR5B#20-21 = IR_TWO

- AR9A#1-2 = ITRGB

Bits are labeled from bit-1 to bit-16 in the figures. Most of the non-scaling and testing trigger setups are not included in this appendix.

Pre-HNC Configuration

In pre-HNC setups, the spectrometer used SM39/1-4 and the CTC used SM40/1-4, where SM40/1-4 means Summing Module number 40, prescaler output number one to four. In table B.1 the order of the rows in each setting is realized as multiplicity binning, scaling factors, and optionally other requirements. In this configuration over 20 trigger setups were created within the period of Jul.20 '88 – Aug.17 '88, only those could be unscaled are listed.

Table B.1: Pre-HNC trigger processor settings.

	Spectrometer Branch				CTC Branch			
	SM39/1	SM39/2	SM39/3	SM39/4	SM40/1	SM40/2	SM40/3	SM40/4
TPM2	1-20	21-47	48-82	83-240	1-20	21-47	48-82	83-240
	2	3	2	1	2	3	2	1
TPM3	1-20	21-60	61-92	93-240	1-20	21-60	61-92	93-240
	3	6	2	1	3	6	2	1
TPM4	1-20	21-60	61-100	101-240	1-20	21-60	61-100	101-240
	4	8	3	1	4	8	3	1
TP02100	1-40	41-80	81-120	121-240	121-240	121-240	121-240	121-240
	3	2	1	1	1	1	1	1
TP02040	1-40	41-80	81-120	121-240	1-40	41-80	81-120	121-240
	3	2	1	1	60	40	20	1
TP04100	1-40	41-80	81-120	121-240	121-240	121-240	121-240	121-240
	9	7	2	1	1	1	1	1
TP04040	1-40	41-80	81-120	121-240	1-40	41-80	81-120	121-240
	9	7	2	1	60	40	20	1
TP04060	1-40	41-80	81-120	121-240	1-40	41-80	81-120	121-240
	9	7	2	1	120	80	40	1
TP04120	1-40	41-80	81-120	121-240	1-40	41-80	81-120	121-240
	9	7	2	1	240	160	80	1
TPT9	1-40	41-80	81-120	121-240	1-20	21-60	61-100	101-240
	17	13	4	1	4	8	3	1
TP09100	1-40	41-80	81-120	121-240	121-240	121-240	121-240	121-240
	17	13	4	1	1	1	1	1
TP09120	1-40	41-80	81-120	121-240	1-40	41-80	81-120	121-240
	17	13	4	1	240	160	80	1
ST09120	$TP09120 * \bar{p} > 1$							
TP09120A	$TP09120 * ((ECU>16)\ .or.\ (ECD<50))$							
TQTEST	1-8	9-58	59-122	123-240	1-8	9-58	59-122	123-240
	1	1	1	1	1	1	1	1
	$(ECU>16)\ .or.\ (ECD<50)$							
TQ09330A	1-8	9-58	59-122	123-240	1-8	9-58	59-122	123-240
	3	24	9	1	120	960	240	1
	$(ECU>16)\ .or.\ (ECD<50)$							
TQ05200A	1-8	9-58	59-122	123-240	1-8	9-58	59-122	123-240
	2	12	4	1	60	480	160	1
	$(ECU>16)\ .or.\ (ECD<50)$							
TQ05200B	1-8	9-58	59-122	123-240	SM39/4			
	2	12	4	1				
	–	–	–	EC>5	$(EC>5) \equiv (ECU>5) * (ECD>5)$			

HNC Configuration

The HNC configuration was used between Aug.18 '88 and Sep.28 '88. The most commonly used settings were HNC and HNCP. HT and HR are synonymous to HNCP. TRIGG2 and other unlisted setups were just transitional and shouldn't be taken too seriously. The convention of table B.2 is the same as table B.1. Non-scaling triggers in HNC configuration normally used TTS and CTTS channels with all high multiplicity windows disabled.

Table B.2:   HNC trigger processor settings.

	Spectrometer Branch				CTC Branch			
	SM39/5 TTS	SM39/6 R3	SM39/7 R2	SM39/8 R1	SM39/1 CTTS	SM39/2 CR3	SM39/3 CR2	SM39/4 CR1
HNC	0-240	62-79	80-94	95-240	0-240	105-119	120-129	130-240
	80	1	1	1	480	1	1	1
	−	−	EC>11	EC>11	−	EC>11	EC>11	EC>11
HNCP	0-240	63-79	80-94	95-240	0-240	107-119	120-129	130-240
	80	1	1	1	480	1	1	1
	−	−	EC>11	EC>11	−	EC>11	EC>11	EC>11
HNCQ	0-240	63-79	80-94	95-240	0-240	107-119	120-129	130-240
	80	1	1	1	480	1	1	1
	−	−	−	−	−	EC>11	EC>11	EC>11
TRIGG2	0-240	65-79	80-94	95-240	0-240	105-119	120-129	130-240
	80	1	1	1	480	1	1	1
	−	−	EC>11	EC>11	−	EC>11	EC>11	EC>11

HS Configuration

HS configuration was used for the rest of the '88-'89 runs. After a few tries the HS series settled for HS6. S1 series were basically HS6 with different scaling factors plus spectrometer track requirements.

Table B.3: HS trigger processor settings.

	SM39/5 TTS	SM39/6 R3	SM39/7 R2	SM39/8 R1	SM39/1 CTTS	SM39/2 CR3	SM39/3 CR2	SM39/4 CR1
HS1	2-57	58-73	74-83	84-101	102-111	112-119	120-135	136-240
	174	14	6	7	2	1	1	1
	–	–	–	–	EC>11	EC>11	EC>11	EC>11
	–	–	–	–	–	–	$\bar{p}>4$	$\bar{p}>4$
HS2	2-57	58-73	74-83	84-101	102-111	112-119	120-135	136-240
	87	16	8	7	3	1	1	1
	–	–	–	–	EC>11	EC>11	EC>11	EC>11
	–	–	–	–	–	–	$\bar{p}>4$	$\bar{p}>4$
HS3	2-57	58-73	74-83	84-101	102-111	112-119	120-135	136-240
	60	20	10	8	4	2	1	1
	–	–	–	–	EC>11	EC>11	EC>11	EC>11
	–	–	–	–	–	–	$\bar{p}>4$	$\bar{p}>4$
HS4	2-57	58-73	74-83	84-101	102-111	112-119	120-135	136-240
	60	26	14	10	6	3	2	1
	–	–	–	–	EC>11	EC>11	EC>11	EC>11
	–	–	–	–	–	–	$\bar{p}>4$	$\bar{p}>4$
HS5	2-57	58-73	74-83	84-101	102-111	112-127	128-143	144-240
	60	26	14	10	6	3	2	1
	–	–	–	–	EC>11	EC>11	EC>11	EC>11
	–	–	–	–	–	–	$\bar{p}>4$	$\bar{p}>4$
HS6	2-57	58-73	74-83	84-101	102-111	112-127	128-143	144-240
	60	26	14	10	6	3	1	1
	–	–	–	–	EC>11	EC>11	EC>11	EC>11
	–	–	–	–	–	–	$\bar{p}>4$	$\bar{p}>4$

Table B.3   (Continued)

	SM39/5 TTS	SM39/6 R3	SM39/7 R2	SM39/8 R1	SM39/1 CTTS	SM39/2 CR3	SM39/3 CR2	SM39/4 CR1
S1A	2-57	58-73	74-83	84-101	102-111	112-127	128-143	144-240
	1	1	1	1	1	1	1	1
	-	-	-	-	EC>11	EC>11	EC>11	EC>11
	-	-	-	-	-	-	$\bar{p} > 4$	$\bar{p} > 4$
S1A2	S1A with scaling factors = 2							
S2A2	Same as S1A2							
S1A4	S1A with scaling factors = 4							
S1B	2-57	58-73	74-83	84-101	102-111	112-127	128-143	144-240
	6	5	5	4	2	1	1	1
	-	-	-	-	EC>11	EC>11	EC>11	EC>11
	-	-	-	-	-	-	$\bar{p} > 4$	$\bar{p} > 4$
S1C	2-57	58-73	74-83	84-101	102-111	112-127	128-143	144-240
	20	16	14	10	6	3	1	1
	-	-	-	-	EC>11	EC>11	EC>11	EC>11
	-	-	-	-	-	-	$\bar{p} > 4$	$\bar{p} > 4$
S1BC	2-57	58-73	74-83	84-101	102-111	112-127	128-143	144-240
	12	9	8	6	3	2	1	1
	-	-	-	-	EC>11	EC>11	EC>11	EC>11
	-	-	-	-	-	-	$\bar{p} > 4$	$\bar{p} > 4$
S1D	2-57	58-73	74-83	84-101	102-111	112-127	128-143	144-240
	35	27	23	16	10	5	2	1
	-	-	-	-	EC>11	EC>11	EC>11	EC>11
	-	-	-	-	-	-	$\bar{p} > 4$	$\bar{p} > 4$

APPENDIX C. THE MAXIMUM ENTROPY METHOD

The maximum entropy method in the information theory[57] provides a constructive criterion for setting up probability distributions on the basis of partial knowledge. It is referred to as the least biased estimate on the given information; i.e. maximally noncommittal with regard to missing information[58]. Although thermodynamical terms, such as entropy function, are employed in the theory, the method can be derived without involving those concepts or any subjective considerations[59, 60].

Consider a problem as the following. A quantity x is capable of assuming the discrete values x_i, where $i = 1, 2, \cdots, n$. We want to find the corresponding probability distribution p_i with the knowledge of just a set of constraints in the form of the expectation values of the functions $A_k(x)$:

$$\sum_{i=1}^{n} p_i A_{ik} = b_k, \qquad \text{(C.1)}$$

where $k = 1, 2, \cdots, m$ and $m < n$.

The theory states that the solution should be the probability distribution that maximizes the entropy subject to the known constraints. Where, entropy is defined as :

$$S = - \sum_{i=1}^{n} p_i \ln p_i. \qquad \text{(C.2)}$$

This problem can be solved by using the Lagrangian multiplier method. To

maximize S, we require

$$\delta S = - \sum_{i=1}^{n} [(\delta p_i) \ln p_i + \delta p_i] = 0. \tag{C.3}$$

Meanwhile, eq. (C.1) gives

$$\sum_{i=1}^{n} (\delta p_i) A_{ik} = 0. \tag{C.4}$$

Now, introduce the Lagrangian multipliers λ_k and sum eq. (C.4) into eq. (C.3). We obtain

$$- \sum_{i=1}^{n} (\ln p_i + 1) \delta p_i + \sum_{k=1}^{m} \lambda_k \sum_{i=1}^{n} A_{ik} \delta p_i = 0$$

or

$$- \sum_{i=1}^{n} (\ln p_i + 1 - \sum_{k=1}^{m} \lambda_k A_{ik}) \delta p_i = 0. \tag{C.5}$$

Since $\delta p_i \neq 0$, we come to the solution

$$p_i = \exp(\sum_{k=1}^{m} \lambda_k A_{ik} - 1), \tag{C.6}$$

which, put into eq. (C.1), gives

$$\sum_{i=1}^{n} A_{ik} \exp(\sum_{k=1}^{m} \lambda_k A_{ik} - 1) = b_k. \tag{C.7}$$

The last expression is a set of m non-linear equations with m unknown λ_k's. Together with eq. (C.6) the probability distribution p_i is uniquely determined. In this thesis eq. (C.7) was solved with Newton-Raphson method and the linear algebraic equations involved in the Newton-Raphson method was solved with LU decomposition[61].

BIBLIOGRAPHY

[1] L. J. Gutay et. al., "Search for a deconfined quark gluon phase of strongly interacting matter in $\overline{P}$-P interactions at $\sqrt{s} \approx 2$ TeV," Proposal for E-735, 1983.

[2] L. Van Hove, "Multiplicity dependence of P_t Spectrum as a possible signal for a phase transition in hadronic collisions," Phys. Lett. 118 B (1982) 138.

[3] UA5 Collaboration, G.J.Alner et al; "Multiplicity distributions in different pseudorapidity intervals at a CMS energy of 540 GeV," Phys Lett. 160B (1985) 193.

[4] UA5 Collaboration, G.J.Alner et al; "A new empirical regularity for multiplicity distributions in place of KNO scaling," Phys Lett. 160B (1985) 199.

[5] UA5 Collaboration, G.J.Alner et al; " Charged particle multiplicity distributions at 200 and 900 GeV C.M. energy," Z Phys. C 43 357 (1989).

[6] R.Szwed, "Present status of KNO scaling and negative binomial distribution," Proceedings of XVII international Symposium on Multiparticle Dynamics, Seewinkel, Austria, 1986, p.663.

[7] R.Szwed, "Multiplicity distributions in proton-proton and nucleus-nucleus collisions," Warsaw Univ. Preprint IFD/6/1989, FNAL#91751.

[8] UA5 Collaboration, C.Fuglesang, " UA5 multiplicity distributions and fits of various functions," Preprint CERN-EP/89-135 (1989), Proc. of Multiparticle Dynamics, La Thuile, Italy, 10-22 March 1989.

[9] G.Giacomelli, "Inclusive and Semi-Inclusive Hadron Interactions at ISR and Collider Energies," Int'l Jr. of Mod. Phys. 5A (1990) 223.

[10] A.Breakstone, et al; "Charged Multiplicity Distributions in rapidity bins for pp collisions at $\sqrt{s} = 31, 44$ and 62 GeV," CERN/EP 88-123.

[11] R.V.Gavi and H.Satz, *"Charged Hadron Multiplicity at collider energies,"*Phys. Lett. 112B (1982) 413.

[12] R.P.Feynman, *"Very High-Energy Collisions of Hadrons,"* Phys. Rev. Lett. 23 (1969) 1415.

[13] E.Fermi, Progr. Theor. Phys. 1 (1950) 570.

[14] L.D.Landau, *"On the Multiple Production of Particles during Collisions of Fast Particles,"* Izv. Akad. Nauk SSSR, ser. fiz.,17 (1953) 51.

[15] A.H.Mueller, *"On the Multiplicity of Hadrons in QCD Jets,"* Phys. Lett. 104B (1981) 161.

[16] A.Wroblewski, *"Multiplicity Distributions in Proton-Proton Collisions,"* Acta Phys. Pol. B4 (1973) 857.

[17] Z.Koba, H.B.Nielsen, P.Olesen, *"Scaling of Multiplicitiy Distributions in High Energy Hadron Collisions,"* Nucl. Phys. B40 (1972) 317.

[18] A.Chodos, M.H.Rubin, R.L.Sugar, *"Koba-Nielsen-Olesen Scaling at Finite Energies,"* Phys. Rev. D8 (1973) 1620.

[19] A.I.Golokhvastov, *"Possible Generalization of the Concept of similarity of the Multiplicity Distributions for Nonasymptotic Energies,"* Sov. J. Nucl. Phys. 27 (1978) 430.

[20] A.I.Golokhvastov, *"On the Energy Dependence of the Multiplicity of Negative Particles in pp Interactions,"* Sov. J. Nucl. Phys. 30 (1979) 128.

[21] R.Szwed, *"Recent Status of KNO Scaling and Negative Binomial Distribution,"* Proc. of the XVII Int'l Symp. on Multiparticle Dynamics, Seewinkel, Austria 1986, p.663, Preprint IFD/3/86.

[22] R.Szwed, G.Wrochna, *"New ISR and SPS collider multiplicity data and the Golokhvastov generalization of the KNO Scaling,"* Z. Phys. C29 (1985) 255-265.

[23] A.J.Buras, et al., *"Multiplicity Scaling at Low Energies, A Generalized Wroblewski-Formula and the Leading Particle Effect,"* Phys. Lett. 47B (1973) 251.

[24] R.Szwed, G.Wrochna, A.K.Wroblewski, *"Mystery of the Negative Binomial Distribution,"* Acta Phys. Pol. B19 (1988) 763.

[25] A.Giovannini, L.Van Hove, *"Negative Binomial Multiplicity Distributions in High Energy Hadron Collisions,"* Z. Phys. C30 (1986) 391.

[26] A.Giovannini, L.Van Hove, *"Negative Binomial Properties and Clan Structure in Multiplicity Distribution,"* Acta Phys. Polon. B19 (1988) 495.

[27] T.K.Gaisser, et al., *"Multiplicities in a QCD-Motivated Description of Very High Energy Particle Interactions,"* Phys. Lett. 166B (1986) 219.

[28] G.J.Alner, et al., *"UA5: A General Study of Proton-Antiproton Physics at sqrts = 546 GeV,"* Phys. Rep. 154 (1987) 247-383.

[29] A.Breakstone, et al., *"Charged Multiplicity Distribution in pp Interactions at CERN ISR Energies,"* Phys. Rev. D30 (1984) 528.

[30] C.W.Schmidt, et. al., *"A 50-mA Negative Hydrogen-Ion Source,"* IEEE Trans. on Nucl. Sci. 26 (1979) 4120.

[31] C.D.Curtis, et. al., *"LINAC H⁻ Beam Operation and Uses at Fermilab,"* IEEE Trans. on Nucl. Sci. 26 (1979) 3760.

[32] D.F.Cosgrove, et. al., *"Injection Method in the Fermilab Booster,"* IEEE Trans. on Nucl. Sci. 24 (1977) 1423.

[33] C.Hojvat, et. al., *"The Multiturn Charge Exchange Injection System for the Fermilab Booster Accelerator,"* IEEE Trans. on Nucl. Sci. 26 (1979) 3149.

[34] C.Hojvat, et. al., *"Stripping Foils for Multiturn Charge Exchange Injection Into the Fermilab Booster,"* IEEE Trans. on Nucl. Sci. 26 (1979) 4009.

[35] R.C.Webber, et. al., *"Measurement of the Electron Loss Cross Sections for Negative Hydrogen Ions on Carbon at 200 MeV,"* IEEE Trans. on Nucl. Sci. 26 (1979) 4012.

[36] D. A. Edwards, *"The Tevatron; Introduction,"* Physics of Particle Accelerators, AIP Conference Proceedings 184, (1989).

[37] Emittance is the dimension of the beam in the phase space. Definitions of some accelerator terminologies can be found in :
E.J.N.Wilson, *"Proton Synchrotron Accelerator Theory,"* CERN 77-07, Lectures given in the Academic Training Programme of CERN 1975-1976
F.Bonaudi, *"Introduction to Particle Accelerators,"* Lectures given in the Academic Training Programme of CERN 1969-1970.

[38] J. Peoples, *"Antiproton Source,"* Physics of Particle Accelerators, AIP Conference Proceedings 184, (1989).
For a description of stochastic cooling see D.Mohl, et. al., *"Physics and Technique of Stochastic Cooling,"* Phys. Rep. 58C (1980) 73-119.

[39] G. Dugan, *"Tevatron Status"* Fermilab publication TM-1576. Presented at the 1989 IEEE Particle Accelerator Conference, Chicago, Illinois,March 20-23, 1989.

[40] C. Allen et al., *"A Cylindrical Drift Chamber for the Measurement of High Charged-Particle Multiplicities in Hadronic Events,"* Nucl. Instr. Meth. A294 (1990) 108-116.

[41] S. Tufte and C. Findeisen, *"Some Preliminary End Cap Chamber Results,"* E-735 internal report, 10-Dec-89.

[42] C. S. Lindsey et al., *"Degradation of Plastic Scintillator Exposed to Tevatron Tunnel Background Radiation,"* Nucl. Inst. & Meth. A 254 (1987) 212.

[43] E. W. Anderson et al., *"A Scintillator Hodoscope at the Tevatron Collider,"* Nucl. Inst. & Meth. A295 (1990) 86-93.

[44] T. Alexopoulos, et al., *"A One Meter Long Low-mass Mini Drift Vertex Chamber Used at the Tevatron Collider,"* Submitted to Nucl. Inst. & Meth.

[45] S. Oh et al., *"Design and performance of straw tube drift chambers,"* To be published.

[46] S. Banerjee, et al., *"Design and Performance of a Time-Of-Flight System for Particle Identification at the Fermilab Collider,"* Nucl. Inst. & Meth. A 269 (1988) 121.

[47] C. Hojvat, et al., *"Multiplicity Trigger Processor for a Quark-Gluon Plasma Search,"* To be submitted to Nucl. Inst. & Meth.

[48] D. Burch, V. White, *"An RSX-11M Device Driver Implementing Network Protocols on the DR-11W,"* Fermilab Computing Department Library, PN-162, Nov,1982.

[49] *"Bison Interrupt & Gate Control,"* Fermilab Computing Department Library, IIN-3.2.

[50] D. Quarrie, *"Data Acquisition System Programmers Reference Manual,"* CDF Note no. 166, Fermilab Computing Department Library, PN-251.03.

[51] C.Wang, E.W.Anderson, *"Beam Shift Effects on Hodoscope,"* E735-ISU-1-5-90, E735 internal report.

[52] N. Morgan, *"Beam Location in x, y as measured by the CTC,"* E735-VPI-1-29-90, E735 internal report.

[53] G.J.Alner, et al., *"The UA5 High Energy $\bar{p}p$ Simulation Program,"* Nucl. Phys. B291 (1987) 445-502.

[54] R.Brun et al., *"GEANT3 – User's Guide,"* DD/EE/84-1, Sep.1987, Data Handling Division, CERN.

[55] C.Fuglesang, *"A Method for Correcting Observed Distributions of Multiplicities using the Maximum Entropy Principle,"* Nucl. Inst. & Meth. A278 (1989) 765-773.

[56] J.Skilling, *"The maximum entropy method,"* Nature 309 (1984) 748.

[57] C.E. Shannon, *"A Mathematical Theory of Communication,"* The Bell System Tech. J. 27 (1948) 379, 623. Reprinted in C.E.Shannon and W.Weaver, *"The Mathematical Theory of Communication,"* (Univ. of Ill. Press, Urbana, (1949).

[58] E.T.Janes, *"Information Theory and Statistical Mechanics,"* Phys. Rev. 106 (1957) 620.

[59] Y.Tikochinsky et. al., *"Consistent Inference of Probabilities for Reproducible Experiments,"* Phys. Rev. Lett. 52 (1984) 1357.

[60] J.E.Shore, R.W.Johnson, *"Axiomatic Derivation of the Principle of Maximum Entropy and the Principle of Minimum Cross-Entropy,"* IEEE Trans. Inform. Theory IT-26 (1980) 26, and IT-29 (1983) 942.

[61] W.H.Press, B.P.Flannery, S.A.Teukolsky, W.T.Vetterling, *"Numerical Recipes,"* Cambridge University Press, 1987.